

# **Irradiation Effects on Reinforced Concrete Structures – Experimental and Analytical Study on Irradiated Concrete – Steel Bonding, Modeling and Simulation of Structural Response**



## AVAILABILITY OF REFERENCE MATERIALS IN NRC PUBLICATIONS

### NRC Reference Material

As of November 1999, you may electronically access NUREG-series publications and other NRC records at NRC's Library at [www.nrc.gov/reading-rm.html](http://www.nrc.gov/reading-rm.html). Publicly released records include, to name a few, NUREG-series publications; *Federal Register* notices; applicant, licensee, and vendor documents and correspondence; NRC correspondence and internal memoranda; bulletins and information notices; inspection and investigative reports; licensee event reports; and Commission papers and their attachments.

NRC publications in the NUREG series, NRC regulations, and Title 10, "Energy," in the *Code of Federal Regulations* may also be purchased from one of these two sources.

#### 1. The Superintendent of Documents

U.S. Government Publishing Office  
Washington, DC 20402-0001  
Internet: <http://bookstore.gpo.gov/>  
Telephone: 512-1800  
Fax: (202) 512-2104

#### 2. The National Technical Information Service

5301 Shawnee Road  
Alexandria, VA 22312-0002  
Internet: <http://www.ntis.gov/>  
1-800-553-6847 or, locally, (703) 605-6000

A single copy of each NRC draft report for comment is available free, to the extent of supply, upon written request as follows:

Address: **U.S. Nuclear Regulatory Commission**  
Office of Administration  
Program Management and Design  
Service Branch  
Washington, DC 20555-0001  
E-mail: [Reproduction.Resource@nrc.gov](mailto:Reproduction.Resource@nrc.gov)  
Facsimile: (301) 415-2289

Some publications in the NUREG series that are posted at NRC's Web site address [www.nrc.gov/reading-rm/doc-collections/nuregs](http://www.nrc.gov/reading-rm/doc-collections/nuregs) are updated periodically and may differ from the last printed version. Although references to material found on a Web site bear the date the material was accessed, the material available on the date cited may subsequently be removed from the site.

### Non-NRC Reference Material

Documents available from public and special technical libraries include all open literature items, such as books, journal articles, transactions, *Federal Register* notices, Federal and State legislation, and congressional reports. Such documents as theses, dissertations, foreign reports and translations, and non-NRC conference proceedings may be purchased from their sponsoring organization.

Copies of industry codes and standards used in a substantive manner in the NRC regulatory process are maintained at—

#### The NRC Technical Library

Two White Flint North  
11545 Rockville Pike  
Rockville, MD 20852-2738

These standards are available in the library for reference use by the public. Codes and standards are usually copyrighted and may be purchased from the originating organization or, if they are American National Standards, from—

#### American National Standards Institute

11 West 42nd Street  
New York, NY 10036-8002  
Internet: <http://www.ansi.org/>  
(212) 642-4900

Legally binding regulatory requirements are stated only in laws; NRC regulations; licenses, including technical specifications; or orders, not in NUREG-series publications. The views expressed in contractor prepared publications in this series are not necessarily those of the NRC.

The NUREG series comprises (1) technical and administrative reports and books prepared by the staff (NUREG-XXXX) or agency contractors (NUREG/CR-XXXX), (2) proceedings of conferences (NUREG/CP-XXXX), (3) reports resulting from international agreements (NUREG/IA-XXXX), (4) brochures (NUREG/BR-XXXX), and (5) compilations of legal decisions and orders of the Commission and Atomic and Safety Licensing Boards and of Directors' decisions under Section 2.206 of NRC's regulations (NUREG-0750), Knowledge Management prepared by NRC staff or agency contractors (NUREG/KM-XXXX).

**DISCLAIMER:** Where the papers in these proceedings have been authored by contractors of the U.S. Government, neither the U.S. Government nor any agency thereof, nor any U.S. employee makes any warranty, expressed or implied, or assumes any legal liability or responsibility for any third party's use or the results of such use, of any information, apparatus, product, or process disclosed in these proceedings, or represents that its use by such third party would not infringe privately owned rights. The views expressed in these proceedings are not necessarily those of the U.S. Regulatory Commission.

# **Irradiation Effects on Reinforced Concrete Structures – Experimental and Analytical Study on Irradiated Concrete – Steel Bonding, Modeling and Simulation of Structural Response**

Manuscript Completed: November 2024

Date Published: July 2025

Prepared by:

Y. Le Pape

M. Alnaggar

E. Tajuelo Rodriguez

A. Brooks

Oak Ridge National Laboratory

One Bethel Valley Road

Oak Ridge, TN 37831

Madhumita Sircar

Technical Lead and NRC Project Manager



## ABSTRACT

This report summarizes the research accomplishments of U.S. Nuclear Regulatory Commission project IAA # 31310018S0021, “Effects of Irradiation on Bond Strength in Concrete Structures”. This project includes a scoping irradiation experiment on reinforced concrete specimens and a numerical simulation study of concrete biological shields that supports the reactor pressure vessel in a pressurized water reactor.

A first-of-a-kind irradiation experiment of reinforced concrete was designed and executed by the Oak Ridge National Laboratory and the Centrum Vizkumu Rež in the Czech Republic. The raw materials for the two types of studied concretes are (1) coarse aggregate consisting of a quartz metachert and a terrigenous felsic sandstone and (2) fine aggregate and cement—were provided by the Japan Concrete Aging Management Program (JCAMP). Use of the same concrete constituents enables comparison with the previously published results obtained by JCAMP regarding plain concrete irradiated in the JEEP II Reactor in Norway. This approach was preferred instead of attempting to choose aggregates to represent those from a particular U.S. Nuclear Power Plant (NPP). This is because aggregates in an NPP are site dependent and vary from plant to plant, and their characterization data are not publicly available. In general, quartz-bearing rocks and sandstones are quite common in the United States.

In this experiment, specimens were irradiated for the duration of approximately 800 days (accounting for outages) in an out-of-core position in the LVR-15 test reactor to achieve  $\sim 10^{19}$  n.cm<sup>-2</sup> ( $E > 0.1$  MeV) of fast neutron fluence and  $\sim 1$  GGy of gamma dose while keeping the irradiation temperatures of the specimens in the 37–52 °C range. A companion experiment exposing a different set of specimens to the temperature from the monitored irradiation temperature alone was conducted in parallel to distinguish the effects of prolonged curing at a moderate temperature from the combined effects of irradiation and temperature. Unirradiated specimens at room temperature were also tested to provide baseline data of reference. Pre- and post-irradiation examination (PIE) and testing included visual and optical microscopy, x-ray computed tomography, mass and dimensional measurements, ultrasound wave velocity measurements, splitting tests, direct compression tests, and bond tests. The PIE and testing data were interpreted using literature data, as well as analytical and numerical models including fast Fourier transform–based nonlinear simulation of aggregate polycrystalline assemblage and meso-scale simulation of plain and reinforced concrete using the lattice discrete particles model (LDPM). A scaling effects study for unirradiated specimens was campaigned by using specimens at three different sets of parameters: specimen size, rebar diameter, and aggregate size. The main findings of the scoping irradiation experiment are (1) the irradiation experiment provided evidence of the importance of fast neutron flux on the radiation-induced expansion of concrete aggregates, and (2) the bond strength of steel reinforcement bars embedded in concrete is governed by the square root of residual compressive strength of the surrounding irradiated concrete. However, an additional scaling factor of approximately 0.75–0.85 was required to determine the bond strength of the specimens built with the #2 bar. Finally, the report also presents the results of the numerical simulation study using LDPM and finite element analysis with the objective of proposing methodological guidelines for the assessment of irradiation effects on in-service irradiated concrete biological shields, specifically the irradiation-induced damage depth in the concrete biological shields.



## FOREWORD

The Office of Regulatory Research (RES) of the U.S. Nuclear Regulatory Commission (NRC) has performed research on the effects of irradiation on concrete structures to support subsequent license renewal activities and long-term operation for nuclear power plants in response to a 2015 User Need Request (UNR) from the Office of Nuclear Reactor Regulation (NRR). In the Staff Requirements Memorandum SRM-SECY-014-0016, the Commission had directed the staff to keep the Commission informed regarding progress on concrete research activities, including the effects of irradiation on concrete. NUREG/CR 7153 Vol. 4, 'Expanded Materials Degradation Assessment (EMDA): Aging of Concrete and Civil Structures,' 2014, had identified irradiation-related concrete degradation as an area of low knowledge and high significance. Irradiation-related concrete degradation has been identified as a potential issue for two-loop and three-loop pressurized water reactors because they accumulate higher neutron fluence in the concrete around the RPV supports during long term operations. Since then, knowledge has improved globally through research, which includes this accelerated irradiation experimental study using research reactors.

Potential impacts of irradiation-related damage of concrete depend on several factors including the type of concrete, type of aggregates, level of irradiation, design configurations, and details of the RPV supports. Structures exposed to radiation are usually difficult to access for existing inspection methods which limits the options for monitoring and aging management. The RES research program addresses technical issues for which remaining uncertainties challenge applicants as well as staff guidance and reviews of applications for license renewal. The NRC research activities collaborate with domestic and international institutions through Memoranda of Understanding (MOUs) with the Electric Power Research Institute (EPRI) and the Department of Energy (DOE) and a bi-lateral agreement with the Nuclear Regulation Authority of Japan (NRAJ).

The RES "Radiation Effects on Concrete Structures" research program on irradiation-related concrete addresses uncertainties in the current state of knowledge and deepens that knowledge to inform possible regulatory guidance updates for long term operations. The research results and research reports are also available for use in licensing reviews as appropriate. Under this research UNR, RES has published the following reports:

1. Biwer, B., Ma, D., Xi, Y. and Jing, Y. (2021). Review of Radiation-Induced Concrete Degradation and Potential Implications for Structures Exposed to High Long-Term Radiation Levels in Nuclear Power Plants, NUREG/CR-7280, ANL/EVS-20/8, U.S. Nuclear Regulatory Commission,
2. Xi, Y., Jing, Y., (2021). Radiation Effects on Concrete – An Approach for Modeling Degradation of Concrete Properties, RIL 2021-07, U.S. Nuclear Regulatory Commission,
3. Xi, Y., Jing, Y. (2022). User's Manuals for Coupled Analysis of Irradiated Concrete (CAICE), Technical Letter Report, U.S. Nuclear Regulatory Commission. ML22356A140,
4. Risner, J., Alpan, A. and Yang, J. (2020). Radiation Evaluation Methodology for Concrete Structures, No. NUREG/CR-7281 ORNL/SPR-2020/1572, U.S. Nuclear Regulatory Commission.

5. Le Pape. Y, Tajuelo Rodriguez. et. al (2022). Assessment of the San Onofre Concrete Susceptibility against Radiation Damage, RIL 2022-07, U.S. Nuclear Regulatory Commission
6. Le Pape. Y, Alnaggar. M., Tajuelo Rodriguez. E., Brooks. A. (2025). Irradiation Effects on Reinforced Concrete Structures. Experimental and Analytical Study on Irradiated Concrete-Steel Bonding, Modeling and Simulation of Structural Response, NUREG/CR-7312, U.S. Nuclear Regulatory Commission, ML25015A130

Research Report Number 6, summarizes contract accomplishments of Oak Ridge National Laboratory for the U.S. Nuclear Regulatory Commission project IAA # 31310018S0021, "Effects of Irradiation on Steel-Concrete Bond Strength in Concrete Structures". The project includes a scoping irradiation experiment on reinforced concrete specimens and accompanying numerical modeling and simulation studies in an effort to understand the potential behavior of structural concrete (i.e., reinforced concrete) in a biological shield that supports the reactor pressure vessel in a pressurized water reactor. The Road Map of this report for accomplishing this undertaking for the objectives met in the Executive Summary is listed below:

#### Road Map

Chapter 1 presents introduction to this research, including background, overview (why this effort), project scope and strategy, and chapter by chapter research accomplishments.

Chapter 2-5 present the details of the various aspects of this unique experiment which explain the challenges and difficulties of this research.

Chapter 6 -8 present the experimental results of the post-irradiated, post-heat cured, and cold specimens. They provide a glimpse of the trend for bond behaviors pointing out similarities and differences in the pullout strength performances.

Chapter 9 presents the study of scale effects using unirradiated specimens.

Chapter 10 presents the interpretation of all test results, and the comparison of the data obtained from this research versus research performed under Japan Concrete Aging Management Program (JCAMP).

Chapter 11 presents modeling strategies and numerical simulations to design the specimen for pull out strength tests ensuring failure mode is governed by the bond strength at the interface of the steel rebar and the concrete.

Chapter 12 and 13 presents the effects of irradiation on the concrete and its constituents, interpretation of the data, and modelling and simulations.

Chapter 14 presents the structural performance of irradiated reinforced concrete.

Chapter 15 concludes this research. It presents limitations encountered and summarizes results of the study, modeling and simulation of scoping study tests, assessment of flux attenuation, quantification of damage, and comparison of computational methodologies.

A compendium of references concludes the study that provide additional detailed information regarding the state of the knowledge. It is followed by Appendix A, which sheds additional light on bond test results and scaling effects presented in Chapter 9.

Of course, as all research has limitations there are some in this effort as well. Most significant are those noted below:

- In the test reactor irradiation conditions, imposed limitations on the dimensions of the specimens (diameter: 40 mm same as Japanese experiment), so a companion study was conducted at the University of Tennessee, Knoxville, to analyze the sensitivity of reinforcement, aggregate, and concrete specimen sizes using unirradiated specimens.
- Accumulated fluence was limited by the duration of the project.
- Limited scope first of a kind experiment, only one capsule was exposed to one level of accumulated radiation (neutron and gamma)
- Mechanical testing and microscopic measurements inside a hot cell are difficult and challenging.
- Irradiation capsule, gamma shield, testing frames, holders were designed using simulations and fabricated specially to meet the experimental requirements.

In conclusion, the intent of this research as well of previous efforts within the “Radiation Effects on Concrete Structures,” program, were to gain new or improve the knowledge on the subject to support regulatory activities in general and NOT to be used for direct application of findings in plant specific licensing actions.





# TABLE OF CONTENTS

<b>ABSTRACT .....</b>	<b>iii</b>
<b>FOREWORD.....</b>	<b>v</b>
<b>LIST OF FIGURES.....</b>	<b>xiii</b>
<b>LIST OF TABLES .....</b>	<b>xxiii</b>
<b>EXECUTIVE SUMMARY .....</b>	<b>xxvii</b>
<b>ACKNOWLEDGMENTS .....</b>	<b>xxxiii</b>
<b>ABBREVIATIONS AND ACRONYMS .....</b>	<b>xxxv</b>
<b>1 INTRODUCTION .....</b>	<b>1-1</b>
1.1 Background .....	1-1
1.2 Research Overview .....	1-1
1.2.1 State of Knowledge and Research Needs .....	1-1
1.2.2 Project Scope and Strategy .....	1-5
1.3 Organization of the Report.....	1-8
<b>2 EFFECTS OF IRRADIATION ON THE BOND PROPERTIES OF STEEL EMBEDDED IN CONCRETE – EXPERIMENT DESIGN AND SETUP .....</b>	<b>2-1</b>
2.1 Test Reactor and Irradiation Conditions.....	2-1
2.2 Materials .....	2-4
2.2.1 Concrete .....	2-4
2.2.2 Low Carbon Steel Reinforcing Bar .....	2-5
2.3 Specimen Geometry .....	2-5
2.4 Capsule Design .....	2-8
2.4.1 Helium Gap .....	2-8
2.4.2 Irradiation Capsule and Rig.....	2-8
2.4.3 Neutron Fluence and Gamma Field Estimates .....	2-11
2.5 In-Situ Temperature and Irradiation Monitoring .....	2-13
2.5.1 Irradiation Temperature Estimates .....	2-14
2.5.2 Operational Limits .....	2-22
<b>3 SPECIMEN FABRICATION AND CURING .....</b>	<b>3-1</b>
3.1 Materials .....	3-1
3.2 Fabrication and Curing .....	3-1
3.2.1 Materials Preparation.....	3-1
3.2.2 Molds and Casting .....	3-1
3.2.3 Casting.....	3-3
3.2.4 Curing and Specimens Preparation .....	3-4
<b>4 IRRADIATION EXPERIMENT .....</b>	<b>4-1</b>
4.1 In-Situ Irradiation Conditions .....	4-1
4.1.1 Time Evolution of Neutron Fluence and Gamma Dose .....	4-1

4.1.2	Irradiation Temperature .....	4-4
4.2	Companion Irradiation-Temperature Experiment .....	4-10
<b>5</b>	<b>CHARACTERIZATION AND TESTING METHODS .....</b>	<b>5-1</b>
5.1	Mass Change .....	5-1
5.2	Dimensional Change .....	5-1
5.3	Bond Testing .....	5-2
5.3.1	Consideration on Failure Mode .....	5-2
5.3.2	Specimens Jacketing .....	5-3
5.3.3	Bond Testing Apparatus at CVR .....	5-4
5.4	Splitting Test.....	5-8
5.5	Compression Tests.....	5-9
<b>6</b>	<b>POST-IRRADIATION EXAMINATION.....</b>	<b>6-1</b>
6.1	Extraction of Irradiated Specimens.....	6-1
6.2	Visual Observations.....	6-2
6.3	Dimension and Mass Changes.....	6-10
6.4	Bond Tests .....	6-16
6.5	Splitting Tests .....	6-21
6.6	Compression Tests.....	6-21
<b>7</b>	<b>POST HEAT CURING TESTING .....</b>	<b>7-1</b>
7.1	Dimension and Mass Changes.....	7-1
7.2	Bond Tests .....	7-4
7.3	Splitting Tests .....	7-7
7.4	Compression Tests.....	7-8
<b>8</b>	<b>COLD SPECIMENS TESTING .....</b>	<b>8-1</b>
8.1	Dimension and Mass Changes.....	8-1
8.2	Bond Tests .....	8-1
8.3	Splitting Tests .....	8-4
8.4	Compression Tests.....	8-5
<b>9</b>	<b>SCALE EFFECTS TESTING .....</b>	<b>9-1</b>
9.1	Objectives .....	9-1
9.2	Materials .....	9-2
9.2.1	Concrete Made with Tennessee Aggregate.....	9-2
9.2.2	Transitioning from Japanese Aggregates to Tennessee Aggregates .....	9-4
9.3	Compression Test and Mix Design Optimization.....	9-5
9.3.1	Concrete Made with Tennessee Aggregates.....	9-5
9.4	Bond-Test Results .....	9-7
9.5	Conclusions .....	9-15
<b>10</b>	<b>INTERPRETATION OF TEST RESULTS.....</b>	<b>10-1</b>
10.1	Dimensional Change of Irradiated Aggregates .....	10-1
10.2	Mass Change of Concrete Specimens.....	10-4
10.2.1	Dimensional Changes of Concrete Specimens .....	10-6
10.3	Acoustic Wave Velocities .....	10-9
10.4	Strength Tests.....	10-11
10.4.1	Splitting Strength.....	10-11

10.4.2	Compressive Strength .....	10-14
10.5	Bond Tests .....	10-16
10.6	Conclusions .....	10-19
<b>11</b>	<b>BOND TEST MODELING .....</b>	<b>11-1</b>
11.1	Preliminary Simulation of Bond Test Experiments .....	11-1
11.1.1	Modeling Strategy .....	11-1
<b>11.2</b>	<b>Lattice Discrete Particle Model .....</b>	<b>11-3</b>
11.2.1	Constitutive Laws for Concrete in LDPM .....	11-5
11.2.2	Constitutive Laws for Concrete-Rebar Interaction in LDPM .....	11-6
11.2.3	Model Calibration .....	11-8
11.2.4	Calibration of the Bond Model Parameters .....	11-10
<b>12</b>	<b>IRRADIATED PROPERTIES OF CONCRETE CONSTITUENTS .....</b>	<b>12-1</b>
12.1	Neutron Irradiation Effect on Concrete Constituents .....	12-1
12.1.1	Radiation-Induced Volumetric Expansion .....	12-1
12.1.2	Irradiated Elastic Properties .....	12-2
12.2	Gamma Irradiation Effect on Concrete Constituents .....	12-5
12.2.1	Cement Hydrates .....	12-5
12.2.2	Cement Paste .....	12-5
12.2.3	Concrete .....	12-6
<b>13</b>	<b>INTERPRETATION OF IRRADIATED AGGREGATE AND CONCRETE DATA .....</b>	<b>13-1</b>
13.1	Aggregate Expansion .....	13-1
13.1.1	Analytical Model .....	13-1
13.1.2	MOSAIC .....	13-2
13.2	Aggregate Young's Modulus .....	13-3
13.3	Mesoscale Modeling of Concrete Dimensional Changes and Damage .....	13-4
13.3.1	Thermal Deformation .....	13-4
13.3.2	Shrinkage .....	13-5
13.3.3	Radiation-Induced Volumetric Expansion (RIVE) .....	13-6
13.3.4	Effects of Other Exposure Conditions .....	13-8
13.4	Interpretation of Concrete Dimensional Changes Results .....	13-8
13.4.1	Simulation of Shrinkage Deformations .....	13-8
13.4.2	Simulation of RIVE Deformations .....	13-11
13.5	Interpretation of Concrete Mechanical Strength Results .....	13-13
13.5.1	Interpretation of Difference Between Donut and Cylinder Compressive Strength .....	13-13
13.5.2	Simulation of RIVE Effects on Donut and Cylinder Compressive Strength .....	13-15
13.5.3	Simulation of Donut Splitting Strength .....	13-17
13.6	Interpretation of Bond Test Results .....	13-18
13.7	Case Study for Higher RIVE Expansions .....	13-23
<b>14</b>	<b>STRUCTURAL PERFORMANCE OF IRRADIATED REINFORCED CONCRETE .....</b>	<b>14-1</b>
14.1	Introduction .....	14-1
14.2	State of the Art .....	14-1
14.3	Finite Element Model .....	14-5

14.3.1	Model Geometry and Mesh .....	14-5
14.3.2	Mesh .....	14-8
14.3.3	Boundary Conditions .....	14-9
14.3.4	In-Service Conditions and Loading.....	14-9
14.3.5	Concrete Constitutive Model.....	14-9
14.3.6	Steel Constitutive Model .....	14-13
14.3.7	Simulation Results .....	14-13
14.4	Meso-Scale Structural Models .....	14-17
14.4.1	Irradiation-Induced Damage Depth.....	14-17
14.4.2	In-Service Irradiation Effects on the Bond Strength of Steel Reinforcement .....	14-21
<b>15</b>	<b>CONCLUSIONS .....</b>	<b>15-1</b>
15.1	Irradiation Scoping Study.....	15-1
15.1.1	Irradiation Scoping Study Summary .....	15-1
15.1.2	Irradiation Scoping Study Results.....	15-2
15.2	Modeling and Structural Significance of Irradiation on the Integrity of the Biological Shield Wall .....	15-3
15.2.1	Simulation of Scoping Study Tests.....	15-4
15.2.2	Structural Integrity of the CBS Wall.....	15-4
<b>16</b>	<b>REFERENCES .....</b>	<b>16-1</b>
<b>APPENDIX A</b>	<b>BOND TEST RESULTS – SCALE EFFECTS CAMPAIGN .....</b>	<b>A-1</b>

## LIST OF FIGURES

Figure 1-1	Illustration of the Models of Irradiated Aggregates, Concrete, and Concrete Structures Employed in this Research.....	1-7
Figure 1-2	Summary of the 4 Groups of Testing Conditions and List of the Pre/Post-Irradiation or Temperature Curing Examination and Testing.....	1-9
Figure 2-1	LVR-15 Representation (Left), Cross Section Showing the Core Position and the XK0 and XK1 Positions Outside the Core Alongside the Neutron Beam Channel (Right) (Images Courtesy of CVR).....	2-3
Figure 2-2	Photograph of #2 Low Carbon Steel Bar .....	2-5
Figure 2-3	Schematics of the Specimen Stack for Irradiation Experiments and Companion Irradiation-Temperature Model Experiments.....	2-7
Figure 2-4	Drawing of the Irradiation Capsule with Close-Up Views of the Gas Inlet-Outlet (Bottom-Left Drawing, Cross-Section A), the Mid-Height Section (B) Showing the Alumina Holder and the Isolated Reinforcing Steel Bar and the Bottom Section (C) .....	2-9
Figure 2-5	Photographs of the Capsules (Left) and Upper Plugs (Right) Fabricated at CVR.....	2-9
Figure 2-6	Complete Irradiation Rig: 3D Model (Left), and Fabricated Rig (Right).....	2-10
Figure 2-7	Schematics of the Neutron Moderator and the Gamma Shield Assembly .....	2-10
Figure 2-8	Neutron Flux Profiles in XK0 (Black Lines) and XK1 (Red Lines) Positions for Energies Higher Than 10 keV (Left) and 0.1 MeV (Right).....	2-11
Figure 2-9	Neutron Flux Profiles in XK0 (Black Lines) and XK1 (Red Lines) Positions for Energies Higher Than 0.1 MeV (Right). The X-Axis was Distorted to Correspond to the Actual Position of the Specimens in the Stack. Each Specimen is Located Between Two Dashed Lines. ....	2-12
Figure 2-10	Gamma Dose Rate Profile in the XK1 Position .....	2-13
Figure 2-11	(Left) View of the Thermocouple (TC) Placed at the Capsule Mid-Height, (Center) View of the Two TCs Installed in the Top Specimen, and (Right) Drawing Showing the TC Locations .....	2-13
Figure 2-12	Photograph of the Cross Junction Showing the Helium Outlet Located at the Top of the Capsule and the TC Wiring .....	2-14
Figure 2-13	Computational Domain for the Thermal Analysis .....	2-15
Figure 2-14	Model Mesh .....	2-16
Figure 2-15	Colormap of the Temperature Field in the Specimens During Irradiation (Axisymmetric Model).....	2-17
Figure 2-16	Temperature Axial Profiles Derived from the CFD Simulations in the XK0 and XK1 Positions (Left) at the Concrete Surface and (Right) at the Center of the Specimens in the Reinforcing Steel Bars .....	2-17
Figure 2-17	Temperature Radial Profiles Derived from the CFD Simulations in the XK0 (Left) and XK1 (Right) Positions .....	2-18

Figure 2-18	Radial Temperature Fields Across the Concrete Specimens Accounting for Possible Misalignment of the Specimen Axis with the Capsule Axis .....	2-18
Figure 2-19	Reactor Power Level (a) and Coolant Temperature (b) During a shutdown Occurring in Winter.....	2-20
Figure 2-20	Measured Temperatures (a) During Shutdown at Four Locations in the Irradiation Capsules, and (b) TC Locations .....	2-20
Figure 2-21	Simulation Results Showing (a) the Temperature Difference Between the Two Pairs of TCs, and (b) the TC Locations .....	2-21
Figure 2-22	Temperature Field in the Capsules and the Tungsten Shielding.....	2-22
Figure 3-1	Design Drawings and Photographs of the Mold to Cast Pullout Specimens .....	3-2
Figure 3-2	Design Drawings and Photograph of the Mold to Cast Donut Specimens .....	3-3
Figure 3-3	Photographs of 5 Sets of Specimens Immediately After Demolding .....	3-4
Figure 3-4	(Left) Specimen A05R (Concrete Con-A) Showing a Few Small Surface Pores, (Center) Specimen A06R Showing Larger Surface Defects, and (Right) Specimen A11R Showing a Large Defect Near the Top Surface .....	3-8
Figure 3-5	Preliminary Drawing Showing TC Locations in the Specimen Stack (Note that this Drawing Does Not Represent the Actual Stack. The Alumina Holder is Not Represented in This Drawing) .....	3-9
Figure 3-6	Irradiation Testing Specimens Cut to Create a 2 × 2 mm Groove for Placement of the TC at Mid-Height of the Specimen Stack .....	3-9
Figure 4-1	(Left) Sketch Showing Initial and Shifted Positions of the Irradiation Rig. (Right) Photograph Taken in September 2023 Showing the Position of the Out-Of-Core Irradiation Rig. ....	4-2
Figure 4-2	Fast Neutron Fluence ( $E > 10$ keV) History (14 Irradiation Cycles) in the Concrete and Aggregate Specimens. The Thick Solid Line Represents Average Fluence, and the Thin Dashed Lines Indicate Min./Max. Fluences.....	4-3
Figure 4-3	Gamma Dose (14 Irradiation Cycles) in the Concrete and Aggregate Specimens. The Thick Solid Line Represents Average Gamma Dose, and the Thin Dashed Lines Indicate Min./Max. Gamma.....	4-4
Figure 4-4	Temperature Variation Field in the Concrete Specimens During Irradiation. The Reference Temperature was Taken at the Location of the TC Placed Near the Mid-Elevation of the Stack. x and y Axes are Shown in Meters, and Blue Squares Mark the TC Locations.....	4-6
Figure 4-5	Monitored Temperatures During the 14 Irradiation Cycles (Ks). (Red Solid Line) TC Placed Near the Mid-Elevation of the Stack ( $T > 25$ °C); (Blue Solid Line) TC Placed at the Top of the Stack Near the Reinforcement Bar of the Top Pullout Specimen; (Black Solid Line) TC Placed at the Same Elevation but Near the Outer Diameter of the Concrete Specimen. (Thick Black Solid Line) Reactor Power. (Dashed Blue) Start Dates of Irradiation Cycles; (Dashed Red Line) End Dates of Irradiation Cycles.....	4-8
Figure 4-6	Difference of Monitored Temperatures Between the TCs During Irradiation Cycles (Ks). Reference: TC Placed Near the Mid-Elevation of	

	the Stack. (Blue Solid Line) TC Placed at the Top of the Stack Near the Reinforcement Bar of the Top Pullout Specimen; (Black Solid Line) TC Placed at the Same Elevation but Near the Outer Diameter of the Concrete Specimen. (Black and Blue Dashed Lines) Simulated Temperature Difference. ....	4-9
Figure 4-7	Temperatures Recorded in the TCs Placed in the Irradiation Capsule Replica Subject to Heat Curing Cycles. Data from All Three TCs are Plotted (Invisible Difference Between the Three Plots in the Graph). Dashed Blue and Red Lines Indicate the Start and Finish of Each Cycle.....	4-11
Figure 5-1	(Left) Vertex Touch Probe Measurement Device; (Right) Pullout Specimen Setup for Height Measurement.....	5-1
Figure 5-2	Locations of the Dimensional Measurements Using the Micro-Vu Vertex System for the Pullout Specimens (Left), the Donut Specimens (Center), and the Aggregate Specimens (Right) .....	5-2
Figure 5-3	Preliminary Testing and Post-Pullout Test Photographs .....	5-3
Figure 5-4	Jacketing of Pullout Specimens in Hot Cells: (a) Specimen and Jacket Centering and Placement in Fixture, and (b) Full Setup Fixture for Epoxy Casting .....	5-4
Figure 5-5	Preliminary Design Assembly of Bond Testing Apparatus at CVR.....	5-6
Figure 5-6	Photographs of the Bond Testing Apparatus.....	5-7
Figure 5-7	Post Irradiation Pullout Testing Showing the Test Fixture, the Test Specimen, and the LVDT Locations.....	5-8
Figure 5-8	3D Sketch of the Splitting Test Fixture Designed by CVR.....	5-9
Figure 5-9	Compression Test Setup Showing (Left) the Specimens Placed Between the Unbonded Caps (UTK) and (Right) Specimen B04D at the End of the Test Conducted in CVR's Hot Cell .....	5-10
Figure 5-10	Post Compression Test Showing the Fractured Surface of the Concrete Specimen .....	5-10
Figure 6-1	Photographs Taken During Capsule Opening and Extraction of Irradiated Specimens.....	6-1
Figure 6-2	Photographs of the Extracted Specimens .....	6-2
Figure 6-3	Photographs of the Con-A Pullout Specimens Taken from the Free Ends Before and After Irradiation .....	6-3
Figure 6-4	Additional Photographs of the Con-A Pullout Specimens Showing Marks Left by Fluence Monitors .....	6-4
Figure 6-5	Photographs of the Con-B Pullout Specimens Taken from the Free Ends Before and After Irradiation .....	6-5
Figure 6-6	Additional Photographs of the Con-A Pullout Specimens Showing Marks Left by Fluence Monitors .....	6-6
Figure 6-7	Photographs of the Con-A Donut Specimens Taken Before and After Irradiation .....	6-6



Figure 6-8	Photographs of the Con-B Donut Specimens Taken Before and After Irradiation .....	6-7
Figure 6-9	Photographs of the Aggregate Specimens Before and After Irradiation.....	6-8
Figure 6-10	Observed Post-Irradiation Cracking in the Con-A Donut Specimens .....	6-9
Figure 6-11	Observed Post-Irradiation Cracking in the Con-B Donut Specimens .....	6-10
Figure 6-12	Results of the Pullout Tests Conducted on Irradiated Specimens A and B.....	6-17
Figure 6-13	Bond Test Results Obtained on Irradiated Specimen A02R .....	6-18
Figure 6-14	Bond Test Results Obtained on Irradiated Specimen A03R .....	6-19
Figure 6-15	Bond Test Results Obtained on Irradiated Specimen A06R .....	6-19
Figure 6-16	Bond Test Results Obtained on Irradiated Specimen B04R .....	6-20
Figure 6-17	Bond Test Results Obtained on Irradiated Specimen B07R .....	6-20
Figure 6-18	Bond Test Results Obtained on Irradiated Specimen B09R .....	6-21
Figure 6-19	Compression Test of Specimen A06D in CVR Hot-Cell. Snapshot Taken Close to the End of the Test Showing Neoprene Bulging and the Tilting of the Specimen. ....	6-22
Figure 7-1	Bond Test Results Obtained on Specimen A01R Cured at Irradiation Temperature.....	7-5
Figure 7-2	Bond Test Results Obtained on Specimen A07R Cured at Irradiation Temperature.....	7-5
Figure 7-3	Bond Test Results Obtained on Specimen A09R Cured at Irradiation Temperature.....	7-6
Figure 7-4	Bond Test Results Obtained on Specimen B02R Cured at Irradiation Temperature.....	7-6
Figure 7-5	Bond Test Results Obtained on Specimen B03R Cured at Irradiation Temperature.....	7-7
Figure 7-6	Bond Test Results Obtained on Specimen B11R Cured at Irradiation Temperature.....	7-7
Figure 8-1	Bond Test Results Obtained on Specimen A05R Cured at Room Temperature.....	8-1
Figure 8-2	Bond Test Results Obtained on Specimen A08R Cured at Room Temperature.....	8-2
Figure 8-3	Bond Test Results Obtained on Specimen A11R Cured at Room Temperature.....	8-2
Figure 8-4	Bond Test Results Obtained on Specimen B01R Cured at Room Temperature.....	8-3
Figure 8-5	Bond Test Results Obtained on Specimen B05R Cured at Room Temperature.....	8-3
Figure 8-6	Bond Test Results Obtained on Specimen B08R Cured at Room Temperature.....	8-4

Figure 9-1	Sketch Showing the Geometries of the #2, #4, and #8 Specimens .....	9-2
Figure 9-2	Sieving Curves of the Fine and Coarse Crushed Limestone Aggregates .....	9-3
Figure 9-3	Comparison of the 3-, 7-, and 28-day Compressive Strength for All Studied Mixes .....	9-6
Figure 9-4	Comparison of the 3-, 7-, and 28-Day Compressive Strength for 0.5 w/c Mixes .....	9-6
Figure 9-5	Comparison of the 3-, 7-, and 28-day Compressive Strength for 0.45 w/c Mixes .....	9-7
Figure 9-6	Summary of Bond Test Results of the Scale Effect Campaign Showing Normalized Pullout Force vs. Normalized Slippage for the #2 Specimens (Detailed plots are in Appendix A) .....	9-8
Figure 9-7	Summary of Bond Test Results of the Scale Effect Campaign Showing Normalized Pullout Force $F/(\kappa^2)$ vs. Normalized Slippage (Detailed Plots are in Appendix A) .....	9-10
Figure 9-8	Summary of Bond Test Results of the Scale Effect Campaign Showing Normalized Pullout Force $F/(\kappa^2 \sqrt{f_c})$ vs. Normalized Slippage for the #2 Specimens (Detailed Plots are in Appendix A) .....	9-11
Figure 9-9	Summary of Bond Test Results of the Scale Effect Campaign Showing Normalized Pullout Force $F/(\kappa^2 \sqrt{f_c})$ vs. Normalized Slippage (Detailed Plots are in Appendix A) .....	9-12
Figure 9-10	Summary of Bond Test Results of the Scale Effect Campaign Showing Normalized Pullout Force $F/(\kappa^2 \sqrt{f_c f_r^{0.8}})$ vs. Normalized Slippage (Detailed Plots are in Appendix A) .....	9-14
Figure 9-11	Sketch Showing the Wall Effect Around the Reinforcing Bar .....	9-15
Figure 10-1	Summary of Post-Irradiation Dimensional Changes of Aggregates .....	10-1
Figure 10-2	Comparison of the Aggregate Dimensional Change Observed on the Aggregate Specimens Irradiated in the JEEP-II Reactor (Red) and the LVR-15 Reactor (Blue). Fluence Given in $\times 10^{20}$ n.cm <sup>-2</sup> .....	10-3
Figure 10-3	Mass Loss of Irradiated Specimens Against their Axial Positions in the Capsule (Thick Black Solid Lines and Circle Marks; see Figure 2-3 for capsule). Gamma Dose Rate Axial Profile (Thin Black Solid Line) and Fast Neutron Flux Profile (Red Solid Line and Circle Marks) .....	10-5
Figure 10-4	Mass Loss of the Heat-Cured Specimens Against their Axial Position (Mean Value) in the Capsule (See Figure 2-3 for Specimen Positions) .....	10-6
Figure 10-5	Summary of Post-Irradiation Dimensional Changes of Concrete Specimens (Black Indicates Pullout Specimens and Red Indicates Donut Specimens) .....	10-7
Figure 10-6	Summary of the Dimensional Changes of the Heat-Cured Concrete Specimens (Black Indicates Pullout Specimens and Red Indicates Donut Specimens) .....	10-8
Figure 10-7	Comparison of the Concrete Dimensional Change Observed in the Concrete Specimens Irradiated in the JEEP-II Reactor (Red) and the	

	LVR-15 Reactor (Blue). Diamonds Indicate Diameter Change, and Stars Indicate Height Change. The Distance Between the Unshaded and Shaded Blue Ellipses Corresponds to the Estimated Shrinkage Caused by Pre-Drying Curing.....	10-9
Figure 10-8	P-Wave Velocities Measured on Donut Specimens .....	10-10
Figure 10-9	Comparison of the Concrete Elastic Modulus Change Observed in Concrete Specimens Irradiated in the JEEP-II Reactor (Red) and the LVR-15 Reactor (Blue). The Neutron Fluence Values are Provided in $\times 10^{20} \text{n/cm}^2$ . .....	10-11
Figure 10-10	Apparent Tensile Stress vs. Press Stroke Measured During Splitting Tests.....	10-12
Figure 10-11	Apparent Tensile Strength (Splitting Tests): <i>rt</i> Indicates Specimens Cured at Room Temperature, <i>hc</i> Indicates Specimens Cured at Irradiation Temperature, and <i>irr</i> Indicates Irradiated Specimens .....	10-14
Figure 10-12	Apparent Compressive Strength (Capped Compression Tests) <i>rt</i> Indicates Specimens Cured at Room Temperature, <i>hc</i> Indicates Specimens Cured at Irradiation Temperature, and <i>irr</i> Indicates Irradiated Specimens.....	10-15
Figure 10-13	Comparison of the Relative Compression Strength of the Heat-Cured Specimens (JCAMP Data in Red; This Study's Data in Blue).....	10-16
Figure 10-14	Summary of Bond Test Data on the #2 Pullout Specimens .....	10-17
Figure 10-15	Summary of Bond Test Data on the #2 Pullout Specimens, with Bond Force Normalized by $f_t^{2/3}$ .....	10-18
Figure 10-16	Summary of Bond Test Data on the #2 Pullout Specimens, with Bond Force Normalized by $\sqrt{f_t}$ . .....	10-19
Figure 11-1	Typical Bond Stress $\tau$ vs. Relative Slippage $S$ Showing Full Pullout Failure and Splitting Failure with Idealized Model Fits .....	11-2
Figure 11-2	Failure Modes and Crack Development During a Pullout Test: (a) Splitting Failure Mode, and (b) Slipping Failure Mode .....	11-3
Figure 11-3	Illustration of Generation Process of the Internal Mesostucture of Concrete Using LDPM Showing Resulting Cells and Discrete Deformation Measure .....	11-4
Figure 11-4	Details of the Interface Elements and Bond-Slip Law in the Axial Direction.....	11-5
Figure 11-5	Experimental Particle Size Distribution and Fitted Fuller Curves for (a) Con-A and (b) Con-B .....	11-9
Figure 11-6	Numerically Simulated Uniaxial Compression Stress-Strain Curves for Con-A and Con-B .....	11-10
Figure 11-7	Numerically Simulated Pullout Test Results for Con-A Specimens Showing Bond Stress vs. Experimentally Measured Slippage of the (a) Loaded End, (b) Free End, and Corrected Experimental Slippage of the (c) Loaded End and (d) Free End.....	11-12

Figure 11-8	Numerically Simulated Pullout Test Results for Con-B Using $\kappa = 1.5$ Showing Bond Stress vs. Experimentally Measured Slippage at (a) the Loaded End and (b) the Free End, and Numerically Simulated Results Using $\kappa=2.25$ at (c) the Loaded End and (d) the Free End .....	11-13
Figure 11-9	Stages of Crack Formation within the Mesostructure of Concrete as Splitting Failure Develops.....	11-14
Figure 11-10	Parametric Study Results, Including (a) the Effect of Changing the Rib Effect Parameter, (b) the Effect of Changing Tensile Strength, and (c) the Effect of Changing the Initial Fracture Energy.....	11-15
Figure 12-1	Young's Modulus of Irradiated Aggregates (Relative to the Pristine Value) and Aggregate RIVE .....	12-5
Figure 13-1	Schematic Representation of LDPM Modeling of Aggregate RIVE Effects.....	13-7
Figure 13-2	Effects of Relative Humidity Conditions: (a) Water Content Changes During Pre-drying Stage (168 Hours = 7 Days), (b) Water Content Changes for the First 300 Days After Initial Curing (Includes Pre-Drying), and (c) Mass Loss % for the First 300 Days After Initial Curing (Includes Pre-Drying) .....	13-10
Figure 13-3	Predicted Linear Shrinkage of the Donut Specimens for the First 300 Days Caused by Water Loss – Upper and Lower Bounds are Based on Shrinkage Coefficient Values from the Literature (Adbellatef et al., 2019, Di Luzio and Cusatis, 2013) .....	13-10
Figure 13-4	Predicted Linear Expansion of the Irradiated Donut Specimens Caused by Aggregate Expansion up to 0.2%: (Blue) Accounting Only for Coarse Aggregate Expansion; (Black) Accounting for Fine and Coarse Aggregates .....	13-11
Figure 13-5	Simulated Deformations of the Donut Samples Under Predicted RIVE from Aggregate Expansion Measurements (0.02%) Showing the Difference Between (a) Considering Only Coarse Aggregate vs. (b) Considering All Aggregates to Expand. The Top Row Shows Axial (Vertical) Displacement, the Middle Row Shows Radial Displacement, and the Bottom Row Shows Displacement Magnitude; All Displacement was Measured from the Center of Mass of the Donut. ....	13-12
Figure 13-6	Four Boundary Conditions Used to Model the Compression Tests.....	13-14
Figure 13-7	Simulation Results Showing LDPM Prediction of Compression Tests for Different Conditions: (a) Prediction of 2 in. $\times$ 4 in. Cylinders Showing Numerical Average and its Range Compared with Experimental Average, (b) Donut Uniaxial Compression with Different Boundary Conditions Based on 2 in. $\times$ 4 in. Cylinder Calibrations of Room Temperature–Cured Specimens.....	13-15
Figure 13-8	Difference in RIVE-Induced Cracking When Considering All Aggregates to Expand (Left) vs. Considering Only Coarse Aggregates to Expand (Right).....	13-16
Figure 13-9	Simulated Uniaxial Compressive Strength Tests for Irradiated and Room Temperature (Cold) Cases Compared with the Reference 2 $\times$ 4 Cylinder	

	Strength at Room Temperature: (a) 2 × 4 Cylinder Results, and (b) Donut Results .....	13-16
Figure 13-10	Simulation of Donut Splitting Test Showing the Loading Rods and Internal Aggregate Structure (Left), the Simulated Splitting Crack (Middle), and the Crack Location Around the Aggregate (Right).....	13-17
Figure 13-11	Prediction of Donut Splitting Strength and Comparison with Experimental Ranges: rt Samples (a), irr Samples (b) .....	13-18
Figure 13-12	Cross View and External View of the Bond Test Model .....	13-20
Figure 13-13	Lateral Pressure Applied by the Steel-Epoxy Jacketing During the Bond Test Where $P_{r_i}$ is the Pressure at $i$ cm from the Free End Side of the Steel Jacket .....	13-20
Figure 13-14	Simulation of the Bond Tests Assuming No Effects of the Concrete Strength on the Steel-Concrete Bond Constitutive Model. rt: Room Temperature, irr: Degradation of the Concrete Caused by Irradiation, irr-Reduced: Same as irr with a Degradation of the Steel-Concrete Bond Strength .....	13-22
Figure 13-15	Simulation of the Bond Tests Assuming Effects of the Concrete Strength on the Steel-Concrete Bond Constitutive Model .....	13-23
Figure 13-16	Prediction of Bond Strength Reduction Caused by Extended Irradiation Not Accounting for the Effect of Irradiated Concrete Compressive Strength Reduction .....	13-25
Figure 13-17	Prediction of Bond Strength Reduction Caused by Extended Irradiation Accounting for the Effect of Irradiated Concrete Compressive Strength Reduction .....	13-26
Figure 14-1	Illustration of Varied Supporting System for the RPV (Biwer et al., 2021): (a) PWR RPV with a Support Skirt, (b) PWR RPVs Supported on Columns and Anchored to CBS for Lateral Support ( for Seismic, Accident, Stability, etc.) (c) PWR Supported on Cantilevered Beams or Extended Supports, and (d) PWR RPV Supports Mounted on a Neutron Shield Tank .....	14-7
Figure 14-2	3D View of the Mesh Showing the Main Structural Elements in the Model: Blue Basemat, Green Concrete Shield, and Gray Liner.....	14-8
Figure 14-3	Calculated Fast Neutron Fluence ( $E > 10$ keV) Field at 80 Years of Operation.....	14-14
Figure 14-4	Fast Neutron Profile ( $E > 10$ keV) Across the RPV, the Reactor Cavity, and the CBS at 80 Years.....	14-14
Figure 14-5	Simulation Results at 80 Years of Operation. (Clockwise from Top Left Figure): Amplified ( $\times 1500$ ) Structural Deformation (m); Radial Stress Field; Axial (Vertical) Stress Field; and Hoop (Orthoradial) Stress Field.....	14-16
Figure 14-6	(Left) Radial Profiles of the Radial ( $r$ ), Hoop ( $\theta$ ) and Vertical ( $z$ ) Stress Across the Depth of the CBS at 40 and 80 Years of Operation. (Right) Radial Profiles of the Fast Neutron Fluence ( $E > 10$ keV, Solid Lines) and Cumulative Damage (Dashed Lines) Across the Depth of the CBS at 40, 60 and 80 Years of Operation .....	14-16

Figure 14-7	Top View Showing the Crack Opening Width CBS Wedge LDPM at Varied Operation Duration.....	14-18
Figure 14-8	Comparison of the Damage Profile in the CBS Obtained Using LDPM (Solid Lines) and Finite Element Model (Dashed Lines) at 40, 60 and 80 Years of Operation (in Black, Blue and Red, Respectively) .....	14-20
Figure 14-9	Details of the CBS Wedge Model Used to Simulate the Effects of In-Service Irradiation on the Bond Strength of the Embedded Reinforcement...	14-21
Figure 14-10	Cracking in the CBS at 80 Years of Service: (Top Left and Right) Before Rebar Pullout, (Bottom Left) at 1.0 mm Slippage, and (Bottom Right) at 2.0 mm Slippage .....	14-23
Figure 14-11	Prediction of Pullout Behavior of a #8 Rebar in the CBS at Different Operation Times: (Left) Neglecting the Influence of the Loss of Concrete Strength on Bond Law Parameters; (Right) Considering that Influence.....	14-24
Figure A-1	Normalized Pullout Force $F/(\kappa^2)$ vs. Normalized Slippage. #2   TN Coarse Aggregate (0.375 in.)   GB Sand.....	A-2
Figure A-2	Normalized Pullout Force $F/(\kappa^2)$ vs. Normalized Slippage. #2   TN Coarse Aggregate (0.500 in.)   GB Sand.....	A-2
Figure A-3	Normalized Pullout Force $F/(\kappa^2)$ vs. Normalized Slippage. #4   GB Coarse Aggregate (0.375 in.)   GB Sand.....	A-3
Figure A-4	Normalized Pullout Force $F/(\kappa^2)$ vs. Normalized Slippage. #4   GB Coarse Aggregate (0.500 in.)   GB Sand.....	A-3
Figure A-5	Normalized Pullout Force $F/(\kappa^2)$ vs. Normalized Slippage. #4   GB Coarse Aggregate (0.750 in.)   GB Sand.....	A-4
Figure A-6	Normalized Pullout Force $F/(\kappa^2)$ vs. Normalized Slippage. #4   GB Coarse Aggregate (1.000 in.)   GB Sand.....	A-4
Figure A-7	Normalized Pullout Force $F/(\kappa^2)$ vs. Normalized Slippage. #4   GB Coarse Aggregate (0.375 in.)   GB Sand.....	A-5
Figure A-8	Normalized Pullout Force $F/(\kappa^2)$ vs. Normalized Slippage. #4   GB Coarse Aggregate (0.500 in.)   GB Sand.....	A-5
Figure A-9	Normalized Pullout Force $F/(\kappa^2)$ vs. Normalized Slippage. #4   GB Coarse Aggregate (0.750 in.)   GB Sand.....	A-6
Figure A-10	Normalized Pullout Force $F/(\kappa^2)$ vs. Normalized Slippage. #4   GB Coarse Aggregate (1.000 in.)   GB Sand.....	A-6
Figure A-11	Normalized Pullout Force $F/(\kappa^2\sqrt{f_c})$ vs. Normalized Slippage. #2 TN Coarse Aggregate (0.375 in.)   GB Sand.....	A-7
Figure A-12	Normalized Pullout Force $F/(\kappa^2\sqrt{f_c})$ vs. Normalized Slippage. #2 TN Coarse Aggregate (0.500 in.)   GB Sand.....	A-7
Figure A-13	Normalized Pullout Force $F/(\kappa^2\sqrt{f_c})$ vs. Normalized Slippage. #4   GB Coarse Aggregate (0.375 in.)   GB Sand.....	A-8

Figure A-14	Normalized Pullout Force $F/(\kappa^2\sqrt{f_c})$ vs. Normalized Slippage. #4   GB Coarse Aggregate (0.500 in.)   GB Sand.....	A-8
Figure A-15	Normalized Pullout Force $F/(\kappa^2\sqrt{f_c})$ vs. Normalized Slippage. #4   GB Coarse Aggregate (0.750 in.)   GB Sand.....	A-9
Figure A-16	Normalized Pullout Force $F/(\kappa^2\sqrt{f_c})$ vs. Normalized Slippage. #4   GB Coarse Aggregate (1.000 in.)   GB Sand.....	A-9
Figure A-17	Normalized Pullout Force $F/(\kappa^2\sqrt{f_c})$ vs. Normalized Slippage. #8   GB Coarse Aggregate (0.375 in.)   GB Sand.....	A-10
Figure A-18	Normalized Pullout Force $F/(\kappa^2\sqrt{f_c})$ vs. Normalized Slippage. #8   GB Coarse Aggregate (0.500 in.)   GB Sand.....	A-10
Figure A-19	Normalized Pullout Force $F/(\kappa^2\sqrt{f_c})$ vs. Normalized Slippage. #8   GB Coarse Aggregate (0.750 in.)   GB Sand.....	A-11
Figure A-20	Normalized Pullout Force $F/(\kappa^2\sqrt{f_c})$ vs. Normalized Slippage. #8   GB Coarse Aggregate (1.000 in.)   GB Sand.....	A-11
Figure A-21	Normalized Pullout Force $F/(\kappa^2\sqrt{f_c}f_r^{0.8})$ vs. Normalized Slippage. #2   GB Coarse Aggregate (0.375 in.)   GB Sand .....	A-12
Figure A-22	Normalized Pullout Force $F/(\kappa^2\sqrt{f_c}f_r^{0.8})$ vs. Normalized Slippage. #2   GB Coarse Aggregate (0.500 in.)   GB Sand .....	A-12
Figure A-23	Normalized Pullout Force $F/(\kappa^2\sqrt{f_c}f_r^{0.8})$ vs. Normalized Slippage. #4   GB Coarse Aggregate (0.375 in.)   GB Sand. ....	A-13
Figure A-24	Normalized Pullout Force $F/(\kappa^2\sqrt{f_c}f_r^{0.8})$ vs. Normalized Slippage. #4   GB Coarse Aggregate (0.500 in.)   GB Sand .....	A-13
Figure A-25	Normalized Pullout Force $F/(\kappa^2\sqrt{f_c}f_r^{0.8})$ vs. Normalized Slippage. #4   GB Coarse Aggregate (0.750 in.)   GB Sand .....	A-14
Figure A-26	Normalized Pullout Force $F/(\kappa^2\sqrt{f_c}f_r^{0.8})$ vs. Normalized Slippage. #4   GB Coarse Aggregate (1.000 in.)   GB Sand .....	A-14
Figure A-27	Normalized Pullout Force $F/(\kappa^2\sqrt{f_c}f_r^{0.8})$ vs. Normalized Slippage. #8   GB Coarse Aggregate (0.375 in.)   GB Sand .....	A-15
Figure A-28	Normalized Pullout Force $F/(\kappa^2\sqrt{f_c}f_r^{0.8})$ vs. Normalized Slippage. #8   GB Coarse aggregate (0.500 in.)   GB Sand. ....	A-15
Figure A-29	Normalized Pullout Force $F/(\kappa^2\sqrt{f_c}f_r^{0.8})$ vs. Normalized Slippage. #8   GB Coarse Aggregate (0.750 in.)   GB Sand .....	A-16
Figure A-30	Normalized Pullout Force $F/(\kappa^2\sqrt{f_c}f_r^{0.8})$ vs. Normalized Slippage. #8   GB Coarse Aggregate (1.000 in.)   GB Sand .....	A-16

## LIST OF TABLES

Table 2-1	Initial Comparison of Estimated Irradiation Conditions Between JEEP-II Reactor (JCAMP Experiment) LVR-15 (This Experiment) and a Prototypical PWR – Data (Maruyama et al, 2017; Remec,2013.....	2-4
Table 2-2	Material Thermal Properties .....	2-5
Table 3-1	Visual Assessment of the Specimens After the 45-Day Curing.....	3-6
Table 4-1	Fast Neutron Fluences at the End of the 14 Irradiation Cycles for Varied Energy Thresholds .....	4-1
Table 4-2	Summary of the Monitored Temperatures in the Irradiation Capsule Replica Subject to Heat Curing Cycles.....	4-12
Table 6-1	Pre- and Post-Irradiation Height and Volume Measurements and Dimensional Change of the Pullout Specimens (Concrete Con-B). See Figure 5-2 for the Locations of the Measurements (A–D). .....	6-11
Table 6-2	Pre- and Post-Irradiation Diameter and Mass Measurements and Dimensional Change of the Pullout Specimens (Concrete Con-B). See Figure 5-2 for the Locations of the Measurements (–35 through –5). .....	6-12
Table 6-3	Pre- and Post-Irradiation Height and Volume Measurements and Dimensional Change of the Pullout Specimens (Concrete Con-A). See Figure 5-2 for the Locations of the Measurements (A – D). .....	6-12
Table 6-4	Pre- and Post-Irradiation Diameter and Mass Measurements and Dimensional Change of the Pullout Specimens (Concrete Con-A). See Figure 5-2 for the Locations of the Measurements (–5 through –35).....	6-13
Table 6-5	Pre- and Post-Irradiation Height, Mass and Volume Measurements, and Dimensional Change of the Donut Specimens (Concrete Con-B). See Figure 5-2 for the Locations of the Measurements (* – ****). .....	6-13
Table 6-6	Pre- and Post-Irradiation Diameter Measurements and Dimensional Change of the Donut Specimens (Concrete Con-B). See Figure 5-2 for the Locations of the Measurements (–12 through –48).....	6-14
Table 6-7	Pre- and Post-Irradiation Height, Mass and Volume Measurements and Dimensional Change of the Donut Specimens (Concrete Con-A). See Figure 5-2 for the Locations of the Measurements (1–4). .....	6-14
Table 6-8	Pre- and Post-Irradiation Diameter Measurements and Dimensional Change of the Donut Specimens (Concrete Con-A). See Figure 5-2 for the Locations of the Measurements (–5 through –25).....	6-15
Table 6-9	Pre- and Post-Irradiation Height Measurements and Dimensional Change of the Aggregate Specimens. ....	6-15
Table 6-10	Pre- and Post-Irradiation Diameter Measurements and Dimensional Change of the Aggregate Specimens .....	6-16
Table 6-11	Maximum Bond Force and Corresponding Slippage Recorded on the Irradiated Pullout Specimens .....	6-18



Table 6-12	Results of the Splitting Tests for the Irradiated Specimens.....	6-21
Table 7-1	Pre- and Post-Heat Curing Diameter and Measurements and Changes of the Pullout Specimens (Concrete Con-A Made of GA(F) Aggregates). See Figure 5-2 for the Locations of the Measurements (* – ****). .....	7-1
Table 7-2	Pre- and Post-Heat Curing Diameter and Measurements and Changes of the Pullout Specimens (Concrete Con-B Made of GB(E) Aggregates). See Figure 5-2 for the Locations of the Measurements (* – ****). .....	7-2
Table 7-3	Pre- and Post-Heat Curing Diameter Measurements and Dimensional Changes of the Donut Specimens (Concrete Con-A). See Figure 5-2 for the Locations of the Measurements (* – ****). .....	7-2
Table 7-4	Pre- and Post-Heat Curing Height and Mass Measurements and Changes of the Donut Specimens (Concrete Con-A). See Figure 5-2 for the Locations of the Measurements (* – ****). .....	7-3
Table 7-5	Pre- and Post-Heat Curing Diameter Measurements and Changes of the Donut Specimens (Concrete Con-B). See Figure 5-2 for the Locations of the Measurements (* – ****). .....	7-3
Table 7-6	Pre- and Post-Heat Curing Height and Mass Measurements and Changes of the Donut Specimens (Concrete Con-B). See Figure 5-2 for the Locations of the Measurements (* – ****). .....	7-4
Table 7-7	Maximum Bond Force and Corresponding Slippage Recorded on the Pullout Specimens Cured at Irradiation Temperature .....	7-4
Table 7-8	Results of the Splitting Tests for the Specimens Cured at Irradiation Temperature .....	7-8
Table 7-9	Results of the Compression Tests for the Specimens Cured at Irradiation Temperature .....	7-8
Table 8-1	Maximum Bond Force and Corresponding Slippage Recorded on the Pullout Specimens Cured at Room Temperature.....	8-1
Table 8-2	Results of the Splitting Tests for the Specimens Cured at Room Temperature .....	8-4
Table 8-3	Results of the Compression Tests for the Specimens Cured at Room Temperature.....	8-5
Table 9-1	Main Dimensions (mm) of the Pullout Specimens for the Scale Effect Campaign .....	9-1
Table 9-2	Aggregate Absorption Coefficients and Density .....	9-3
Table 9-3	Con-A Mix Design .....	9-3
Table 9-4	Mix Design Testing Matrix .....	9-4
Table 9-5	Testing Matrix for Transitioning from Japanese to Tennessee Aggregates .....	9-5
Table 10-1	Irradiation Conditions in JEEP-II (Data from Table 22–23 of Maruyama et al., 2017, and this Study’s Experiment in LVR-15/XK1) .....	10-4
Table 10-2	Summary of the Mass and Dimensional Changes and Mechanical Properties Obtained by the JCAMP Team (Maruyama et al., 2017) and	

	Found During this Study (* Fig. 40 in Maruyama et al. (2017); ** Dynamic Modulus; (#) Confined Compression Test; (a) Outlier Data) .....	10-20
Table 11-1	Mix Design Parameters Used for the LDPM Mesostructured Generation .....	11-8
Table 11-2	Calibrated LDPM Parameters .....	11-10
Table 11-3	Bond-Slip Model Parameters .....	11-11
Table 11-4	LDPM Calibrated Parameters for the Different Parametric Study Cases .....	11-15
Table 12-1	Pristine and Irradiated Density and Young's Modulus of Minerals (Krishnan et al., 2018) .....	12-3
Table 13-1	Post-Irradiation Volumetric Change of Aggregate GA(F) and GB(E) Irradiated in the JEEP-II Reactor (Maruyama et al., 2017) and the LVR-15 Reactor (XK1 Position): Comparison Between Post-Irradiation Measurement and Theoretical Estimates .....	13-2
Table 13-2	MP-LDPM Parameters for Cement Hydration and Moisture Transport .....	13-6
Table 13-3	Initial Water Content in Concrete Con-A and Con-B .....	13-9
Table 13-4	Compression Test Friction Parameters .....	13-14
Table 13-5	Predicted Compressive Strength Reduction in Concrete Con-A Caused by Aggregate RIVE under the Irradiation Conditions Tested in the XK1 Position (LVR-15 Reactor) .....	13-17
Table 13-6	Elastoplastic and Density Parameters for Epoxy, Steel Bar, and Steel Jacket .....	13-19
Table 13-7	Bond-Slip Model Parameters for Con-A at Different Exposure Conditions ....	13-23
Table 13-8	Prediction of the Effect of Extended Irradiation on Concrete Compressive Strength .....	13-24
Table 13-9	Scaled Bond Law Parameters for the Extended Radiation Cases .....	13-24
Table 14-1	Bond-Slip Model Parameters for #8 Rebar in Pristine Concrete Con-A .....	14-24
Table 14-2	Effect of Irradiation on Compressive and Bond Strength Ratios .....	14-24



## EXECUTIVE SUMMARY

**Context.** Nuclear power plants (NPPs) were originally designed and licensed for 40 years of operation. The U.S. Nuclear Regulatory Commission (NRC) staff has defined subsequent renewal (SLR) to be the period of extended operation from 60 years to 80 years. The Generic Aging Lessons Learned for Subsequent License Renewal (GALL-SLR) Topical Report (NUREG-2191) is the NRC staff's generic evaluation of plant aging management programs and provides guidance for SLR applicants. NUREG-2191 establishes the technical basis for the adequacy of the applicants' aging management programs that are found to be consistent with its guidance. NUREG-2192 (Standard Review Plan for Review of Subsequent License Renewal for Nuclear Power Plants – SRP-SLR) provides NRC staff with guidance for the review of the content of applications for renewal of the initial renewed license.

In addition, the Expanded Material Degradation Assessment (EMDA) Report, NUREG/CR-7153 Vol. 4, "Aging of Concrete and Civil Structures," dated October 2014, identifies radiation effects on concrete as low-knowledge but high significance related to SLR. The work under this contract covers research activities related to the significance of irradiation on the bond strength of embedded steel in concrete.

The literature lacks data to assess the effects of irradiation on concrete reinforced by embedded steel elements, and in some plants, liners are attached with the concrete wall facing the reactor. This understanding of steel and concrete bonding and characterization is important for the assessment of irradiation effects in the concrete biological shields (CBSs) of light-water reactors (LWRs). The portion of the CBS that provides support to the reactor pressure vessel (RPV) is located in the reactor cavity in a region subjected to high neutron fluence that includes steel reinforcement, structural steel embedments, and anchorages that enable the structural functions of the CBS.

**Objectives.** This project had two objectives: (1) to develop, conduct, and analyze an experimental scoping study to characterize the effects of irradiation on the bond properties of carbon-steel elements embedded in concrete when subject to high-levels of irradiation, and (2) to develop and validate a modeling strategy to assess the effects of irradiation on reinforced CBSs in LWRs.

### Accomplishments

#### **Objective 1 – Experimental Scoping Study on Effects of Irradiation on Concrete–Steel Bond Strength**

Oak Ridge National Laboratory (ORNL) developed a research plan to conduct a first-of-a-kind neutron irradiation experiment on reinforced concrete specimens. For the benefit of building the research on a well-documented baseline, the same two concrete formulations that were previously tested by the Japan Concrete Aging Management Program (JCAMP) team in the JEEP-II test reactor were used in this study. Although the intent was to conduct the NRC experiment in the same reactor, the permanent shutdown of the JEEP-II reactor in 2019 led NRC and ORNL to investigate other options. An alternative irradiation facility was found at the CV-REZ LVR-15 test reactor (Czech Republic). This change of reactor required a technological solution to mitigate the radiation-induced heating which is higher in the LVR-15 reactor than in the JEEP-II reactor. Another critical aspect stemming from the change of reactor is that the neutron flux for the out-of-core position in the LVR-15 reactor is approximately 10 times lower

than the flux at the JEEP-II reactor. The introduction of this additional variable provided an opportunity to study neutron flux effects on the properties of irradiated concrete, which is a major unknown. Obtaining more data on neutron effects on irradiated concrete will aid in understanding the significance of accelerated irradiation against actual conditions in LWRs. Such effects are an order of magnitude lower than those in the out-of-core position of the LVR-15 reactor.

A total of 12 specimens were irradiated in a single irradiation rig placed outside the reactor core and shielded by a 10 mm thick tungsten wall to reduce gamma heating of the specimens. The study considered two concrete formulations that were used in the JCAMP project which differed on the type of aggregates used. One formulation, Con-A, uses aggregates called GA(F) which are considered more susceptible to neutron fluence, and the other formulation, Con-B, uses the aggregates known as GB(E), which are considered less susceptible to neutron fluence. Specimen geometry design is constrained by irradiation-induced heating, which has the potential to causing a thermal gradient-induced cracking at an early stage of the irradiation experiment, as well as a gradient of irradiation-induced damage. These factors make it difficult to interpret post-irradiation examination (PIE) results. To maximize the use of the space in the irradiation capsule and to obtain irradiated data on plain and reinforced concrete specimens, two specimen geometries were tested:

- Six plain hollow concrete cylinders (40 mm in diameter and 40 mm in height: 3 specimens of concrete formulation Con-A, and 3 specimens of concrete formulation Con-B), and
- Six single-reinforcement concrete cylinders (40 mm in diameter and 60 mm in height, with 6 mm diameter steel reinforcement bar: 3 specimens of concrete formulation Con-A, and 3 specimens of concrete formulation Con-B).

These two geometries made it possible to stack the 12 specimens in the ~600 mm high region of fast neutron flux in LVR-15 position XK1. An additional silica holder was placed at the mid-height of the stack to include 10 mm diameter aggregate cylindrical specimens. Having plain concrete and aggregate specimens allowed for direct comparison with the JCAMP results study of the rate effects caused by a fast-neutron flux 10 times lower than that of the JEEP-II reactor.

The specimen geometry design is constrained by the irradiation-induced heating and has the potential to causing thermal gradient-induced cracking at an early stage of the irradiation experiment, as well as gradient of irradiation-induced damage.

At the end of the irradiation experiment, the average fast neutron final fluence was  $\sim 1.12 \times 10^{19} \text{ n.cm}^{-2}$  ( $E > 0.1 \text{ MeV}$ ), and the average gamma dose was close to 1 GGy. The irradiation experiment lasted approximately 800 days (accounting for outages). The monitored irradiation temperature ranged between 37 °C and 52 °C. The fluence is directly comparable<sup>1</sup> to the JCAMP irradiation experiment for the Physical Property Test Capsule C (PPT-C).

In addition to the irradiation experiment, a companion experiment was conducted in a capsule replica placed in an oven in which the temperature controlled to match the irradiation temperature monitored by thermocouples inside the irradiation capsule. A third set of specimens was kept at room temperature.

---

<sup>1</sup> Comparable fast neutron fluence at energy above 10 keV.

Definition of the three sets of specimens, referred to as cold or room temperature, heat cured, and irradiated, make it possible to separate the effects of temperature and irradiation on concrete properties.

Because the irradiation conditions impose severe limitations on the concrete specimen dimensions, a separate experimental campaign was conducted in conjunction with the University of Tennessee in Knoxville to study possible scale effects on the bond strength of reinforced concrete. Reinforcement bar diameters of 6.3, 12.7, and 25.4 mm were used. The dimensions of the concrete specimens were scaled accordingly with a maximum diameter of 160 mm.

Pre- and post-irradiation (or post-heat curing) examination and testing included visual and optical microscopy, x-ray computed tomography (XCT), mass and dimensional measurements, ultrasound wave velocity measurements, splitting tests, direct compression tests, and bond testing.

The main research findings in support of Objective 1 are as follows:

Fast Neutron Flux Effect – The post-irradiation dimensional changes of the aggregate specimens provide evidence of the importance of the fast neutron flux, which was one order of magnitude lower in the present experiment than in the JCAMP experiment conducted at the JEEP-II reactor. The dimensional changes of the LVR-15-irradiated specimens were at least four times lower than the corresponding changes measured on the specimens irradiated in the JEEP-II reactor. This result highlights the importance of flux (fluence rate) effect and defects recovery on the development of radiation-induced volumetric expansion (RIVE). Because the fast neutron flux of the CBS is at least one order of magnitude lower in a pressurized water reactor (PWR), it can be hypothesized that the effects of flux and defects recovery may be even more pronounced. The characterization results of in-service irradiated concrete from decommissioning plants will be crucial to address this question in the future.

Mass Change for Irradiated Concrete – The changes of mass in the irradiated and heat-cured concrete specimens are comparable. Note that all specimens were pre-cured at the expected irradiation temperature before the irradiation experiment and the companion heat curing experiment. Hence, it can be inferred that the gamma irradiation produced limited additional dehydration of the water present in the cement hydrates.

Dimensional Change of Irradiated and Heat-Cured Concrete – The dimension changes in irradiated and heat-cured specimens are also comparable.

Bond Strength – The results from the analysis of the scale effects campaign show that the bond strength scales with the diameter of the reinforcement bar and the square root of the concrete compression strength. The maximum aggregate size was not found to be a parameter influencing the bond strength. The bond strength for the unirradiated and irradiated specimens was comparable and controlled, approximately, by the square root compressive strength of the unirradiated and irradiated specimens, respectively.

## **Objective 2 – Modeling Strategy for Assessing the Effects of Irradiation on the Reinforced Concrete Biological Shield Supporting the Reactor Pressure Vessel**

ORNL conducted various types of simulations to analyze the experiments that had been conducted to address Objective 1, as well as structural simulations to assess the irradiation-induced damage depth in a CBS of a PWR.

The simulation of the irradiated aggregates was conducted with the fast Fourier transform (FFT)-based code MOSAIC (Microstructure Oriented Scientific Analysis of Irradiated Concrete) using multiple characterization techniques, including petrography, x-ray diffraction (XRD), energy-dispersive x-ray spectroscopy, and micro x-ray fluorescence imaging, to produce high-resolution (~15 microns) mineral phase maps. With this modeling, each mineral property is associated with the Irradiated Minerals, Aggregates and Concrete (IMAC) database created by ORNL. The radiation-induced expansion of individual minerals is modeled using empirical expression derived from the literature (Le Pape et al., 2018) and obtained from PIE of minerals tested in various test reactors. The two aggregates included in this study were modeled, and it was found that the calculated expansions overestimate the post-irradiation dimensional changes measured after irradiation in the LVR-15 reactor. This result confirms that the flux effect discussed previously has a major effect on the expansion rate.

Simulation of the irradiated plain and reinforced concrete specimens was conducted using the lattice discrete particle model (LDPM), a meso-scale model that accounts for the aggregate size distribution. The LDPM can capture data on microcracking and fracture of concrete subject to static and dynamic loading. Heat transfer and moisture transport data are also included in this model. The radiation-induced expansions of aggregates are modeled as eigenstrains. The LDPM was applied to model the specimen's loss of mass and the associated shrinkage. The aggregate expansion was modeled using the experimental data collected from the post-irradiation measurements and microcracking. The simulation results are in good agreement with the post-irradiation data, providing confidence in LDPM's capabilities to model the mechanical effects of irradiation in concrete. The irradiation-induced drying shrinkage compensates for the reduced aggregates' RIVE caused by the observed flux effects. This explains the relatively low amplitude and scatter of post-irradiation dimensional change. LDPM was then used to model the bond strength tests.

The simulation of the bond tests (*pullout*) was first conducted on unirradiated specimens. This analysis was used to inform modification to the test setup to ensure that the specimen failure mode would conform to the expectation of a slipping failure mode rather than a splitting failure mode. Then LDPM was used to successfully analyze the irradiated specimens. The objective of this work was to determine the properties of the bond interface between a reinforcing bar and the surrounding concrete. Herein, the term *interface* describes the layer of mortar located between the bar ribs and extending slightly beyond the tips of the ribs. This corresponds to the location of the shear fracture during the bar slippage. Analysis of the bond tests results obtained in this study led to the conclusion that the bond strength of the rebar-concrete interface is a direct function of the square root of the residual compressive strength.

The modeling and simulation approaches described in the literature for the CBS structural response and those developed by ORNL were reviewed. This analysis drew on aggregate RIVE data from earlier studies, such as the JCAMP studies, but it did not address the effect of fluence rate in the RIVE. The ORNL models used the VERA-Shift irradiation transport model to obtain the neutron flux field used as inputs for the structural simulations. Two modeling strategies were employed. First, the LDPM was used to simulate a representative wedge model of the biological shield. Second, a simplified finite element model of the entire biological shield was simulated using the Grizzly finite element code based on the MOOSE (Multiphysics Object Oriented Simulation Environment) platform developed by Idaho National Laboratory. It is important to note that the conclusions of these studies use the radiation-induced expansion of the aggregates obtained from test reactor data generated before the present study. Hence, the radiation-induced expansion is likely overestimated.

All models reach the same conclusions: (1) radiation-induced expansion of the concrete that occurs mainly in a region that includes the concrete cover causes the formation of biaxial compressive stresses in the vertical and hoop (orthoradial) direction; (2) the combination of irradiation-induced microcracking and the biaxial loading causes crack formation predominantly opening along the radial direction; (3) the largest crack opening occurs near the surface of the concrete facing the reactor cavity, and the crack opening decreases along the radial direction; (4) the damaged depth found by the LDPM and finite element model are comparable; and (5) the residual strength of the concrete within the damage depth should not be accounted for in subsequent structural assessments.

The main conclusions of the comparison between the finite element analysis (FEA) and the LDPM results are (1) the damage depth evolves nonlinearly with the operating duration with the propagation rate decreasing with time, and (2) FEA tends to marginally underestimate the damage depth by ~20 mm compared to LDPM, which is judged to be more capable of representing the absence of scale separation between the aggregate size and the strong gradient of radiation-induced expansion. Assuming RIVE rate and amplitude as derived from test reactor data (i.e., under accelerated condition), the damage depth estimate reaches the location of the reinforcement.





## ACKNOWLEDGMENTS

This research was conducted by Oak Ridge National Laboratory in collaboration with the following institutions:

1. Centrum Výzkumu Řež (CVR) for designing and fabricating the irradiation capsule and test rig, executing the irradiation experiment, and performing the post-irradiation examination and testing.
2. The University of Tennessee, Knoxville (UTK) for developing and executing the scale effects study.
3. The University of Nagoya for providing the concrete aggregates and cement, which enabled replication of the concrete formulation used in specimens previously irradiated by the Japan Concrete Aging Management Program.

The following individuals are gratefully acknowledged for their contributions to this research: Martina Pazderova, Alica Fedoriková, Tomáš Melichar, Jaroslav Šoltés, Miroslav Vinš, Karel Dočkal, Marel Mikloš, Zbyněk Hlaváč, Jakub Šivr, Michael Sovadina, Leoš Křivký and Kateřina Hrdličková (CVR), Pr. Z. John Ma, Syed Muhammad Aqib, Lee Andrew Baker, Mohammed Abdelrahman Salih Abdelrahman (UTK), and Pr. Ippei Maruyama (University of Tokyo, formerly at Nagoya University).

The authors would like to acknowledge the outstanding guidance and thorough review performed by the following US Nuclear Regulatory Commission staff members: Madhumita Sircar, Jose Pires and Andrew Prinaris. Their support was key to the success and quality of the work presented in this report.



## ABBREVIATIONS AND ACRONYMS

ASR	alkali-silica reaction
BC	boundary condition
BWR	boiling water reactor
CA	coarse aggregate
CAC	calcium aluminate cement
CBS	concrete biological shield
CEA	Commissariat à l'Energie Atomique
CFD	computational fluid dynamics
CMD	continuum model domain
CNWG	Civil Nuclear Energy Research and Development Working Group
CSH	calcium-silicate hydrate
CTE	coefficient of thermal expansion
CVR/CV-ReZ	Centrum Vyzkumu Rež.
DOE	US Department of Energy
EDS	energy dispersive x-ray spectroscopy
EMDA	Expanded Materials Degradation Analysis
ENDF	Evaluated Nuclear Data File
FE	finite element
FEA	finite element analysis
FFT	fast-Fourier transform
GALL-SLR	Generic Aging Lessons Learned for Subsequent License Renewal
GIF	Gamma Irradiation Facility
hcp	hardened cement paste
HF	high friction
IFE	Institute for Energy Technology
IAI	intra-aggregate interfaces
IMAC	Irradiated Minerals, Aggregates and Concrete
IPI	inter-particle interface
ITZ	interfacial transition zone
JA	Japanese aggregate
JAEA	Japan Atomic Energy Agency
JCAMP	Japan Concrete Aging Management Program
JG	Japanese gradation
JMTR	Japan Materials Testing Reactor
LDPM	lattice discrete particle model
LF	low friction
LWR	light-water reactor
LWRS	Light Water Reactor Sustainability Program
MARS	Multiphysics Analyses of the Response of Structures
MCNP	Monte Carlo N-Particle
MD	molecular dynamics
METI	Ministry of Economy, Trade and Industry

MOSAIC	Microstructure Oriented Scientific Analysis of Irradiated Concrete
MOOSE	Multiphysics Object Oriented Simulation Environment
MP	multiphysics
MSMD	meso-scale model domain
mXRF	micro x-ray fluorescence
NMAS	nominal maximum aggregate sizes
NPP	nuclear power plant
NRC	US Nuclear Regulatory Commission
NSSS	nuclear steam supply system
OPC	ordinary Portland cement
ORNL	Oak Ridge National Laboratory
PIE	post-irradiation examination
PPT-C	Physical Property Test capsule C
PVC	polyvinyl chloride
PWR	pressurized water reactor
RBSM	rigid body spring model
RC	reinforced concrete
RIVE	radiation-induced volumetric expansion
RH	relative humidity
RPV	reactor pressure vessel
SEM	scanning electron microscopy
SLR	subsequent license renewal
SNL	Sandia National Laboratories
SUJB	Czech State Office for Nuclear Safety
TA	Tennessee aggregate
TC	thermocouple
TG	Tennessee gradation
TH	thermohydraulic
w/c	water-to-cement ratio
XCT	x-ray computed tomography
XRD	x-ray diffraction
XRF	x-ray fluorescence

# 1 INTRODUCTION

## 1.1 Background

Nuclear power plants (NPPs) were originally designed and licensed for 40 years of operation. Now that 40 years have passed, many plants have undergone a license renewal process to extend plant operation to 60 years, and the same extension is planned for most other remaining NPPs. Currently, subsequent license renewals (SLRs) are underway to extend plant operation for a range of 60 to 80 years. In addition, research meetings have been held to explore the feasibility of operation beyond 80 years.

The Expanded Material Degradation Assessment (EMDA) Report, NUREG/CR-7153 Vol. 4, “Aging of Concrete and Civil Structures” (Graves et al., 2014), identifies radiation effects on concrete as low-knowledge but high significance related to SLR. Since that publication, knowledge has continued to progress through various research activities. The work performed under this contract covers activities related to the significance of irradiation on the bond strength of embedded steel in concrete.

## 1.2 Research Overview

### 1.2.1 State of Knowledge and Research Needs

Concrete biological shield (CBS) walls that are subjected to high neutron flux include steel reinforcement and anchorages. The literature lacks the data needed to assess the effects of irradiation on concrete reinforced with embedded steel elements. The primary purpose of this study is to generate data and gain further understanding of the effects of irradiation on the interactions between concrete and embedded steel for use in the assessment of irradiation effects in light-water reactor (LWR) CBSs that support the reactor pressure vessel (RPV). This study’s two main objectives are (1) to develop, conduct, and analyze an experimental scoping study to characterize the effects of irradiation on the bond properties of carbon-steel elements embedded in concrete when subject to high levels of irradiation, and (2) to develop and validate a modeling strategy to assess the effects of irradiation on reinforced CBSs in LWRs. In addition, this study also investigated rate and scale effects in limited scope in accelerated experiments of test reactors and typical CBSs in pressurized water reactors (PWRs).

The CBS wall in LWRs is exposed to high-energy neutron flux and gamma rays emitted from the reactor core and transported through the RPV. This research topic has been considered high priority in the U.S. and Japan in relation to extending LWR operation. At ~80 years of operation, it is currently estimated that the bounding fluence approaches  $2\text{--}7 \times 10^{19} \text{ n.cm}^{-2}$  at  $E > 0.1 \text{ MeV}$  (Esselman and Bruck, 2018), which is approximately 6–7 times the threshold fluence level recommended by researchers for onset of irradiation-induced concrete damage:  $10^{19} \text{ n.cm}^{-2}$  at  $E > 0.1 \text{ MeV}$  (Field et al., 2015). It is important to note that current knowledge regarding the effects of irradiation on concrete and concrete constituents is almost exclusively based on data obtained in test reactors under accelerated irradiation aging conditions.

The susceptibility of concrete to neutron irradiation greatly varies as a function of its constituents: coarse aggregates, sand, and hardened cement paste (hcp). Higher irradiation susceptibility has been expressed as a direct function of aggregates’ radiation-induced volumetric expansion (RIVE), which is the propensity of swelling as a function of the minerals’ contents, structures, and textures. Irradiation-induced amorphization—also referred to as

*metamictization* when occurring naturally by alpha-decay in rocks bearing isotopes such as those of U or Th—also induces significant density change, especially in silicates. For example, the maximum volumetric expansion of quartz and feldspars—a group of rock-forming tectosilicate minerals that make up as much as 60% of the Earth’s crust—has been shown to be as large as ~18% for quartz and ~8% for feldspars, although the change of density in calcite remains rather low (~0.3%). Depending on the mineralogical content, considerable variations in aggregate RIVE have been observed as described in the comprehensive review by Field et al. (2015). Incompatible RIVEs in adjacent aggregate-forming minerals lead to the formation of intra- and inter- granular cracks, thus reducing the aggregate’s mechanical properties. In addition, some observed post-irradiation expansions exceed the level considered as detrimental by alkali-silica reaction (ASR) researchers. Because the CBS wall’s structural concrete comprises ~70% of aggregates by volume, RIVE induces severe stresses on the surrounding hcp. In the absence of relaxation, high levels of RIVE are expected to cause cracking or even fracturing of concrete. Limited post-irradiation visual observations do not show visible ASR-like crack patterns, which supports the hypothesis of an irradiation-assisted relaxation mechanism in the cement paste. Nevertheless, concrete exhibits a trend toward decreased engineering properties when exposed to fast neutron fluence of  $10^{19}$  n.cm<sup>-2</sup> at  $E > 0.1$  MeV.

These observations were obtained from concrete specimens irradiated in test reactors, which implies that (1) the neutron and gamma irradiation fields are quite uniform in the specimens, and (2) specimen RIVE is not intentionally constrained.

These conditions are different in CBS walls of LWRs. Caused notably by the presence of shielding elements such as hydrogen present in the constitutive water, strong gamma and neutron attenuations are expected from neutron transport simulations. According to Remec (2013), the fast-neutron flux in 2- and 3-loop PWRs drops by an order of magnitude over a depth of ~10–15 cm from the surface of concrete that was directly exposed to reactor radiation at the elevation of the fuel core midplane. This attenuation results in a similar gradient of RIVE. Because the CBS wall is a massive concrete structure, its RIVE is structurally constrained, thus causing high biaxial compressive elastic stresses in the vertical and hoop directions of the wall near the reactor cavity, as well as limited elastic tensile hoop stresses toward its back (Le Pape, 2015). Simultaneously, the prolonged moderate temperature exposure (<65 °C by design) and strong internal moisture content gradient in the absence of a liner affect the degree of concrete hydration, and thus they affect the wall’s mechanical properties. These conditions can lead to the development of lower strengths toward the reactor cavity (Yokokura et al., 2017). As mentioned previously, the dissipation of the RIVE-induced elastic stresses results from a competition between the development of cracking and potential relaxation in the hcp.

Preliminary studies based on unreinforced irradiated concrete structural analysis suggest that the extent of radiation-induced concrete damage (spalling) appears to be limited to a depth of approximately <20 cm of the CBS wall, but it exceeds the reinforcement depth. These results require confirmation, and the consequences of this damage to the structural performance under seismic and accident conditions (e.g., impact on the RPV supports, sudden increase of temperature in the cavity) require investigation. The effects of neutron irradiation–induced damage from the concrete constituents to the biological shield can be summarized as follows. Neutron irradiation bombardment causes the distortion of the pristine rock-forming mineral crystals. This amorphization and subsequent disordering leads to a change of density and other physical properties of the irradiated minerals. In general, the change of density results in an anisotropic expansion of the minerals, increasing with the total fast neutron fluence. The expansion kinetics and final amplitude depend on the minerals’ chemical compositions and the

irradiation temperature (defects recovery increases with higher temperatures). Although the final expansion reaches the same level, the expansion is slower at the higher temperature. Because rocks are complex assemblages of minerals, adjacent minerals exhibit different expansions, and mismatch strains develop, causing cracking in the irradiated aggregates. The loss of mechanical properties of aggregates, combined with their expansion imposing stresses to the surrounding cement paste, generally leads to a reduction of Young's modulus and the strength properties of the concrete. This phenomenon manifests itself for fast neutron fluences higher than  $10^{19}$  n.cm<sup>-2</sup> ( $E > 0.1$  MeV). Such a fluence is expected to be exceeded at the surface of the biological shield for all U.S. PWRs at an extended operation of 80 years. Neutron attenuation is caused by interaction with large cross-section elements, including hydrogen present in the constitutive water in the concrete. Hence, the neutron flux field in the CBS is subject to important spatial variations. Because the resulting irradiation-induced expansion and the loss of mechanical properties are governed by the cumulative fast neutron fluence, these factors are also subject to important spatial variations in the biological shield.

Several knowledge challenges persist to confidently predict the degree and location of the irradiation-induced damage, as well as its long-term significance to structures exposed to a sustained high level of radiation:

1. *Neutron rate effect*: The aggregate-forming minerals are subject to neutron irradiation–induced amorphization. This phenomenon is the result of two competitive mechanisms: the ballistic effect resulting in primary and secondary knocked-off atoms and defects recovery as indicated by a RIVE rate that decreases with increasing temperature. In test reactors, the neutron flux is one-to-two orders of magnitude higher than in LWRs, which raises the question of the significance and interpretation of test data.
2. *Irradiation-induced stress relaxation*: The hcp is subject to internal stresses caused by the expansion of the aggregates and the restraining structural effects. The resulting mechanical stresses in the hcp can be relaxed by two mechanisms: cracking and relaxation, the latter of which is related to the creep properties of the hcp. Although the effects of moisture content and temperature on creep rate are well documented, the effects of neutron irradiation are mostly unknown. The scarce literature on the subject (Gray, 1971) indicates a large increase of the creep rate, which would be beneficial for limiting crack formation.
3. *Synergies with chemical degradation*: Examination of harvested concrete from the internal concrete wall at Hamaoka NPP, a boiling water reactor (BWR), showed that aluminum-bearing silicates (here feldspar) gradually dissolved and reacted with cement-bearing Portlandite— $\text{Ca}(\text{OH})_2$ —to precipitate into amorphous C–(A)–S–H hydrates (Rymeš et al., 2019). This result illustrates that long-term exposure to moderate temperature ( $\sim 40\text{--}50$  °C) can lead to dissolution–precipitation mechanisms between aggregate-forming minerals and cement hydrates. In CBS wall designs that include a liner trapping the moisture content in the concrete, in-service irradiated concrete is exposed to a comparable temperature, combined with in-service irradiation. It has been established that irradiation-induced amorphization causes a significant increase in the dissolution properties of rock-forming silicates in an alkaline medium (Pignatelli et al., 2016), possibly promoting enhanced dissolution–precipitation mechanisms, including ASR. The possibility of irradiation-induced ASR has not yet been fully investigated.



4. *The interactions between embedded steel and concrete:* The potential effects of irradiation on a combined system that includes concrete and embedded steel are detailed below:
  - a. Confining effect of the aggregate's RIVE: This effect is largely unknown. It can be hypothesized that the presence of steel creates a restraining effect in the direction of the reinforcement of the otherwise isotropic volumetric expansion of the aggregates. There is limited experimental evidence of that effect during irradiation because the data available in the open literature on neutron-irradiated concrete report that the post-irradiation examination (PIE) of concrete specimens are placed in a condition to allow "free" irradiation-induced expansion. However, it can be inferred from unwanted restraint during irradiation that such a mechanism exists and affects the radiation-induced damage. Conditions of restrained expansion have been observed by Dubrovskii et al. (1966) and Maruyama et al. (2017). In both cases, the design of the gap between the specimens and the irradiation capsule's wall was underestimated for the prolonged irradiation of concrete made of aggregates containing >90% of quartz, which caused high levels of RIVE. Interestingly, the residual Young's modulus and strength, both measured when loading the cylindrical specimens in their axial direction after neutron irradiation at  $8\text{--}10 \times 10^{19} \text{ n.cm}^{-2}$  ( $E > 0.1 \text{ MeV}$ ), showed an increase relative to the values of irradiation at  $4\text{--}5 \times 10^{19} \text{ n.cm}^{-2}$  ( $E > 0.1 \text{ MeV}$ ). When the specimens were unconfined, it was observed that the irradiated mechanical properties decreased with increasing RIVE. It can be inferred that the partial mechanical or structural confinement of the RIVE affects formation of irradiation damage. The presence of embedded steel will cause such a confinement. The questions are:
    1. How does the presence of embedded steel in concrete modify the radiation-induced expansion and damage from plain irradiated concrete?
    2. How does the development of radiation-induced damage in the concrete surrounding the embedded steel elements affect the bond strength between these two constituents?
  - b. The different forms of water in concrete constituents are subject to radiolysis.

*Reactor gamma rays interact with concrete constituents primarily by Compton scattering (Kontani et al., 2013), which is the interaction and ejection of orbital electrons accompanied by a loss of energy. The primary effect of gamma in concrete is water radiolysis, which is the decomposition of water molecules due to ionizing radiation (Le Caër, 2017). The energy levels of electrons ejected by Compton scattering are too low to affect the solid phase of cement paste and aggregates (Le Pape, 2020).*

The decomposition of water leads to the formation of radiolytic gases, mainly  $\text{H}_2$  and  $\text{O}_2$ , that can theoretically increase the susceptibility of corrosion of the embedded steel. Corrosion is known to affect the bond strength of embedded reinforcement with concrete and the formation of concrete cracking at high levels of corrosion product formation. The first question to be addressed is: does combining neutron and gamma irradiation in reinforced concrete cause formation of corrosion in embedded steel? Recent experimental results (Dabrowski et al., 2022) suggest an increase in corrosion current density by an order of magnitude.

This project aims to address the gap in data needed to assess the effects of irradiation on concrete reinforced with embedded steel elements. Understanding and characterizing these effects is important for evaluating irradiation impacts on LWR CBSs. This is particularly important because the portion of the biological shield wall exposed to high neutron flux is situated at the reactor cavity and includes embedded steel reinforcement, support anchorage, liner anchorage, and in some cases, steel section anchorage.

### 1.2.2 Project Scope and Strategy

The first main objective of this research is threefold: (1) to study the interaction between concrete and embedded steel elements under irradiation (neutron fluence and gamma heating), (2) to develop a modeling framework to account for the irradiation-induced damage occurring at the microscale level, and (3) to assess the structural performance of PWR and BWR CBS walls. The second main objective is to determine the penetration of irradiation-induced damage, referred to in this report as *damage depth* in the biological shield.

Additionally, the preliminary design work and the search for adequate irradiation test reactors led to the design of an irradiation experiment conducted in the LVR-15 reactor at the Centrum Výzkumu Řež (CVR) facility (Czech Republic) instead of at the JEEP-II reactor at IFE, Norway, as originally intended. The fast neutron flux in LVR-15 is approximately one order magnitude lower than the flux in the JEEP-II reactor. This characteristic made it possible to gain an initial understanding of the neutron flux effects by performing irradiation experiments in a lower flux reactor.

The project objectives include two tasks to be addressed in parallel with mutual interaction:

1. **Irradiation testing of a composite element made of concrete and embedded steel:** Closing the gap of literature data on irradiated reinforced concrete is critical for understanding and characterizing the interactions of these two constituents under irradiation. Their interactions can be studied by harvesting materials irradiated in service or (not exclusive) by performing accelerated irradiation. The first option requires finding viable harvesting opportunities (fluence  $>10^{19}$  n.cm<sup>-2</sup> at  $E > 0.1$  MeV and silica-rich aggregate). Ongoing studies and opportunities are currently being sought. The second option requires performing irradiation tests on a relatively small-scale because of the dimensional constraints for space and irradiation-induced heating. Irrespective of the scale of the experiment, such testing is undeniably invaluable. However, the objective is to quantitatively assess the effects of irradiation at the structural scale, which requires development of scaling laws.
2. **Modeling strategy validated by test data:** Although the structural design of reinforced concrete is typically conducted within the framework of continuum mechanics, which assumes that concrete is a homogeneous material, applying this approach to account for irradiation effects is challenging because there is a lack of clear scale separation—a fundamental requirement for continuum mechanics. In most engineering problems, the characteristic length of materials at the continuum level is much smaller than the characteristic wavelength of the loading on the structure. The fast neutron flux is significantly attenuated by high cross-section elements such as the hydrogen in the water that is present in shielding concrete. Consequently, the neutron flux varies within the CBS. At the mid-elevation of the fuel core, the flux at the surface of the CBS (inner diameter) is an order of magnitude higher than a depth of approximately 15 cm: the exact depth depends on the concrete's chemical composition and moisture content.

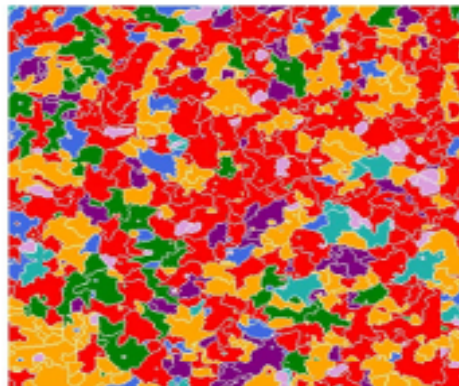
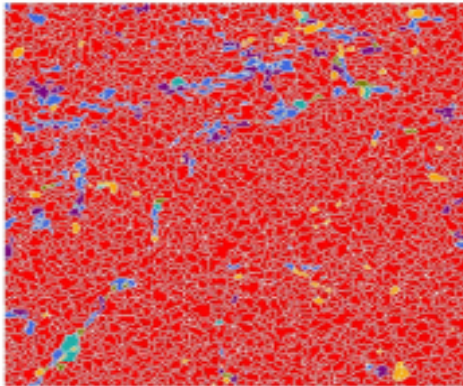
Because of the irradiation attenuation in concrete, the properties of irradiated concrete vary significantly with location. Therefore, the variation in RIVE over a depth of 10 to 20 cm—corresponding to the size of a representative concrete volume—cannot be ignored. Because RIVE drives the internal loading in concrete, the characteristic length of this variation cannot be considered much greater than the size of a representative volume of concrete. This lack of scale separation challenges the use of continuum mechanics for analysis of homogeneous materials such as finite element analysis (FEA). Consequently, this study employed a discrete meso-scale modeling strategy to simulate the mechanical tests performed on irradiated concrete specimens and to assess the structural effects of irradiation on the CBS, as illustrated in Figure 1-1:

- 1) At the microscale, a high-resolution imaged-based modeling approach is adopted. It leverages the efforts of the DOE LWR Sustainability (LWRS) Program to develop the fast Fourier transform (FFT)-based simulation tool MOSAIC (Torrence et al., 2021). At that scale, the complexity of the aggregate assemblage is explicitly accounted for, and direct comparison with the Japan Concrete Aging Management Program (JCAMP) irradiated data (Maruyama et al., 2017) was performed to validate the models.
- 2) At the mesoscale, reinforcement is introduced into the model. Concrete is modeled as a composite material formed of aggregate and cement paste using the lattice discrete particle model (LDPM), which provides an effective description of cracking caused by the mechanical interaction between steel reinforcement and concrete (Cusatis et al., 2011a, 2011b).
- 3) At the structural scale, the portion of the structure subjected to high-irradiation exposure is modeled using the exact strategy that is used at the mesoscale, whereas the portion of the structure subjected to low-irradiation exposure is classically modeled using continuum mechanics. A comparison with a classical continuum approach using FEA is also presented.

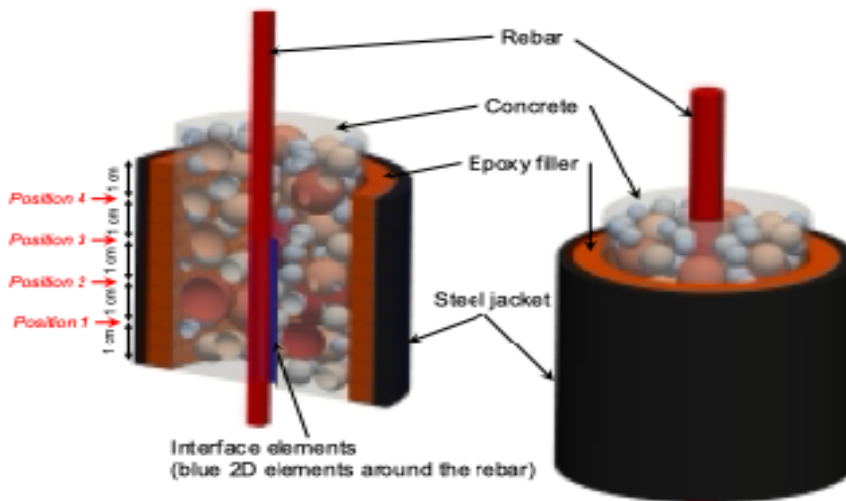
## Microstructures of aggregate – MOSAIC

GA / F

GB / E



## Bond test model – LDPM



## CBS wedge model – LDPM

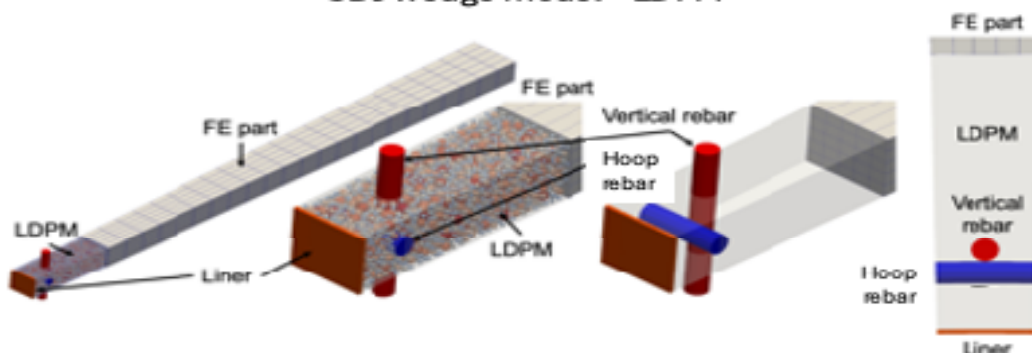


Figure 1-1 Illustration of the Models of Irradiated Aggregates, Concrete, and Concrete Structures Employed in this Research

### 1.3 Organization of the Report

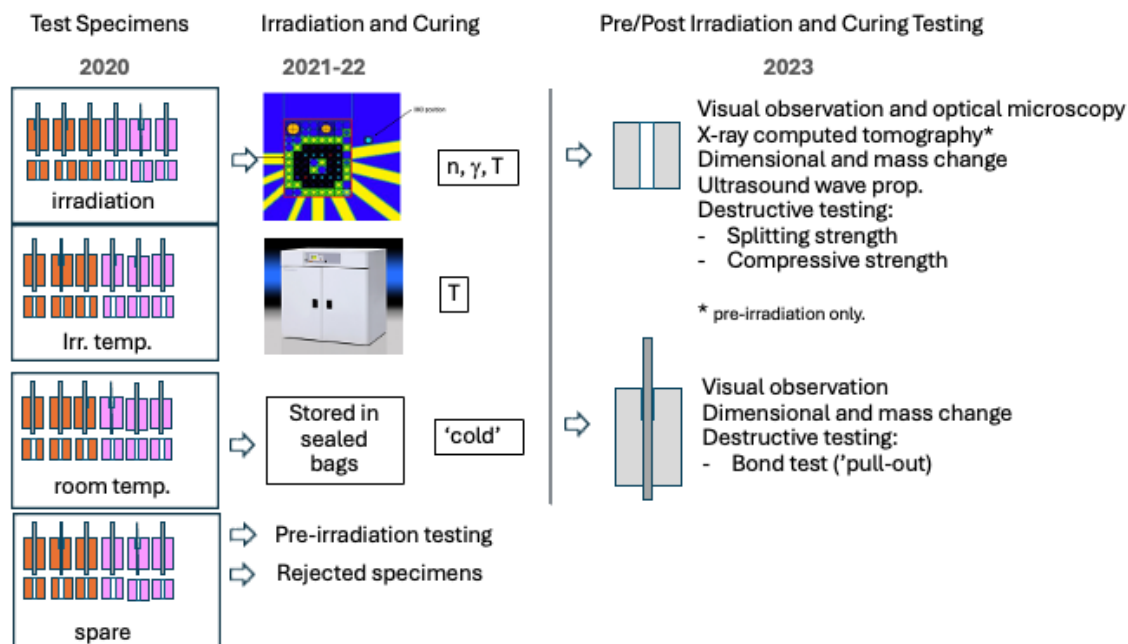
Chapter 2 details the design of an irradiation experiment aimed at studying the effects of neutron exposure on concrete. The experiment targeted a neutron fluence exceeding  $10^{19}$  n/cm<sup>2</sup> ( $E > 0.1$  MeV) and maintained an irradiation temperature below 70 °C. Conducted at the LVR-15 test reactor in the Czech Republic, specifically in out-of-core position XK1, the study utilized concrete constituents sourced from Nagoya University. These constituents were chosen to mirror two specific formulations previously irradiated in the JEEP-II reactor under the Japan Concrete Aging Management Program. This reactor is now undergoing decommissioning. The rationale for replicating these concrete formulations was to establish a reliable baseline for comparing the properties of unirradiated and irradiated materials. The experiment encompassed various types of specimens, including plain concrete, reinforced concrete to assess the impact of irradiation on the bond strength of embedded steel reinforcement with concrete, and aggregate specimens. The irradiation setup featured meticulous design of the capsule and rig to precisely control the irradiation conditions. By replicating the concrete formulations from the Japan program, the study aimed to enhance the understanding of how neutron irradiation affects concrete, thereby contributing valuable insights to the field of concrete aging and performance in nuclear environments.

Chapter 3 elaborates on the meticulous fabrication protocol employed for both concrete and reinforced concrete specimens in the irradiation experiment. The primary focus was on optimizing specimen geometry to prevent excessive heating caused by irradiation and to minimize the risk of thermal cracking. This optimization also ensured efficient positioning of specimens within the active neutron flux in the irradiation position. The dimensions of the specimens were carefully controlled: plain concrete specimens were limited to 40 mm in diameter and either 40 mm or 60 mm in height, depending on the specific requirements. For reinforced concrete specimens, which included #2 ribbed steel bars, dimensions were adjusted accordingly to maintain consistency and to facilitate accurate testing. To achieve uniformity and precision in specimen production, specific polyvinyl chloride (PVC) molds were custom-machined. Each concrete formulation involved the preparation of twelve plain concrete specimens, often referred to as *donuts*, and twelve reinforced concrete specimens known as *pullout specimens*.

The 48 specimens were organized into four distinct groups for testing and evaluation purposes:

1. **Irradiated specimens:** subjected to neutron irradiation at CVR.
2. **Heat-cured specimens:** tested at Oak Ridge National Laboratory (ORNL) under conditions replicating irradiation temperature in a dedicated replica irradiation capsule.
3. **Room temperature-cured specimens:** maintained at ambient conditions for comparative analysis.
4. **Spare specimens:** reserved for contingency and additional testing needs.

This systematic approach ensured comprehensive testing across different curing and irradiation conditions, providing valuable data regarding the effects of neutron exposure on concrete and reinforced concrete materials. Figure 1-2 provides a summary of the four groups and a short list of the examination and testing conducted before and after the irradiation experiments or the extended curing at room or irradiation temperature.



**Figure 1-2 Summary of the 4 Groups of Testing Conditions and List of the Pre/Post-Irradiation or Temperature Curing Examination and Testing**

Chapter 4 of this report delves into the detailed irradiation conditions endured over a span of 14 reactor cycles totaling approximately 800 days of testing, accounting for scheduled outages. The temperatures within the irradiation capsules were meticulously monitored using three thermocouples, revealing a range between 36 °C and 51.5 °C throughout the experiment. To assess the thermal impact on the specimens, a heat transfer analysis was conducted using a finite element (FE) model. This analysis demonstrated that the temperature variation within each irradiated specimen did not exceed 7 °C, ensuring controlled and consistent thermal conditions during irradiation. Neutron fluence and gamma dose were quantified using the Monte Carlo N-Particle (MCNP) code. Calibration of these results was achieved through post-irradiation analyses measured from metal foil coupons strategically placed among the concrete specimens at various positions within the test stack. By the conclusion of the irradiation experiment, the average fast neutron fluence exceeded  $1.12 \times 10^{19} \text{ n/cm}^2$  (with energy > 0.1 MeV), whereas the accumulated gamma dose reached approximately 940 MGy ( $9.4 \times 10^{10} \text{ rad}$ ). Throughout the experiment, temperature data recorded at CVR were regularly transmitted to ORNL after each cycle. This exchange of information facilitated precise monitoring and control of specimen heating within the replica irradiation capsule at ORNL, ensuring consistent testing conditions across different phases of the experiment. Chapter 4 thus provides a comprehensive overview of the irradiation environment, the thermal management strategies used, and the precise measurement and calibration techniques employed to validate the irradiation effects on the concrete specimens under study.

Chapter 5 details the characterization and testing methodologies utilized to assess various properties of the concrete specimens, including mass and dimensional changes, wave velocity, splitting strength, compressive strength, and bond strength of steel reinforcement embedded in concrete. Notably, these tests were custom designed for the specific experimental conditions

and did not adhere to established standards, thus necessitating adaptations to meet operational constraints within CVR's hot cells. Custom protocols were developed to accurately measure changes in mass and dimensions of the specimens under different testing and curing conditions (irradiated, heat-cured, and room temperature-cured). Techniques were devised to measure the ultrasonic wave velocity through the concrete specimens. Specific methodologies were designed to evaluate the splitting and compressive strengths of the concrete specimens. Finally, innovative approaches were employed to determine the bond strength between steel reinforcement and concrete. This involved specialized testing setups to assess the integrity of reinforced concrete structures under irradiation. Given the unique operational constraints within CVR's hot cells, each testing method was meticulously adapted to ensure accuracy and reliability of the results. Chapter 5 provides a detailed account of these customized methodologies.

Chapters 6, 7, and 8 comprehensively present the results obtained from the observation, characterization, and testing of the concrete specimens subjected to different conditions. Chapter 6 focuses on the visual observation and qualitative assessment of the specimens irradiated in the LVR-15 reactor. It details any visible changes in appearance, such as cracking or surface degradation, which may indicate the effects of irradiation on the concrete. Chapter 7 investigates the detailed characterization of specimens that were cured at the irradiation temperature, simulating thermal conditions experienced during neutron exposure. In Chapter 8, the focus shifts to the testing results of specimens cured at room temperature. These chapters include quantitative analysis of properties such as mass changes, dimensional stability, wave velocities, and both splitting and compressive mechanical strengths.

Chapter 9 presents the objectives, methods, and test results of a companion scaling study conducted at the University of Tennessee, Knoxville (UTK). This study was motivated by the need to establish bond scaling laws, making it possible for the test data on small-size specimens to be extrapolated to reinforcement diameters relevant for nuclear structures. A scaling law was developed as parameterized on the bar diameter, the height and spacing of bar ribs, and the strength of the concrete.

Chapter 10 thoroughly interprets the test data presented in Chapters 6 through 8, comparing the data extensively with findings from the JCAMP experiment conducted in the JEEP-II reactor. A key discovery highlights aggregate RIVE's sensitivity to fast neutron flux. Specifically, aggregate GA(F), which contains 92% quartz, exhibited dimensional changes 3 to 6 times higher in the JEEP-II experiment compared to the material from the LVR-15 experiment. This difference is primarily attributed to the significantly lower fast neutron flux in the LVR-15 experiment ( $3.6 \times 10^{11} \text{ n/cm}^2 \text{ s}$ ,  $E > 0.1 \text{ MeV}$ ) compared to results from the JEEP-II experiment ( $3.6 \times 10^{12} \text{ n/cm}^2 \text{ s}$ ,  $E > 0.1 \text{ MeV}$ ). The underlying mechanism driving these flux-dependent effects requires further identification and characterization to facilitate accurate extrapolations for irradiation conditions in PWRs during service.

Chapter 11 focuses on modeling the bond test using the LDPM. It details the bond model that describes the mechanical behavior of the interface between concrete and steel reinforcement, including the calibration of constitutive parameters. The LDPM allows for an explanation of two distinct failure modes observed during testing—*splitting mode*, which leads to fracture of the concrete specimen, and *slipping mode*, in which there is complete failure of the bond between concrete and steel. Given the dimensions of the test specimens, there was a significant risk of the concrete specimens splitting during testing. Therefore, the model was crucial for mitigating this risk and providing insights into both fracture modes observed. Chapter 11 provides a thorough explanation of how LDPM was employed to simulate and elucidate the bond behavior

under various conditions. It highlights the importance of accurate modeling in predicting and interpreting experimental results related to the bond strength between concrete and steel reinforcement.

Chapter 12 provides a comprehensive summary of the impact of neutron and gamma irradiation on the mechanical properties of concrete and its constituents. It serves as an introduction to the models discussed in Chapter 13, which are used for interpreting the post-irradiation characterization and test data.

Chapter 13 presents the analysis of properties observed in aggregates and plain concrete specimens irradiated in the LVR-15/XK1 position. The expansion of aggregates is scrutinized using analytical models and MOSAIC simulations. Both methods successfully predict properties matching those of aggregates irradiated in the JEEP-II reactors (JCAMP study), but they tend to overestimate the RIVE and the loss of elastic modulus in aggregates from the LVR-15/XK1 experiment. This discrepancy underscores the combined effects of fast neutron flux and defects recovery kinetics which will require further research in the future. The interpretation of plain concrete specimen properties employs the LDPM. Here, the RIVE of aggregates relies on dimensional change measurements, whereas cement paste shrinkage is inferred from mass loss. The total expansion attributed to RIVE aligns closely with estimated shrinkage values. The cumulative shrinkage and RIVE collectively explain the limited and sporadic dimensional changes observed experimentally, including instances in which specimens experienced minor volume decreases rather than expansion.

Chapter 14 explores the impact of irradiation on the long-term structural performance of CBSs in PWRs. It starts with an extensive review of various modeling strategies found in the literature. The chapter then introduces two methodological approaches: FEA using the GRIZZLY code for a simplified, lined, reinforced CBS, and application of the LDPM to a representative structural wedge of the CBS at the mid-elevation of the core fuel assembly. Irradiation transport analysis was performed using the VERA code. Both the Grizzly and LDPM simulations enable the prediction of irradiation damage depth in concrete over varying operation times. The estimated damage depths derived from both modeling strategies are found to be comparable. Additionally, the chapter analyzes the effects of irradiation on the bond strength of steel reinforcement in the irradiated CBS using the LDPM.

The main conclusions of this work are provided in Chapter 15.





## 2 EFFECTS OF IRRADIATION ON THE BOND PROPERTIES OF STEEL EMBEDDED IN CONCRETE – EXPERIMENT DESIGN AND SETUP

Whereas several irradiation experiments on plain irradiated concrete have been conducted and published previously (e.g., Dubrovskii et al., 1967; Gray, 1971; Maruyama et al., 2017), this study presents a pioneering irradiation experiment on steel-reinforced concrete. This chapter outlines the design of this irradiation experiment. The experiment was designed as an iterative process guided by (1) the targets for irradiation conditions (neutron fluence, gamma dose, fluence rate [flux] and dose rate, and temperature); (2) the achievable conditions in test reactors (flux profile, neutron moderation, and gamma shielding); and (3) the geometry of the specimens to meet PIE objectives.

First, target irradiation conditions were established. The fast neutron fluence that is needed to exceed  $10^{19}$  n/cm<sup>2</sup> ( $E > 0.1$  MeV) to induce damage in the concrete specimens was determined. Although this fluence target can be reached in many reactors, irradiation-induced heating had to be controlled to avoid detrimental effects such as thermal cracking or phase changes. Test reactors capable of maintaining low irradiation temperatures ( $<70$  °C) are limited. Section 2.1 details the target irradiation conditions and the selection process for the test reactor and the irradiation position. This process led to the choice of an out-of-core irradiation position, designated XK1, in the LVR-15 test reactor operated by CVR in the Czech Republic. A second adjacent position, XK0, was used for pre-irradiation testing.

Second, the geometry of the test specimens and the selection of the concrete constituents were established. To ensure a reliable baseline for comparison, the concrete constituents and formulation were made identical to those tested by JCAMP. The aggregates and cement were generously provided by JCAMP. Section 2.2 describes the tested materials. To complete the scoping study on the bond strength of embedded steel reinforcement in concrete, direct pullout specimens—single reinforcing bars in concrete cylinders, or *pullout* specimens—were used because of size limitations. Studying the interactions between irradiated steel and concrete required obtaining reliable data from separate concrete, aggregate, and steel specimens. Thus, plain concrete specimens, referred to as *donut* specimens, and aggregate cylinders were included in the stack of specimens. The geometry of these specimens was optimized considering the irradiation constraints (flux and irradiation temperature fields). The design of the specimen stack is detailed in Section 2.3.

Third, the irradiation experiment required designing a capsule to enclose the test specimens and a test rig to support the irradiation capsule and moderate the neutron flux and gamma dose rate. Section 2.4 details the design of the capsule and the complete irradiation rig.

A tungsten shield and an aluminum box were designed, fabricated, and installed to reduce gamma heating and to flatten the axial neutron flux profile, respectively.

Finally, Section 2.5 describes monitoring of the irradiation temperature and the expected temperature conditions obtained through simulation.

### 2.1 Test Reactor and Irradiation Conditions

The objective of this research is to develop and perform an experimental scoping study to observe the effects of neutron irradiation on reinforced concrete specimens. To achieve

irradiation to a fluence level  $\geq 10^{19}$  n.cm<sup>-2</sup> at E > 0.1 MeV in a timely manner, it is necessary to perform the irradiation in accelerated conditions in test reactors. Although several test reactors are available around the world, irradiation conditions and test setup must meet several criteria to ensure that the effects of irradiation-induced temperature do not impair the interpretation of the test data. Whereas most concrete aggregates are thermally stable up to 300–350 °C, the hardened cement exhibits much lower resistance to temperature because of the presence of varied forms of water: evaporable water, absorbed water, and chemically bonded water. Dehydration of portlandite, Ca(OH)<sub>2</sub>, is complete at ~600 °C (Tajuelo et al., 2015). At 105 °C, all evaporable water is driven off the materials. Below 105 °C, the evaporable water is gradually driven off the pore structure of the hcp (Naus, 2005). Concrete mechanical and physical properties are very sensitive to the variation of internal moisture content (Maruyama, 2014). Hence, it is known that irradiation experiments performed on concrete and concrete constituents should be conducted at the lowest temperature possible. If achievable, it is recommended to maintain the irradiation temperature below 65 °C in relevance to the reactor cavity temperature for existing LWR NPPs in the United States.

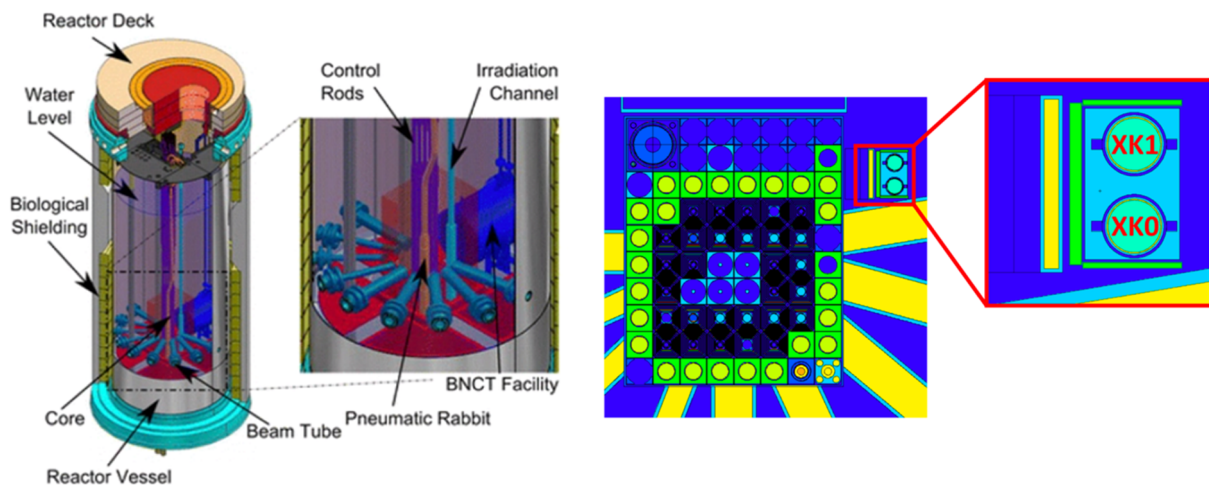
Irradiation temperature in the test specimens is governed by the energy deposition resulting from neutrons and gamma-induced heating. This condition drastically limits the number of test reactors of interest that can be used for the irradiation experiments on concrete. In a previous study, Maruyama et al. (2017) evaluated four test reactors for viability in conducting concrete irradiation testing. They found that suitable conditions could be achieved in the JEEP-II reactor (Kjeller, Norway) and the Japan Materials Testing Reactor (JMTR, Oarai, Japan, under decommission). The initial intent of this project was to conduct the experiment in the JEEP-II heavy water reactor at Kjeller, Norway, to benefit from the baseline data developed by JCAMP (Maruyama et al., 2017). However, as noted on the Institute for Energy Technology (IFE) website, “The JEEP-II reactor has been permanently shut down since December 2018 for scheduled maintenance and control. IFE’s board of directors decided on April 25, 2019 to permanently close operations at the reactor, based on an overall technical and economical assessment. Both reactors are currently being decommissioned” (IFE information, 2019). Consequently, a search for alternate reactors was conducted, and it was concluded that the LVR-15 reactor at CVR (Czech Republic) offered adequate irradiation conditions for this experiment. The following irradiation conditions were specified:

- Average irradiation temperature in the specimens below 70 °C
- Fast neutron flux (E > 0.1 MeV):  $< 7.5 \times 10^{12}$  n.cm<sup>-2</sup> s<sup>-1</sup>
- Thermal flux  $< 3 \times 10^{13}$  n.cm<sup>-2</sup> s<sup>-1</sup>
- Gamma heating  $< 0.15$  W.g<sup>-1</sup>
- Target fluence  $10^{19}$  n.cm<sup>-2</sup> at E > 0.1 MeV

Using these specifications, CVR identified two potential outside-of-core positions—XK0 and XK1— as seen in Figure 2-1. Further analysis as described in Section 2.4.3 led to the selection of XK0 for pre-irradiation testing and XK1 for the irradiation test.

The average irradiation conditions in LVR-15/XK0, JEEP-II, and a prototypical PWR are presented in

Table 2-1. (Note that the values provided in this table correspond to initial estimates. The final values obtained from the MCNP simulation calibrated on the activity of metal coupons placed in the irradiation capsule are provided in Table 10-1). Gamma heating is approximately 1.5 to 2 times higher in the XK0 position than in the JEEP-II reactor for the JCAMP experiments but is maintained at a relatively low level by a shield made of tungsten plate to avoid detrimental thermal gradient in the specimens. The main difference between the JCAMP experiment and the present experiment is that the fast flux is approximately 6 to 10 times faster in the JEEP-II reactor: a factor of 6 corresponds to the initial estimate, and a factor of 10 corresponds to the final analysis of the actual irradiation condition. Accounting for periodic outages at the LVR-15 reactor, the duration of the irradiation experiment requires approximately 8 times longer to reach the same target fluence if performed in the JEEP-II reactor. Although this characteristic limits the final fluence, it is advantageous to study the possible flux effects. However, the actual flux in a PWR is still 30 to 60 times lower than in the present experiment.



**Figure 2-1 LVR-15 Representation (Left), Cross Section Showing the Core Position and the XK0 and XK1 Positions Outside the Core Alongside the Neutron Beam Channel (Right) (Images Courtesy of CVR)**

The effective fast neutron flux is limited to a height of approximately 60 cm in both XK0 and XK1 positions, which is the height of the uranium layer in the reactor core. The neutron flux at  $E > 0.1$  MeV is quite uniform in the XK1 position ( $\approx 5 - 6 \times 10^{11} \text{ n.cm}^{-2} \text{ s}^{-1}$  over a height of 600 mm), but the fast flux in the XK0 position exhibits significant variations:  $\approx 4.5 - 10 \times 10^{11} \text{ n.cm}^{-2} \text{ s}^{-1}$ , with a notable peak near mid-elevation. These variations in the XK0 position are attributed to the proximity of the neutron beam channel.

Therefore, the XK0 position was allocated to the pre-irradiation test, and the XK1 was allocated to the full irradiation experiment. The main objective of the pre-irradiation test was to assess that the temperature of the irradiated specimens did not exceed the theoretical estimates. The actual gamma dose rate profile in XK1 exhibits a parabolic trend with a maximum value of  $34 \text{ Gy.s}^{-1}$  at mid-height ( $z = 0 \text{ mm}$ ) and  $\sim 25 \text{ Gy.s}^{-1}$  at the lower and higher extremities ( $z = \pm 300 \text{ mm}$ ). These values account for the presence of an additional gamma shield. The estimated cumulative gamma dose is between 0.9 and 1.3 GGy. Note that this gamma dose accounts for the presence of a tungsten shield.

**Table 2-1 Initial Comparison of Estimated Irradiation Conditions Between JEEP-II – Reactor (JCAMP Experiment) LVR-15 (This Experiment) and a Prototypical PWR Data (Maruyama et al, 2017; Remec, 2013)**

	JEEP-II/ PPT-C <sup>(i)</sup>	LVR-15.XK1 <sup>(l)</sup>	PWR <sup>(p)</sup>	Ratio <sup>(l/l)</sup>	Ratio <sup>(l/p)</sup>
	<b>Fast neutron flux (<math>\times 10^{11}</math> n.cm<sup>-2</sup>s<sup>-1</sup>)*</b>				
E > 0.1 MeV	34 36	5.6 6.0	$\approx 0.1$ 0.2	$\times \approx 6^{**}$	$\times \approx 30$ 60
	<b>Target fluence (<math>\times 10^{19}</math> n.cm<sup>-2</sup>)</b>				
E > 0.1 MeV	1.5	2.0***	< 6.0	$\times 0.75$	$\times > \frac{1}{3}$
E > 10 keV	2.5	2.3		$\times 1.05$	
	<b>Target gamma dose (GGy)</b>				
	0.9 1.3				
	<b>Gamma heating (W g<sup>-1</sup>)</b>				
	0.04 0.06	0.09	0.02	$\approx 0.5$	$\times \approx 0.2$
	<b>Surface-to-center temperature (°C)</b>				
	62 73	58 73	<65	$\times 0.9$ 1.1	$\times 0.9$ 1.1
	<b>Duration (full power year)</b>				
	0.25	$\approx 2$	<80 <sup>†</sup>	$\times \frac{1}{8}$	$\times \frac{1}{40}$

<sup>p</sup> Current operation extension, \* at fuel core mid-elevation, \*\* theoretical estimate based on simulation results, \*\*\* initial fluence target

## 2.2 Materials

### 2.2.1 Concrete

The objective of this research is to create a first-of-a-kind set of bond strength data for irradiated reinforced concrete. This goal requires that the properties of unirradiated and irradiated concrete, concrete constituents, and the reinforcing steel be well characterized. The need for an irradiated concrete properties baseline leads to the option to replicate concrete formulations that have already been tested and documented in the literature. Although many irradiated concrete formulations can be found in the literature (e.g., Dubrovskii et al., 1967; Gray, 1971; Elleuch et al., 1972), detailed documentation is often lacking, and determining the source of the concrete constituents several decades after the completion of the irradiation testing is challenging. Instead, JCAMP developed, completed, and published the design, protocol, and test results of the most comprehensive concrete irradiation study to date (Maruyama et al., 2017). Hence, the materials for this study have identical constituents and replicate the two JCAMP concrete formulations, namely Con-A and Con-B. The aggregates and cement were shipped to ORNL from Nagoya University. The shipped aggregates are from the same batch of aggregates that was used for the JCAMP experiment.

The two concrete formulations are recalled here:

**Con-A formulation** with  $w/c = 0.5$  includes a high-early strength cement ( $\rho_c = 3.14 \text{ g.cm}^{-3}$ , Taiheiyo Cement Corp.), and sand, sandstone (Shizuoka Prefecture:  $s = 799 \text{ kg.m}^{-3}$  ( $\rho_s = 2.61 \text{ g.cm}^{-3}$ ) and 5–13 mm crushed thermally altered tuff GA(F) recently re-qualified as *metachert* (Aichi prefecture:  $g = 995 \text{ kg.m}^{-3}$  [ $\rho_g = 2.66 \text{ g.cm}^{-3}$ ]) as coarse aggregates. The weight fractions of cement, water, sand, and coarse aggregates are 15.6%, 7.8%, 34.1% and 42.5%, respectively. The total occupied volume of the mixed constituents is  $0.979 \text{ m}^3$ , which theoretically corresponds to 2.1% of entrapped air. Assuming negligible contraction of fresh concrete, the volume fractions of the sand and aggregates are respectively 31.2% and 38.2%, for a total volume fraction of 69.4%.

**The concrete Con-B** formulation with  $w/c = 0.5$  includes the same high-early strength cement, as well as sand and sandstone. The coarse aggregates are 5–13 mm felsic sandstone (GB(E), Shizuoka Prefecture,  $\rho_g = 2.64 \text{ g.cm}^{-3}$ ). The weight fractions of cement, water, sand, and aggregate of Con-B are 15.1%, 7.5%, 32.3%, and 45.1%, respectively. The quartz contents in aggregates GA(F) and GB(E) are respectively 92% and 47%. Hence, RIVE is higher in aggregate GA(F) than in aggregate GB(E) (Maruyama et al., 2017).

Using the concrete constituents that were used in the JCAMP project enables comparison with the previously published results obtained by JCAMP on plain concrete irradiated in the JEEP II reactor in Norway. This approach was preferred to attempting to choose aggregates representative of a particular NPP in the United States, primarily because aggregates in an NPP are site dependent and vary from plant to plant, and their characterization data are not publicly available.

## 2.2.2 Low Carbon Steel Reinforcing Bar

A specially ordered #2 (nominal yield stress  $\sim 420 \text{ MPa}$ ) rebar with a nominal diameter of  $\frac{1}{4}$  in. (6.35 mm), shown in Figure 2-2, was embedded centrally in concrete. The average height of ribs is 0.008 in. (0.205 mm), and the distance between ribs is 0.216 in. (5.5 mm).



**Figure 2-2 Photograph of #2 Low Carbon Steel Bar**

## 2.3 Specimen Geometry

As mentioned above, the irradiation-induced heating is a limiting factor for the dimensions of the specimens in the horizontal direction ( $\lesssim 50 \text{ mm}$ ), and the effective fast-neutron flux height is approximately 600 mm. Hence, the experiment consisted of cylindrical specimens stacked upon one another. To optimize the occupancy of the available space, two types of specimens were stacked upon each other: pullout concrete cylinders reinforced with a single steel bar in the center to use when performing post-irradiation bond tests, and donut hollow plain concrete cylinders used to characterize the properties of irradiated concrete, including dimensional change and mechanical properties.

The heights of the unreinforced hollow donut concrete specimens and the reinforced pullout concrete specimens were 40 and 60 mm, respectively. Each pair corresponded to a height of 100 mm, making it possible to stack 6 pairs equally divided between concrete Con-A and concrete Con-B, as shown in Figure 2-3. Because of the near symmetry of the axial flux (Figure 2-9), the Con-A and Con-B concrete specimens were placed on each side of the mid-height plane of the core. The irradiation of plain reinforced specimens provided a baseline for the irradiated concrete properties in the LVR-15 irradiation conditions. The fast-neutron flux in LVR-15 is approximately 10 times<sup>2</sup> lower than in JEEP-II reactor. Hence, the aggregate RIVE, which is the main contributor to the irradiation-induced expansion and damage in the concrete specimens, could possibly be decreased as a result of defects recovery effects. To correctly interpret post-irradiation bond strength testing, the extent of irradiation-induced damage at the end of the irradiation must be determined. Therefore, it is critical to recreate a baseline of the physical and mechanical properties of the concrete's aggregates and the cement paste's constituents. To this aim, aggregate GA(F) and GB(E) aggregate specimens measuring 10 mm in diameter and 10 mm height were added to the stack and placed in a separate alumina (99.8% Al<sub>2</sub>O<sub>3</sub>) holder at mid-elevation of the stack, separating the Con-A specimens composed of aggregate GA(F) and Con-B specimens composed of aggregate GB(E). The aggregate specimens were provided to ORNL as part of a collaborative research effort with JCAMP (Civil Nuclear Working Program jointly managed by the US Department of Energy [DOE] and the Japan Minister of Economy, Trade, and Industry). Because of the higher silicious mineral content, aggregate GA(F) expands more than aggregate GB(E) under irradiation.

In addition, pre-dried C–S–H compressed pellets (diameter 10 mm) were added to the set of testing specimens. Similar pellets have been tested under gamma irradiation for the DOE LWRS program at ORNL and Sandia National Laboratories (SNL). Post gamma irradiation testing found that

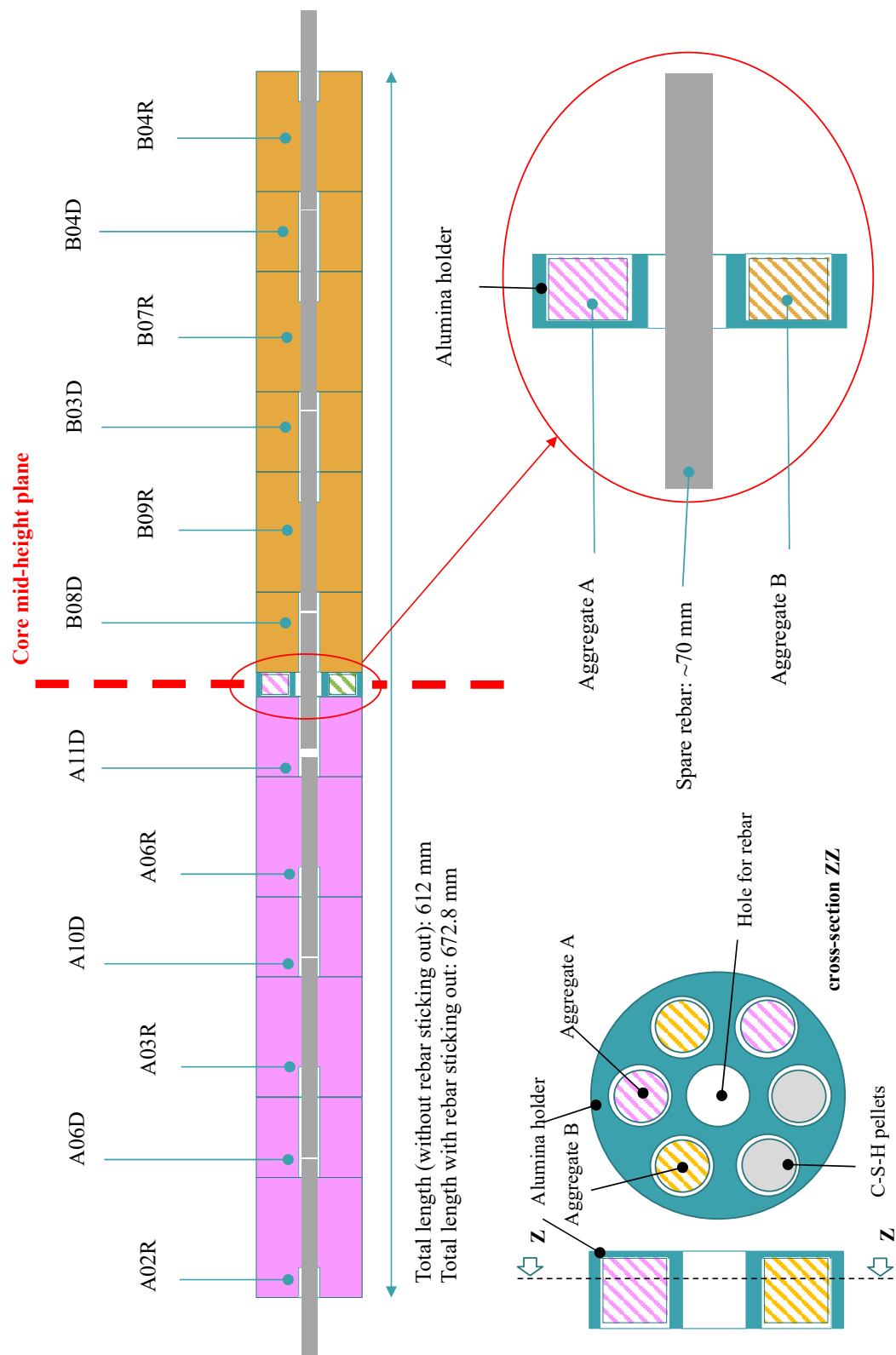
*irradiation decreases C-S-H basal spacing ( $\sim 0.6 \pm 0.1$  Å for 189 MGy) and increases its young's modulus, which is attributed to the lower basal spacing as the nano porosity potentially increased and microporosity remained unchanged. Irradiation also decreased the molecular water content and increased hydroxyl groups in C-S-H, showing that interlayer water removal reduces the basal spacing. Finally, <sup>1</sup>H (proton) and <sup>29</sup>Si (silicon) NMR (nuclear magnetic resonance of proton and silicon) results indicate some disorder in the local proton CaO-H species and slight depolymerization of the silicate structure. Together, these results indicate that the C-S-H gel stiffens upon ultrahigh gamma irradiation dosage (Baral et al., 2022).*

Including similar specimens in the LVR-15 irradiation test will provide a characterization of the combined gamma and neutron irradiation effects on cement. This ongoing research is sponsored by the LWRS Program and is not documented in this report.

The mechanical properties of low-carbon steel are not expected to be substantially affected at the target fast-neutron fluence (Murty, 1984), but this hypothesis must be validated by additional post-irradiation direct tensile tests. An additional low carbon reinforcement bar is also added to the specimen stack. A bar approximately 70 mm long was placed in a center hole of the alumina holder, as shown in Figure 2-3.

---

<sup>2</sup> Final value obtained after analysis of the activity of metal coupons placed in the irradiation capsule.



**Figure 2-3 Schematics of the Specimen Stack for Irradiation Experiments and Companion Irradiation-Temperature Model Experiments**



## 2.4 Capsule Design

Post-irradiation bond strength data will be obtained from pullout testing of a steel bar embedded in concrete cylinders. The diameter of the concrete cylinder is limited by the available space in the reactor's position and the irradiation temperature. Calcium-silicate-hydrates (C–S–H), the main constituents of the hydrated cement paste, undergo changes at temperatures as low as ~65 °C (Maruyama et al., 2014a; 2014b; 2014c). In addition, the irradiation-induced energy deposition results in nonuniform heating of the specimens, causing temperature variation mainly in the form of a radial gradient because the center of the specimen is subjected to a higher temperature than that of its surface.

The center-to-surface temperature variation is governed by the diameter of the specimen and the dimension of the air gap between the specimen and the capsule. Both the specimen diameter and the air gap dimension must be reduced to avoid thermally induced surface cracking during reactor operation, restart, and shutdown. A sufficient air gap is also needed to avoid mechanical interactions caused by concrete RIVE, which can lead to unwanted confinement or coolant leakage in the capsule (Dubrovskii et al., 1967; Maruyama et al., 2017).

### 2.4.1 Helium Gap

In the JCAMP experiment, the gap between the concrete specimens and the capsule wall was designed at 1% of the 40 mm diameter, or 0.400 mm. Hence, the maximum linear expansion allowed in the radial direction was 2%. That expansion level was reached in Con-A concrete specimens (92% quartz content aggregate) for fluence approaching  $8 \times 10^{19}$  n.cm<sup>-2</sup> at  $E > 0.1$  MeV. At  $\sim 4.5 \times 10^{19}$  n.cm<sup>-2</sup> and  $\sim 1.25 \times 10^{19}$  n.cm<sup>-2</sup>; the linear expansion of Con-A specimens reached ~1 and 0.25%, respectively.

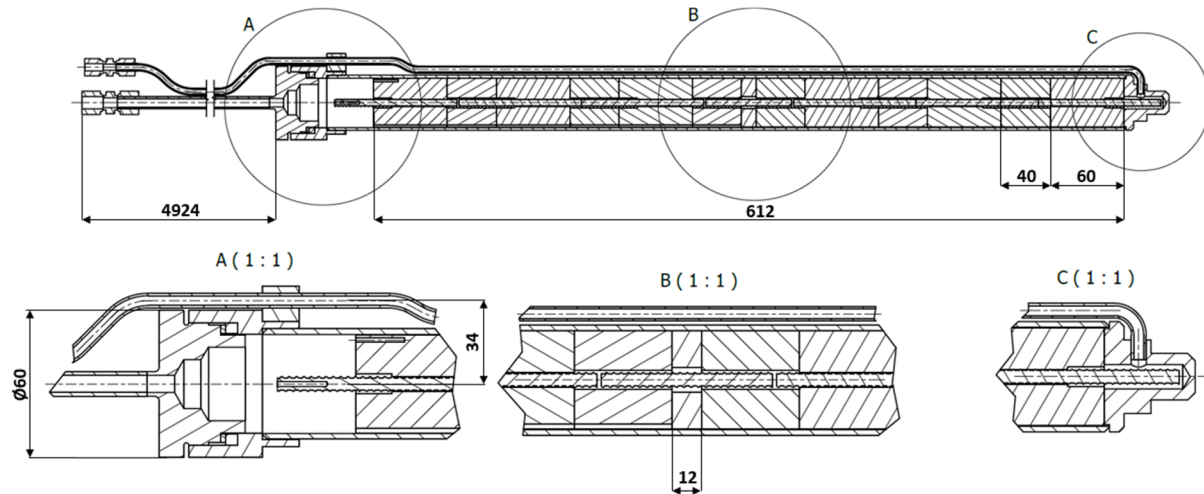
Con-B specimens exhibited lower expansion as the result of lower quartz content. Hence, if the irradiation temperature in the foreseen experiment in LVR-15 is comparable or higher (RIVE rate decreases with increasing temperature [Bykov et al., 1981]), then it is conservative to assume that at the bounding fluence of  $\sim 2 \times 10^{19}$  n.cm<sup>-2</sup>, the maximum linear expansion of Con-A plain concrete specimens, should not exceed ~0.5%. In the reinforced concrete specimens, the presence of the steel bar placed in the longitudinal direction of the capsule is expected to cause some level of mechanical confinement in that direction. It is not known how the RIVE will be redistributed in the unconfined directions. From a design perspective, the adopted working hypothesis is that the RIVE is fully redistributed in the radial and orthoradial directions, leading to an increased radial expansion of ~0.75%. It must be noted that the thermal strains during irradiation are negligible in comparison with the radiation-induced deformations. Therefore, a gap of 1% of the specimen radius was adopted to ensure unconstrained expansion of specimens in the capsule at the target fluence.

### 2.4.2 Irradiation Capsule and Rig

#### 2.4.2.1 Irradiation Capsules

The testing section of the rig is formed by capsules made of aluminum alloy AlMgSi<sub>0.5</sub> (EN AW-6060) as seen in Figure 2-4 and Figure 2-5. Two identical capsules were built for the XK0 and XK1 positions. Their tube thickness is 2.25 mm, their inner diameter is 40.5 mm, and their outer diameter is 45 mm. The total length of the capsule is 729 mm. The tube is equipped with bottom and upper plugs. A capillary tube ( $\varnothing 6 \times 1$  mm) that guides inert gas into the capsule is connected to the bottom plug. The bottom plug is welded to the bottom part of the tube. The

upper plug is equipped with a tube ( $\varnothing 10 \times 1.5$  mm) that acts as to guide the thermocouples (TCs) in the capsule and also serves as an outlet for the inert gas. After the concrete specimens are loaded, the upper plug is connected to the tube using a threaded joint. Capsule tightness is ensured by applying a graphite seal. The capsules' external surfaces were anodized to improve their corrosion resistance in the reactor coolant environment.



**Figure 2-4** Drawing of the Irradiation Capsule with Close-Up Views of the Gas Inlet-Outlet (Bottom- Left Drawing, Cross-Section A), the Mid-Height Section (B) Showing the Alumina Holder and the Isolated Reinforcing Steel Bar, and the Bottom Section (C)

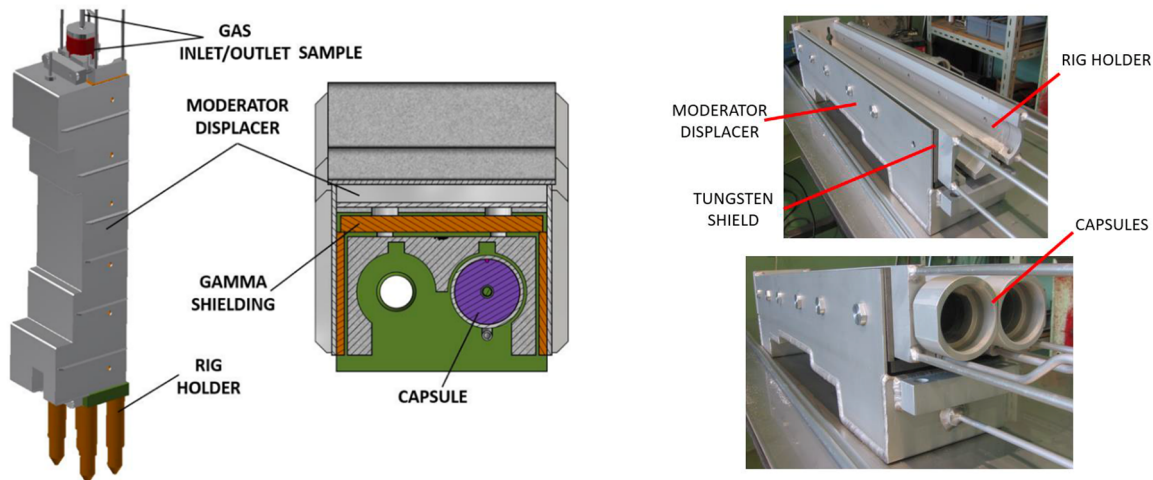


**Figure 2-5** Photographs of the Capsules (Left) and Upper Plugs (Right) Fabricated at CVR

#### 2.4.2.2 Rig Holder

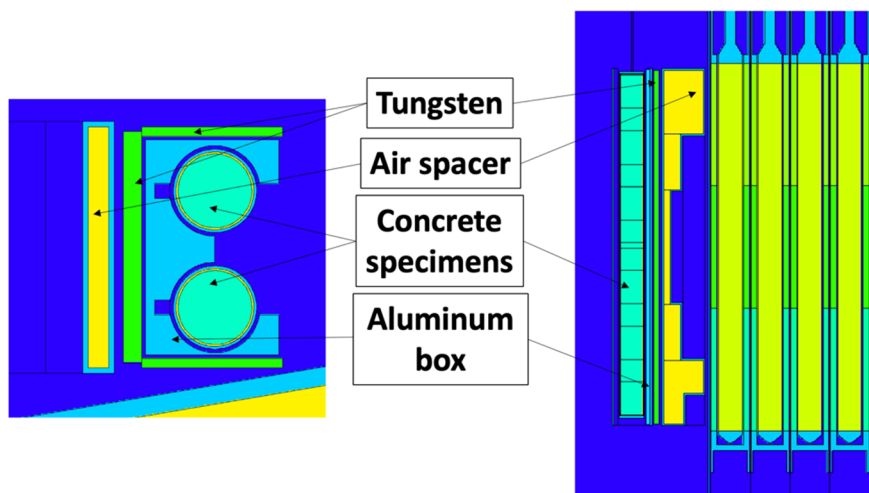
A dedicated rig holder was designed and fixed to the reactor grid using four pins to ensure proper positioning of the capsules. The shielding assembly, which is composed of a moderator displacer and a tungsten gamma shield (Figure 2-6), is located between the testing section and the reactor core and is also connected to the rig holder. The moderator displacer is composed of aluminum plates welded together. The tungsten plates are connected to the moderator displacer using bolts, and the entire assembly is then fixed to the rig holder. For manipulation purposes in the reactor, four additional tubes are welded to the upper part of the holder. The function of the shielding assembly is to reduce the gamma heating, and thus the irradiation

temperature, in the samples and to flatten the axial neutron flux profile. The efficiency of the shield is associated with the thickness of the tungsten plates, which were designed using MCNP 6.1 code to reduce gamma heating in the irradiation position by a factor of ~2. and thus to reduce the temperature in the specimens.



**Figure 2-6 Complete Irradiation Rig: 3D Model (Left), and Fabricated Rig (Right)**

The second part of the shielding assembly consists of a fast-neutron field moderator comprising a sealed aluminum box filled with gas; the dimension of the box varies according to the axial position. Once the moderator is in place in the reactor, its function is to shape the axial fast neutron profile to become as uniform as possible. At the highest neutron flux position facing the mid-height of the reactor core, the shield's thickness is minimal, but it increases toward the upper and lower extremities of the rig, as shown in Figure 2-7.



**Figure 2-7 Schematics of the Neutron Moderator and the Gamma Shield Assembly**

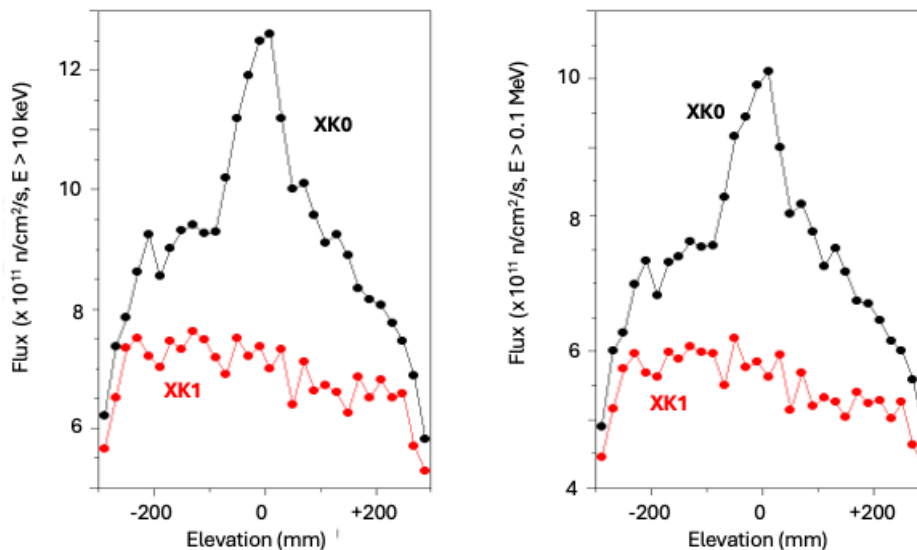
The release of the tungsten particles into the reactor coolant was observed during the pre-irradiation test. The release led to increased activation of the coolant. To mitigate this effect, the moderator was covered with aluminum alloy plates before starting the irradiation experiment.

### 2.4.3 Neutron Fluence and Gamma Field Estimates

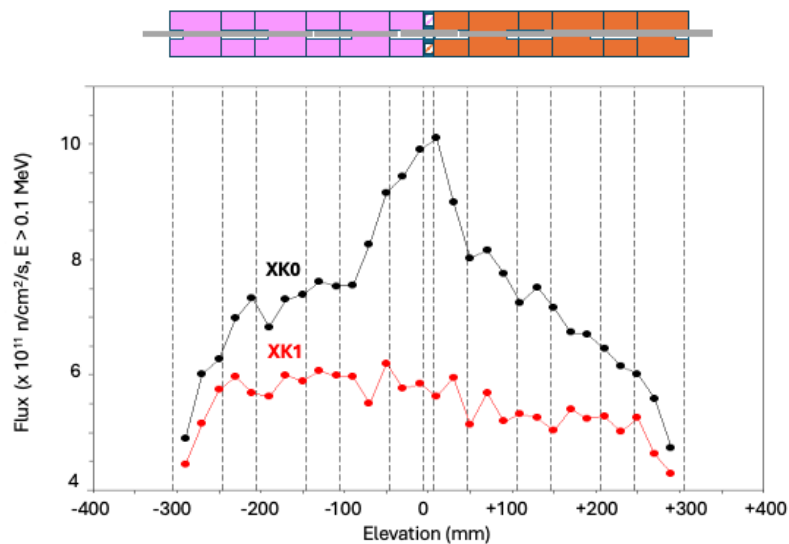
The analysis of the neutron and gamma fluence in the rig structure was performed using the MCNP 6.1 transport code with the Evaluated Nuclear Data File (ENDF)/B-VII.0 library. The software used was approved for the LVR-15 reactor applications by the Czech State Office for Nuclear Safety (SUJB). A series of calculations was carried out to assess the neutron and gamma flux axial profiles in the XK1 and XK0 positions.

#### 2.4.3.1 Fast Neutron Flux

The axial neutron profiles in both positions are presented in Figure 2-8 for energies above 10 keV and 0.1 MeV, respectively. Qualitatively, the profiles are quite similar for both energies. However, significant differences can be seen for the two positions considered. Whereas the average flux is higher in the XK0 position, important flux variations (by a factor of  $\sim 2$  between the lowest flux location and the highest flux location) attributed to the adjacent neutron beam line are anticipated. Not only would these variations affect the exposure consistency between the varied specimens, but they would also produce flux variation along the heights of specimens (see circled locations in Figure 2-9). In contrast, the axial fast-neutron flux profiles in position XK1 are more uniform and centered around an estimated value of  $\sim 7 \times 10^{11} \text{ n.cm}^{-2}.\text{s}^{-1}$ , varying within a range of  $\sim \pm 10\%$  except for the very extremities of the specimen stack. Note that the flux profiles presented in this figure are design estimates and do not account for the complete rig design and the actual operation of the reactor during the irradiation experiment. The XK1 position is dedicated to the irradiation experiment, whereas the XK0 position is used for a pre-irradiation test and a subsequent irradiation performed by CVR for its own purposes.



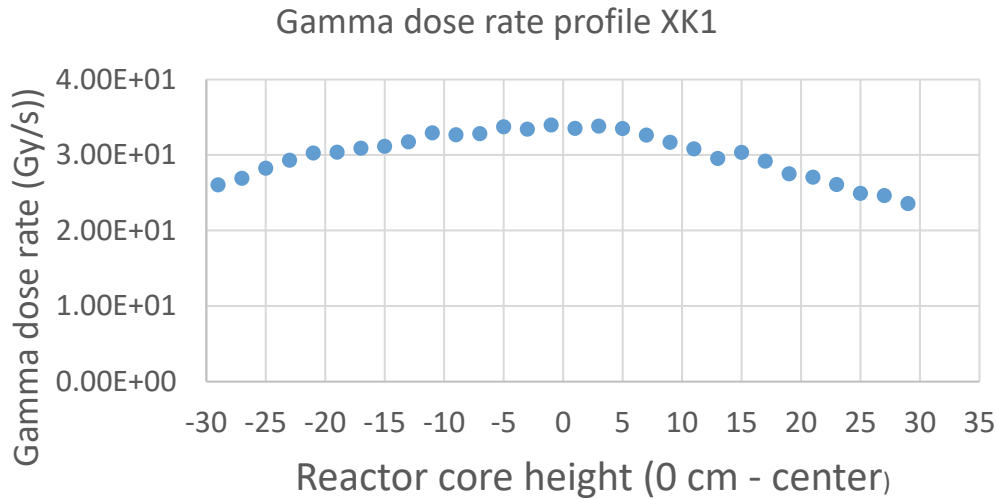
**Figure 2-8 Neutron Flux Profiles in XK0 (Black Lines) and XK1 (Red Lines) Positions for Energies Higher Than 10 keV (Left) and 0.1 MeV (Right)**



**Figure 2-9 Neutron Flux Profiles in XK0 (Black Lines) and XK1 (Red Lines) Positions for Energies Higher Than 0.1 MeV (Right). The X-Axis was Distorted to Correspond to the Actual Position of the Specimens in the Stack. Each Specimen is Located Between Two Dashed Lines**

#### 2.4.3.2 Gamma Dose Rate

The anticipated gamma dose rate profile in the XK1 position presents a parabolic shape as shown in Figure 2-10. The gamma dose rate ranges between 25 and 35  $\text{Gy}\cdot\text{s}^{-1}$ . After 2 years of irradiation, the expected gamma dose varies between 0.9 and 1.3 GGy.



**Figure 2-10 Gamma Dose Rate Profile in the XK1 Position**

## 2.5 In-Situ Temperature and Irradiation Monitoring

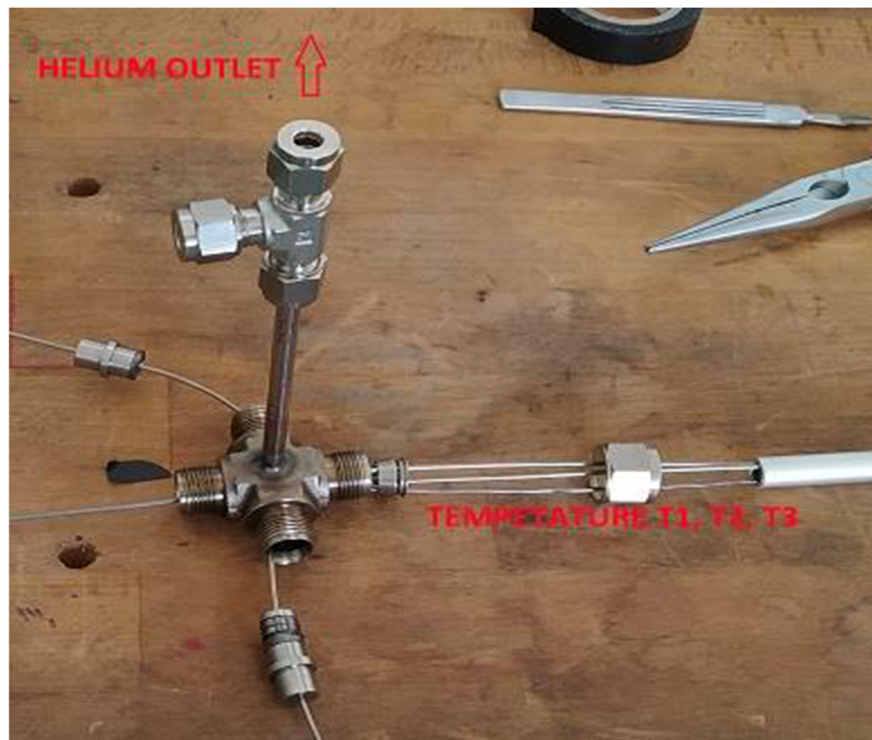
Samples in the form of concrete cylinders were inserted into the capsule, along with three TCs. Two TCs were inserted at the top sample: one in the debonding zone between the steel reinforcement and the concrete, and the other in a 2 mm hole drilled toward the outer diameter of the concrete specimen. The third TC was located at the mid-height of the capsule guided by a groove that was machined on the outer side of the samples. The locations of the TC in the groove are shown in Figure 2-11 (left); installation of all three TCs in the testing capsule is depicted in Figure 2-11 (center).



**Figure 2-11 (Left) View of the Thermocouple (TC) Placed at the Capsule Mid-Height, (Center) View of the Two TCs Installed in the Top Specimen, and (Right) Drawing Showing the TC Locations**



Each TC cable was 10 m long. The TCs were guided through the upper tube above the reactor coolant level. At the top of the tube, the TCs were passed through the cross junction, and the bushings were sealed. The TCs were then connected to a dedicated data acquisition system. The cross junction was also equipped with an outlet to allow the inert gas to leave the capsule, as shown in Figure 2-12.



**Figure 2-12** Photograph of the Cross Junction Showing the Helium Outlet Located at the Top of the Capsule and the TC Wiring

## 2.5.1 Irradiation Temperature Estimates

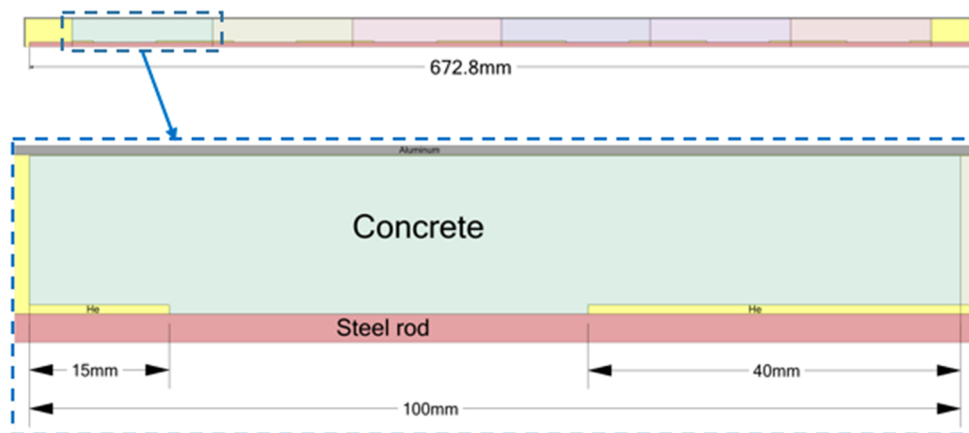
### 2.5.1.1 In-Service Temperature Fields

For design purposes, CVR's estimates were based on an analytical calculation using the following equations:  $\Delta T = \gamma \rho r^2 / 4k$  in solid cylinder (concrete), and  $\Delta T = \gamma \varpi r / 2k$  thin hollow cylinders (helium gap), where  $r$  is the outer radius of the solid cylinder,  $\gamma$  is the specific heat deposition caused by gamma rays,  $\varpi$  is the thickness of the helium gap,  $\rho$  is the density, and  $k$  is the thermal conductivity

Within concrete,  $\gamma = 0.09 \text{ W.g}^{-1}$ ,  $\rho = 2.5 \text{ g.cm}^{-3}$ , and  $k = 0.02 \text{ W.cm}^{-1}.\text{°C}^{-1}$ , thus leading to  $\Delta T = 11.2 \text{ °C}$  ( $r = 20 \text{ mm}$ ). Hence, the equivalent thermal strain difference between the surface and the center of the specimen is approximately 0.112 mm/m, or 0.0112%. Therefore, the risk of thermal cracking at reactor startup is unlikely. Note that online temperature monitoring in the capsule showed that the temperature difference between the center and the surface of the specimen was  $< 5 \text{ °C}$ .

Subsequent thermal analyses were performed using the software ANSYS and computational fluid dynamics (CFD) code FLUENT 17 as approved and standardized by the State Office for Nuclear Safety in the Czech Republic at CVR for simulations of components in the LVR-15 reactor. CVR conducted an irradiation-induced energy deposition study and thermal analysis of the irradiation rig to best estimate the temperature field in the steady-state regime.

An axisymmetric 2D model of the capsule was created to model the temperature field. The total length of the specimen stack is 672.8 mm (including protruding rebar), and each pair of specimens is 100 mm long (*pullout* reinforced concrete specimen = 60 mm, plain concrete specimen = 40 mm). The radial gap between the outer tube and specimen is 0.200 mm. The model consists of four volumes: (1) the concrete specimens, (2) the steel bars, (3) the external aluminum tube, and (4) the helium gap occupying the remainder of the computational domain. The alumina space holder containing the C–S–H and aggregates specimens is not represented. The concrete specimens form a continuous volume, and no contact resistance between the samples is assumed. The reinforcing bars present in the pullout specimens are also modeled using a continuous bar. The volume occupied by helium is modeled as a low conductivity solid. An insignificant effect of natural convection in a thin gap is expected. The heat is transferred through the gas layer mainly by conduction. Only the active part of the rig is considered. The temperature of the upper part where the capsule plug is located on the rig will be equal to the coolant temperature because there is no heat source. The computational domain is shown in Figure 2-13.



**Figure 2-13 Computational Domain for the Thermal Analysis**

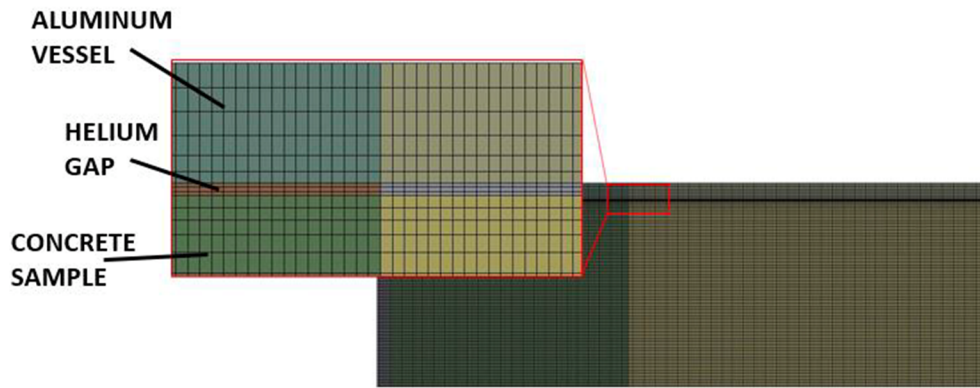
Gamma heating is represented by volumetric heat sources in the solid domains. The heat source is applied for each solid volume as a polynomial function of temperature along the axial direction. Values of the volumetric heat source are obtained from the MCNP calculations. The second boundary condition (BC) is associated with the heat removal. A convective BC is applied on the external surface of the aluminum vessel. This BC is characterized by the bulk temperature and the heat transfer coefficient. A value of 45 °C was assumed for the bulk temperature, which corresponds to the coolant inlet temperature that was used for rig design. (The actual inlet coolant temperature varies between 39 °C and 47 °C). A value of the heat transfer coefficient of 200 W.m K<sup>-1</sup> for the aluminum rig was assumed based on previous experiments performed in this position. The low velocities of the coolant flow justify that convective heat transfer is neglected at the surface of the capsule.



The thermal properties of the materials are provided in Table 2-2. The computational mesh was prepared using ANSYS Meshing tool shown in Figure 2-14. Structured hexahedral elements are used in the whole domain. To ensure the quality of the mesh, the size of the elements is relatively small ( $\sim 0.2$  mm). The mesh was refined in the radial gap of 0.2 mm to have 4 elements in the thickness of the gap. Steady-state simulations were performed using second order discretization schemes with a minimum residual of  $10^{-6}$ .

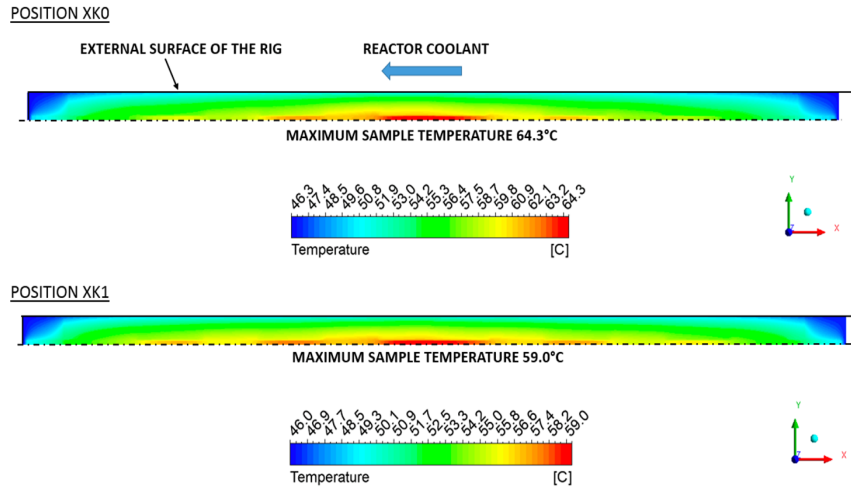
**Table 2-2 Material Thermal Properties**

Material	Thermal conductivity W.m K <sup>-1</sup>	Density g.cm <sup>-3</sup>
Aluminum	202.4	2.72
Helium	$0.0003 T + 0.1466$	—
Steel	16.3	8.03
Concrete	2	2.5



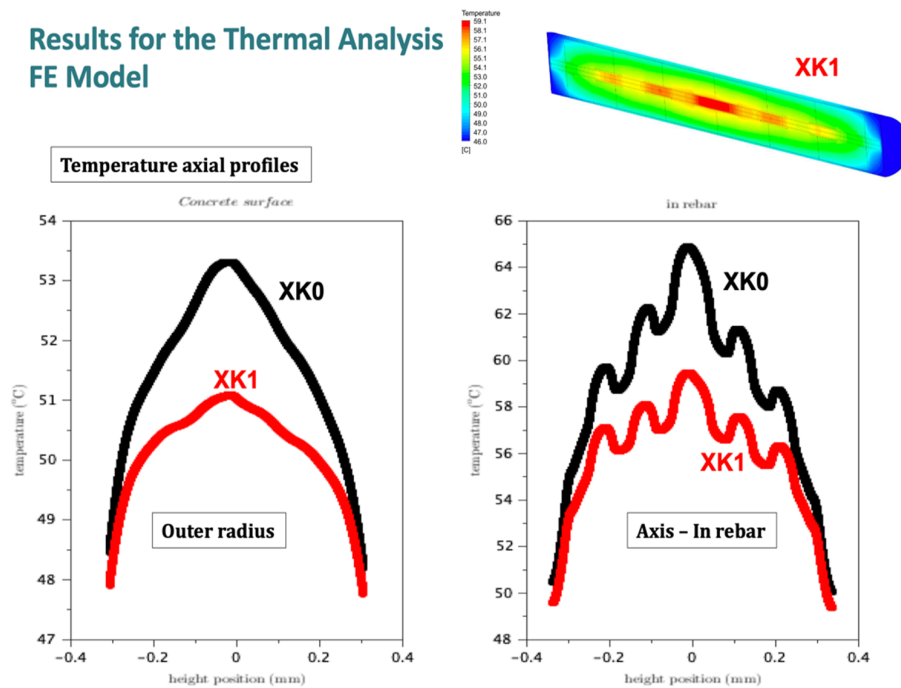
**Figure 2-14 Model Mesh**

The simulated in-service irradiation temperature fields are presented in Figure 2-15 through Figure 2-18. The variations of temperature along the vertical axis at the surface of the concrete are  $\sim 3$  °C and  $\sim 5$  °C, respectively, in the XK0 and the XK1 positions. The maximum temperature occurs at the mid-height plane and is estimated at  $\sim 53.3$  °C and  $\sim 51$  °C, respectively, in the XK0 and the XK1 positions. Along the vertical axis at the center of the specimen stack in the axis to the reinforcing bars, the temperature profiles show fluctuation caused by air gap in the debonding zone of the bar. The variation of temperature along the vertical axis in the bars is close to 8 °C and  $\sim 14$  °C, respectively, in the XK1 and the XK0 positions. The maximum temperature occurs at the mid-height plane and is estimated at  $\sim 64.5$  °C and  $\sim 58.5$  °C in the XK0 and the XK1 positions, respectively. These temperature values are obtained for a coolant temperature of 45 °C. Additional simulations, the results of which are not presented in this document, showed that a variation of temperature of the coolant caused a comparable variation of temperature in the test specimens.

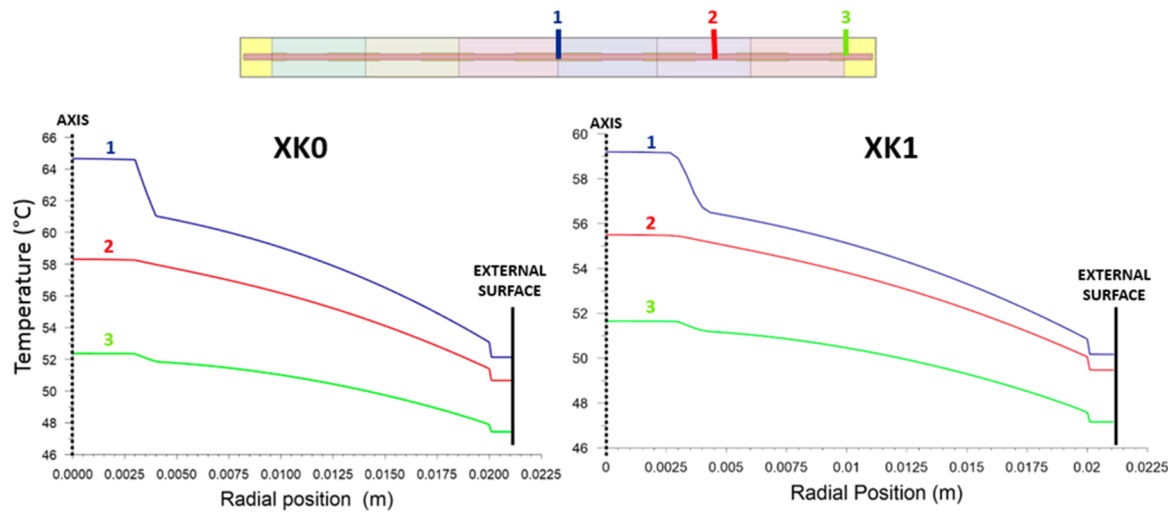


**Figure 2-15 Colormap of the Temperature Field in the Specimens During Irradiation (Axisymmetric Model)**

### Results for the Thermal Analysis FE Model



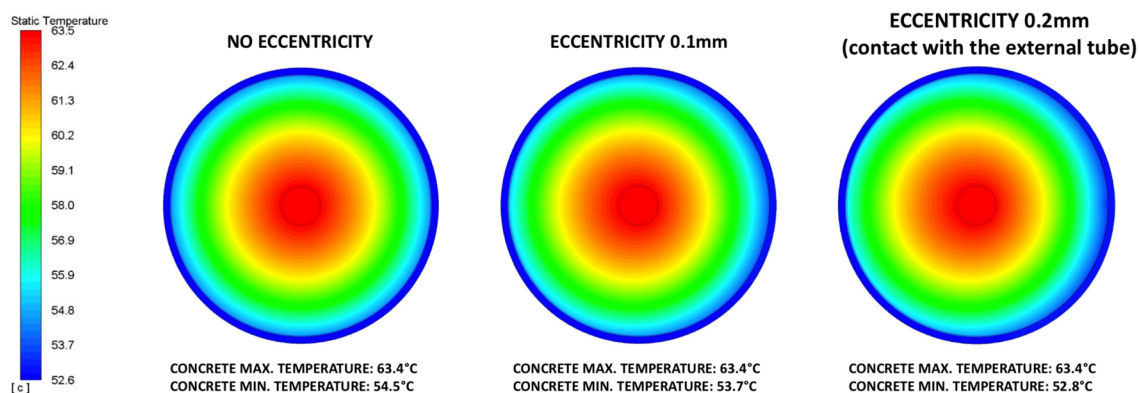
**Figure 2-16 Temperature Axial Profiles Derived from the CFD Simulations in the XK0 and XK1 Positions (Left) at the Concrete Surface and (Right) at the Center of the Specimens in the Reinforcing Steel Bars**



**Figure 2-17 Temperature Radial Profiles Derived from the CFD Simulations in the XK0 (Left) and XK1 (Right) Positions**

The specimens are placed coaxially inside the aluminum capsule. Possible misalignment and movement of the samples within the helium gap during rig transport and manipulation must be addressed. It would be difficult to center elements because of the small thickness of the gap, and it would also make it difficult to remove the samples. Therefore, CVR prepared a computational model assessing the effect of the eccentric layout of the sample. The effect of eccentricity on the temperature field was found to be relatively limited at  $<2^{\circ}\text{C}$ . The temperature fields in the cross section perpendicular to the capsule axis are presented in Figure 2-18.

ASSESSMENT OF ECCENTRIC LAYOUT OF A SAMPLE IN THE ALUMINUM VESSEL



**Figure 2-18 Radial Temperature Fields Across the Concrete Specimens Accounting for Possible Misalignment of the Specimen Axis with the Capsule Axis**

### 2.5.1.2 Temperature Estimates During Reactor Shutdowns

The duration of one reactor cycle is approximately 30 days and is divided into several cycle phases. Cycles are determined by the production of the medical radioisotope molybdenum ( $^{99}\text{Mo}$ ) for technetium generators used in nuclear medicine.  $^{99}\text{Mo}$  is produced from fission byproducts of  $^{235}\text{U}$  targets. Targets are placed and removed during dedicated one-hour-long shutdowns to mitigate possible abrupt reactivity changes. About 15 short-period shutdowns occur during each irradiation cycle.

During any given cycle, the reactor power is set to a nominal level ranging between 9.0 and 9.7 MW. The neutron flux and gamma dose rate are proportional to the reactor's power, resulting in temperature variations from one cycle to another. The main temperature changes are associated with reactor shutdowns. Immediately after shutdown, upon loss of the heat source, coolant temperature drops rapidly. The circulation pumps of the cooling loop remain in operation for approximately 30 min.

During reactor outage, the circulation pumps of the cooling loop are mostly in shutdown mode. However, because of the heat generated from the irradiated nuclear fuel caused by decay of fission and activation products, the core temperature gradually increases. To avoid core overheating, the circulation pumps are switched on for a few minutes at a frequency of twice per day to once every two days, depending on reactor personnel presence.

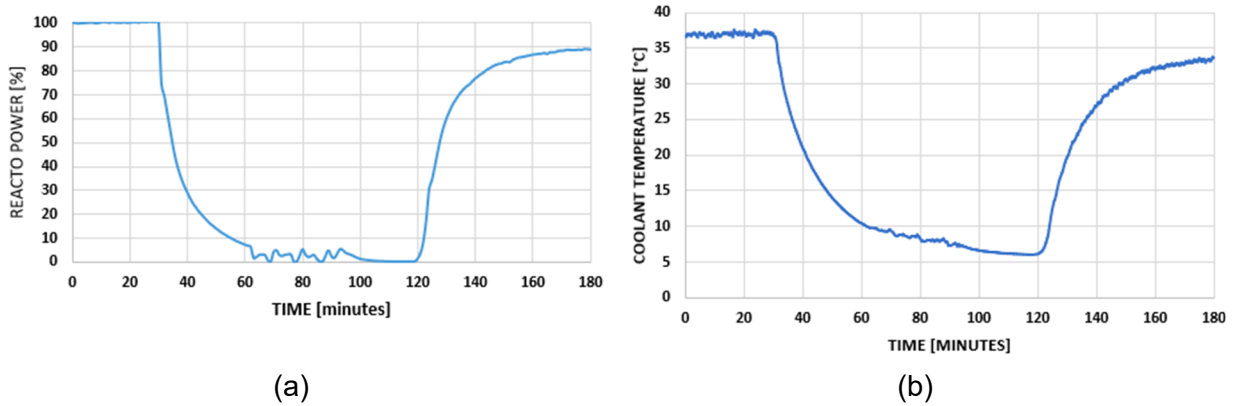
Finally, the coolant temperature is subject to the seasonal variations of the Vltava river's temperature, which ranges from approximately 8 °C to 22 °C between winter and summer seasons. The corresponding temperature of the reactor coolant varies between 41 °C and ~49 °C in operation.

In consequence, reactor operation affects not only the neutron flux, but also the temperature in the concrete specimens. Although the neutron flux follows an on-and-off history, the temperature field in the specimens is subjected to seasonal and operation-induced time variation. The possible effects of temperature can be addressed in two related questions:

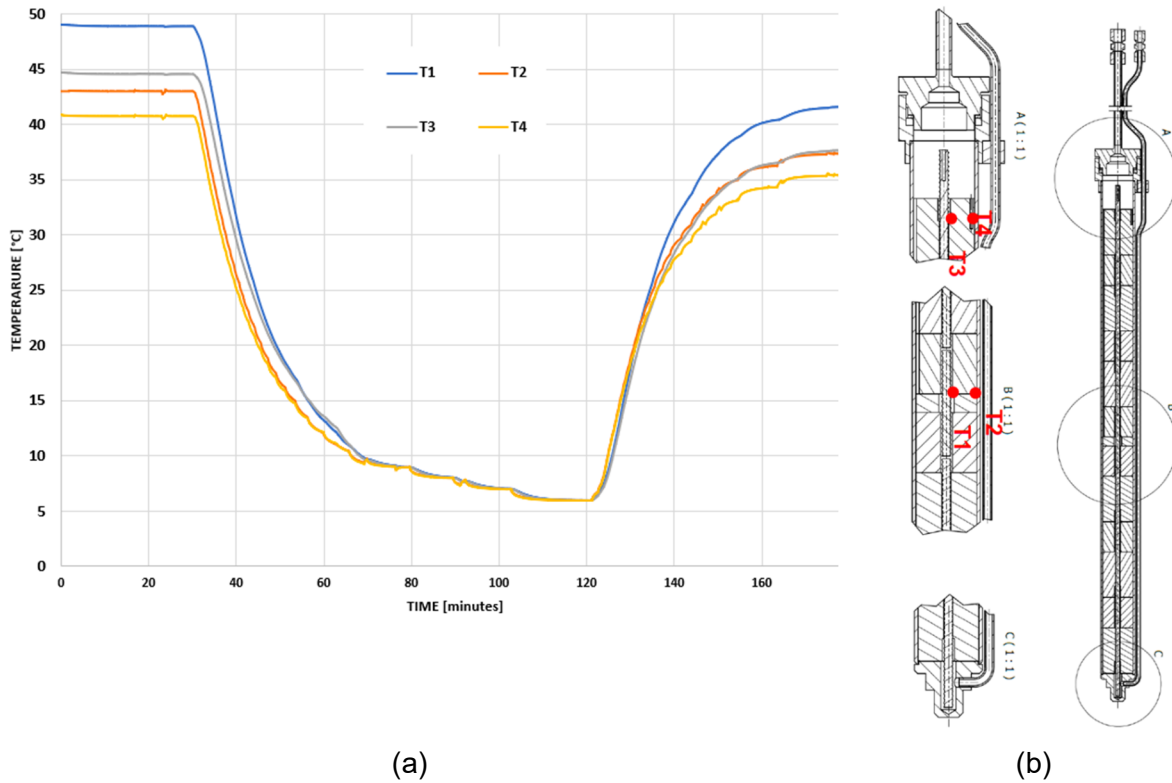
1. **What are the effects of the average temperature during irradiation?** The irradiation temperature affects the RIVE rate. Higher temperature leads to greater defects recovery, thus decreasing the radiation-induced expansion rate in rock-forming minerals. These effects are accounted for in the mineral RIVE models developed by Le Pape, et al. (2018). These empirical models were derived from literature data for irradiation temperature ranging mostly between 40 °C to 270 °C. The MOSAIC simulations of the JCAMP aggregates (irradiation temperature of ~53 °C in the JEEP-II reactor) are in good agreement with the post-irradiation dimensional changes (Cheniour et al., 2022).
2. **What are the effects of sudden temperature changes?** The relevant approach is to study the possible changes of temperature gradient within the specimens during sudden drops or increase of the coolant temperature caused by reactor shutdowns and restarts. To answer this question, CVR conducted a transient thermohydraulic (TH) simulation, as detailed below.

The TH simulation was conducted using a 2D axisymmetric model of the irradiation capsule and the specimens placed inside it. The coolant temperature provided the boundary conditions, and the irradiation-induced heat source was a function of the reactor power. Figure 2-19 shows the reactor power level and coolant temperature during a ~90 min. shutdown. These data

correspond to an actual shutdown that occurred in January 2021. The coolant temperature dropped from approximately 37 °C to 6 °C. During the summer, the temperature drop was not as significant. The power level and coolant temperature data are mostly correlated, although the temperature of the coolant decreases to its lower value more slowly than the reactor power. The simulation modeled the corresponding reactor shutdown, with the transient starting after 30 min, and restart starting after 120 min. The simulation time step was 5 s.



**Figure 2-19 Reactor Power Level (a) and Coolant Temperature (b) During a Shutdown Occurring in Winter**

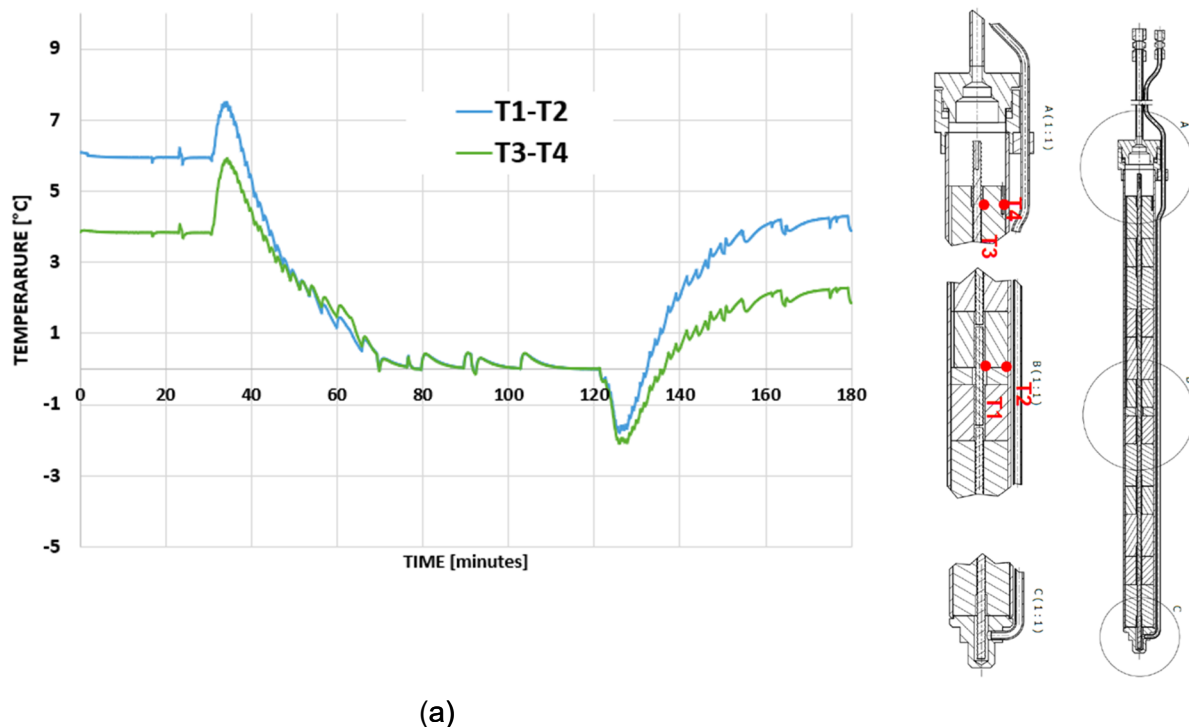


**Figure 2-20 Measured Temperatures (a) During Shutdown at Four Locations in the Irradiation Capsules, and (b) TC Locations**

Figure 2-20 shows the monitored temperatures at the locations of the four TCs in the capsule during a ~90-min shutdown. Before shutdown, the steady temperatures varied between 41 °C and 48 °C, depending on location. Higher temperatures were recorded at the mid-elevation of the specimen stack because of the vertical variation of the flux. At 40 min after the start of the shutdown phase, all four temperatures were the same at all locations and were equal to the coolant temperature. Therefore, it took approximately 40 min to remove the temperature gradient in the concrete specimens caused by irradiation heating. Once the reactor was restarted, it took about 10 min to observe a separation of temperature curves. Based on the monitored data, it can be inferred that maximum temperature gradient occurs when the reactor power is at its maximum.

Figure 2-21 shows the results of the TH simulations in temperature differences for the two pairs of TCs located at the mid-height or top of capsule. This representation makes it possible to study the effects of the coolant's rapid temperature change on the temperature gradient in the concrete specimens. The simulation results indicate that the maximum temperature difference occurs during the reactor's operation at full power. The simulation also shows a temperature spike and a temperature drop of approximately 2 °C at the beginning of shutdown and restart, respectively. These events were not recorded by the TCs and were likely a simulation artifact caused by the boundary conditions.

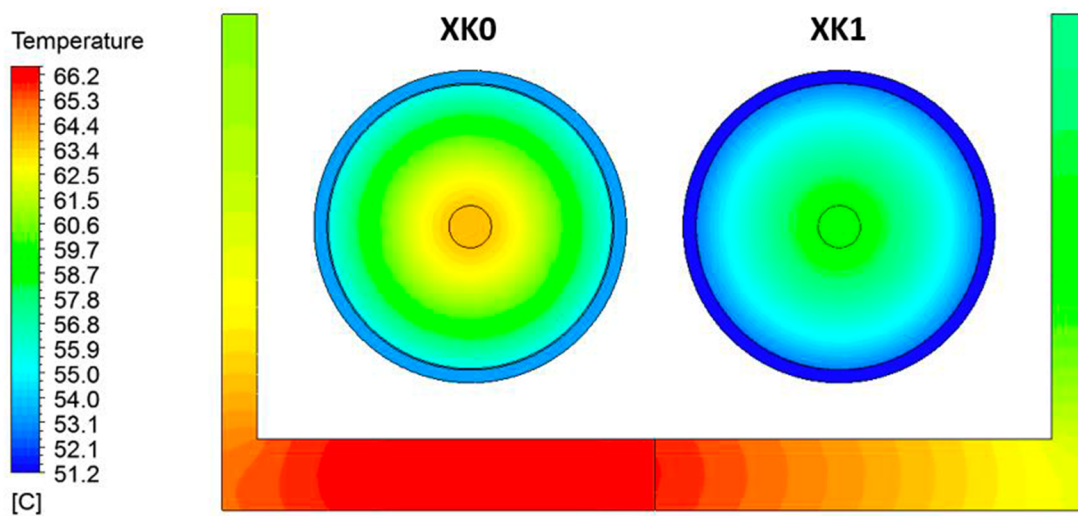
Based on this assessment, it can be concluded that the reactor's shutdowns and restarts do not cause increased temperature gradient in the specimen, so they are unlikely to produce thermal cracking.



**Figure 2-21 Simulation Results Showing (a) the Temperature Difference Between the Two Pairs of TCs, and (b) the TC Locations**

### 2.5.2 Operational Limits

The effects of the testing rig on the reactor's operational conditions and limits were also evaluated. The rig is a non-pressure piece of equipment operated at a low temperature level and is fabricated with relatively standard materials. From a reactor safety point of view, the temperature of the coolant that comes in contact with the testing rig must avoid boiling condition. A simplified model of the tungsten shield was created to evaluate temperatures on the surface of this component. The tungsten shield is directly cooled by the reactor coolant, but because of its high density and resulting high gamma heating, increased temperatures can be expected in this component. The simulation results are presented in Figure 2-22. Even though the temperature in the tungsten shield is higher than in the capsules, its surface temperature remains below boiling condition, with a maximum temperature of 66 °C.



**Figure 2-22** Temperature Field in the Capsules and the Tungsten Shielding



## **3 SPECIMEN FABRICATION AND CURING**

### **3.1 Materials**

To discern the irradiated concrete properties' baseline, concrete formulations that have already been tested and documented in the literature can be replicated. Whereas many irradiated concrete formulations are detailed in the literature, the level of documentation and the possibility to source the exact same constituents are limited. Replicating concrete formulations that were tested several decades ago is quite difficult because there are no certainties that the original aggregates and cement can be supplied. For example, the specific surface of contemporary Portland cement tends to be higher than for Portland cement used at the time of construction. Another example is that the continuous exploitation of quarries can lead to significant variations in aggregate production. Recent neutron irradiation experiments on concrete are scarce. Fortunately, the JCAMP team has developed, completed, and published the design, protocol, and test results of what is to date the most comprehensive concrete irradiation experimental study (Maruyama et al., 2017). The JCAMP team is an active member of the International Committee on Irradiated Concrete and serves as a research collaborator with ORNL within the DOE Ministry of Economy, Trade and Industry (METI) Civil Nuclear Energy Research and Development Working Group (CNWG) framework. Hence, this study replicates the two concrete formulations tested by JCAMP for this study.

### **3.2 Fabrication and Curing**

#### **3.2.1 Materials Preparation**

##### **3.2.1.1 *Sieving***

All coarse and fine aggregates were sieved to the required dimensions using a sieving machine. The aggregates were washed using tap water and cleansed of any dust.

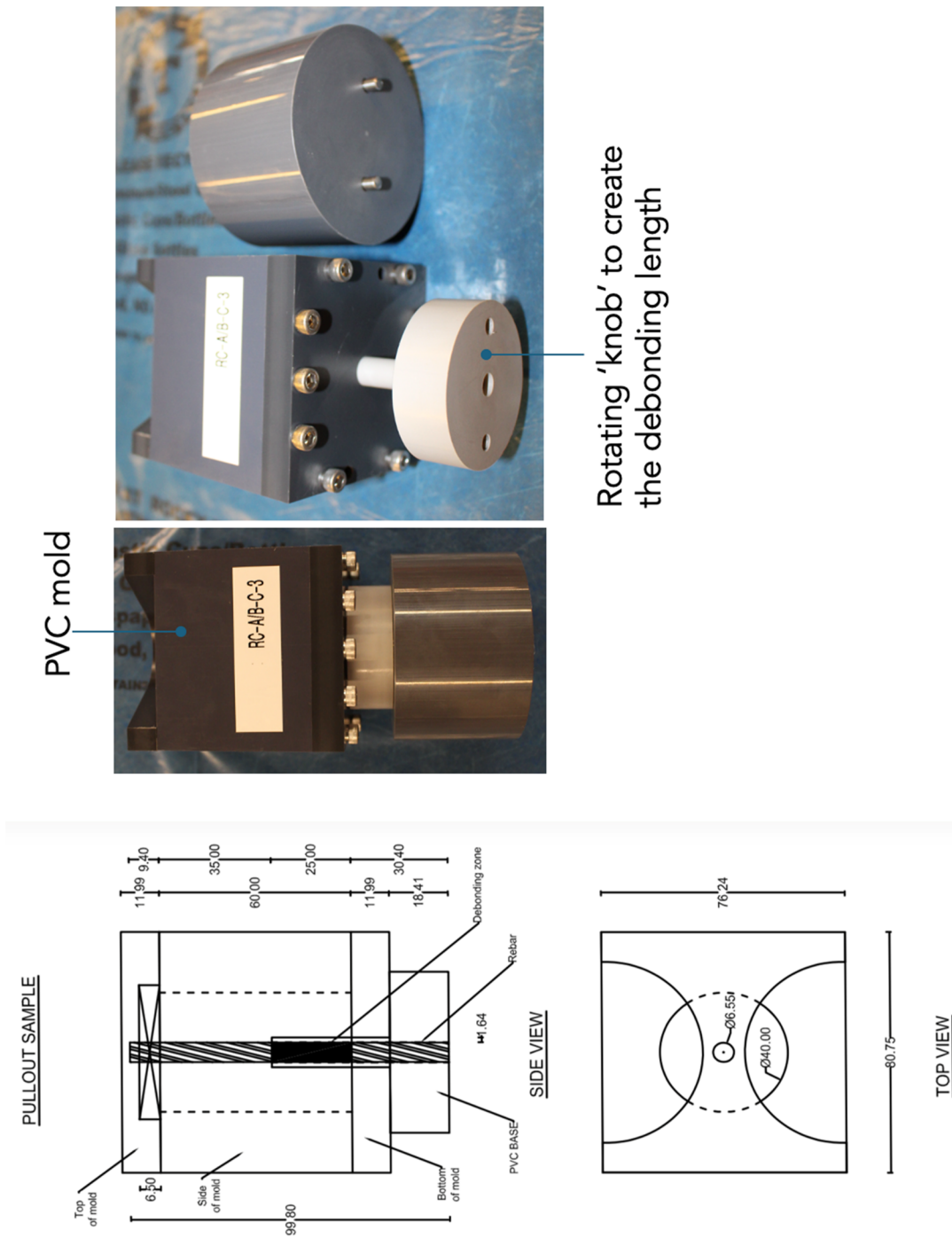
##### **3.2.1.2 *Aggregate Drying***

The coarse and fine aggregates were placed in an oven for 24 hours at 110 °C before casting. The aggregates were removed from the oven, cooled to room temperature, stored in dry buckets, and sealed with plastic sheets to avoid moisture ingress.

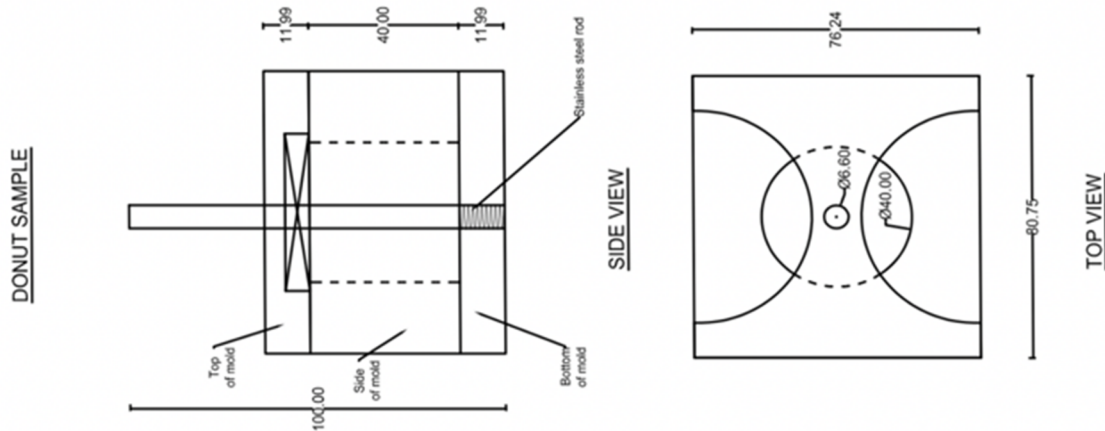
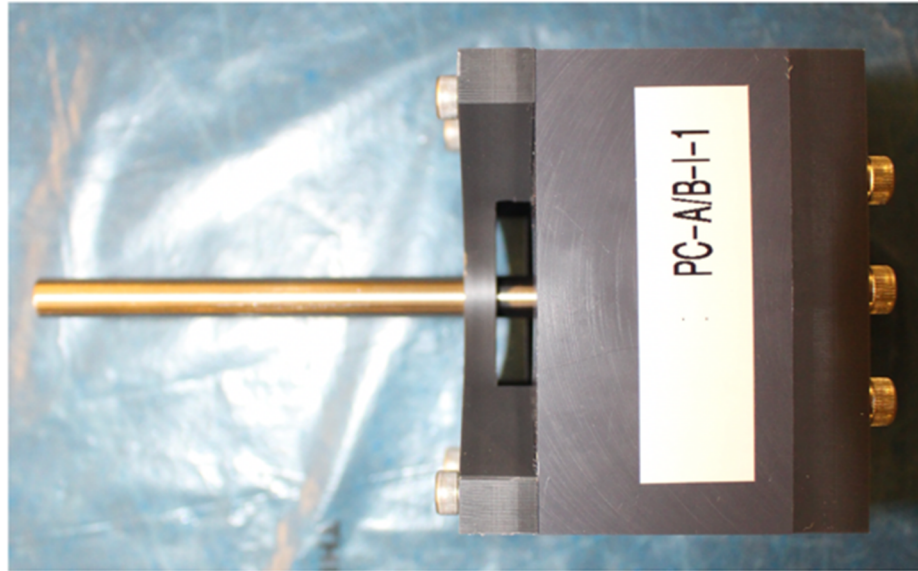
#### **3.2.2 Molds and Casting**

Specific molds were designed and fabricated at UTK. A total of 11 molds were fabricated for the donut specimens, as well as 11 molds for the pullout specimens. These molds were used twice: once for fabrication of concrete Con-A specimens, and once for fabrication of concrete Con-B specimens, with a five-day interval. The molds were machined from PVC blocks because of their planned limited use, lower cost, and ease of fabrication. Drawings of the molds are presented in Figure 3-1 and Figure 3-2. Both mold designs include perforated top and bottom plates to ensure vertical placement of a smooth steel rod donut specimen or a corrugated rebar pullout specimen. The steel smooth rod occupies the hollow space in the donut specimens and is removed after hardening. The pullout specimens are equipped with a rotating knob at the bottom to create a 25 mm debonding length between the rebar and the concrete. The debonding length is necessary to avoid premature failure in compression during the pullout tests.





**Figure 3-1 Design Drawings and Photographs of the Mold to Cast Pullout Specimens**



**Figure 3-2 Design Drawings and Photograph of the Mold to Cast Donut Specimens**

### 3.2.3 Casting

All the constituents of the mixture were weighed using a digital balance with a precision of  $\pm 10$  mg. The mixer parts were washed with tap water. Twenty min before mixing, the inside surface of the bowl and the beaters were wiped and dried with tissue paper to eliminate residual water. Labeled molds were arranged on a large benchtop covered with a plastic sheet to avoid spillage. The molds were mounted on top of a tube piece as shown in Figure 3-1. The areas around the steel bars projecting from the bottoms of the molds were sealed using silicon.

All dried constituents were placed in the mixer. The mixer was covered with a plastic sheet and was run for 1 min. Water was added gradually for 3 min, and the mixer was run for 1 more min, for a total mixing time of 5 min. No bleeding was observed in the concrete Con-A and Con-B batches. All molds were vibrated for 40 s at low speed. The slumped height was refilled, and

then the molds were vibrated for another 30 s. The depth of the vibration rod plunging into the concrete overlapped approximately 1 cm beyond the previous slumped layer. Thin pieces of aluminum plates were used to finish the top surface of the specimens immediately after the consolidation process.

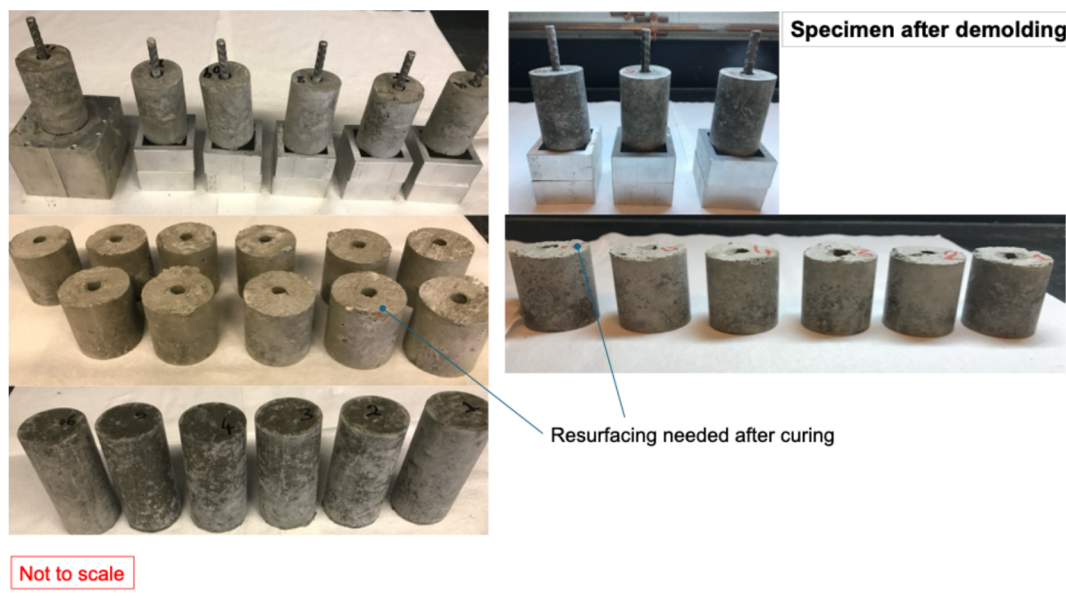
### 3.2.4 Curing and Specimens Preparation

#### 3.2.4.1 Early-Age Curing

Immediately after the top surfaces were finished, all specimens were covered with plastic sheeting to minimize water loss. After the specimens were finished, the bottom rods of the donut molds and the debonding knob of the pullout molds were rotated 5 times counterclockwise and 5 times clockwise every 15 min for 8 h. The rebars were maintained in position during the knob rotation to avoid damaging the bond between the rebar and the concrete. After 8 h, the rods of the donut molds and the debonding knobs of the pullout molds were removed. The specimens were covered with a plastic sheet to avoid evaporation and were stored in a curing chamber at 20 °C.

#### 3.2.4.2 Demolding

All the specimens were demolded after 3 days. Figure 3-3 shows the specimens after demolding. Concrete Con-A specimens were cast on March 12, 2020 and were removed from their molds on March 15. Concrete Con-B specimens were cast on March 17 and were removed from their molds on March 20.



**Figure 3-3 Photographs of 5 Sets of Specimens Immediately After Demolding**

#### 3.2.4.3 Curing

The specimens were cured in lime-saturated water for 45 days in a curing tank in which the temperature was maintained at 24 °C. After 45 days, the specimens were removed from the

curing tanks. Excess water was removed with a cloth, and each specimen was placed in a sealed zip-lock bag to prevent carbonation and moisture exchange. The specimens were then transferred to ORNL.

#### 3.2.4.4 *Visual Inspection*

Once the specimens were received at ORNL, they were visually inspected one by one to identify the presence of surface defects and to sort the specimens into four categories: irradiation testing (\*\*\*), temperature testing (\*\*), control cold specimens (\*) and spares (sp) in Table 3-1.

Pullout specimen B06D was rejected because the rebar was found to be loose. The cause for this defect in specimen B06D has not been determined. In all other pullout specimens, the rebar appeared to be well bonded to the concrete. It is conjectured that while the debonding knob was being rotated after casting, the rebar may not have been maintained in the proper position and may have rotated, resulting in damage to the bond area at an early stage.

Visible surface pores were present in all samples. Their numbers and sizes varied from specimen to specimen. Figure 3-4 shows examples of specimens with very small visible pores (left) and large surface pores/defects (center). However, the overall quality of the specimen surfaces was good and was found to be suitable for the planned testing. In the pullout specimens, the debonding zone appeared clean, and the appearance of the concrete surface that would be loaded perpendicular to the rebar was good. One exception was found in specimen A11R (Figure 3-4, right), which exhibited a defect near the surface.

The specimens of highest visual quality are marked with a \*\*\*quality index in Table 3-1.

These specimens were selected for placement in the irradiation capsule. After surface preparation, these specimens were characterized by x-ray computed tomography (XCT) to determine the presence of inner defects.

**Table 3-1 Visual Assessment of the Specimens After the 45-Day Curing**

Donut specimen	Flatness	Observation	Quality index	Category	Polishing
^01D	poor	lateral defect / void		(sp)	
^02D	fair	lateral defect / chipped top		(sp)	
^03D	good	small lateral pores	**	(hc)	x
^04D	fair	lateral pores / small defect	*	(rc)	x
^05D	good	very small pore	**	(hc)	x
^06D	good	very small pore	***	(irr)	x
A07D	fair	small pores and possible defect at the top	*	(rt)	x
A08D	fair	small pores and possible defect at the top	*	(rt)	x
^09D	fair/good	small pores	**	(hc)	x
^10D	good	small pores	***	(irr)	x
^11D	good	small pores	***	(irr)	x
B01D	fair / poor	very small pores / possibly missing concrete near hole	*	(rt)	x
B02D	fair	very small pore / defect at the top		(sp)	
B03D	fair / poor	no visible defect	**	(hc)	x
B04D	fair	very small pore	***	(irr)	x
B05D	fair / poor	very small pore / missing concrete on top	*	(rt)	x
B06D	fair	very small pores	**	(hc)	x
B07D	fair / good	very small pore	***	(irr)	x
B08D	fair / good	very small pore	***	(irr)	x
B09D	fair	some pores	**	(hc)	x
B10D	fair / good	some pores / surface cracks		(sp)	
B11D	fair	some pores	*	(rt)	x

(irr): specimens selected for irradiation experiment, (hc): specimens selected for the extended heat curing test at irradiation temperature, (rt) specimens selected for curing at room temperature, (sp): spare specimen. Visual quality index: irradiation testing (\*\*\*), temperature testing (\*\*), control cold specimens (\*), and spares.

**Table 3-1 Visual Assessment of the Specimens After the 45-Day Curing (Continued)**

<b>Pullout specimen</b>	<b>Flatness</b>	<b>Observation</b>	<b>Label</b>	<b>Category</b>	<b>Polishing</b>	<b>Groove</b>	<b>Drill</b>
A01R	fair	very small pores / extra materials at the bottom	**	(hc)			
^02R	fair	very small pores	***	(irr)	x		
^03R	quite good	some pores	***	(irr)	x		
^04R	quite good	large pore		(sp)			
^05R	good	very small pores	***	(irr)	x		
^06R	quite good	some pores	**	(hc)			
^07R	fair	some defect at the top	**	(hc)			
^08R	poor	some pores	*	(rt)			
^09R	fair	one pore at the top	*	(rt)			
^10R	fair	some pores	*	(rt)			
^11R	good	defect at the top		(sp)			
B01R	poor	no pores but defect at the bottom	*	(rt)			
B02R	fair	very small pores	**	(hc)			
B03R	quite good	some pore	**	(hc)			
B04R	quite good	very small pores	***	(irr)	x	x	x
B05R	fair	very small pores	*	(rt)			
B06R		loose bar		rejected			
B07R	quite good	very small pores	***	(irr)	x	x	
B08R	fair / poor	very small pores	*	(rt)			
B09R	fair	very small pores	***	(irr)	x	x	
B10R	fair	some large pores		(sp)			
B11R	fair	small pores	**	(hc)			

(irr): specimens selected for irradiation experiment, (hc): specimens selected for the extended heat curing test at irradiation temperature, (rt) specimens selected for curing at room temperature, (sp): spare specimen. Visual quality index: irradiation testing (\*\*\*), temperature testing (\*\*), control cold specimens (\*), and spares.

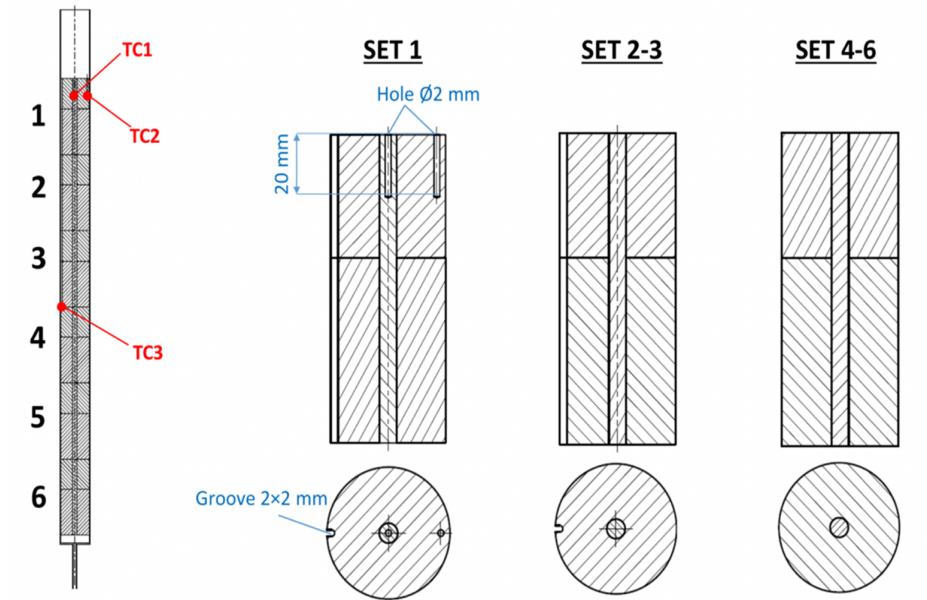




**Figure 3-4 (Left) Specimen A05R (Concrete Con-A) Showing a Few Small Surface Pores, (Center) Specimen A06R Showing Larger Surface Defects, and (Right) Specimen A11R Showing a Large Defect Near the Top Surface**

#### **3.2.4.5 Preparation for TC Placement**

During the irradiation experiment, the temperature was monitored at three locations in/on the specimens: at the surface of the top rebar, in the concrete of the top specimen, and near the surface of the concrete specimen located near the mid-height plane. Temperature monitoring near the mid-height plane required creation of a  $2 \times 2$  mm groove in the top six specimens for placement of the TC wires (Figure 3-5).



**Figure 3-5 Preliminary Drawing Showing TC Locations in the Specimen Stack  
(Note that this Drawing Does Not Represent the Actual Stack.  
The Alumina Holder is Not Represented in This Drawing)**

This groove was created using a GeoCut rock-cutting saw (Figure 3-6). A specific 3D printed fixture was designed and fabricated for this purpose. Dry cutting was preferred to avoid contaminating the specimen.



**Figure 3-6 Irradiation Testing Specimens Cut to Create a 2 × 2 mm Groove for  
Placement of the TC at Mid-Height of the Specimen Stack**



#### 3.2.4.6 *Pre-Irradiation Drying of the Test Specimens*

To limit drying shrinkage and the release of radiolitic gas during irradiation, the specimens were pre-dried in an oven at the anticipated irradiation temperature specified by CVR: ~60–62 °C for 2 months in a dedicated oven (LAC2-18 by Despatch). The temperature was increased from room temperature at a slow rate of ~1 °C/h to avoid thermal cracking. The cooling rate was comparable. After the specimens were cooled, they were placed back into sealed bags to prevent atmospheric moisture ingress and carbonation.

## 4 IRRADIATION EXPERIMENT

### 4.1 In-Situ Irradiation Conditions

#### 4.1.1 Time Evolution of Neutron Fluence and Gamma Dose

Figure 4-1 presents the fast neutron ( $E > 10$  keV) fluence history estimated from the MCNP simulations. The final average fluence is  $1.396 \times 10^{19}$  n.cm<sup>-2</sup> ( $E > 10$  keV). The standard deviation across the irradiated concrete and aggregate specimens is  $0.13 \times 10^{19}$  n.cm<sup>-2</sup>. The corresponding minimum and maximum fluences are respectively  $1.065 \times 10^{19}$  n.cm<sup>-2</sup> and  $1.507 \times 10^{19}$  n.cm<sup>-2</sup>. Note that the fluence plots assume a linear evolution during each cycle. However, there is variation because of the daily outage associated with isotope production and reactor power variation.

Fluence varies with the energy level. To obtain the fast neutron fluence at  $E > 0.1$  MeV, fluence at  $E > 10$  keV is divided by 1.23–1.24 in the XK1 position. To obtain the fast neutron fluence at  $E > 1$  MeV, fluence at  $E > 10$  keV is divided by 2.37–2.45 in the XK1 position. Details are given in Table 4-1.

**Table 4-1 Fast Neutron Fluences at the End of the 14 Irradiation Cycles for Varied Energy Thresholds**

	Fast neutron fluence (n.cm <sup>-2</sup> ) $\times 10^{19}$ n.cm <sup>-2</sup>		
	E > 10 keV	E > 0.1 MeV	E > 1 MeV
Mean	1.40	1.12	0.57
Min.	1.07	0.87	0.45
Max.	1.51	1.23	0.62

Two damaging neutron energy thresholds have been adopted in the literature for rock-forming minerals:  $E > 10$  keV and  $E > 0.1$  MeV:

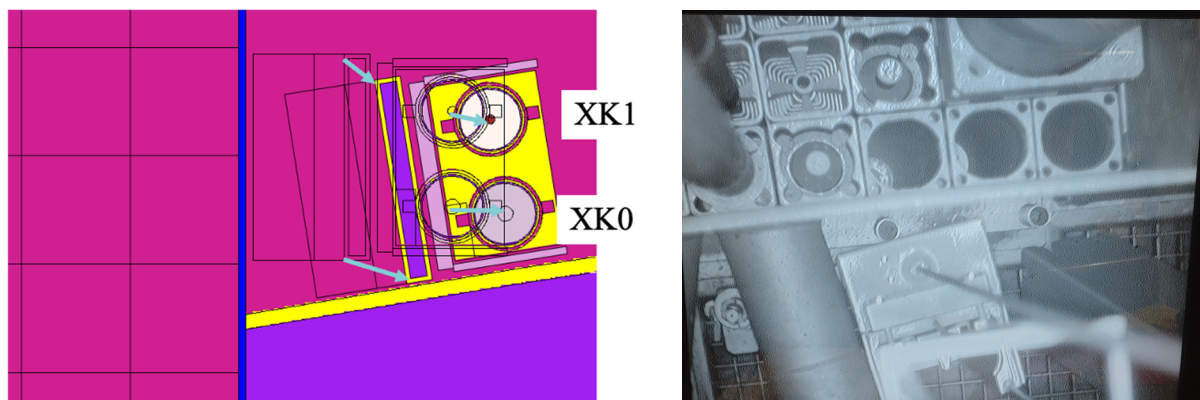
*The displacement per atom (dpa) cross sections for neutrons for a few materials that are widespread rock-forming minerals [quartz, calcite, albite, anorthite, microcline, almandine and fayalite] in concrete aggregates were generated with SPECOMP computer code, which is available as RSICC PSR-263 along with the Specter code and its database (Remec et al., 2018).*

Using neutron spectrums for 2-loop and 3-loop PWRs, Remec showed that ~95% of the dpa is generated by neutrons with energies above 0.1 MeV. The dpa generated was close to 100% when generated by neutrons with energies above 10 keV, and it was only 20–25% when generated by neutrons with energies above 1.0 MeV. Because the neutron spectra in PWRs and test reactors are not identical, the 10 keV threshold is adopted in this research according to the work of Denisov et al. (2012).

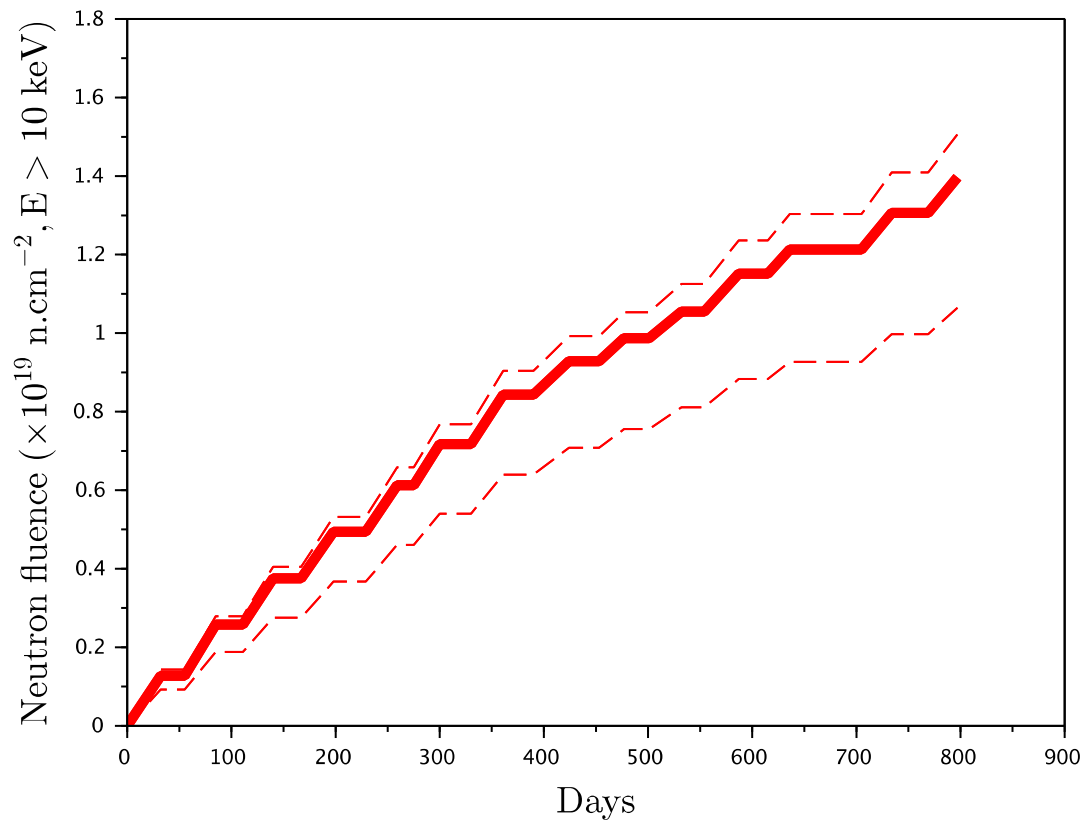
Gamma irradiation's contribution to the dpa in rock-forming minerals is minimal. "Gamma rays do not cause atom displacements directly; they first interact with electrons via Compton

scattering, photoelectric effect, or pair production; the energetic electrons then displace atoms via electron-nucleus collisions” (Remec, 2015). The dpa cross sections for gamma rays (Kwon and Motta, 2000) are only relevant for energies higher than ~20 keV and are 2 to 6 orders of magnitude lower than the corresponding cross sections for neutrons at the same energy. Thus, the contribution of gamma to the dpa of rock-forming minerals is considered negligible in this study. This conclusion does not apply to heavy aggregates such as hematite, ilmenite, or magnetite, all of which are rich in metallic elements.

The time evolutions of the fluence and gamma presented in Figure 4-2 and Figure 4-3 show a change of the general trend at around day 400. The fluence rate is higher before that date than after. The initial MCNP simulations predicted that the final fluences would be approximately 30% higher than those in the data derived from the post-irradiation activation analysis of the metal foil coupons (fluence monitors) inserted in the capsule. After investigation, remote visual inspection (Figure 4-1, right) showed that the irradiation rig shifted position during extraction of the sister capsule placed in the XK0 position. This shift could not be seen directly by visual observation from the operation deck above the reactor pool. The rig was subjected to a translation and a rotation from its initial position, as shown in Figure 4-1, left. Whereas the rig comprises pins for placement in the floor grid, the diameter of the pins does not coincide with the diameter of the floor holes, making shifting possible. The axis of the capsule in the XK1 positions moved by ~5 cm. After CVR accounted for the shifted position, updated simulations were completed which led to a good comparison with the fluence monitor data.

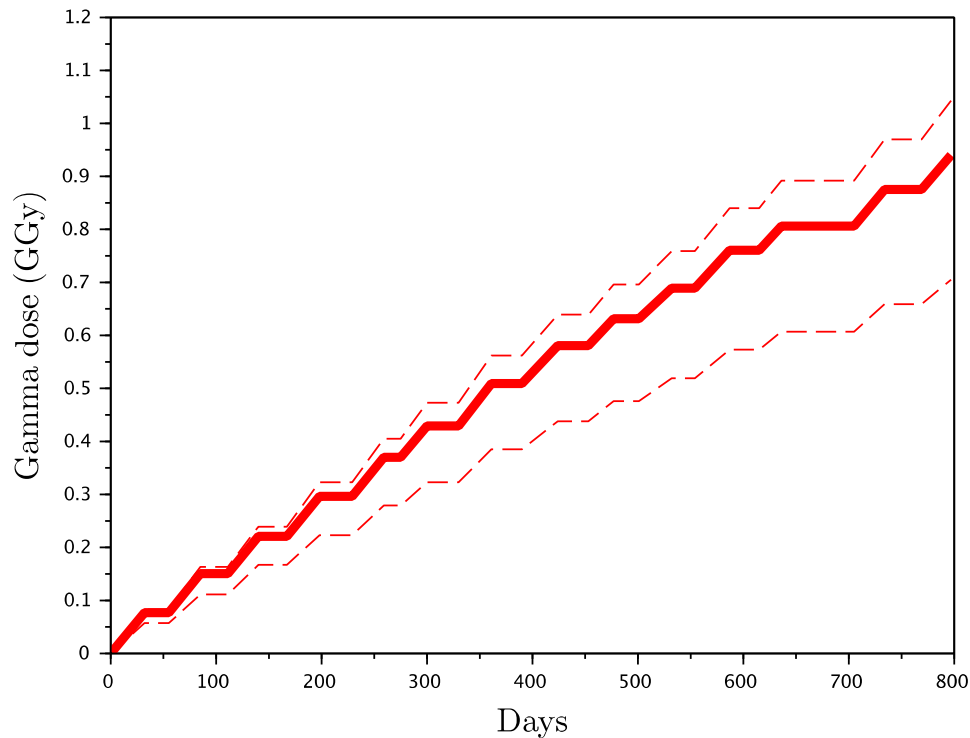


**Figure 4-1 (Left) Sketch Showing Initial and Shifted Positions of the Irradiation Rig. (Right) Photograph Taken in September 2023 Showing the Position of the Out-Of-Core Irradiation Rig**



**Figure 4-2 Fast Neutron Fluence ( $E > 10$  keV) History (14 Irradiation Cycles) in the Concrete and Aggregate Specimens. The Thick Solid Line Represents Average Fluence, and the Thin Dashed Lines Indicate Min./Max. Fluences**

Figure 4-3 presents the gamma dose history estimated from the MCNP simulations. The final average gamma dose is 0.940 GGy. The standard deviation across the irradiated concrete and aggregate specimens is 0.108 GGy. The corresponding minimum and maximum gamma doses are 0.705 and 1.043 GGy, respectively.



**Figure 4-3 Gamma Dose (14 Irradiation Cycles) in the Concrete and Aggregate Specimens. The Thick Solid Line Represents Average Gamma Dose, and the Thin Dashed Lines Indicate Min./Max. Gamma**

The fast neutron flux in the XK1 position is approximately one order of magnitude lower than the corresponding flux in the JEEP-II reactor. This characteristic makes it possible to assess potential flux effects because the aggregates and concrete specimens of the same composition have been tested in both reactors. The fast neutron flux in the XK1 position is at least approximately one order of magnitude higher than the corresponding flux in PWRs. The gamma dose and dose rate are approximately 5 to 20 times and 250 to 1,000 times higher in the XK1 position than in PWRs, respectively.

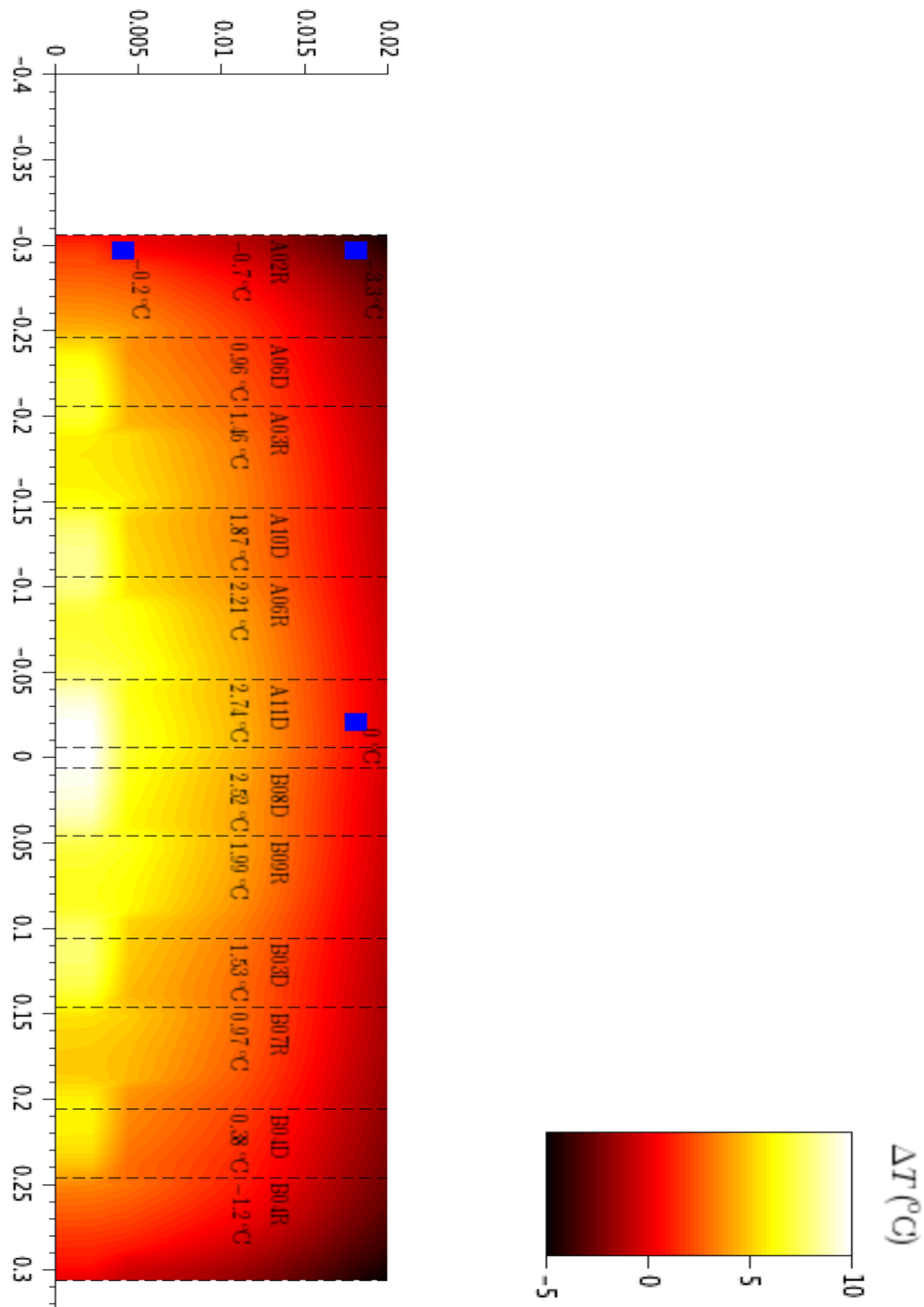
#### 4.1.2 Irradiation Temperature

##### 4.1.2.1 Temperature Variation Across the Irradiated Specimens

Based on TH simulations of irradiation capsules, including all specimens analyzed by CVR, the temperature spatial field can be estimated during irradiation. The simulations were performed assuming an axisymmetric model. This assumption is accurate to represent the geometries of the capsule and the test specimens. Although this approach only approximates the irradiation-induced energy deposition affected by the relative location of the test rig and the reactor core, it does provide useful information about the temperature variations across the concrete specimens during irradiation because temperature variations affect thermal expansion and RIVE.

Because the history of temperatures was monitored by embedded TCs, it was convenient to interpret the TH simulation results from the perspective of temperature differences with the temperature at the locations of the TCs. Figure 4-4 shows the temperature variation field in the concrete specimens during irradiation. The reference temperature was taken at the location of the TC placed near the mid-elevation of the stack (blue square marked at 0 °C). The two other TCs were placed toward the top of the specimen stack. The z-axis along the stack was oriented toward the bottom. The respective temperature differences of the two TCs compared with those of the central TC are +3.3 °C and -0.2 °C. On the simulated irradiation date of September 19, 2021, the recorded temperature differences ranged from -3.1 °C to -3.5 °C and 0.0 °C to -0.5 °C, respectively. The consistency of the monitored and simulated temperatures makes it possible to assume that the temperature variation map presented in Figure 4-4 is sound.

The core design changes between the varied cycles may have affected the irradiation-induced energy deposition in the concrete specimens, and in turn, the accuracy of the temperature variation map may have been affected. Nevertheless, the maximum temperature variation across a given specimen is <7 °C and was observed in the centrally located specimens A11D and B08D. Hence, thermally induced cracking was quite unlikely to occur during irradiation. Figure 4-6 also presents the difference between the mean temperature in each specimen and the temperature recorded by the centrally located TC. This difference varied by +2.74 °C and -1.28 °C in specimens A11D and B04R, respectively. The irradiation temperature variations in the concrete and aggregate specimens were used in the RIVE models.

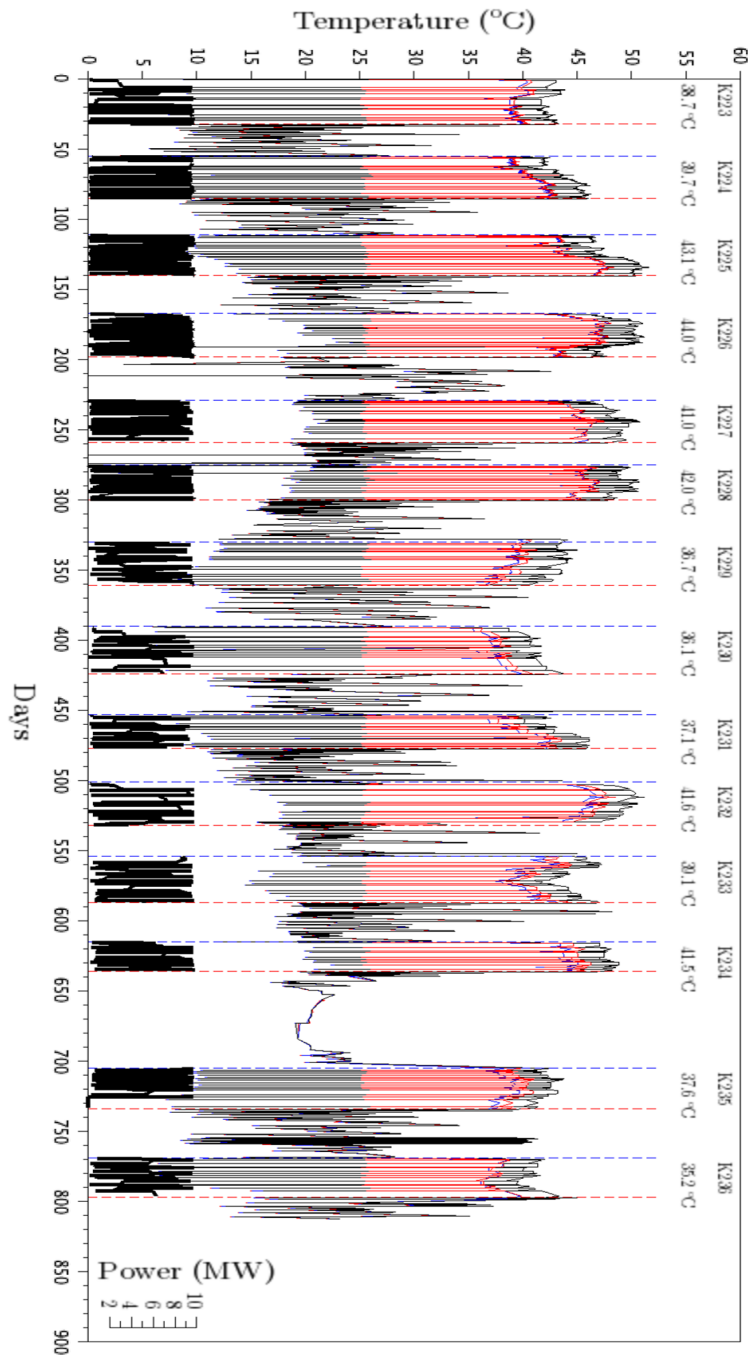


**Figure 4-4** Temperature Variation Field in the Concrete Specimens During Irradiation. The Reference Temperature was Taken at the Location of the TC Placed Near the Mid-Elevation of the Stack. x and y Axes are Shown in Meters, and Blue Squares Mark the TC Locations

#### 4.1.2.2 *Irradiation Temperature*

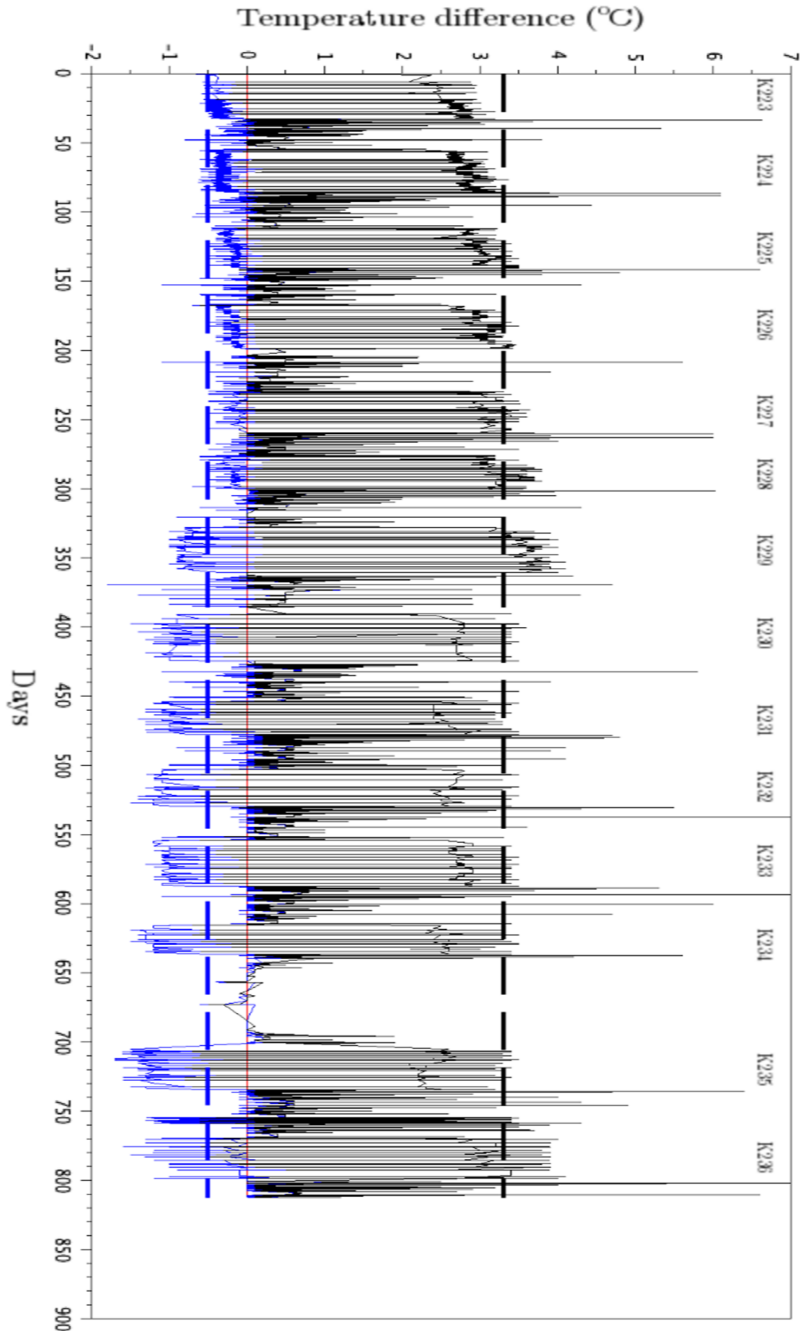
The temperatures monitored by three TCs placed in the concrete specimen stack are presented in Figure 4-5. During each cycle, temperature variations were caused by reactor operation (molybdenum production). Whereas seasonal variations affect reactor coolant temperature (bottom envelop of the temperature graphs), when the reactor power is above 7 MW, each monitored irradiation temperature remains in a limited range estimated at approximately  $\pm 5$  °C. The average temperature measured by the reference TC located near the mid-elevation of the stack for each cycle is displayed in Figure 4-5. The mean temperature accounting for molybdenum production–related outage during each cycle ranges between 35.2 °C and 44.0 °C. The recorded temperatures during reactor operation range between 36 °C and 51.5 °C. For the sake of comparison, the specimen temperature calculated estimates ranged initially from ~51 °C to ~58 °C. The recorded irradiation temperatures are lower than the data reported from the experiment conducted for JCAMP in the JEEP-II reactor. Hence, in absence of flux effects, it can be inferred that the post-irradiation expansion measurements should be higher on the specimens irradiated at comparable fast-neutron fluences in LVR-15-XK1 (e.g., Bykov et al., 1981; Le Pape et al., 2018).





**Figure 4-5** Monitored Temperatures During the 14 Irradiation Cycles (Ks). (Red Solid Line) TC Placed Near the Mid-Elevation of the Stack ( $T > 25^{\circ}\text{C}$ ); (Blue Solid Line) TC Placed at the Top of the Stack Near the Reinforcement Bar of the Top Pullout Specimen; (Black Solid Line) TC Placed at the Same Elevation but Near the Outer Diameter of the Concrete Specimen. (Thick Black Solid Line) Reactor Power. (Dashed Blue) Start Dates of Irradiation Cycles; (Dashed Red Line) End Dates of Irradiation Cycles

Figure 4-6 shows the temperature differences between the TCs placed at the top of the specimen stack and the TC taken as a reference and located near the mid-elevation of the stack. The dashed lines indicate the temperature differences obtained from TH simulations. It can be observed that the monitored differences vary in a range of approximately  $\pm 1$  °C around the simulated temperature differences.

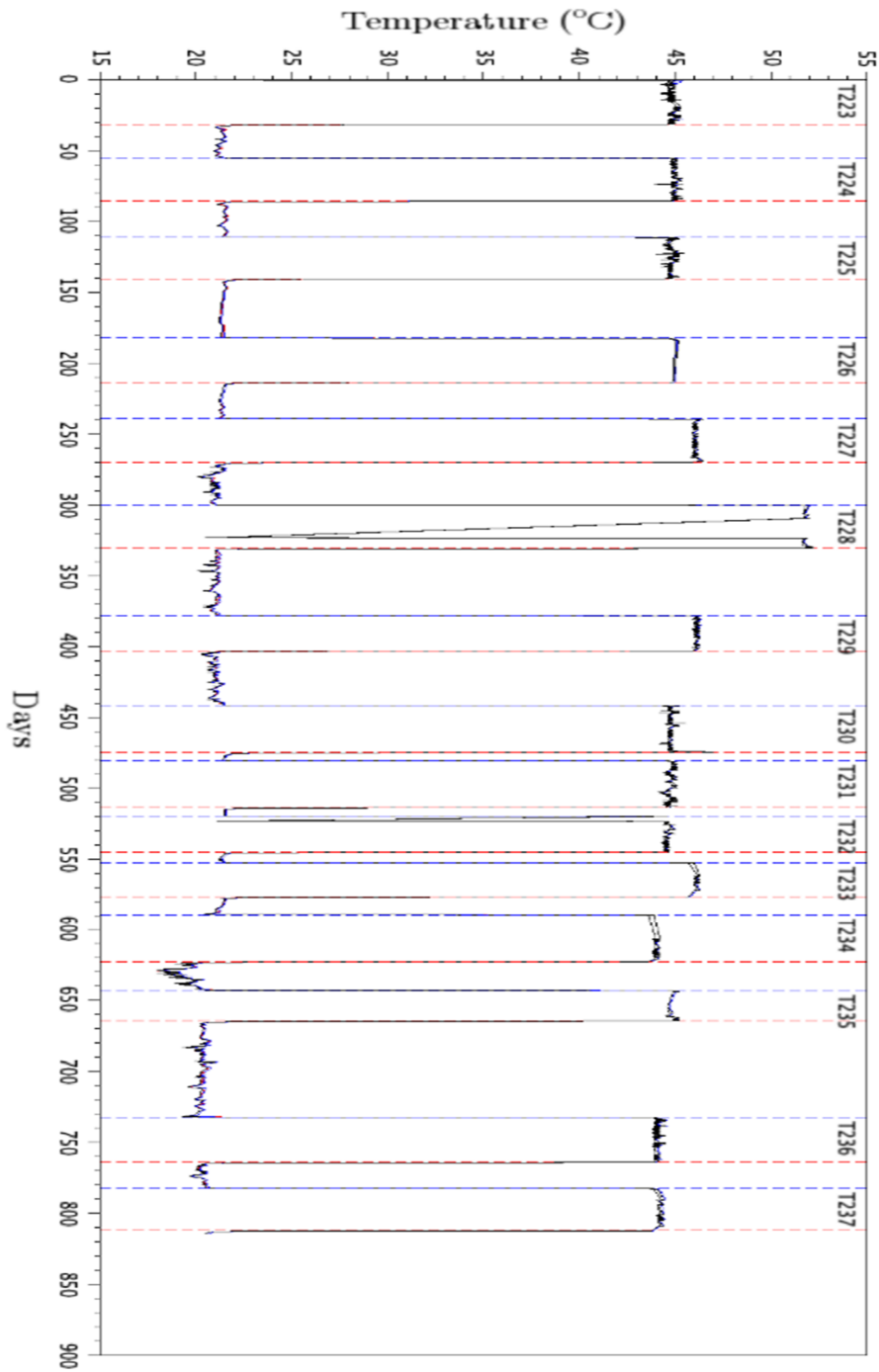


**Figure 4-6** Difference of Monitored Temperatures Between the TCs During Irradiation Cycles (Ks). Reference: TC Placed Near the Mid-Elevation of the Stack. (Blue Solid Line) TC Placed at the Top of the Stack Near the Reinforcement Bar of the Top Pullout Specimen; (Black Solid Line) TC Placed at the Same Elevation but Near the Outer Diameter of the Concrete Specimen. (Black and Blue Dashed Lines) Simulated Temperature Difference

## 4.2 Companion Irradiation-Temperature Experiment

The temperature measurements obtained from the three TCs placed in the irradiation capsule replica are presented in Figure 4-7. The absence of an internal heat source caused by irradiation-induced energy deposition leads to uniform temperature measurements at the three TC locations. Note that the three different plots are almost perfectly superimposed and can barely be distinguished in the figure. Heat cycles are labeled using a system similar to that used for the irradiation cycles. The first heat cycle is denoted as *T223* and corresponds to the irradiation cycle K223. During a heat cycle, the temperature remains almost constant. Minor temperature oscillations in the range of  $\pm 0.5$  °C around the mean temperature are recorded.

Table 4-2 presents the average, standard deviation, and maximum temperatures recorded for each cycle. Note that the minimum and maximum temperatures may include sporadic misreading (e.g., cycle T228), thus accounting for initial heating and final cooling ramps. The total duration of the heating cycles is 441 days. The mean temperature of all combined cycles ranges from 37.5 °C to 46.1 °C and averages approximately 44 °C.



**Figure 4-7** Temperatures Recorded in the TCs Placed in the Irradiation Capsule Replica Subject to Heat Curing Cycles. Data from All Three TCs are Plotted (Invisible Difference Between the Three Plots in the Graph). Dashed Blue and Red Lines Indicate the Start and Finish of Each Cycle

**Table 4-2 Summary of the Monitored Temperatures in the Irradiation Capsule Replica Subject to Heat Curing Cycles**

Cycle	Duration (days)	Temperature (°C)		
		Average	Standard deviation	Maximum
T223	31.5	44.8	5.5	45.3
T224	30.5	44.9	5.1	45.4
T225	29.5	44.7	5.9	45.5
T226	31.3	45	4.6	45.2
T227	30.6	46.1	0.6	46.5
T228	30.8	44.6	7.9	52.0
T229	24.8	46.1	1.5	46.3
T230	33.1	44.8	0.5	47.0
T231	33.1	44.3	0.2	45.1
T232	25.6	42.7	5.8	45.0
T233	24.0	37.5	0.5	46.3
T234	33.5	44	0.5	44.2
T235	21.3	44.8	1.6	45.3
T236	31.9	44.1	1.1	44.5
T237	29.8	39.5	0.4	44.4
	441.3 <sup>(a)</sup>	43.9 <sup>(b)</sup>	2.78 <sup>(b)</sup>	52.0 <sup>(c)</sup>

*(a) total duration, (b) mean value, and (c) maximum value*

## 5 CHARACTERIZATION AND TESTING METHODS

### 5.1 Mass Change

The pre- and post-irradiation mass measurement is needed to assess any moisture uptake or loss. The risk of carbonation-induced mass change is considered limited as a result of the constant He flow in the irradiation and companion capsules. The weight of the concrete specimens was measured using Radwag scale model AS 82/220.R2 (readability 0.01/0.1 mg, linearity  $\pm 0.06$  mg, repeatability 0.1 mg).

### 5.2 Dimensional Change

The dimensional change caused by irradiation is a critical measure of radiation-induced expansion and loss of mechanical properties. It is mainly caused by amorphization-induced density change in the aggregate-forming minerals. These minerals are randomly distributed in the aggregates. Therefore, at the scale of a representative volume of concrete, the expansion of an unconstrained concrete specimen is considered isotropic.

Because the effects of a central steel bar in the pullout specimens on the isotropy of the irradiation-induced dimensional change required assessment, the vertical and diametral dimensions of the specimens before and after irradiation were measured.

The specimens' dimensions were obtained using the Micro-Vu Vertex system (Figure 5-1) insulated against vibration and equipped with 3D coordinate measuring machine computer numerical control; a measuring camera equipped with a codebook, distribution and comparator chip; and a touch probe placed in the feeder. The dimensions were measured using the touch probe. Marks were drawn on the specimens to ensure that post-irradiation measurement locations matched the pre-irradiation data.



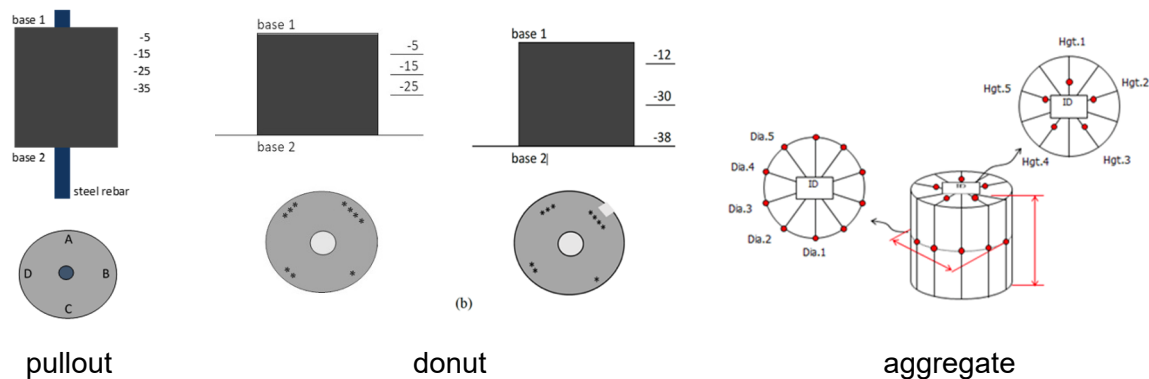
**Figure 5-1 (Left) Vertex Touch Probe Measurement Device; (Right) Pullout Specimen Setup for Height Measurement**

The dimensions of the pullout specimens were measured at several locations. The diameter of pullout specimen was measured at the base 1 level and at 5, 15, 25, and 35 mm below the base 1 level. The heights of specimens were measured at four locations (A, B, C, D, Figure 5-2, left).

Figure 5-2 (center) shows the dimensional measurement locations for the donut specimens. The diameter of concrete Con-A donut specimens (specimen without the lateral groove) was Slipping failure occurs when the radial cracks initiated around the measured at 5,15, and 25

mm below the base 1. The heights were measured at four locations marked \*, \*\*, \*\*\* and \*\*\*\*. The diameters of the concrete Con-B donut specimens (specimen with the groove) were measured at the top, in the middle, and at the bottom. Their heights were measured at four locations, marked as \*, \*\*, \*\*\*, \*\*\*\* on the figure.

The schematics of aggregate dimensional measurements are presented in Figure 5-2 (right). The diameters were measured at five locations (Dia.1–Dia.5) in the middle sections of specimens. Their heights were measured at five locations (Hgt.1–Hgt.5).



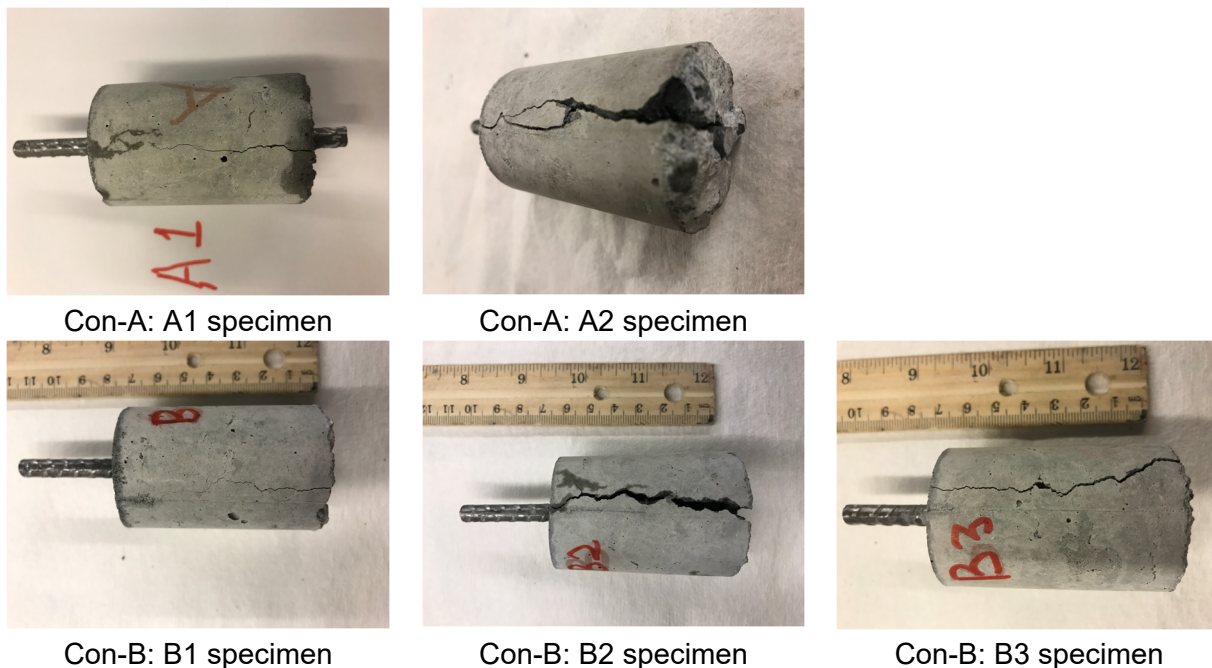
**Figure 5-2** Locations of the Dimensional Measurements Using the Micro-Vu Vertex System for the Pullout Specimens (Left), the Donut Specimens (Center), and the Aggregate Specimens (Right)

### 5.3 Bond Testing

#### 5.3.1 Consideration on Failure Mode

The bond resistance of steel reinforcement embedded in concrete is characterized by pullout testing. The general principle of this test is straightforward. The reinforced concrete specimen consists of a concrete cylinder reinforced by a single reinforcement low-carbon steel bar. The two ends extend out from the concrete. The shorter end is designated as the *free end* and is used to ensure that the placement of the bar is in its axial position during casting. The longer end is called the *loading end* and is designed to provide a grip to exert a force to pull the bar outward while the perpendicular concrete surface is maintained in its original position. To ensure that the failure mode does lead to a concrete cone failure near the loading end, the bar is unbonded over a length of 25 mm for the specimens of 40 mm diameter and 60 mm height. The bonded length is thus 35 mm (ratio of bar diameter to bonded length: 0.18). However, the presence of a debonding length does not preclude the failure mode of the specimen. Two types of failure modes can occur: splitting or slipping failure. Detailed explanations about the formation of these failure mechanisms are given in Chapter 11. Figure 11-2 provides an illustration of crack formation for each mode. Only corrugated or deformed bars are considered in this study. Through the action of a pullout force, the reinforcing bar gradually slips from its initial location in the concrete. The occurrence of slippage implies that bond shear resistance has been reached or exceeded. However, the mechanical interaction between the reinforcement and the concrete also involves radial or lateral stress because of the presence of the bar ribs. Radial cracks initiate around these ribs. A splitting failure mode is caused when those radial cracks propagate through the concrete cover, which may occur before reaching the actual bond resistance of the steel–concrete interface reinforcement do not propagate outward because of lateral confinement. Thicker concrete cover improves lateral confinement. Slipping failure is characterized by a near-cylindrical failure surface around the reinforcement.

The objective of the test is to obtain a clean failure surface, or a slipping failure mode, at the interface to derive the properties of the steel-concrete interface from the bar load-slip measurement. Preliminary tests were conducted at UTK on aged specimens. The average compressive strength of concrete Con-A was 59.3 MPa, and for concrete Con-B it was 50.3 MPa. Figure 5-3 shows photographs of the specimens after bond testing. All specimens exhibit partial-to-complete splitting failure cracking. However, additional simulation work completed independently by Maruyama (University of Nagoya and University of Tokyo) using the rigid body spring model (RBSM, private communication: actual data not presented here) and by ORNL using the LDPM (data presented in the simulation chapters of this report, Section 11 and beyond) concluded that the geometry of the specimen caused it to be prone to splitting failure. To prevent this, a mitigation strategy was implemented.



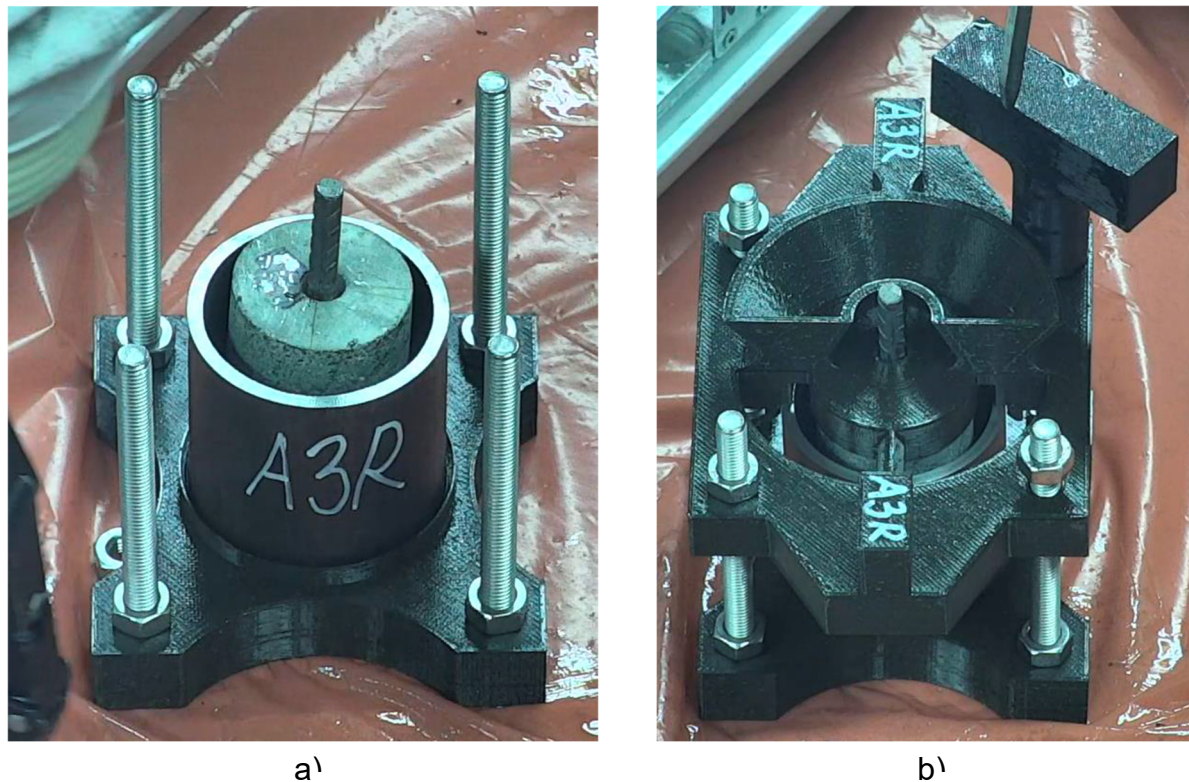
**Figure 5-3 Preliminary Testing and Post-Pullout Test Photographs**

### 5.3.2 Specimens Jacketing

To ensure that steel-concrete bond slipping failure mode occurs, it is necessary to enclose the specimen in a rigid confinement jacket to prevent possible splitting failure. This process is referred to as *jacketing* and is conducted one or two days before bond testing. It must be clarified that jacketing does not exert permanent lateral pressure. It is merely a passive system that gets activated during the bond test because of the radial stresses forming around the bar ribs when slippage occurs. This mechanism is illustrated by simulation results in in Section 13.6 To create a passive lateral confinement, a steel tube (4130 Alloy Steel, thickness: 0.12 in.  $\pm$  0.018 in., inner diameter: 2.01 in., yield stress: 70 ksi, supplier: McMaster-Carr) is mounted on a specially designed rig that is placed and centered around a pullout specimen. The gap between



the steel tube and the concrete specimen is filled with epoxy that hardens within 48 h. The epoxy transmits the lateral confining pressure from the steel tube to avert propagation of radial cracks in the concrete around the reinforcement. LDPM simulations and preliminary tests proved the efficiency of the protocol adopted for all bond testing in this study. Figure 5-4 shows the 3D printed fixtures that were initially developed by ORNL and later modified by CVR to meet the manipulation constraints in hot cells.



**Figure 5-4 Jacketing of Pullout Specimens in Hot Cells: (a) Specimen and Jacket Centering and Placement in Fixture, and (b) Full Setup Fixture for Epoxy Casting**

### **5.3.3 Bond Testing Apparatus at CVR**

The bond testing apparatus at CVR is similar to the apparatus developed at UTK. However, operating in the hot cell environment using a manipulator and a different loading press added specific constraints that necessitated modifications to the original design.

#### *Instrumentation and Testing:*

An Instron 8802 Servo Hydraulic testing system was used for pullout testing of specimens. The entire setup was placed in a hot cell suitable for handling activity up to 300 TBq for  $^{60}\text{Co}$ . The Instron 8802 is capable of a maximum dynamic load up to 250 kN. Acquisition channels make it possible to connect four additional LVDT sensors.

### *LVDT Sensors:*

The LVDT sensors were the same as those used at UTK. Using the same sensors minimizes measurement uncertainties between the different experiments on cold and activated specimens. The sensor type is a Micro-Epsilon DTA-3G8-3-CA.

The main characteristics of these sensors are as follows:

- Measuring range:  $\pm 3$  mm
- Linearity:  $\leq \pm 18$  mm
- Repeatability:  $\leq 0.45$  mm
- Diameter: 8 mm
- Length: 88.2 at zero position

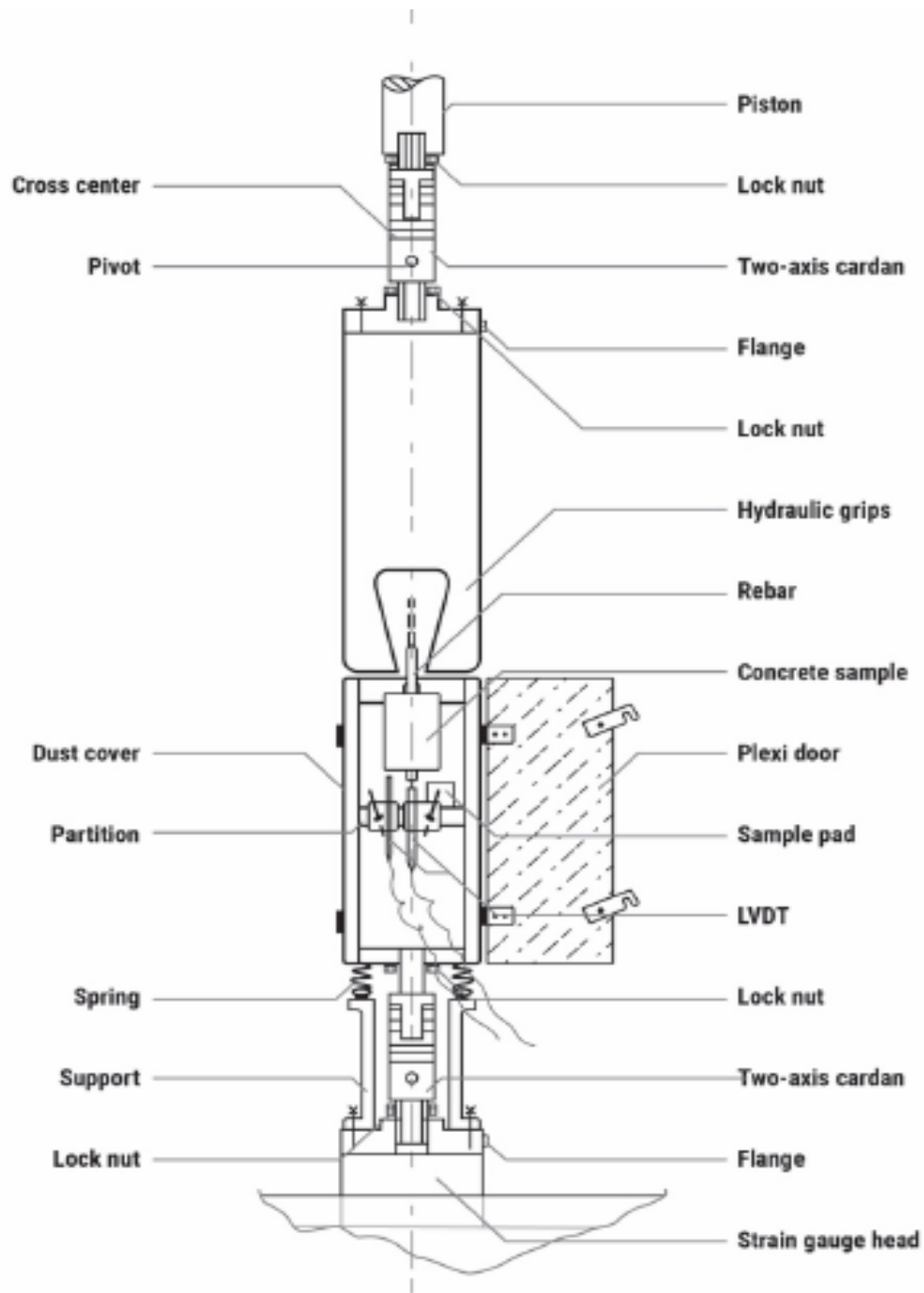
### *Assembly:*

The LVDT sensors were connected directly to the Instron acquisition unit using a Smart connector developed by Instron. Calibration data of the sensors were stored in the Smart connector immediately after calibration.

### *Design and Manufacturing*

The first sketch of the specimen holder was created according to the ORNL assembly drawing for the non-active pullout tests. The design required modification for active specimen testing to prevent contamination of the sealed enclosure, to allow for the possibility of remote handling, and to accommodate the use of hydraulic grips. In the testing position, the specimen was enclosed by a stainless-steel box (Figure 5-5). The box was equipped with a polyacrylic door to allow for specimen insertion and test observation. The box prevented spread of contaminated dust on the large surface in the hot cell.

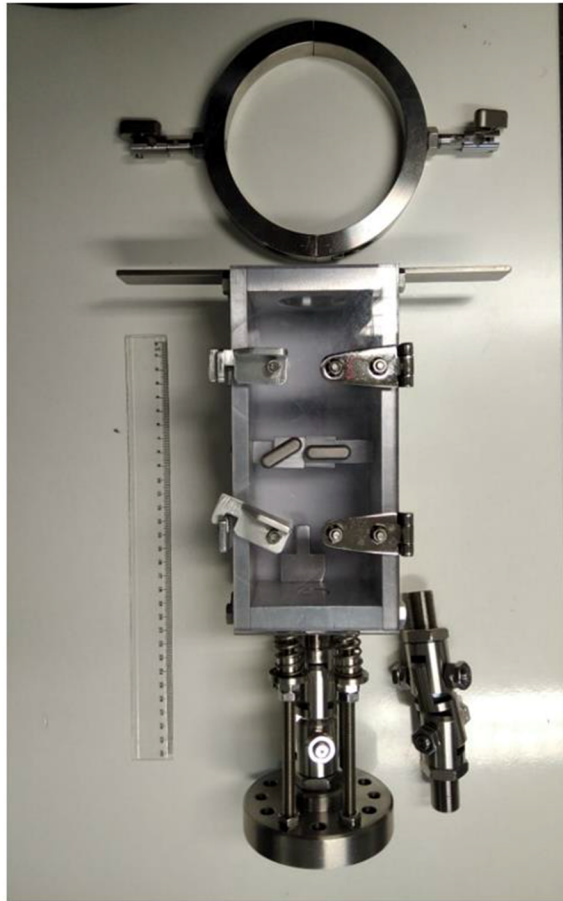
The box was connected to the strain gauge head using a Cardan coupler and was supported using three springs. The specimen was inserted using remote master-slave manipulators to maintain stability. The concrete part of the specimen was leaned against the rigid body of the stainless-steel box. The steel rebar part of the specimen was gripped by a hydraulic jaw.



**Figure 5-5 Preliminary Design Assembly of Bond Testing Apparatus at CVR**

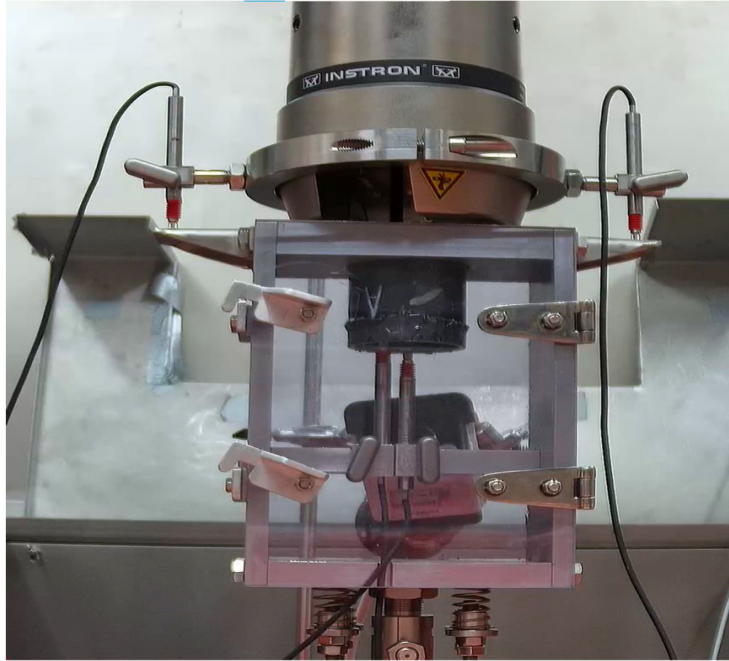
Some parts of the assembly were refined with an emphasis on ensuring that at least three LVDT sensors were used as required. The final design was equipped with four LVDT sensors for more precise results. Two LVDTs monitored possible grip slippage between the steel bar and the hydraulic jaw. One LVDT was placed at the free-loading end and was used to measure the displacement of the concrete. Finally, the fourth LVDT was used to measure steel bar displacement at the free-loading end.

The Research Center Řež workshop manufactured the whole assembly of the specimen holder, as shown in Figure 5-6.



**Figure 5-6 Photographs of the Bond Testing Apparatus**

Once the epoxy had hardened, the test specimen was placed in the setup and clamped using the hydraulic grip. The resulting preloading was  $< 400$  N. The LVDTs were then installed. Testing proceeded by gradually increasing displacement of the grip head at a strain rate of  $0.5$  mm/min. The test ended when the free extremity of the reinforcing bar penetrated inside the concrete specimens. Once the bar was inside the concrete, the bonded length continued to change, and it became more challenging to interpret the test results. Operations were monitored using remote cameras. Figure 5-7 shows a photograph of the complete test setup during the bond test of a Con-A irradiated specimen.

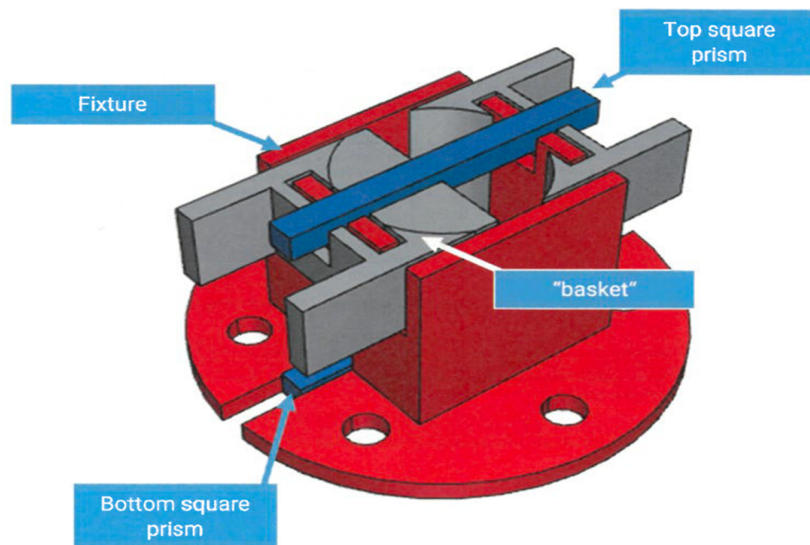


**Figure 5-7 Post Irradiation Pullout Testing Showing the Test Fixture, the Test Specimen, and the LVDT Locations**

#### **5.4 Splitting Test**

The tensile strength of concrete can be measured using results from indirect tensile tests, also known as *Brazilian splitting tests* (ASTM D3967, “Standard Test Method for Splitting Strength of Intact Rock Core Specimens”). These tests consist of applying a force across a cylinder through a plane, including the cylinder axis. Preliminary simulations conducted using LDPM showed that the presence of the central hole in the donut affected the formation of a splitting fracture and created bending forces in the specimen. The proposed alternative consists of applying the force directly on the top and bottom faces of the donut specimen through stainless-steel square rods measuring 6 mm wide. The theoretical fracture area is equal to  $A = 40 \times (40 - 8) = 1280 \text{ mm}^2$ . The apparent tensile strength was calculated by dividing the maximum applied force by the theoretical fracture area. Testing on a dummy specimen showed that brittle fracture occurred, thus separating the donut into two-halves. Because the number of irradiated and heat-cured specimens is limited, two additional splitting tests were conducted on the half-donuts assuming a theoretical fracture area of  $640 \text{ mm}^2$  for the apparent strength calculation. The main difficulties with this test were ensuring the correct placement of the specimen with the bottom and top rod and ensuring the correct overall centering of the setup in the press. These manipulations were evidently almost impossible to perform using a hot-cell manipulator without a supporting fixture. Therefore, a 3D printed fixture was designed and fabricated to this aim and is shown in Figure 5-8. After the full-donut splitting test was completed, the two-halves were removed from the basket. One half of the basket was filled with a 3D printed half-cylinder to facilitate placement of the concrete donut half.





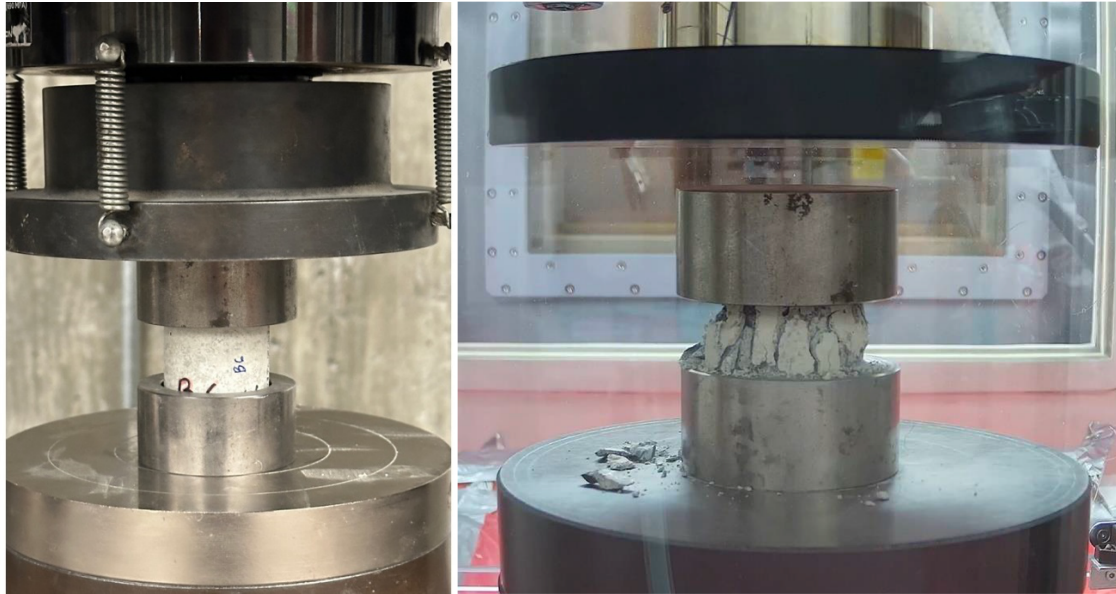
**Figure 5-8 3D Sketch of the Splitting Test Fixture Designed by CVR**

## 5.5 Compression Tests

Compression tests were conducted on the donut specimens. The geometry of the donuts (40 mm in diameter and 40 mm in height) does not comply with standard test methods. The aim of the test was limited to comparing the residual compression strength of specimens subject to room temperature curing, irradiation temperature curing, and irradiation.

Surface preparation and sulfur capping of the irradiated specimens are methods difficult to implement in the hot cell environment. Hence, unbonded caps were designed by adapting ASTM C1231 (Standard Practice for Use of Unbonded Caps in Determination of Compressive Strength of Hardened Cylindrical Concrete Specimens) to the geometry of the test specimens. Steel caps were specifically manufactured to this aim. Figure 5-10 shows residual concrete attached to the metal caps after testing. The caps have an inner diameter of 42 mm, an outer diameter of 60 mm, a total height of 28.7 mm, and a thickness of 8 mm. The thickness of the neoprene pad is 12.7 mm. Figure 5-9 (left) shows the test setup at UTK.

The presence of a neoprene pad does not prevent lateral confinement. Hence, the measured strength is more representative of the triaxial strength of the concrete than the uniaxial strength. At the end of the compression test, the expansion of the neoprene pads around the specimens' edges cause fractured concrete parts to remain attached to the pad and the caps (Figure 5-10). Whereas the residual material could be manually removed from the caps after the unirradiated specimen tests, this task is problematic in the hot cell environment because of difficulties with manipulation and contaminated material dust generation. Therefore, four pairs of caps were fabricated—one pair for each irradiated concrete donut. The caps and residual concrete were treated as nuclear waste materials. Figure 5-9 (right) shows the setup inside the hot cell.



**Figure 5-9**      **Compression Test Setup Showing (Left) the Specimens Placed Between the Unbonded Caps (UTK) and (Right) Specimen B04D at the End of the Test Conducted in CVR's Hot Cell**



**Figure 5-10**      **Post Compression Test Showing the Fractured Surface of the Concrete Specimen**



## 6 POST-IRRADIATION EXAMINATION

### 6.1 Extraction of Irradiated Specimens

At the end of the fourteenth irradiation cycle, the capsule was transported to hot cell No. 6 for extraction of the irradiated specimens. On April 4, 2023, the capsule was cut at the extremities. Because the presence of the TC wire at mid-elevation made it difficult to extract the specimens located in that half of the capsule, the capsule was also cut near the alumina holder. During the cutting operation, the #2 single bar that had been placed through the hole of the holder was partly cut near its middle, thus reducing the length of the bar to approximately 40 mm. This made it difficult to conduct a direct tensile test with the gripping system of the testing machine provided in the hot cells.



Cutting of the capsule extremity

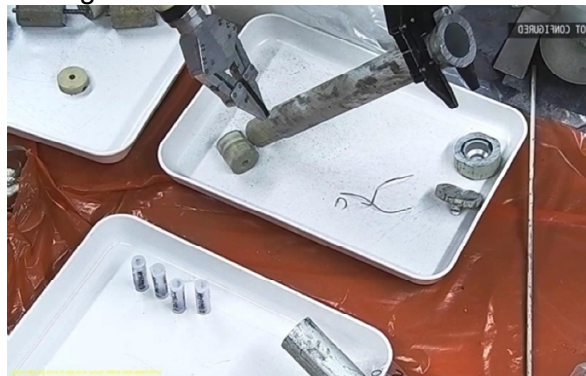
2023-04-04 11:43:39 Tues



Cutting near the alumina holder



View of the inside of the capsule showing a fluence monitor and a pullout specimen



Extraction of the irradiated specimens

**Figure 6-1      Photographs Taken During Capsule Opening and Extraction of Irradiated Specimens**

Figure 6-2 shows photographs of the specimens after extraction. Note that the small amount of dust visible in the holding pans is mainly attributed to the capsule cutting operation.

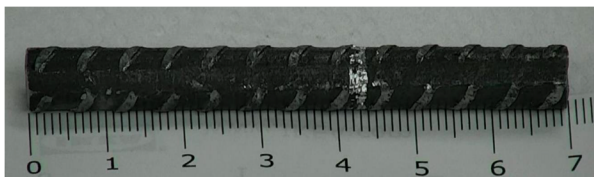




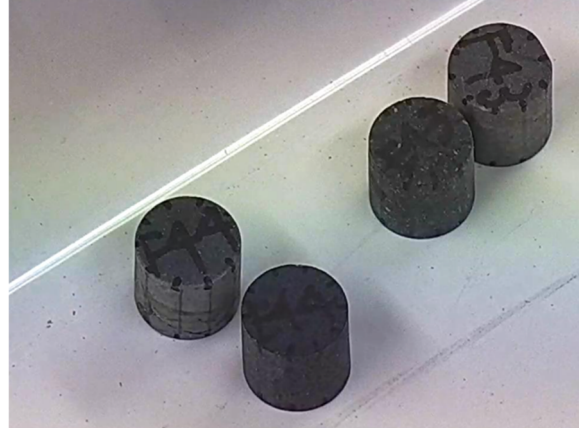
General view of all extracted specimens



Aggregate specimens were placed in plastic tubes



Single #2 bar

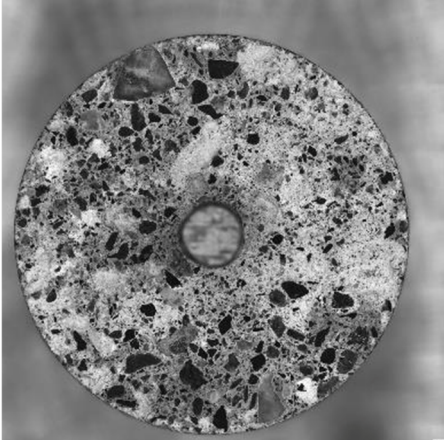
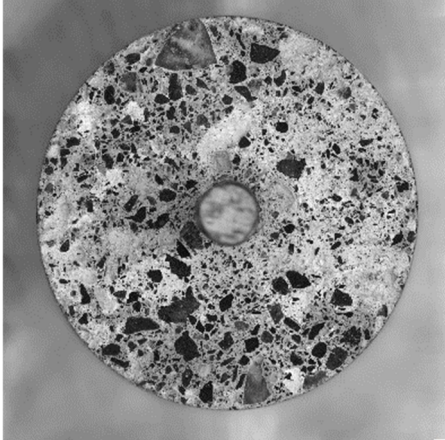
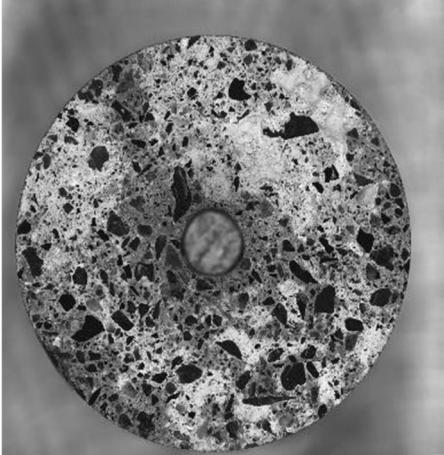
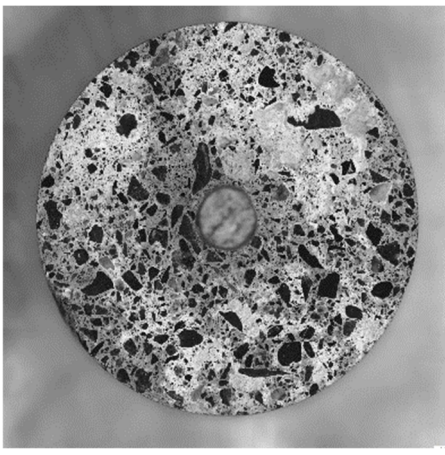
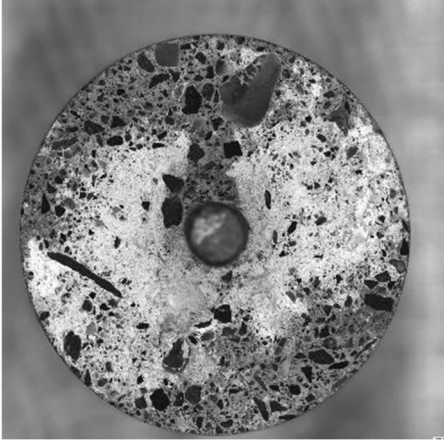
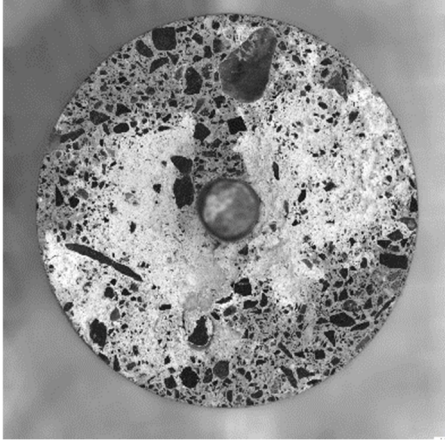


Aggregates

**Figure 6-2 Photographs of the Extracted Specimens**

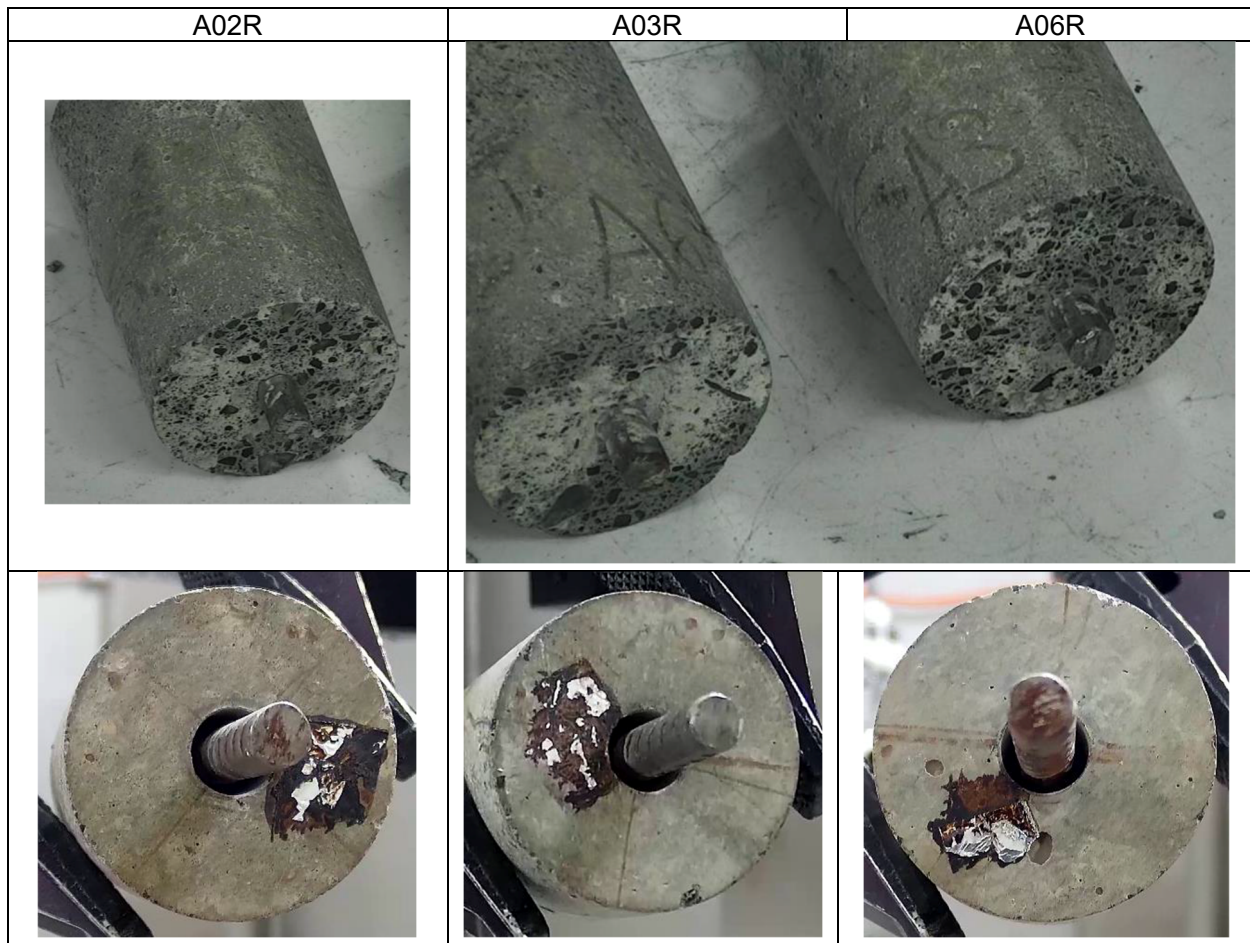
## 6.2 Visual Observations

Photographic documentation of the specimens before and after irradiation is presented in this section. Figure 6-3 and Figure 6-5 display the pre- and post-irradiation photographs of the pullout specimens. Figure 6-7 and Figure 6-8 display the photographs of the donut specimens. Figure 6-9 shows the photographs of the GA(F) and GB(E) specimens. Comparison of the pre- and post-irradiation photographs does not indicate any major change in the concrete and the aggregate specimens' visual appearance. The large light gray areas visible in the photographs taken on the polished sides of the specimens correspond to cement paste attrition that may have occurred during manipulation and shipment. Based on visual examination of the photographs, it is difficult to conclude whether those areas extended further after irradiation and removal from the capsule. Additional photographs (Figure 6-4 and Figure 6-6) taken of the irradiated pullout specimens show marks and traces left by the fluence monitors.

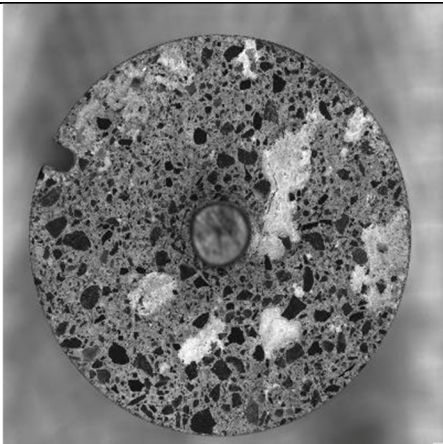
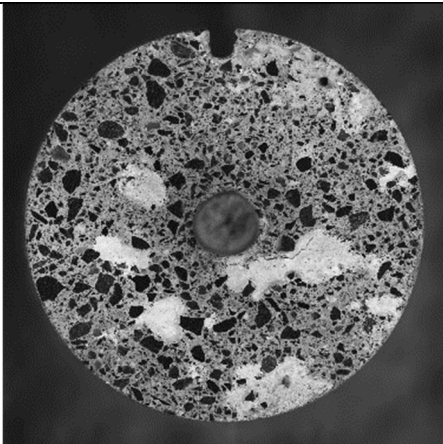
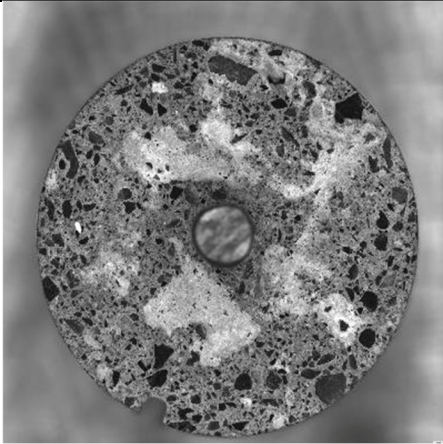
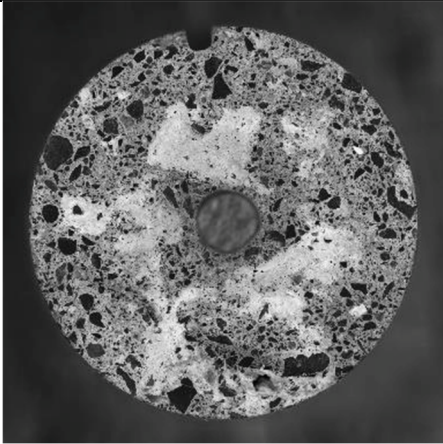
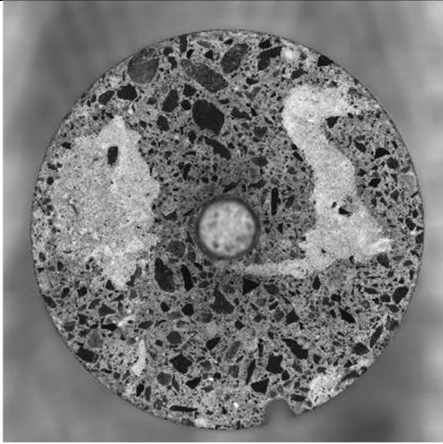
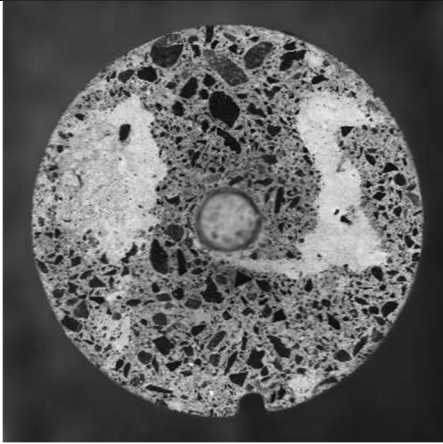
	Before irradiation	After irradiation
A02R		
A03R		
A06R		

**Figure 6-3      Photographs of the Con-A Pullout Specimens Taken from the Free Ends  
Before and After Irradiation**



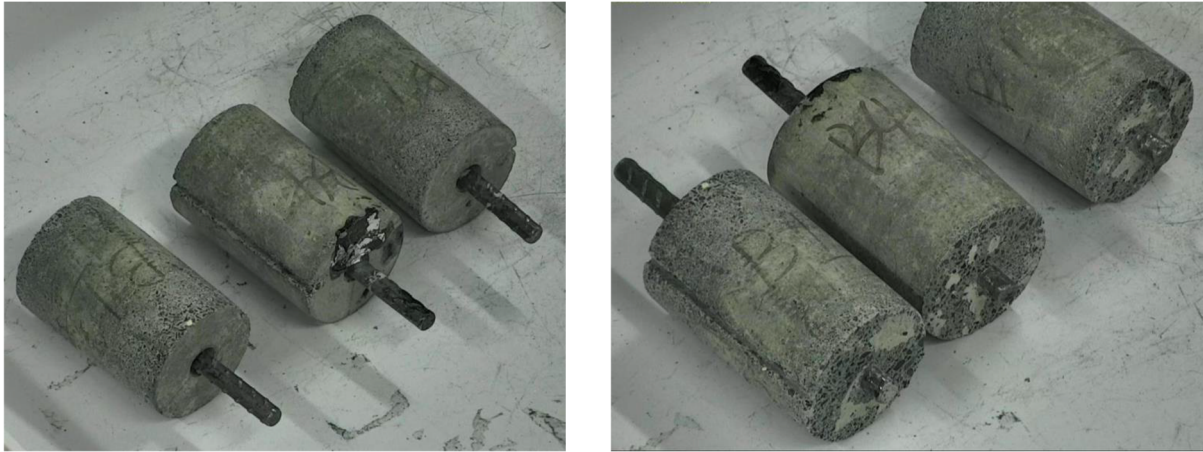


**Figure 6-4 Additional Photographs of the Con-A Pullout Specimens Showing Marks Left by Fluence Monitors**


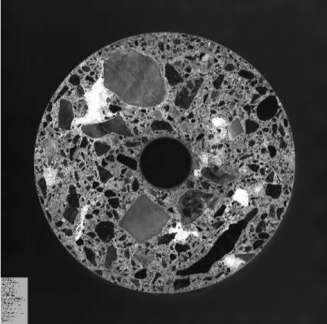
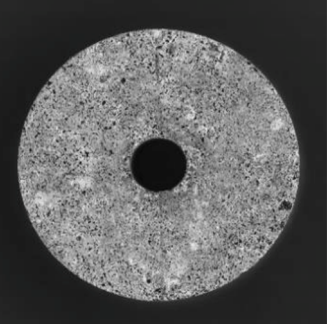
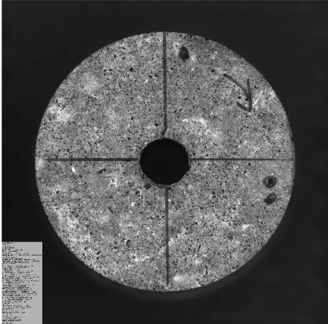
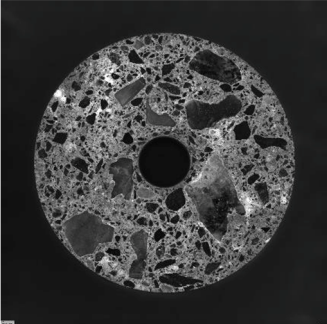
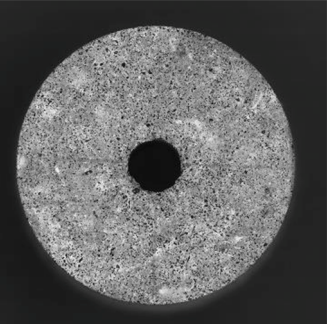
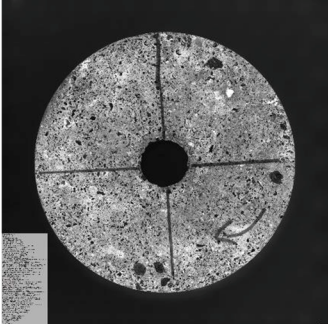
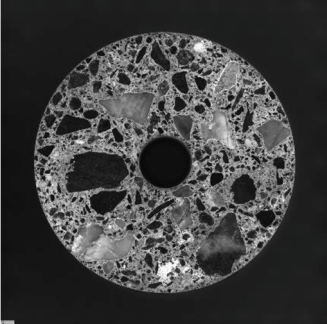
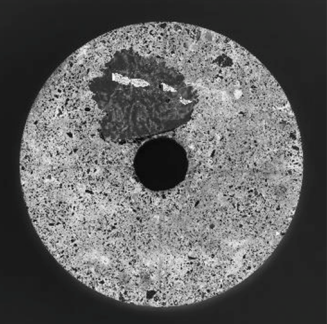
	Before irradiation	After irradiation
B04R		
B07R		
B09R		

**Figure 6-5**      **Photographs of the Con-B Pullout Specimens Taken from the Free Ends Before and After Irradiation**

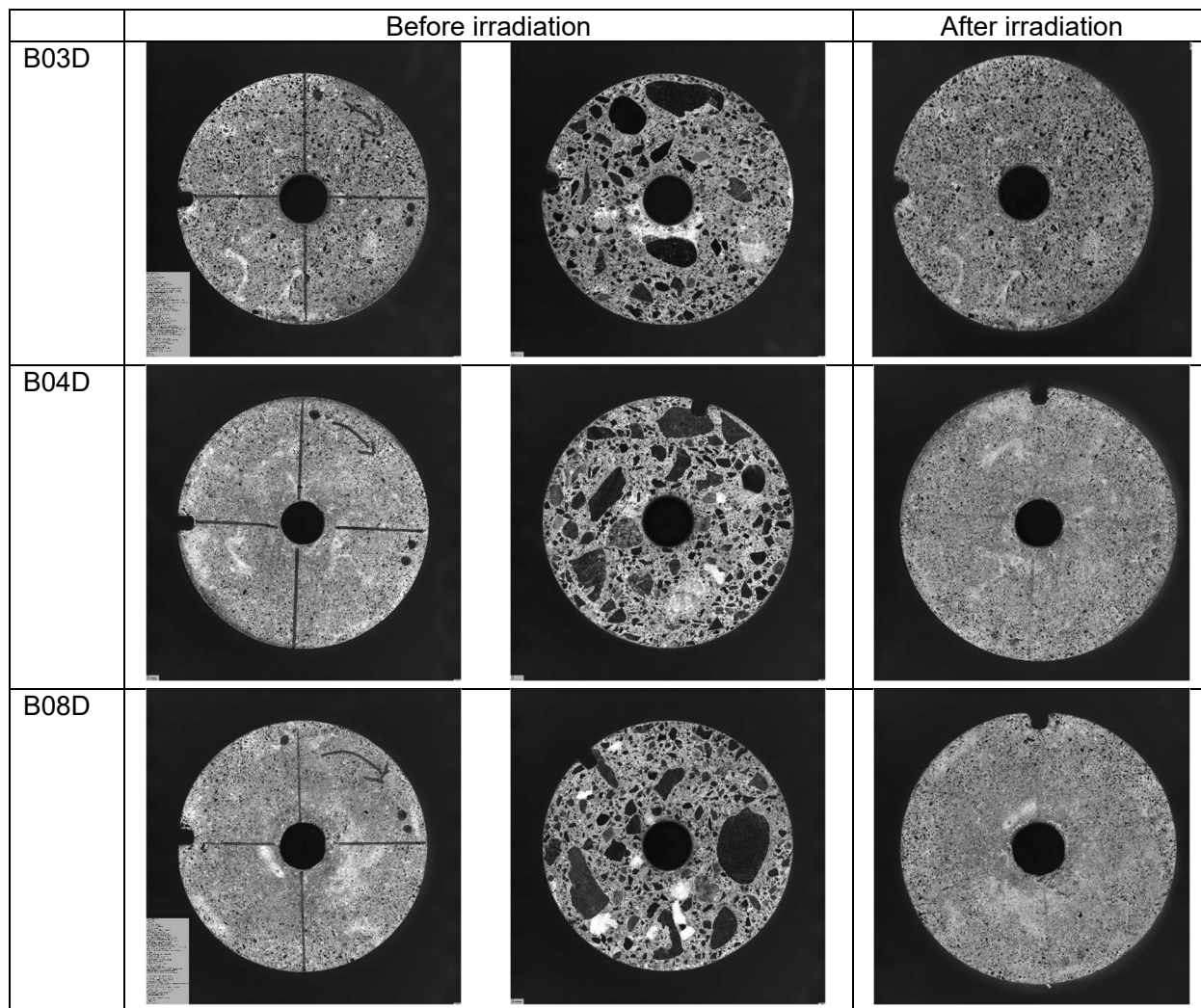




**Figure 6-6 Additional Photographs of the Con-A Pullout Specimens Showing Marks Left by Fluence Monitors**

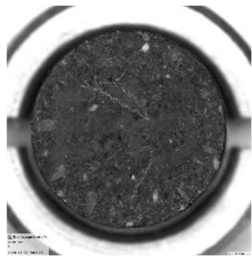
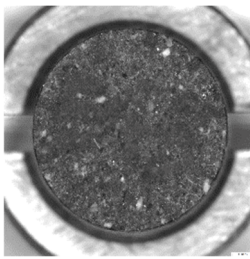


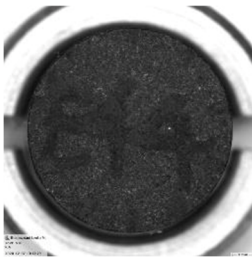
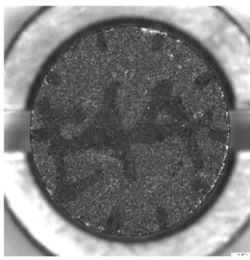


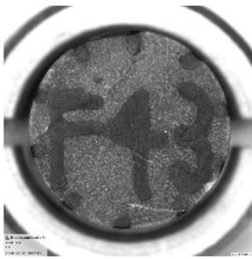
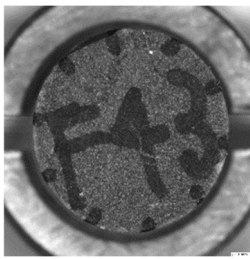


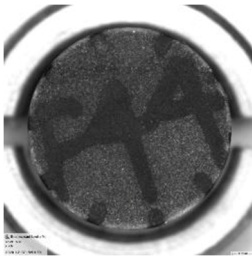
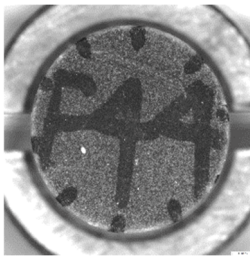


	Before irradiation		After irradiation
A06D			
A10D			
A11D			

**Figure 6-7 Photographs of the Con-A Donut Specimens Taken Before and After Irradiation**



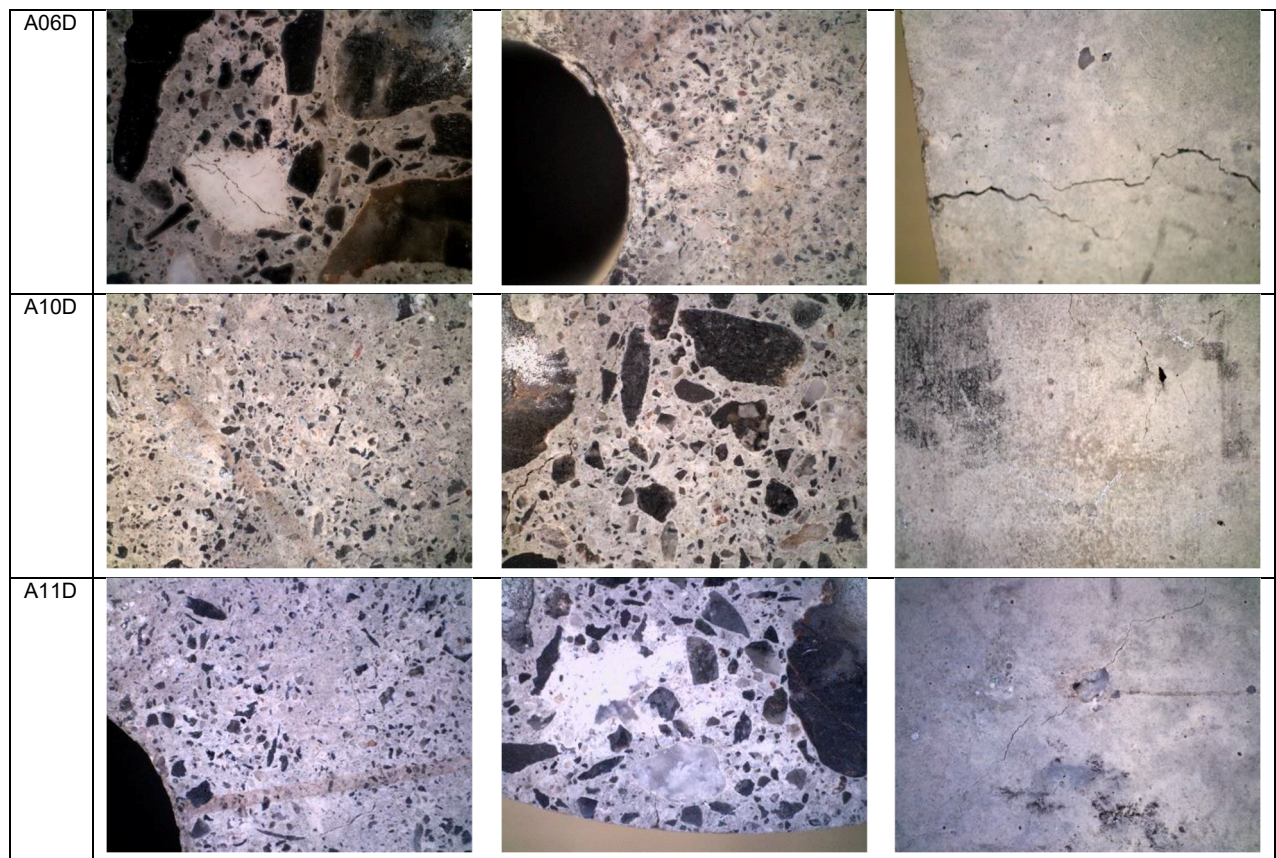
**Figure 6-8**      **Photographs of the Con-B Donut Specimens Taken Before and After Irradiation**



	Before irradiation	After irradiation		
E43				
E44				
F43				
F44				
	Vertex		DinoLite	

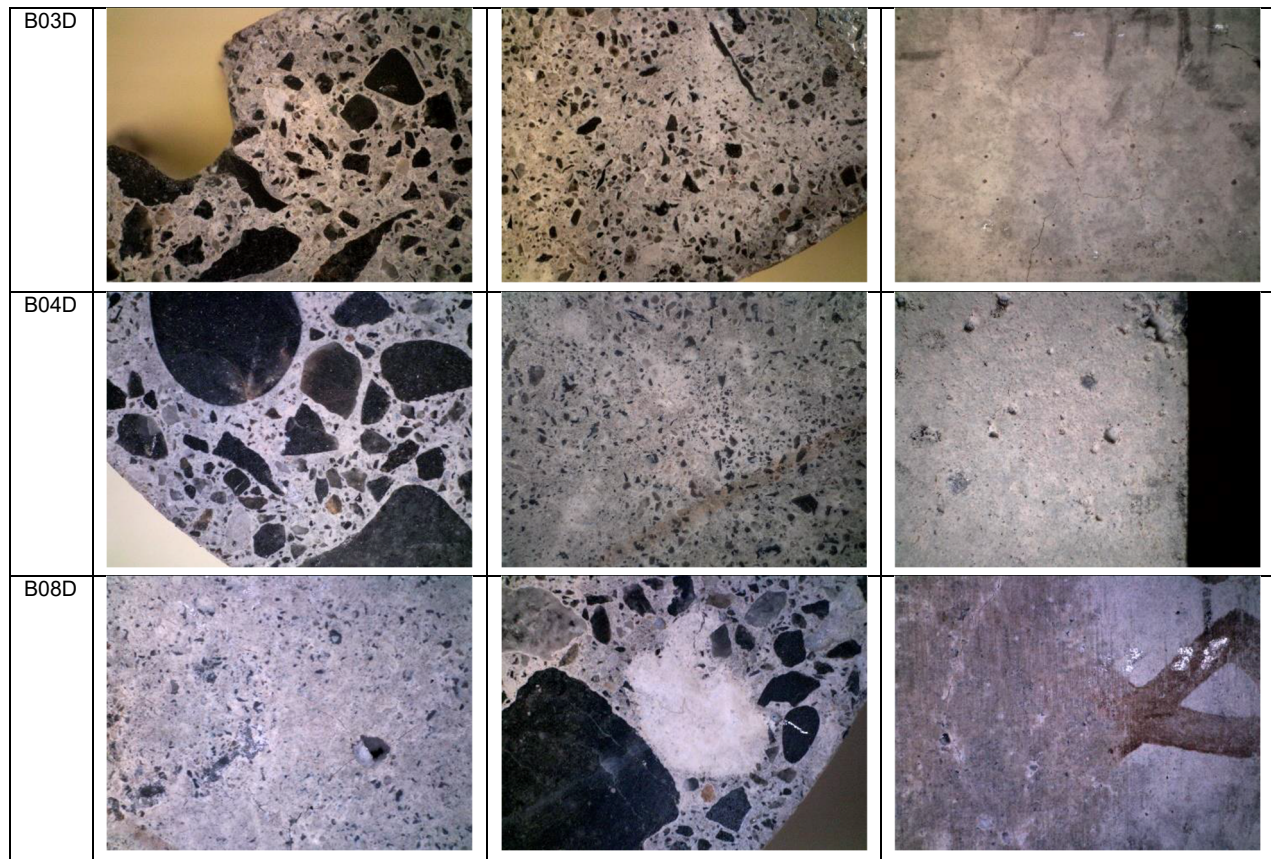
**Figure 6-9      Photographs of the Aggregate Specimens Before and After Irradiation**

Additional close-up photographs (Figure 6-10 and Figure 6-11) of the donut specimens show the presence of cracking that was likely caused by a combination of aggregate RIVE and/or cement paste shrinkage.



**Figure 6-10 Observed Post-Irradiation Cracking in the Con-A Donut Specimens**





**Figure 6-11 Observed Post-Irradiation Cracking in the Con-B Donut Specimens**

### **6.3 Dimension and Mass Changes**

The dimension and mass measurements of the specimens irradiated in the CVR LVR-15 reactor are reported in Table 6-1 through Table 6-10. The measuring locations provided in these tables (dimensional change) are given in Figure 5-2. The main results are summarized below:

1. The volume change of the aggregates is <0.01%–0.18% and 0.20%–0.26% (expansion), respectively, for aggregate GB(E) (felsic sandstone) and aggregate GA(F) (meta-chert).
2. The mass loss of the donut specimens is consistent in the specimens made of aggregate Con-A and Con-B, ranging between –0.5% and –0.7%.
3. The mass loss of the pullout specimens is also consistent in the specimens made of aggregate Con-A and Con-B, ranging between –0.3% and –0.5%.
4. The volume change of the donut specimens made of aggregate GA(F) ranges between –0.9% (overall shrinkage) and 1.9% (expansion).
5. The volume change of the donut specimens made of aggregate GB(E) ranges between –2.8% (overall shrinkage) and 1.9% (expansion).

6. The volume change of the pullout specimens made of aggregate GA(F) ranges between -1.1% (overall shrinkage) and <0.05% (expansion).
7. The volume change of the pullout specimens made of aggregate GB(E) ranges between -1.1% (overall shrinkage) and <0.2% (expansion).

Note: The ranges are for a group (e.g., aggregate, CON-A, CON-B, Donut, pullout) of specimens.

Detailed analysis of the data is provided in Chapter 10.

**Table 6-1 Pre- and Post-Irradiation Height and Volume Measurements and Dimensional Change of the Pullout Specimens (Concrete Con-B). See Figure 5-2 for the Locations of the Measurements (A–D)**

Specimen		Height (mm)								Volume (mm³)
		A	B	C	D	Avg.	Standard deviation	Min.	Max.	
B9R	Before irradiation	61.631	61.589	61.102	61.542	61.466	0.245	61.102	61.631	307065.3908
B7R		60.191	60.544	60.502	60.416	60.413	0.157	60.191	60.544	301864.8309
B4R		60.154	60.133	60.238	60.265	60.197	0.064	60.133	60.265	301439.4262
B9R	Post irradiation	60.672	60.733	60.448	60.655	60.627	0.124	60.448	60.733	303087.2252
B7R		60.347	60.360	60.101	60.530	60.334	0.177	60.101	60.530	301412.6435
B4R		60.138	60.182	60.236	60.302	60.214	0.071	60.138	60.302	301911.9888
B9R	Change	-1.6%	-1.4%	-1.1%	-1.4%	-1.4%	0.2%	-1.6%	-1.1%	-1.1%
B7R		0.3%	-0.3%	-0.7%	0.2%	-0.1%	0.4%	-0.7%	0.3%	0.2%
B4R		0.0%	0.1%	0.0%	0.1%	0.0%	0.1%	0.0%	0.1%	0.1%

**Table 6-2 Pre- and Post-Irradiation Diameter and Mass Measurements and Dimensional Change of the Pullout Specimens (Concrete Con-B). See Figure 5-2 for the Locations of the Measurements (-35 through -5)**

Specimen		Diameter (mm)					Sd. Dev.	Min.	Max.	Mass (g)
		-35	-25	-15	-5	Avg.				
B9R	Before irradiation	39.910	39.925	39.881	39.793	39.877	0.059	39.793	39.925	187.9813
B7R		39.914	39.902	39.889	39.818	39.881	0.043	39.818	39.914	185.7755
B4R		39.951	39.933	39.965	39.848	39.924	0.053	39.848	39.965	186.7832
B9R	Post irradiation	39.938	39.945	39.855	39.828	39.891	0.059	39.828	39.945	187.31
B7R		39.923	39.928	39.893	39.765	39.877	0.076	39.765	39.928	185.15
B4R		39.979	39.935	39.964	39.922	39.950	0.026	39.922	39.979	186.21
B9R	Change	0.1%	0.0%	-0.1%	0.1%	<b>0.0%</b>	0.1%	-0.1%	0.1%	<b>-0.4%</b>
B7R		0.0%	0.1%	0.0%	-0.1%	<b>0.0%</b>	0.1%	-0.1%	0.1%	<b>-0.3%</b>
B4R		0.1%	0.0%	0.0%	0.2%	<b>0.1%</b>	0.1%	0.0%	0.2%	<b>-0.3%</b>

**Table 6-3 Pre- and Post-Irradiation Height and Volume Measurements and Dimensional Change of the Pullout Specimens (Concrete Con-A). See Figure 5-2 for the Locations of the Measurements (A – D)**

Specimen		Height (mm)					Standard Deviation	Min.	Max.	Volume (mm <sup>3</sup> )
		A	B	C	D	Avg.				
A6R	Before irradiation	59.454	59.651	59.597	59.606	59.577	0.085	59.454	59.651	298231.5124
A3R		61.478	61.247	61.599	61.197	61.380	0.190	61.197	61.599	306853.173
A2R		61.460	61.388	61.322	61.354	61.381	0.059	61.322	61.460	307324.8638
A6R	Post irradiation	59.242	59.617	59.620	59.569	59.512	0.182	59.242	59.620	297427.6961
A3R		60.715	60.922	60.644	60.388	60.667	0.220	60.388	60.922	303932.5011
A2R		60.497	60.595	60.642	60.490	60.556	0.075	60.490	60.642	303218.531
A6R	Change	-0.4%	-0.1%	0.0%	-0.1%	<b>-0.1%</b>	0.2%	-0.4%	0.0%	<b>0.0%</b>
A3R		-1.2%	-0.5%	-1.6%	-1.3%	<b>-1.2%</b>	0.4%	-1.6%	-0.5%	<b>-0.5%</b>
A2R		-1.6%	-1.3%	-1.1%	-1.4%	<b>-1.3%</b>	0.2%	-1.6%	-1.1%	<b>-1.1%</b>

**Table 6-4 Pre- and Post-Irradiation Diameter and Mass Measurements and Dimensional Change of the Pullout Specimens (Concrete Con-A). See Figure 5-2 for the Locations of the Measurements (-5 through -35)**

Specimen		Diameter (mm)								Mass (g)
		-35	-25	-15	-5	Avg.	Std. dev.	Min.	Max.	
A6R	Before irradiation	39.901	39.918	39.983	39.868	39.918	0.048	39.868	39.983	189.7755
A3R		39.920	39.903	39.938	39.804	39.891	0.060	39.804	39.938	194.6458
A2R		39.912	39.929	39.970	39.875	39.921	0.039	39.875	39.970	192.1854
A6R	Post irradiation	39.898	39.944	39.877	39.823	39.885	0.050	39.823	39.944	188.83
A3R		39.968	39.945	39.971	39.851	39.934	0.056	39.851	39.971	194.05
A2R		39.895	39.940	39.965	39.892	39.923	0.036	39.892	39.965	191.53
A6R	Change	0.0%	0.1%	-0.3%	-0.1%	-0.1%	0.1%	-0.3%	0.1%	-0.5%
A3R		0.1%	0.1%	0.1%	0.1%	0.1%	0.0%	0.1%	0.1%	-0.3%
A2R		0.0%	0.0%	0.0%	0.0%	0.0%	0.0%	0.0%	0.0%	-0.3%

**Table 6-5 Pre- and Post-Irradiation Height, Mass and Volume Measurements, and Dimensional Change of the Donut Specimens (Concrete Con-B). See Figure 5-2 for the Locations of the Measurements (\* – \*\*\*\*)**

Specimen		Height (mm)							Mass (g)	Volume (mm <sup>3</sup> )	
		Height *	Height **	Height ***	Height ****	Average	Std. Dev.	Min.			Max.
B8D	Before irradiation	40.651	40.533	40.623	40.751	40.640	0.090	40.533	40.751	111.0386	51751.053
B4D		39.224	39.305	39.593	39.515	39.409	0.173	39.224	39.593	106.7844	48712.877
B3D		40.126	39.993	39.787	39.918	39.956	0.142	39.787	40.126	110.8039	49957.074
B8D	Post irradiation	40.096	40.300	40.021	39.799	40.054	0.207	39.799	40.300	110.38	50289.402
B4D		40.232	39.459	39.327	40.114	39.783	0.456	39.327	40.232	106.14	49633.611
B3D		39.960	40.037	40.066	39.948	40.003	0.058	39.948	40.066	110.08	50159.96
B8D	Change	-1.4%	-0.6%	-1.5%	-2.3%	-1.4%	0.7%	-2.3%	-0.6%	-0.6%	-2.8%
B4D		2.6%	0.4%	-0.7%	1.5%	1.0%	1.4%	-0.7%	2.6%	-0.6%	1.9%
B3D		-0.4%	0.1%	0.7%	0.1%	0.1%	0.5%	-0.4%	0.7%	-0.7%	0.4%

**Table 6-6 Pre- and Post-Irradiation Diameter Measurements and Dimensional Change of the Donut Specimens (Concrete Con-B). See Figure 5-2 for the Locations of the Measurements (-12 through -48)**

Specimen		Diameter (mm)						Average	Std. dev.	Min.	Max.
		-12	-30	-48	-12	-30	-48				
B8D	Before irradiation	39.945	39.992	39.990	39.826	39.728	39.815	39.896	0.108	39.728	39.992
B4D		39.956	39.973	39.965	39.866	39.919	39.914	39.936	0.040	39.866	39.973
B3D		39.847	39.899	39.892	39.803	39.773	39.973	39.843	0.072	39.773	39.973
B8D	Post irradiation	40.029	39.999	39.931	39.807	39.793	39.795	39.912	0.108	39.793	40.029
B4D		39.954	39.957	39.912	39.919	39.906	39.844	39.929	0.041	39.844	39.957
B3D		39.912	39.902	39.841	39.975	39.923	39.892	39.911	0.044	39.841	39.975
B8D	Change	0.2%	0.0%	-0.1%	0.0%	0.2%	-0.1%	<b>0.0%</b>	0.1%	-0.1%	0.2%
B4D		0.0%	0.0%	-0.1%	0.1%	0.0%	-0.2%	<b>0.0%</b>	0.1%	-0.2%	0.1%
B3D		0.2%	0.0%	-0.1%	0.4%	0.4%	-0.2%	<b>0.2%</b>	0.3%	-0.2%	0.4%

**Table 6-7 Pre- and Post-Irradiation Height, Mass and Volume Measurements and Dimensional Change of the Donut Specimens (Concrete Con-A). See Figure 5-2 for the Locations of the Measurements (1-4)**

Specimen		Height (mm)							Mass (g)	Volume (mm <sup>3</sup> )
		Height 1	Height 2	Height 3	Height 4	Average	Std. Dev.	Min.	Max.	
A6D	Before irradiation	39.881	39.607	39.292	39.569	39.587	0.241	39.292	39.881	110.0498
A10D		38.973	39.185	39.008	38.800	38.992	0.158	38.800	39.185	109.4351
A11D		39.597	39.486	39.401	39.508	39.498	0.081	39.401	39.597	110.8011
A6D	Post irradiation	39.132	39.219	39.181	39.046	39.144	0.075	39.046	39.219	109.25
A10D		39.647	39.576	39.575	39.646	39.611	0.041	39.575	39.647	108.63
A11D		39.472	39.584	39.624	39.522	39.550	0.067	39.472	39.624	110.22
A6D	Change	-1.9%	-1.0%	-0.3%	<b>-1.3%</b>	-1.1%	0.7%	-1.9%	-0.3%	<b>-0.7%</b>
A10D		1.7%	1.0%	1.5%	<b>2.2%</b>	1.6%	0.5%	1.0%	2.2%	<b>-0.7%</b>
A11D		-0.3%	0.2%	0.6%	<b>0.0%</b>	0.1%	0.4%	-0.3%	0.6%	<b>0.3%</b>

**Table 6-8 Pre- and Post-Irradiation Diameter Measurements and Dimensional Change of the Donut Specimens (Concrete Con-A). See Figure 5-2 for the Locations of the Measurements (-5 through -25)**

Specimen		Diameter (mm)						
		-5	-15	-25	Average	Std. dev.	Min	Max
A6D	Before irradiation	39.934	39.949	39.873	39.919	0.040	39.873	39.949
A10D		39.926	39.952	39.840	39.906	0.059	39.840	39.952
A11D		39.937	39.967	39.910	39.938	0.029	39.910	39.967
A6D	Post irradiation	39.970	40.004	39.940	39.971	0.032	39.940	40.004
A10D		39.964	39.988	39.926	39.959	0.031	39.926	39.988
A11D		40.046	40.024	39.842	39.971	0.112	39.842	40.046
A6D	Change	0.1%	0.1%	0.2%	<b>0.1%</b>	0.0%	0.1%	0.2%
A10D		0.1%	0.1%	0.2%	<b>0.1%</b>	0.1%	0.1%	0.2%
A11D		0.3%	0.1%	-0.2%	<b>0.1%</b>	0.2%	-0.2%	0.3%

**Table 6-9 Pre- and Post-Irradiation Height Measurements and Dimensional Change of the Aggregate Specimens**

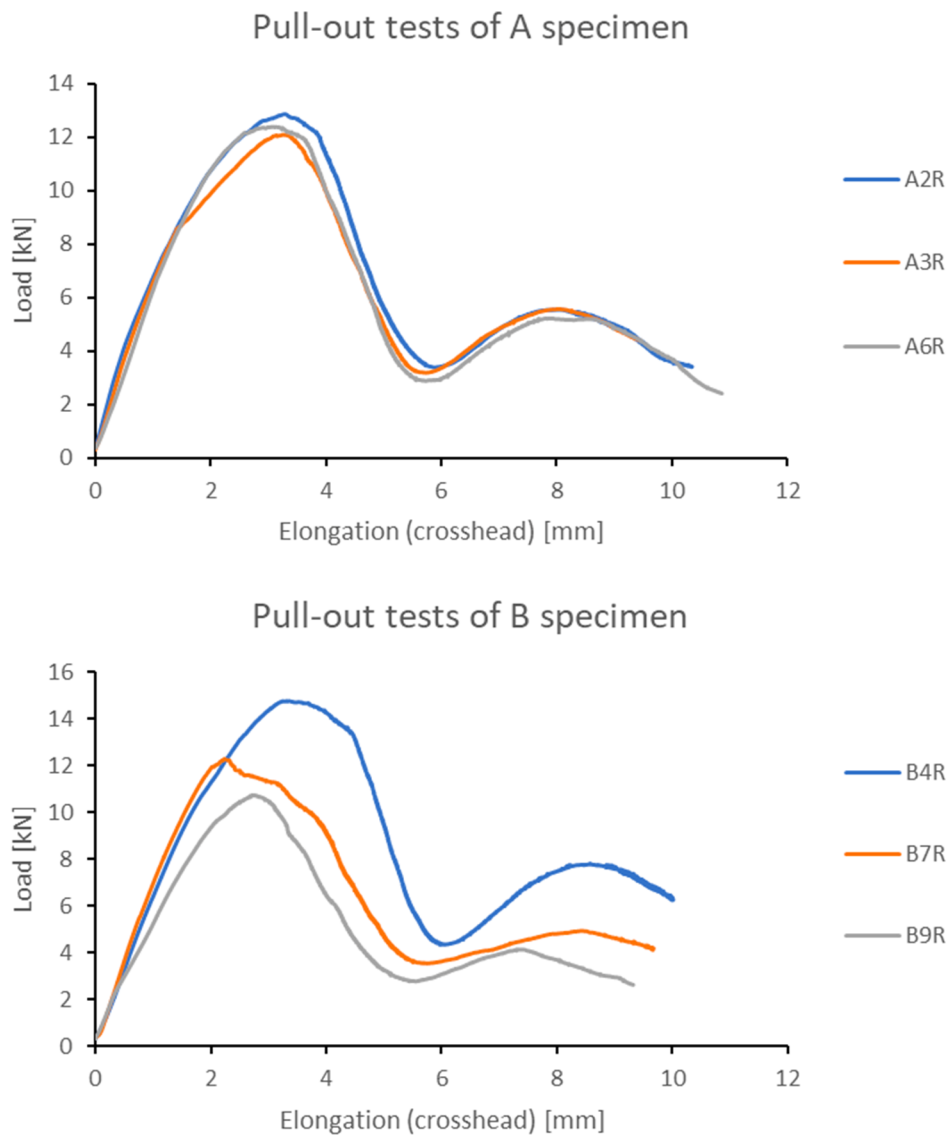
Specimen		Height 1	Height 2	Height 3	Height 4	Height 5	Average height	St. dev. height
E43	Before irradiation	9.653	9.653	9.658	9.669	9.681	9.663	0.011
E44		9.853	9.869	9.874	9.880	9.889	9.873	0.012
F43		9.934	9.967	9.936	9.913	9.927	9.936	0.018
F44		9.858	9.895	9.916	9.923	9.897	9.898	0.023
E43	Post irradiation	9.652	9.648	9.637	9.671	9.686	9.659	0.017
E44		9.865	9.856	9.861	9.888	9.889	9.872	0.014
F43		9.935	9.965	9.947	9.922	9.933	9.940	0.015
F44		9.860	9.915	9.928	9.922	9.903	9.906	0.024
E43	Change	0.0%	-0.1%	-0.2%	0.0%	0.0%	<b>0.0%</b>	0.1%
E44		0.1%	-0.1%	-0.1%	0.1%	0.0%	<b>0.0%</b>	0.1%
F43		0.0%	0.0%	0.1%	0.1%	0.1%	<b>0.0%</b>	0.0%
F44		0.0%	0.2%	0.1%	0.0%	0.1%	<b>0.1%</b>	0.1%

**Table 6-10 Pre- and Post-Irradiation Diameter Measurements and Dimensional Change of the Aggregate Specimens**

Specimen		Diameter 1	Diameter 2	Diameter 3	Diameter 4	Diameter 5	Average diameter	St. dev. diameter	Volume
<b>E43</b>	Before irradiation	9.731	9.776	9.767	9.766	9.735	9.755	0.018	722.189
<b>E44</b>		9.891	9.885	9.877	9.919	9.915	9.897	0.017	759.586
<b>F43</b>		9.658	9.663	9.680	9.688	9.664	9.671	0.011	729.776
<b>F44</b>		9.760	9.801	9.788	9.791	9.785	9.785	0.014	744.302
<b>E43</b>	Post irradiation	9.754	9.757	9.761	9.771	9.742	9.757	0.009	722.158
<b>E44</b>		9.941	9.902	9.876	9.893	9.923	9.907	0.023	760.991
<b>F43</b>		9.662	9.682	9.700	9.694	9.666	9.681	0.015	731.672
<b>F44</b>		9.777	9.793	9.800	9.798	9.785	9.791	0.009	745.760
<b>E43</b>	change	0.2%	-0.2%	-0.1%	0.1%	0.1%	<b>0.0%</b>	0.1%	<b>0.0%</b>
<b>E44</b>		0.5%	0.2%	0.0%	-0.3%	0.1%	<b>0.1%</b>	0.2%	<b>0.2%</b>
<b>F43</b>		0.0%	0.2%	0.2%	0.1%	0.0%	<b>0.1%</b>	0.1%	<b>0.3%</b>
<b>F44</b>		0.2%	-0.1%	0.1%	0.1%	0.0%	<b>0.1%</b>	0.1%	<b>0.2%</b>

## 6.4 Bond Tests

Figure 6-12 shows the main results of the pullout tests. Data are presented as the measured pullout force against the displacement of the press cross bar. The displacement of the cross bar which results from the bar slippage, the bar and concrete deformation and possibly some deformation of the test rig, is not to be confused with the rebar slip which is measured directly by LVDTs measuring the displacement of the bar end relative to the surface of the concrete. The corresponding LVDT measurements are discussed in the interpretation Chapter 10, p. 10-1. The load-displacement curves are very consistent for the three tests conducted on the Con-A specimens. The peak load was measured as  $12.4 \pm 0.3$  kN. Results are more scattered for the pullout test conducted on the Con-B specimens. The maximum load measured on specimen B04R reached 14.8 kN, whereas the maximum loads for specimens B07R and B09R are approximately 10.5 kN and 12 kN. Slipping failure mode was observed for all specimens.



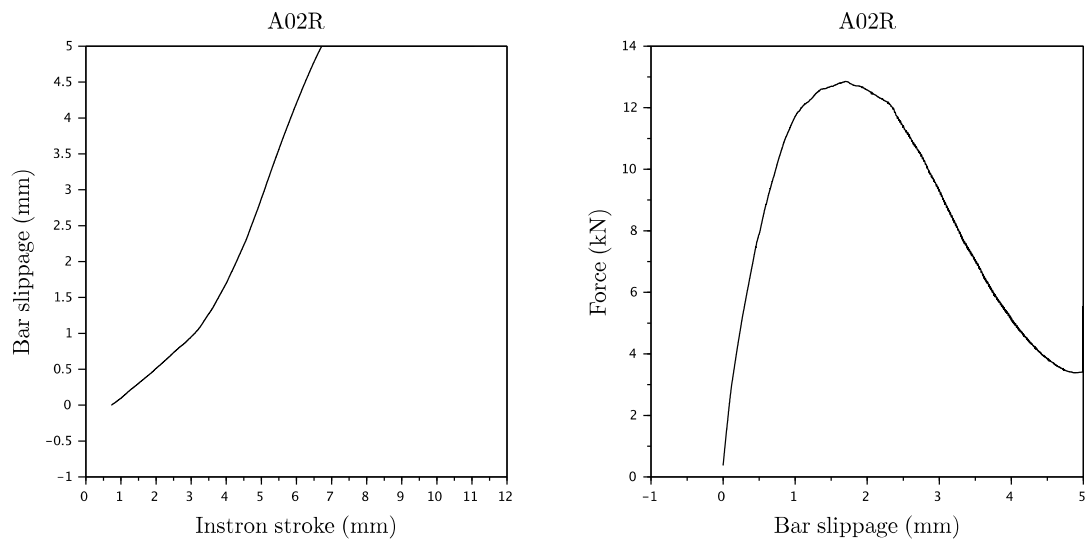
**Figure 6-12 Results of the Pullout Tests Conducted on Irradiated Specimens A and B**

The complete results of the bond pullout tests are presented in Figure 6-13 through Figure 6-18 for each specimen. The bar slippage corresponds to the differential displacement measured between the free (unloaded) end of the steel reinforcement and the surface of the concrete. The left-hand figures show the bar slippage as a function of the machine stroke. The right-hand figures show the force as a function of bar slippage. The maximum forces and slippages recorded during these tests are reported in Table 6-11.

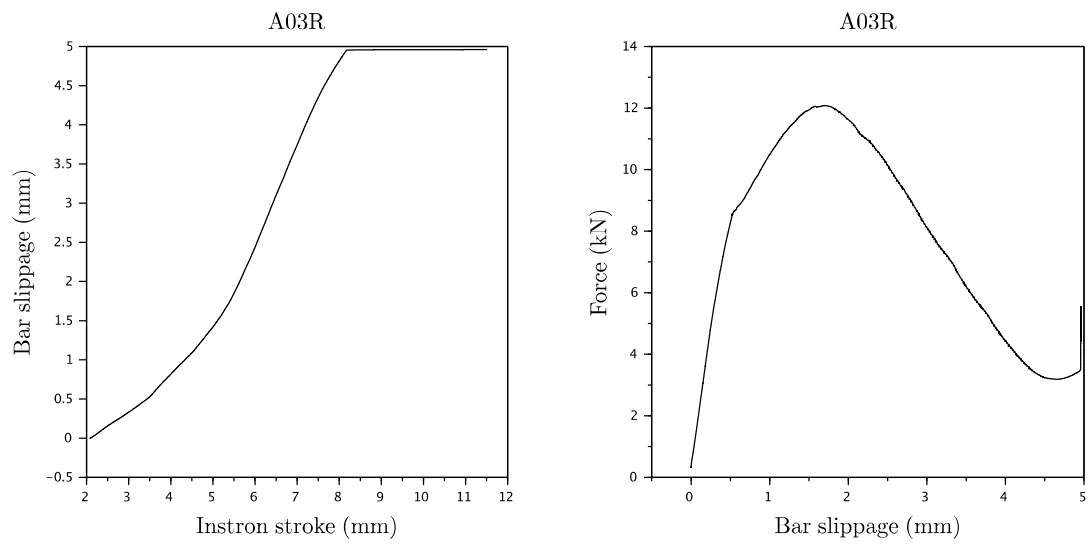


**Table 6-11 Maximum Bond Force and Corresponding Slippage Recorded on the Irradiated Pullout Specimens**

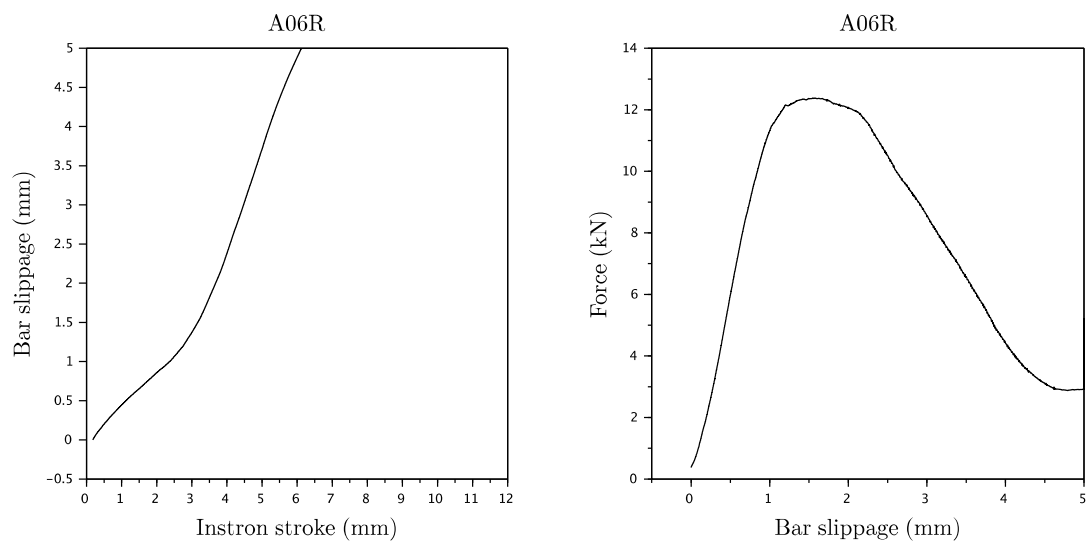
Specimen	Max. force (kN)	Slippage at peak force (mm)
02R	12.9	1.70
03R	12.1	1.69
06R	12.4	1.54
B04R	14.8	1.41
B07R	12.3	0.95
B09R	10.7	1.45



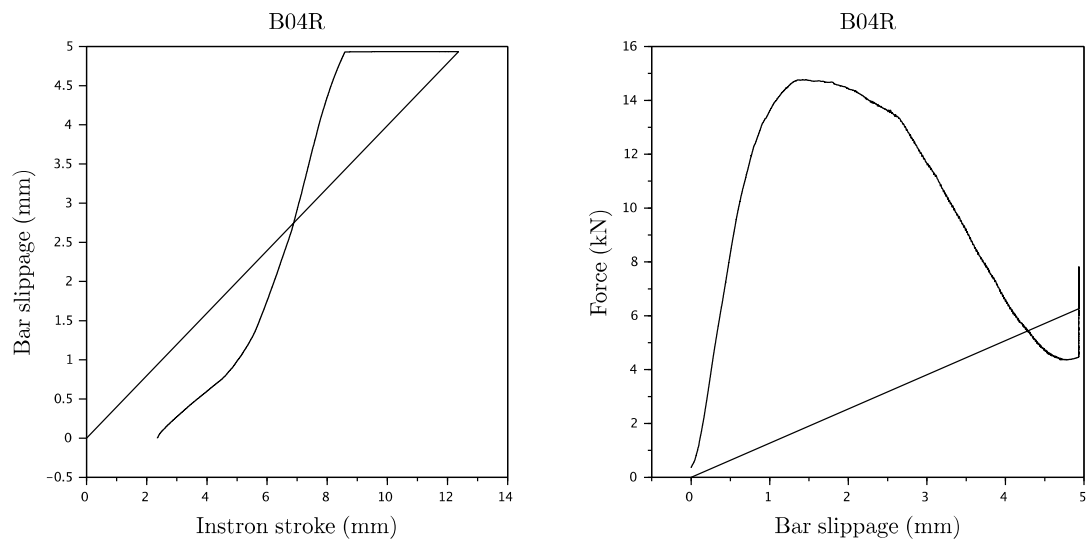
**Figure 6-13 Bond Test Results Obtained on Irradiated Specimen A02R**



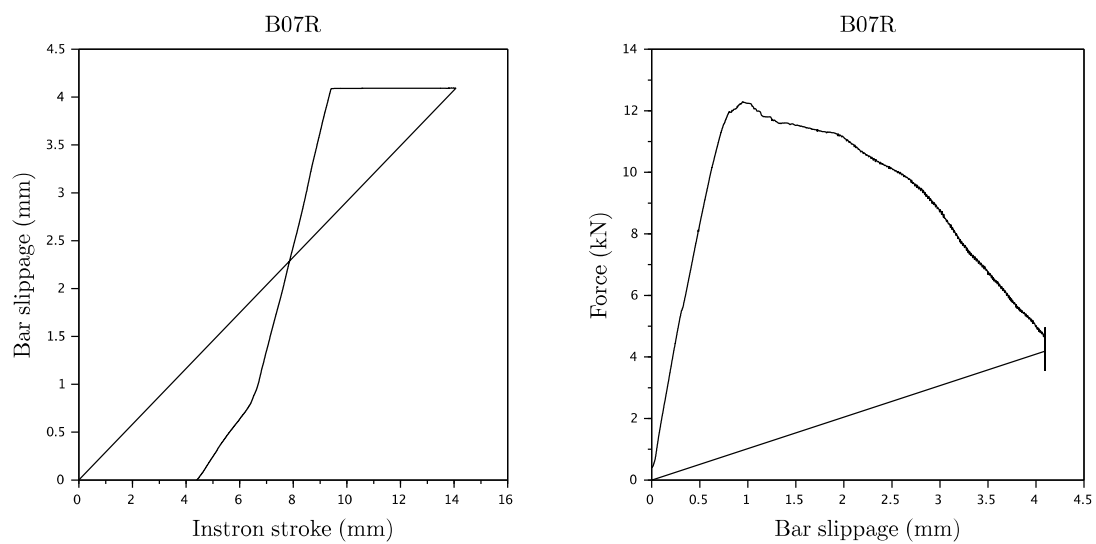
**Figure 6-14 Bond Test Results Obtained on Irradiated Specimen A03R**



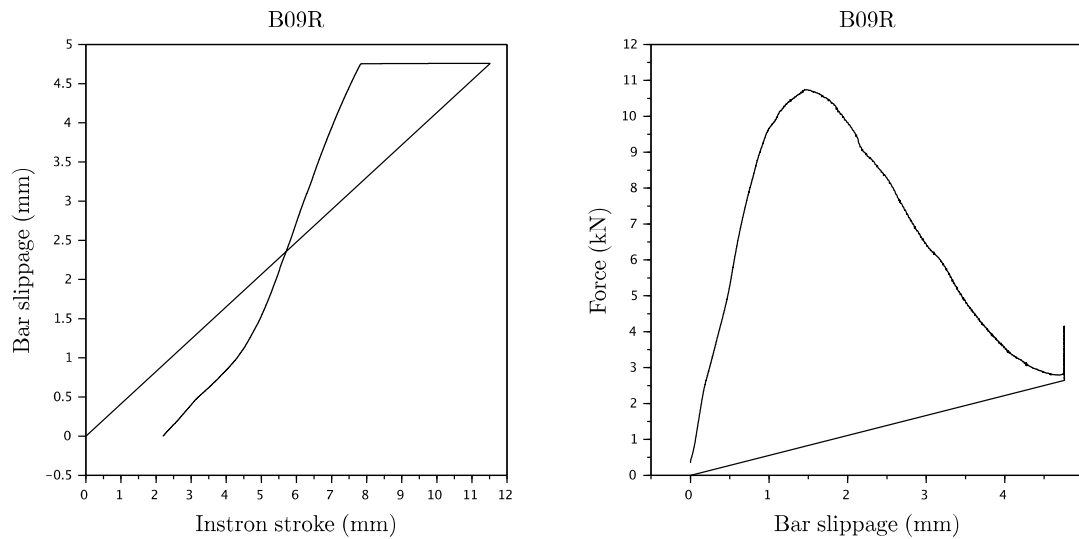
**Figure 6-15 Bond Test Results Obtained on Irradiated Specimen A06R**



**Figure 6-16 Bond Test Results Obtained on Irradiated Specimen B04R**



**Figure 6-17 Bond Test Results Obtained on Irradiated Specimen B07R**



**Figure 6-18 Bond Test Results Obtained on Irradiated Specimen B09R**

## 6.5 Splitting Tests

The results of the splitting tests are presented in Table 6-12. The apparent tensile stress,  $\sigma_t$ , is calculated as  $\sigma_t = 2F/\pi A$ , where  $F$  and  $A$  are the applied force and the concrete cross-section area (1,280 mm<sup>2</sup> for the full donut specimen, and 640 mm<sup>2</sup> for the half donut specimens as described in Section 5.4).

**Table 6-12 Results of the Splitting Tests for the Irradiated Specimens**

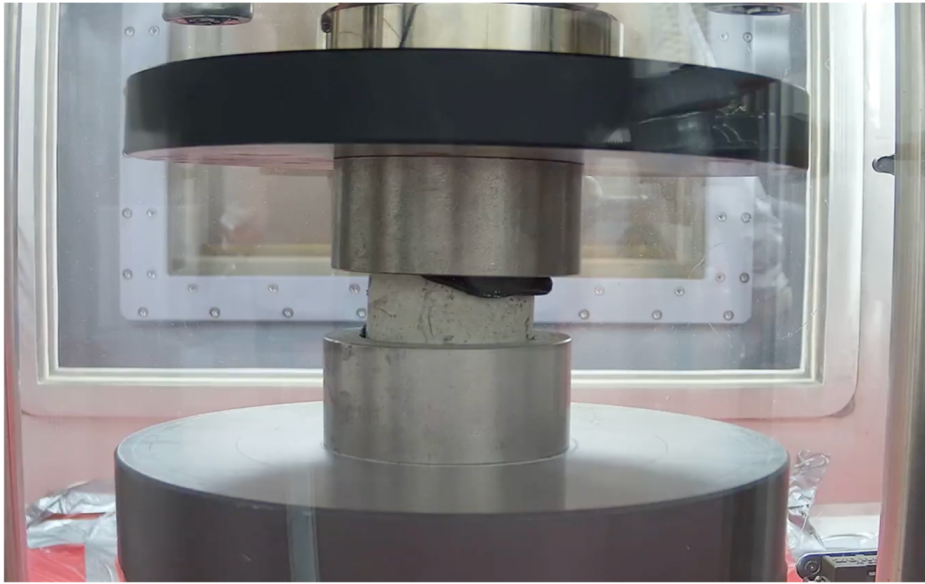
	F [kN] (full)	$t_s$ [MPa] (full)	F [kN] (half)	$t_s$ [MPa] (half)
A11D	10.1	7.9	4.8 / 5.2	7.5 / 8.1
B08D	12.7	9.9	6.3 / 4.4	9.8 / 6.9

*F*: splitting force

: estimated splitting strength

## 6.6 Compression Tests

The failure mode of specimens A06D, A10D and B03D was asymmetric. The specimens appeared to gradually tilt, and the neoprene bulged outside of the steel cap. Figure 6-19 illustrates this observation (specimen A06D). After the formation of the first visible crack, the load vs. stroke curve still exhibits a hardening mode. This indicates that the obtained data are not reliable for specimens A06D, A10D, and B03D. The first cracks were observed at ~130 kN, 137 kN, and 130 kN, respectively. Those values are much higher than the expected target of approximately 100 kN. The failure for specimen B04D occurred at 104 kN, with the first visible crack at 103 kN, and the failure mode was that of a crushing compression. The data are considered reliable and are comparable with the failure loads measured on the room temperature and heat-cured specimens.



**Figure 6-19** Compression Test of Specimen A06D in CVR Hot-Cell. Snapshot Taken Close to the End of the Test Showing Neoprene Bulging and the Tilting of the Specimen

## 7 POST HEAT CURING TESTING

### 7.1 Dimension and Mass Changes

The dimension and mass measurements of the specimens cured at irradiation temperature at ORNL are reported in Table 7-1 through Table 7-6. The heights of the pullout specimens were not measured. The main results are summarized below:

1. The mass loss of the donut and pullout specimens is consistent between the specimens made of aggregate GA(F) and GB(E), ranging between -0.4% and -0.5%. The mass change of specimen B11R made of aggregate GB(E) appears to be an anomaly.
2. The diameter and height changes of the donut specimens made of aggregate GA(F) range between 0 and 0.1% (expansion) and 0 and 0.4%, respectively.
3. The diameter changes of the donut specimens made of aggregate GB(E) are consistently approximately -0.1% (contraction).
4. The height changes of the donut specimens made of aggregate GB(E) range between 0 and 0.1% (expansion).
5. The diameter and height changes of the pullout specimens made of aggregate GA(F) and GB(E) range between 0 and 0.1%

**Table 7-1 Pre- and Post-Heat Curing Diameter and Measurements and Changes of the Pullout Specimens (Concrete Con-A Made of GA(F) Aggregates).  
See Figure5-2 for the Locations of the Measurements (\* – \*\*\*\*)**

Specimen		Diameter (mm)				Average	Std. dev.	Min.	Max.	Mass (g)
		*	**	***	****					
A01R	Before irradiation	39.819	39.726	39.844	39.751	39.785	0.056	39.726	39.844	193.86
A07R		39.810	39.819	39.836	39.776	39.810	0.025	39.776	39.836	192.9
A09R		39.556	39.726	39.556	39.734	39.643	0.100	39.556	39.734	195.67
A01R	Post irradiation	39.844	39.751	39.853	39.751	39.800	0.056	39.751	39.853	193
A07R		39.810	39.844	39.853	39.759	39.817	0.042	39.759	39.853	192
A09R		39.573	39.785	39.539	39.810	39.677	0.140	39.539	39.810	194.8
A01R	Change	0.1%	0.1%	0.0%	0.0%	0.0%	0.0%	0.0%	0.1%	-0.4%
A07R		0.0%	0.1%	0.0%	0.0%	0.0%	0.0%	0.0%	0.1%	-0.5%
A09R		0.0%	0.1%	0.0%	0.2%	0.1%	0.1%	0.0%	0.2%	-0.4%

**Table 7-2 Pre- and Post-Heat Curing Diameter and Measurements and Changes of the Pullout Specimens (Concrete Con-B Made of GB(E) Aggregates). See Figure 5-2 for the Locations of the Measurements (\* – \*\*\*\*)**

Specimen		Diameter (mm)				Average	Std. dev.	Min.	Max.	Mass (g)
		*	**	***	****					
B02R	Before heating	39.886	39.378	39.886	39.285	39.609	0.322	39.285	39.886	187.18
B03R		39.895	39.345	39.954	39.311	39.626	0.346	39.311	39.954	185.75
B11R		39.912	39.751	39.997	39.607	39.817	0.173	39.607	39.997	193.64
B02R	Post heating	39.819	39.395	39.870	39.438	39.630	0.248	39.395	39.870	186.2
B03R		39.912	39.353	39.912	39.336	39.628	0.328	39.336	39.912	184.8
B11R		39.979	39.743	39.988	39.624	39.833	0.180	39.624	39.988	190.2
B02R	Change	-0.2%	0.0%	0.0%	0.4%	<b>0.1%</b>	0.2%	-0.2%	0.4%	<b>-0.5%</b>
B03R		0.0%	0.0%	-0.1%	0.1%	<b>0.0%</b>	0.1%	-0.1%	0.1%	<b>-0.5%</b>
B11R		0.2%	0.0%	0.0%	0.0%	<b>0.0%</b>	0.1%	0.0%	0.2%	<b>-1.8%</b>

**Table 7-3 Pre- and Post-Heat Curing Diameter Measurements and Dimensional Changes of the Donut Specimens (Concrete Con-A). See Figure 5-2 for the Locations of the Measurements (\* – \*\*\*\*)**

Specimen		Diameter (mm)				Average	Std. dev.	Min.	Max.
		*	**	***	****				
A03D	Before heating	39.878	39.878	39.895	39.878	39.882	0.008	39.878	39.895
A05D		39.903	39.920	39.886	39.912	39.906	0.014	39.886	39.920
A09D		39.861	39.946	39.861	39.954	39.906	0.051	39.861	39.954
A03D	Post heating	39.878	39.844	39.870	39.861	39.863	0.014	39.844	39.878
A05D		39.903	39.997	39.937	39.937	39.944	0.039	39.903	39.997
A09D		39.903	39.988	39.912	39.963	39.942	0.041	39.903	39.988
A03D	Change	0.0%	-0.1%	-0.1%	0.0%	<b>0.0%</b>	0.0%	-0.1%	0.0%
A05D		0.0%	0.2%	0.1%	0.1%	<b>0.1%</b>	0.1%	0.0%	0.2%
A09D		0.1%	0.1%	0.1%	0.0%	<b>0.1%</b>	0.0%	0.0%	0.1%

**Table 7-4 Pre- and Post-Heat Curing Height and Mass Measurements and Changes of the Donut Specimens (Concrete Con-A). See Figure 5-2 for the Locations of the Measurements (\* – \*\*\*\*)**

Specimen		Diameter (mm)								Mass (g)
		Height *	Height **	Height ***	Height ****	Average	Std. dev.	Min.	Max.	
A03D	Before heating	39.751	39.268	39.446	39.700	39.541	0.226	39.268	39.751	110.48
A05D		39.776	39.726	39.599	39.599	39.675	0.090	39.599	39.776	111
A09D		39.497	39.268	39.446	39.700	39.478	0.178	39.268	39.700	111.27
A03D	Post heating	39.726	39.700	39.624	39.675	39.681	0.043	39.624	39.726	110
A05D		39.827	39.802	39.700	39.700	39.757	0.067	39.700	39.827	110.4
A09D		39.548	39.345	39.548	39.700	39.535	0.146	39.345	39.700	110.7
A03D	Change	-0.1%	1.1%	0.5%	-0.1%	<b>0.4%</b>	0.6%	-0.1%	1.1%	<b>-0.4%</b>
A05D		0.1%	0.2%	0.3%	0.3%	<b>0.2%</b>	0.1%	0.1%	0.3%	<b>-0.5%</b>
A09D		0.1%	0.2%	0.3%	0.0%	<b>0.1%</b>	0.1%	0.0%	0.3%	<b>-0.5%</b>

**Table 7-5 Pre- and Post-Heat Curing Diameter Measurements and Changes of the Donut Specimens (Concrete Con-B). See Figure 5-2 for the Locations of the Measurements (\* – \*\*\*\*)**

Specimen		Diameter (mm)							
		*	**	***	****	Average	Std. dev.	Min.	Max.
B05D	Before heating	39.937	39.878	39.946	39.759	39.880	0.086	39.759	39.946
B06D		39.937	39.776	39.965	39.810	39.872	0.093	39.776	39.965
B09D		39.946	39.802	39.946	39.810	39.876	0.081	39.802	39.946
B05D	Post heating	39.912	39.785	39.886	39.785	39.842	0.067	39.785	39.912
B06D		39.886	39.751	39.937	39.734	39.827	0.100	39.734	39.937
B09D		39.895	39.759	39.937	39.743	39.834	0.097	39.743	39.937
B05D	Change	-0.1%	-0.2%	-0.1%	0.1%	<b>-0.1%</b>	0.1%	-0.2%	0.1%
B06D		-0.1%	-0.1%	-0.1%	-0.2%	<b>-0.1%</b>	0.1%	-0.2%	-0.1%
B09D		-0.1%	-0.1%	0.0%	-0.2%	<b>-0.1%</b>	0.1%	-0.2%	0.0%



**Table 7-6 Pre- and Post-Heat Curing Height and Mass Measurements and Changes of the Donut Specimens (Concrete Con-B). See Figure 5-2 for the Locations of the Measurements (\* – \*\*\*\*)**

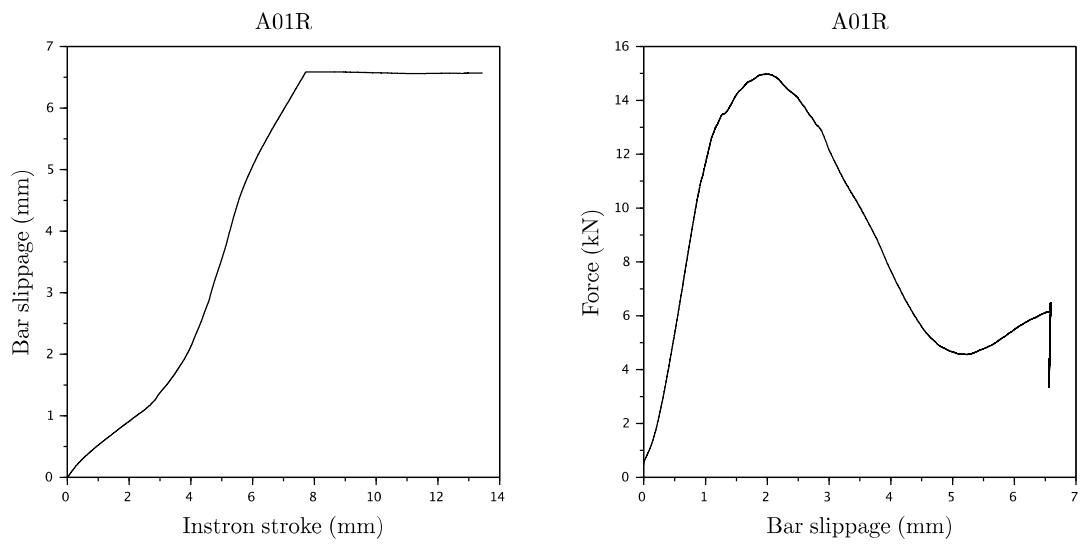
Specimen		Height (mm)				Average	Std. Dev.	Min.	Max.	Mass (g)
		Height *	Height **	Height ***	Height ****					
B05D	Before heating	40.030	40.030	39.751	39.751	39.891	0.161	39.751	40.030	108.9
B06D		40.208	40.589	40.488	40.183	40.367	0.203	40.183	40.589	110.47
B09D		39.776	39.700	39.649	39.649	39.694	0.060	39.649	39.776	109.16
B05D	Post heating	40.005	40.030	39.751	39.726	39.878	0.162	39.726	40.030	108.4
B06D		40.259	40.564	40.488	40.284	40.399	0.150	40.259	40.564	109.9
B09D		39.751	39.700	39.649	39.675	39.694	0.043	39.649	39.751	108.7
B05D	Change	-0.1%	0.0%	0.0%	-0.1%	0.0%	0.0%	-0.1%	0.0%	-0.5%
B06D		0.1%	-0.1%	0.0%	0.3%	0.1%	0.1%	-0.1%	0.3%	-0.5%
B09D		-0.1%	0.0%	0.0%	0.1%	0.0%	0.1%	-0.1%	0.1%	-0.4%

## 7.2 Bond Tests

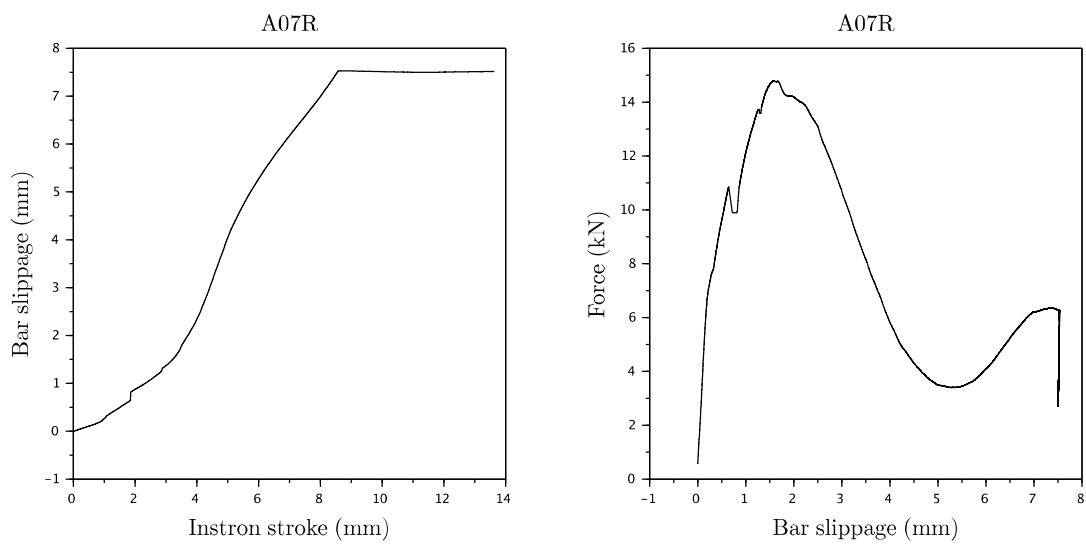
The results of the bond pullout tests are presented in Figure 7-1 through Figure 7-6 for each specimen. The bar slippage corresponds to the differential displacement measured between the free (unloaded) end of the steel reinforcement and the surface of the concrete. The left-hand figures show the bar slippage as a function of the machine stroke. The right-hand figures show the force as a function of bar slippage. The maximum forces and slippages recorded during these tests are reported in Table 7-7.

**Table 7-7 Maximum Bond Force and Corresponding Slippage Recorded on the Pullout Specimens Cured at Irradiation Temperature**

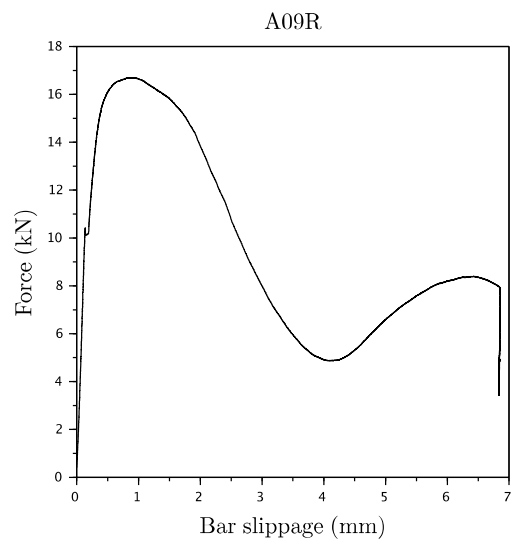
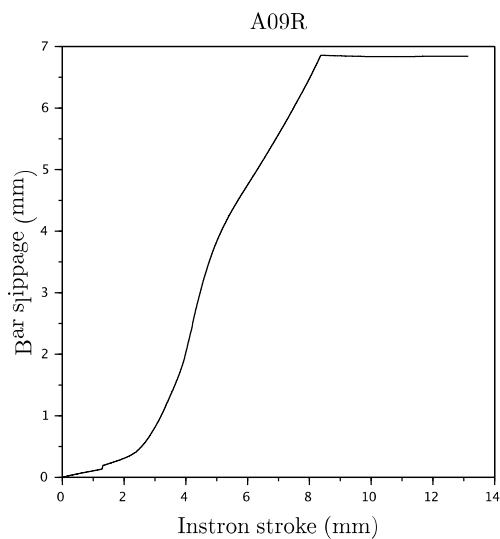
Specimen	Max. force (kN)	Slippage at peak force (mm)
A01R	15.0	1.98
A07R	14.8	1.57
A09R	16.7	0.92
B02R	13.5	1.49
B03R	9.2	1.11
B11R	3.6	1.38



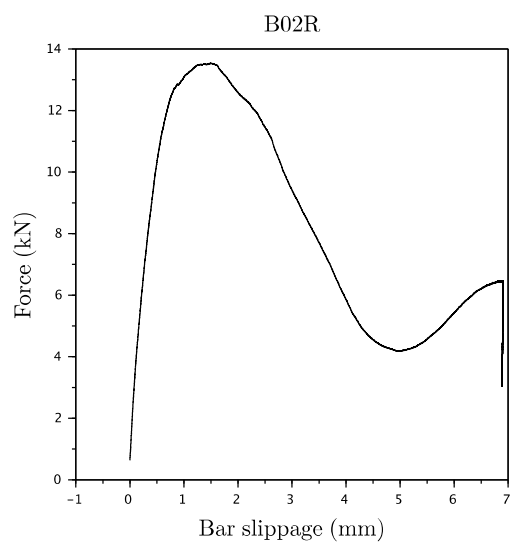
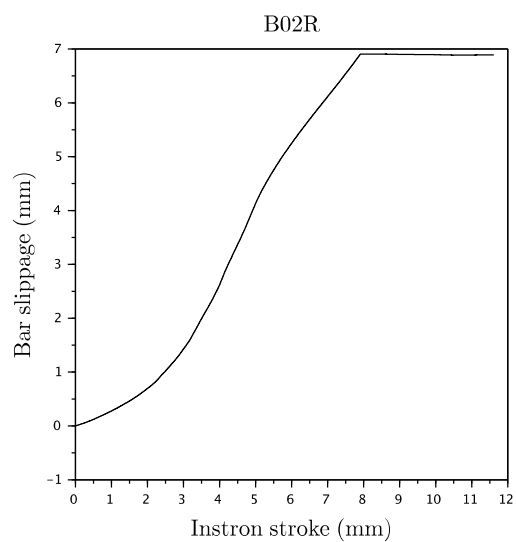
**Figure 7-1 Bond Test Results Obtained on Specimen A01R Cured at Irradiation Temperature**



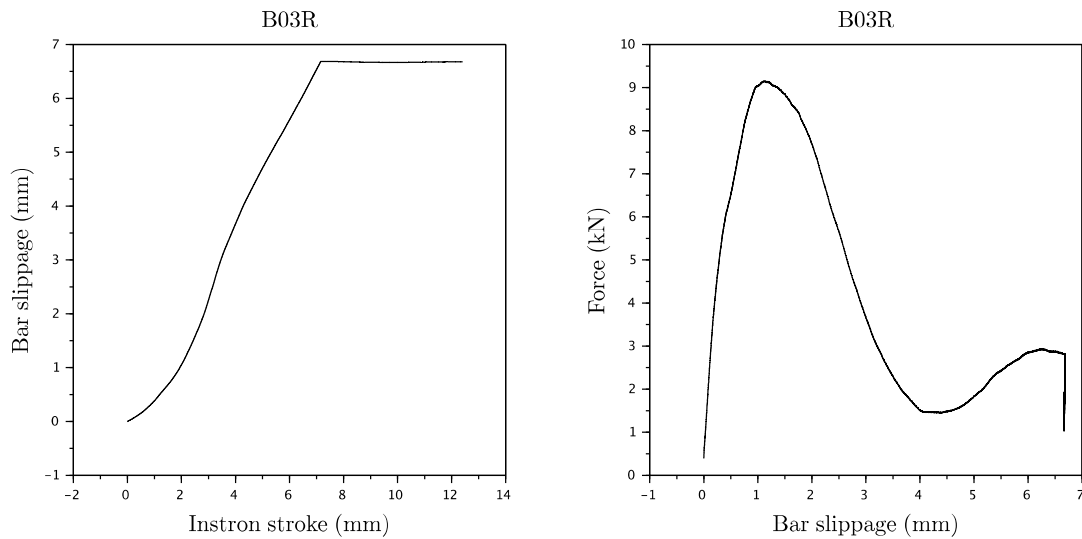
**Figure 7-2 Bond Test Results Obtained on Specimen A07R Cured at Irradiation Temperature**



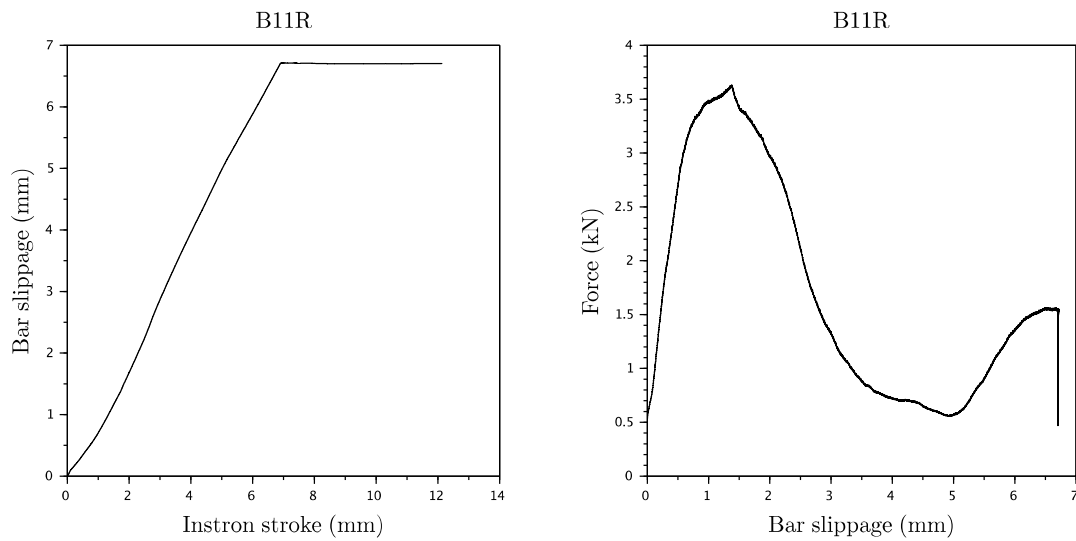
**Figure 7-3 Bond Test Results Obtained on Specimen A09R Cured at Irradiation Temperature**



**Figure 7-4 Bond Test Results Obtained on Specimen B02R Cured at Irradiation Temperature**



**Figure 7-5 Bond Test Results Obtained on Specimen B03R Cured at Irradiation Temperature**



**Figure 7-6 Bond Test Results Obtained on Specimen B11R Cured at Irradiation Temperature**

### 7.3 Splitting Tests

The results of the splitting tests are presented in Table 7-8. The apparent tensile stress,  $\sigma_t$ , is calculated as  $\sigma_t = 2F/\pi A$ , where  $F$  and  $A$  are the applied force and the concrete cross-section area, respectively (1,280 mm<sup>2</sup> for the full donut specimen, and 640 mm<sup>2</sup> for the half donut specimens, as described in Section 5.4).

**Table 7-8 Results of the Splitting Tests for the Specimens Cured at Irradiation Temperature**

	<b>F [kN] (full)</b>	<b><math>f_{ts}</math> [MPa] (full)</b>	<b>F [kN] (half)</b>	<b><math>f_{ts}</math> [MPa] (half)</b>
<b>A05D</b>	14.5	11.3	5.1 / 6.9	8.1 / 10.7
<b>B09D</b>	11.4	8.9	5.8 / 7.9	9.0 / 12.3

*F: splitting force*

*$f_{ts}$ : estimated splitting strength*

#### **7.4 Compression Tests**

The results of the compression tests are presented in Table 7-9.

**Table 7-9 Results of the Compression Tests for the Specimens Cured at Irradiation Temperature**

<b>Specimen</b>	<b>F [kN]</b>	<b><math>f_c</math> [MPa]</b>
<b>A03D</b>	105.1	86.1
<b>A09D</b>	120.7	98.9
<b>B05D</b>	107.9	88.4
<b>B06D</b>	119.8	99.1

*F: splitting force*

*$f_c$ : apparent compression strength*

## 8 COLD SPECIMENS TESTING

### 8.1 Dimension and Mass Changes

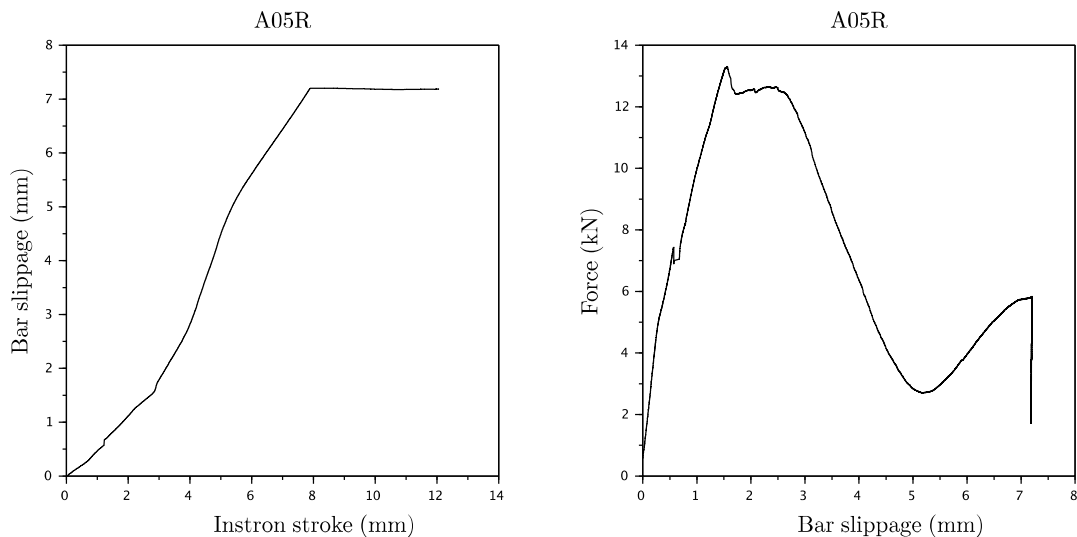
Not assessed.

### 8.2 Bond Tests

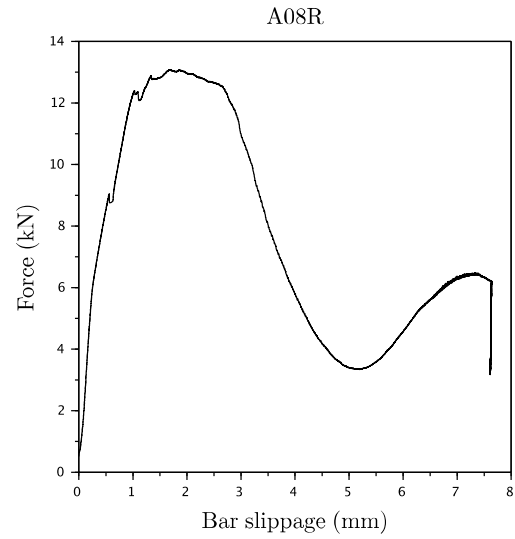
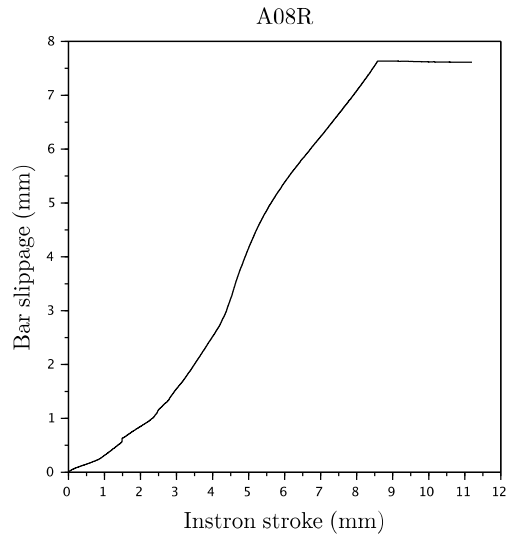
The results of the bond pullout tests are presented in Figure 8-1 through Figure 8-6 for each specimen. The bar slippage corresponds to the differential displacement measured between the free (unloaded) end of the steel reinforcement and the surface of the concrete. The left-hand figures show the bar slippage as a function of the machine stroke. The right-hand figures show the force as a function of bar slippage. The maximum forces and slippages recorded during these tests are reported in Table 8-1.

**Table 8-1 Maximum Bond Force and Corresponding Slippage Recorded on the Pullout Specimens Cured at Room Temperature**

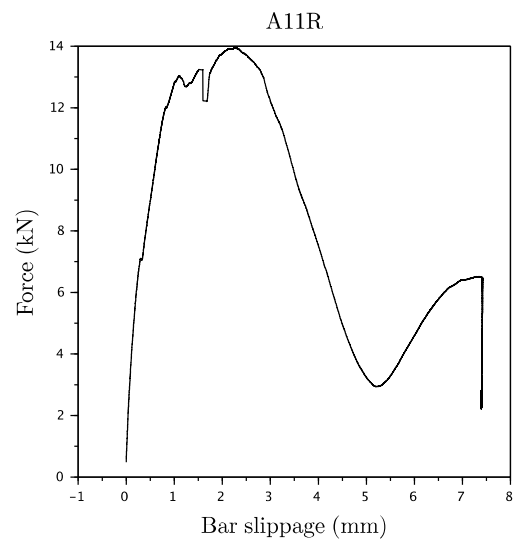
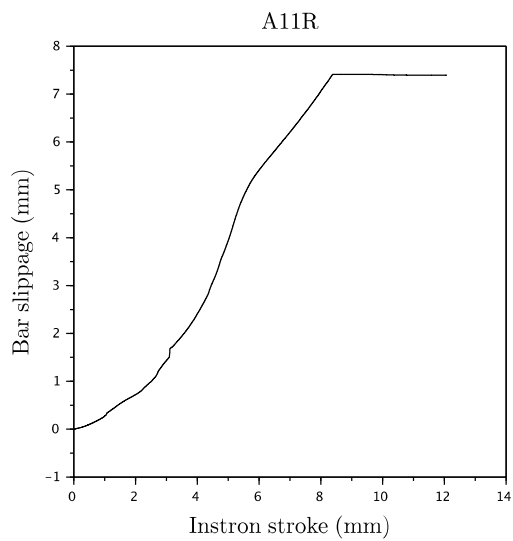
Specimen	Max. force (kN)	Slippage at peak force (mm)
A05R	13.3	1.56
A08R	1	1.70
A11R	14.0	2.27
B01R		0.88
B05R	12.7	0.56
B08R		1.34



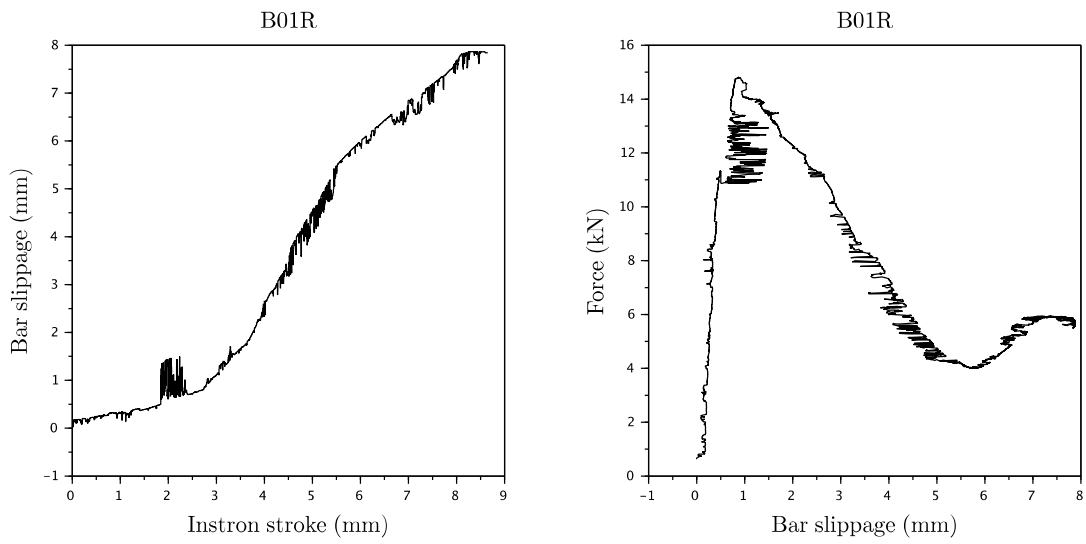
**Figure 8-1 Bond Test Results Obtained on Specimen A05R Cured at Room Temperature**



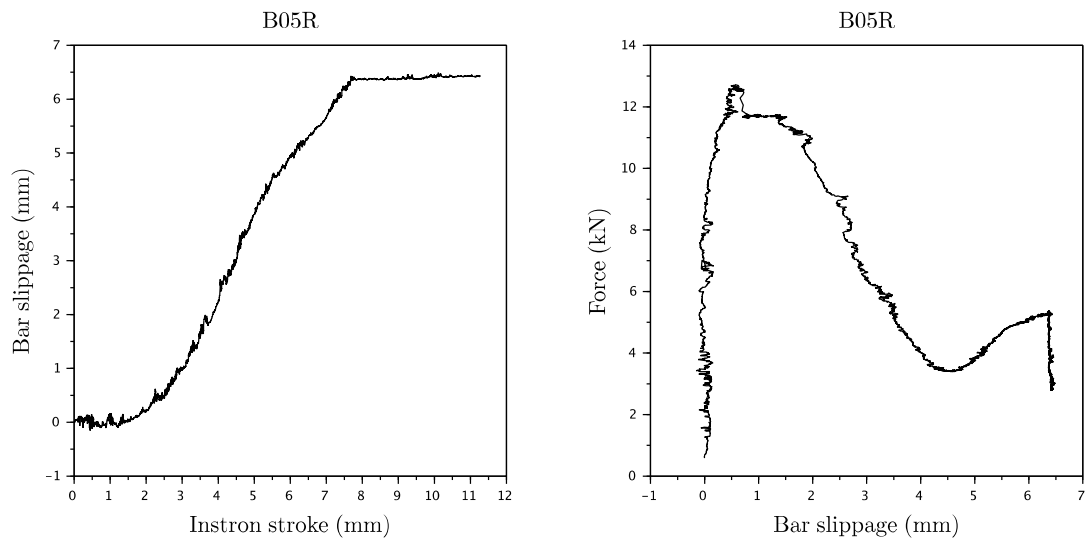
**Figure 8-2 Bond Test Results Obtained on Specimen A08R Cured at Room Temperature**



**Figure 8-3 Bond Test Results Obtained on Specimen A11R Cured at Room Temperature**

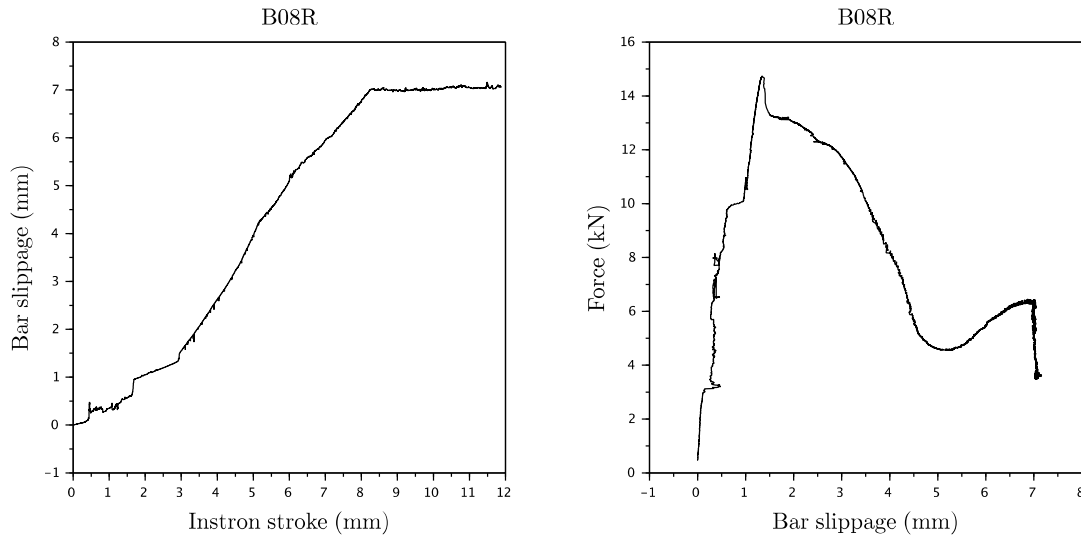


**Figure 8-4 Bond Test Results Obtained on Specimen B01R Cured at Room Temperature**



**Figure 8-5 Bond Test Results Obtained on Specimen B05R Cured at Room Temperature**





**Figure 8-6 Bond Test Results Obtained on Specimen B08R Cured at Room Temperature**

### 8.3 Splitting Tests

The results of the splitting tests are presented in Table 8-2. The apparent tensile stress,  $\sigma_t$ , is calculated as  $\sigma_t = 2F/\pi A$ , where  $F$  and  $A$  are the applied force and the concrete cross-section area (1,280 mm<sup>2</sup> for the full donut specimen and 640 mm<sup>2</sup> for the half donut specimens, as described in Section 5.4).

**Table 8-2 Results of the Splitting Tests for the Specimens Cured at Room Temperature**

	F [kN] (full)	$f_{t,s}$ [MPa] (full)	F [kN] (half)	$f_{t,s}$ [MPa] (half)
<b>A07D</b>	12.2	9.5	4.7 / 8.4	7.3 / 13.1
<b>B07D</b>	7.8	6.1	5.1 / 8.1	8.1 / 12.6

***F*: splitting force**

***f<sub>t,s</sub>*: estimated splitting strength**

#### 8.4 Compression Tests

The results of the compression tests are presented in Table 8-3.

**Table 8-3     Results of the Compression Tests for the Specimens Cured at Room Temperature**

	<b>F [kN]</b>	<b><math>f_c</math> [MPa]</b>
<b>A02D</b>	128.1	105.0
<b>B02D</b>	126.0	103.2
<b>B10D</b>	122.1	100.1

*F*: compression force at failure

$f_c$ : apparent compression strength



## 9 SCALE EFFECTS TESTING

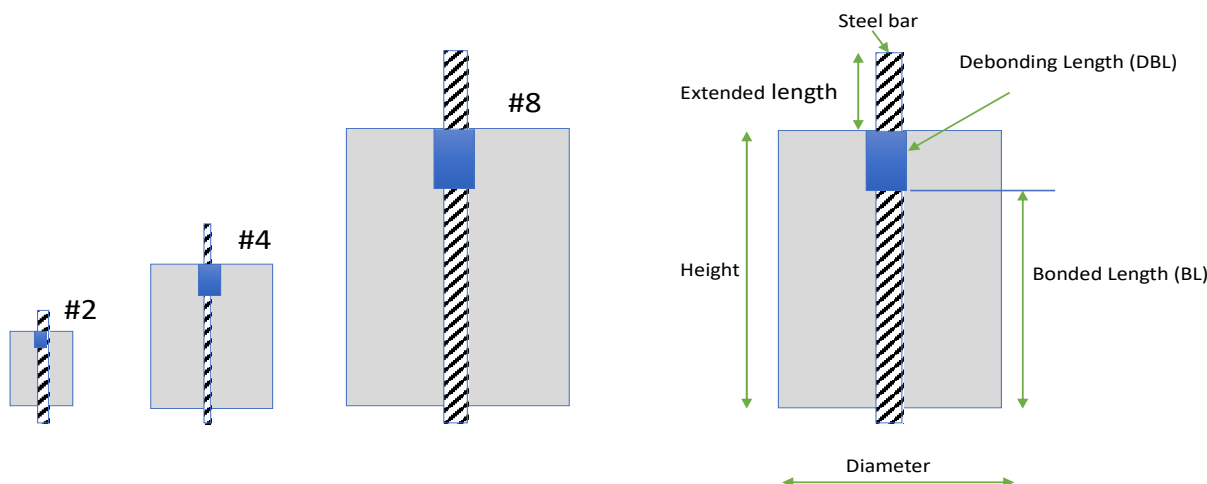
This research was performed in cooperation with the Civil and Environmental Engineering Department of UTK.

### 9.1 Objectives

Irradiation experiment constraints such as the effective neutron flux fields and the risk of adverse irradiation-induced heating led to the choice to limit the diameter of the irradiated specimens to 40 mm and the size of the reinforcement bar to #2 (i.e., ~6 mm). Such a small size brings the significance of the experimental data obtained from mechanical testing into question regarding the actual size of concrete aggregates and the reinforcement dimensions in nuclear facilities. To address this question, a scale effect experimental campaign was designed to test varied combinations of aggregate sizes and reinforcement sizes. The other dimensions of the concrete specimens were directly scaled on the diameter of the reinforcing bar. Three bar sizes were tested: #2 (6.3 mm), #4 (12.7 mm), and #8 (25.4 mm). The dimensions are presented in Table 9-1, and sketches of the different specimen sizes are displayed in Figure 9-1. Because dimensions are scaled according to bar diameter, the pullout specimens are simply referred to as #2, #4 and #8 specimens.

**Table 9-1 Main Dimensions (mm) of the Pullout Specimens for the Scale Effect Campaign**

	Steel bar diameter	Concrete		
		Diameter	Height	Bonded length
#2	6.3	40	60	35
#4	12.	80	12	70
#8	25.4	160	240	140



**Figure 9-1 Sketch Showing the Geometries of the #2, #4, and #8 Specimens**

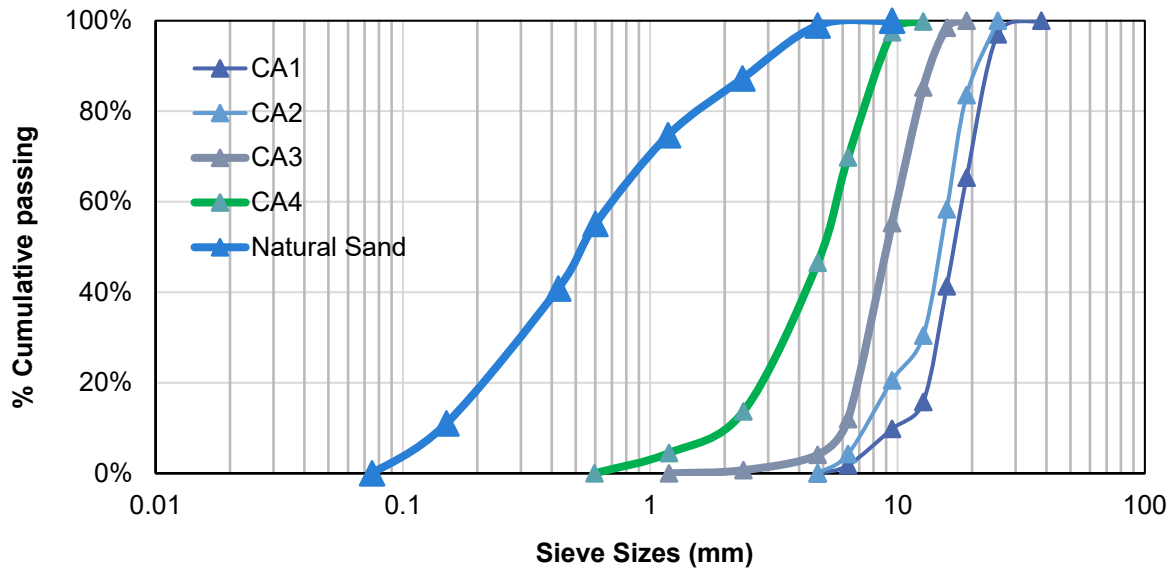
The additional size effect considered in this study is the maximum dimension ( $D_{max}$ ) of the coarse aggregates: here, 0.375 in. (9.5 mm), 0.5 in. (12.7 mm), 0.75 in. (19.0 mm), and 1 in. (25.4 mm). For each pullout specimen size, four concrete mixes were thus prepared to cast three pullout specimens per specimen geometry and maximum aggregate size. The only exception was for the #2 specimens: the thickness of the concrete specimen wall was only 17 mm, making it impossible to use the  $\frac{3}{4}$  in. and 1 in. maximum coarse aggregate sizes.

## 9.2 Materials

### 9.2.1 Concrete Made with Tennessee Aggregate

The nominal maximum aggregate size of GA(F) and GB(E) aggregates for the Con-A and Con-B concrete mixes is 12.5 mm. The proposed scale effects study extended the maximum aggregate size up to 25 mm. The availability of aggregates GA(F) and GB(E) was limited, and sourcing of larger dimensions for these aggregates from Japan is not possible. Therefore, the original Japanese aggregates (JAs) were gradually substituted with local aggregates from Tennessee. Changing the maximum aggregate size affects the entire aggregate gradation and could affect the concrete's mechanical properties. A material study was conducted to determine comparable compressive strengths with the varied mixes.

The ASTM Type I cement used in this study was obtained from Buzzi Unicem USA in Knoxville, Tennessee. The aggregates were obtained from the Rogers Group, Inc., quarry in Oak Ridge, Tennessee. Coarse and fine aggregates were crushed limestone. All the aggregates were stored outdoors in large sacks which were sealed so that no impurities, dust, or rain could infiltrate the contents. Before the aggregates were used, they were dried in an oven at 105 °C for at least 24 h to remove residual moisture. Four different gradations of the coarse aggregates (CAs) were received with nominal maximum aggregate sizes (NMASs) of CA1, NMAS = 1 in. (25.4 mm); CA2, NMAS =  $\frac{3}{4}$  in. (19 mm); CA3, NMAS =  $\frac{1}{2}$  in. (12.7 mm); and CA4, NMAS =  $\frac{3}{8}$  in. (6.3 mm). Results from the sieve analysis shown in Figure 9-2 and the absorption and specific gravity (saturated surface, dry) tests shown in Table 9-2 were obtained in accordance with ASTM C136, and ASTM C127, and ASTM C128, respectively, for all aggregates. The superplasticizer used was a poly-carboxylate type Sika ViscoCrete - 2100 from Sika (density, 1.08 g.cm<sup>-3</sup>).



**Figure 9-2 Sieving Curves of the Fine and Coarse Crushed Limestone Aggregates**

**Table 9-2 Aggregate Absorption Coefficients and Density**

	CA1	CA2	CA3	CA4	Natural sand
<b>Absorption (%)</b>	0.45%	0.44%	0.69%	0.46%	2.98%
<b>Density (g.cm<sup>-3</sup>)</b>	2.92	2	3.00	2.80	2.69

Concrete Con-A mix design is used as the reference mix (Maruyama et al., 2017) for data shown in Table 9-3.

**Table 9-3 Con-A Mix Design**

<b>Water</b>	<b>Cement</b>	<b>Fine aggregate</b>	<b>Coarse aggregate</b>	<b>Water-to-cement ratio (w/c)</b>
<b>lb/yd<sup>3</sup></b> <b>kg/m<sup>3</sup></b>	<b>lb/yd<sup>3</sup></b> <b>kg/m<sup>3</sup></b>	<b>lb/yd<sup>3</sup></b> <b>kg/m<sup>3</sup></b>	<b>lb/yd<sup>3</sup></b> <b>kg/m<sup>3</sup></b>	
309 183	617 366	1,347 799	1,678 995	0.50

A testing plan was designed to evaluate the effect of the four gradations on compressive strength. Two water-to-cement ratio (w/c) ratios were considered: 0.45 and 0.50. With two w/c ratios and four gradations, a total of eight concrete mixes were made, as shown in Table 9-4.

**Table 9-4 Mix Design Testing Matrix**

Mix design	Water lb/yd <sup>3</sup> kg/m <sup>3</sup>	Cement lb/yd <sup>3</sup> kg/m <sup>3</sup>	Fine aggregate lb/yd <sup>3</sup> kg/m <sup>3</sup>	Coarse aggregate lb/yd <sup>3</sup> kg/m <sup>3</sup>	w/c	Coarse aggregate used
CA1-0.45	297 176	657 390	1,347 799	1,842 1,093	0.45	CA1
CA1-0.50	309 183	617 366	1,347 799	1,842 1,093	0.50	CA1
CA2-0.45	297 176	657 390	1,347 799	1,778 1,055	0.45	CA2
CA2-0.50	309 183	617 366	1,347 799	1,778 1,055	0.50	CA2
CA3-0.45	297 176	657 390	1,347 799	1,892 1,122	0.45	CA3
CA3-0.50	309 183	617 366	1,347 799	1,892 1,122	0.50	CA3
CA4-0.45	297 176	657 390	1,347 799	1,766 1,048	0.45	CA4
CA4-0.50	309 183	617 366	1,347 799	1,766 1,048	0.50	CA4

### 9.2.2 Transitioning from Japanese Aggregates to Tennessee Aggregates

To make the transition from Japanese aggregates (JAs) to Tennessee aggregates (TAs), a testing matrix was developed and is shown in Table 9-5 for use in producing pullout samples using #2 size rebar. A set of pullout samples (A-JA-Japanese gradation [JG] and B-JA-JG) was prepared using JAs and gradations for both Con-A and Con-B mix designs.

A second set of pullout samples (A-TA-JG and B-TA-JG) using TAs was prepared using the same mix design as that used in the Japanese gradation. The objective was to evaluate the effect of using different aggregates on the bond strength while keeping all other factors the same.

A third set of pullout samples (A-TA-Tennessee Gradation [TG] and B-TA-TG) using TAs and Tennessee gradation was prepared to complete the transition.

**Table 9-5     Testing Matrix for Transitioning from Japanese to Tennessee Aggregates**

Mix design	Description	Number of pullout specimens
A-JA-JG	Con- <b>A</b> using Japanese <b>A</b> ggregates and Japanese <b>G</b> radation	4
B-JA-JG	Con- <b>B</b> using Japanese <b>A</b> ggregates and Japanese <b>G</b> radation	4
A-TA-JG	Con- <b>A</b> using Tennessee <b>A</b> ggregates and Japanese <b>G</b> radation	4
B-TA-JG	Con- <b>B</b> using Tennessee <b>A</b> ggregates and Japanese <b>G</b> radation	4
A-TA-TG	Con- <b>A</b> using Tennessee <b>A</b> ggregates and Tennessee <b>G</b> radation	4
B-TA-TG	Con- <b>B</b> using Tennessee <b>A</b> ggregates and Tennessee <b>G</b> radation	4

### **9.3     Compression Test and Mix Design Optimization**

#### **9.3.1     Concrete Made with Tennessee Aggregates**

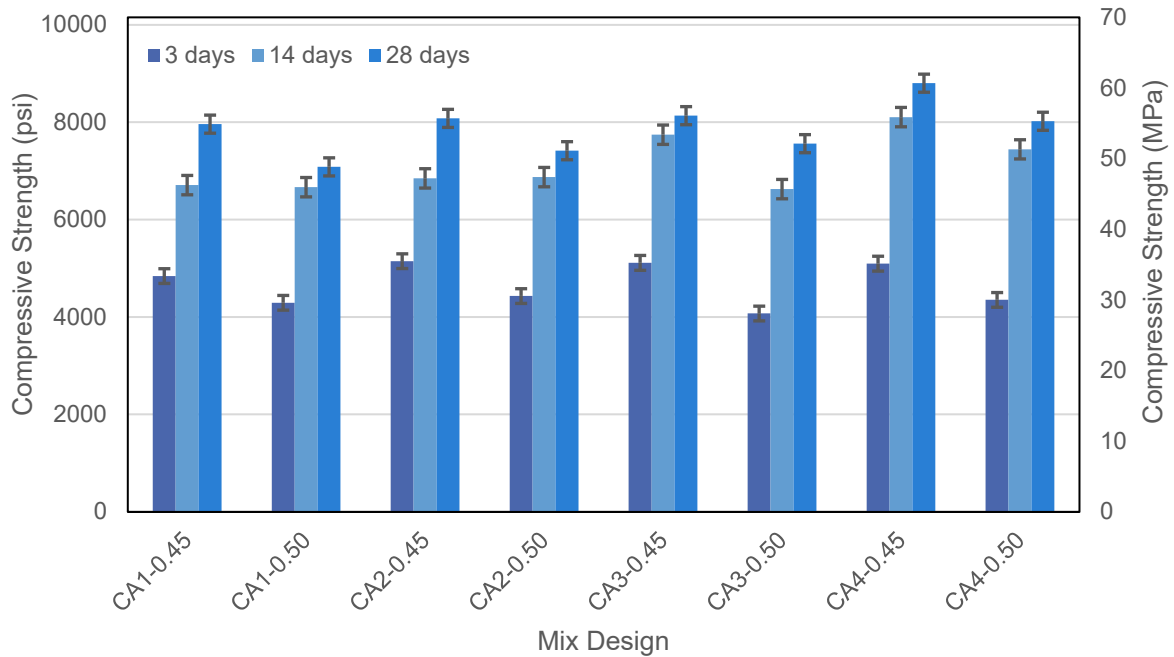
The compressive strength testing was conducted in accordance with ASTM C39 on 4 × 8 in. (100 × 200 mm) concrete cylinders. All cylinders were cured in lime water and tested at 3, 14, and 28 days using a hydraulic compression machine. Prior to testing, the cylinders were sulfur-capped on the top and bottom in accordance with ASTM C617.

The effect of the four gradations on compressive strength is shown in Figure 9-3. For the same gradation, it can be observed that the compressive strength increases as the w/c ratio decreases, as expected. It can also be observed that as the NMAS of the coarse aggregate decreased, the w/c ratio was retained and the compressive strength increased, as shown in Figure 9-4 and Figure 9-5.

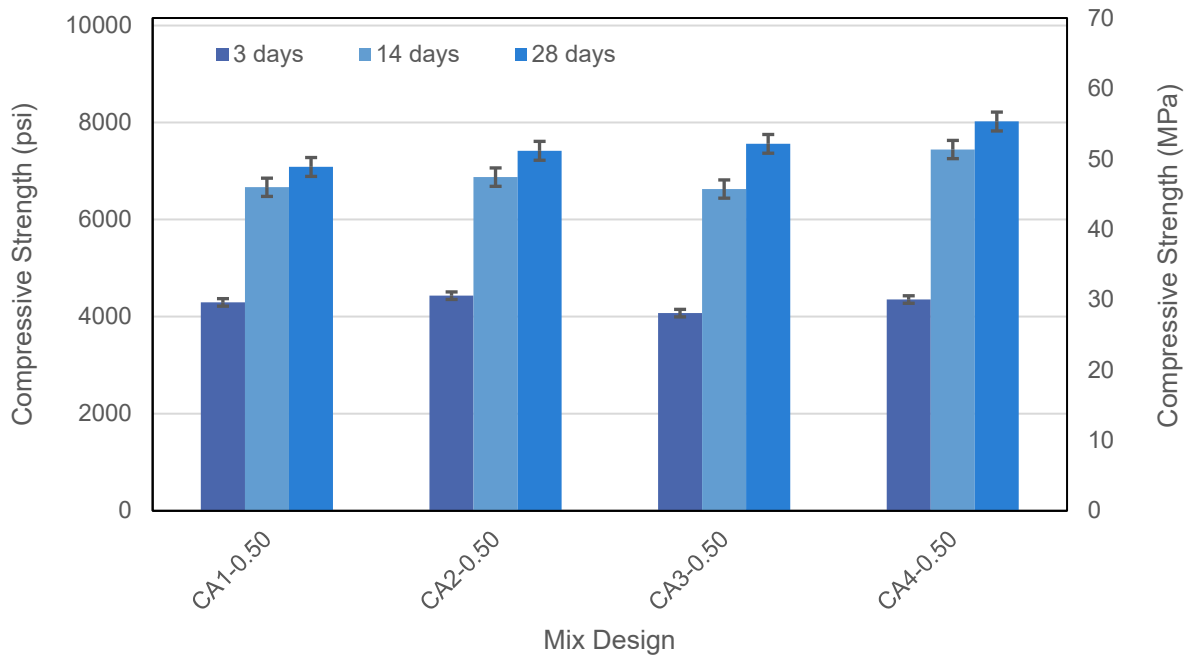
The objective of this study was to obtain comparable 28-day compressive strength using the four aggregate gradations. Based on the experimental results presented in Figure 9-3, the following mix designs were adopted:

- CA1 with w/c = 0.45 (7961.7 psi / 54.9 MPa)
- CA2 with w/c = 0.45 (8077.9 psi / 55.7 MPa)
- CA3 with w/c = 0.45 (8134.0 psi / 56.1 MPa)
- CA4 with w/c = 0.50 (8021.2 psi / 55.2 MPa)

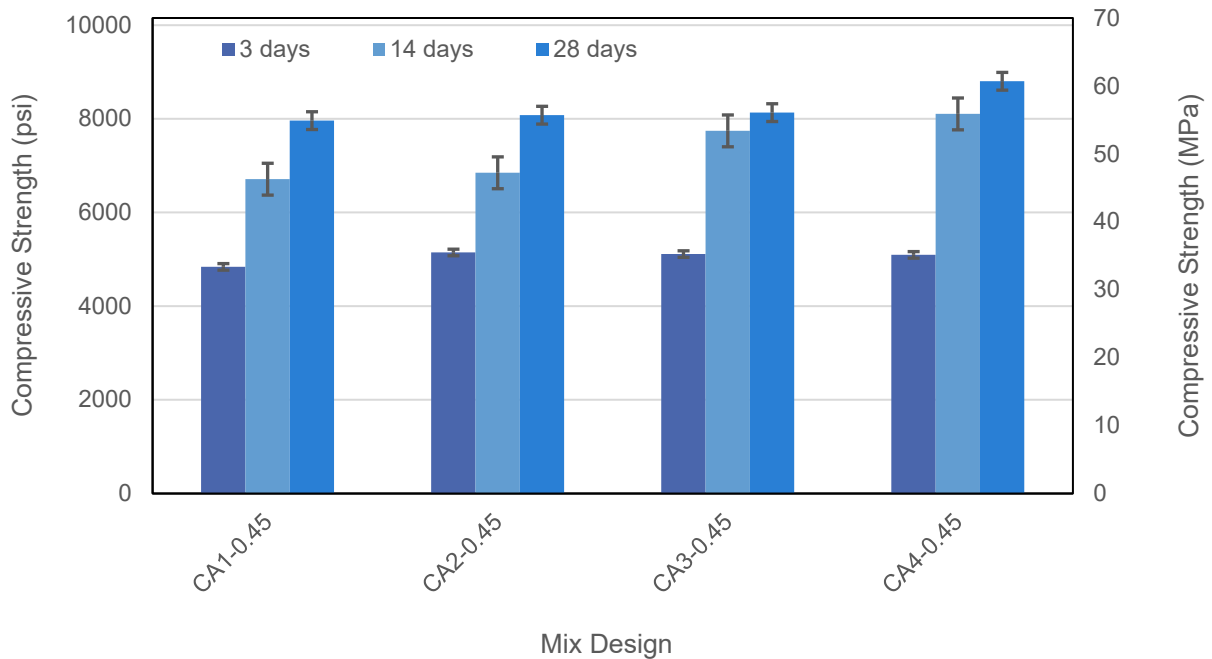




**Figure 9-3 Comparison of the 3-, 7-, and 28-day Compressive Strength for All Studied Mixes**



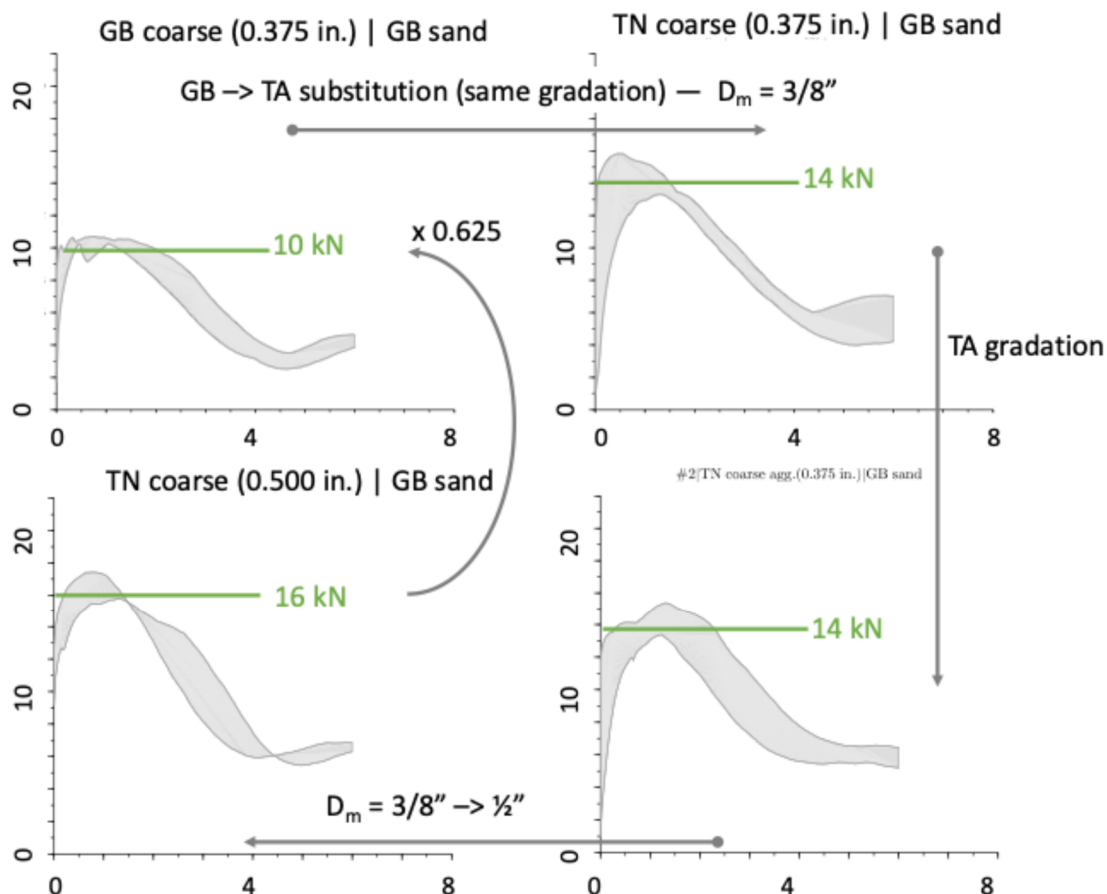
**Figure 9-4 Comparison of the 3-, 7-, and 28-Day Compressive Strength for 0.5 w/c Mixes**



**Figure 9-5 Comparison of the 3-, 7-, and 28-day Compressive Strength for 0.45 w/c Mixes**

#### 9.4 Bond-Test Results

Figure 9-6 summarizes the load vs. slippage obtained during the scale effect campaign for reinforcement bar size (#2) with the maximum aggregate size of 0.375 in. using (1) the Japanese aggregate (top left figure), (2) the Tennessee aggregate using the Japanese aggregate gradation (top right figure), and (3) the Tennessee aggregates with an updated gradation (TA gradation) compatible with larger aggregate size (bottom right figure). Finally, the results for the #2 specimens using 0.5 in. aggregates are presented in the bottom left figure. The most significant change was observed when substituting the Japanese aggregate with the Tennessee aggregate (+4 kN / +40%).



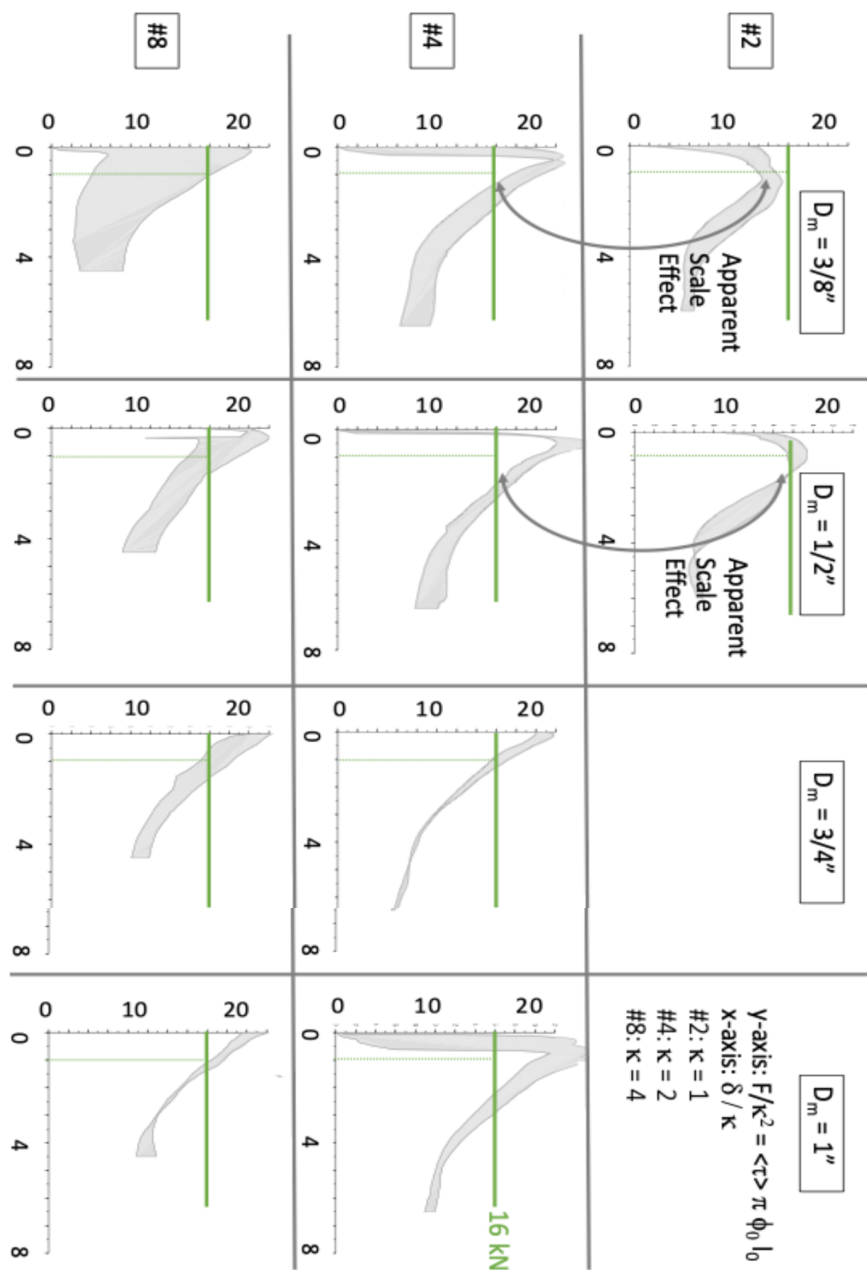
**Figure 9-6 Summary of Bond Test Results of the Scale Effect Campaign Showing Normalized Pullout Force vs. Normalized Slippage for the #2 Specimens (Detailed plots are in Appendix A)**

Figure 9-7 summarizes the normalized load vs. normalized slippage obtained during the scale effect campaign for the three different geometries scaled from the reinforcement bar size (#2, #4 and #8) and the four maximum aggregate sizes (0.375, 0.500, 0.750, and 1.000 in.) using the Tennessee aggregates and gradation. The full-size figures are provided in Appendix A.

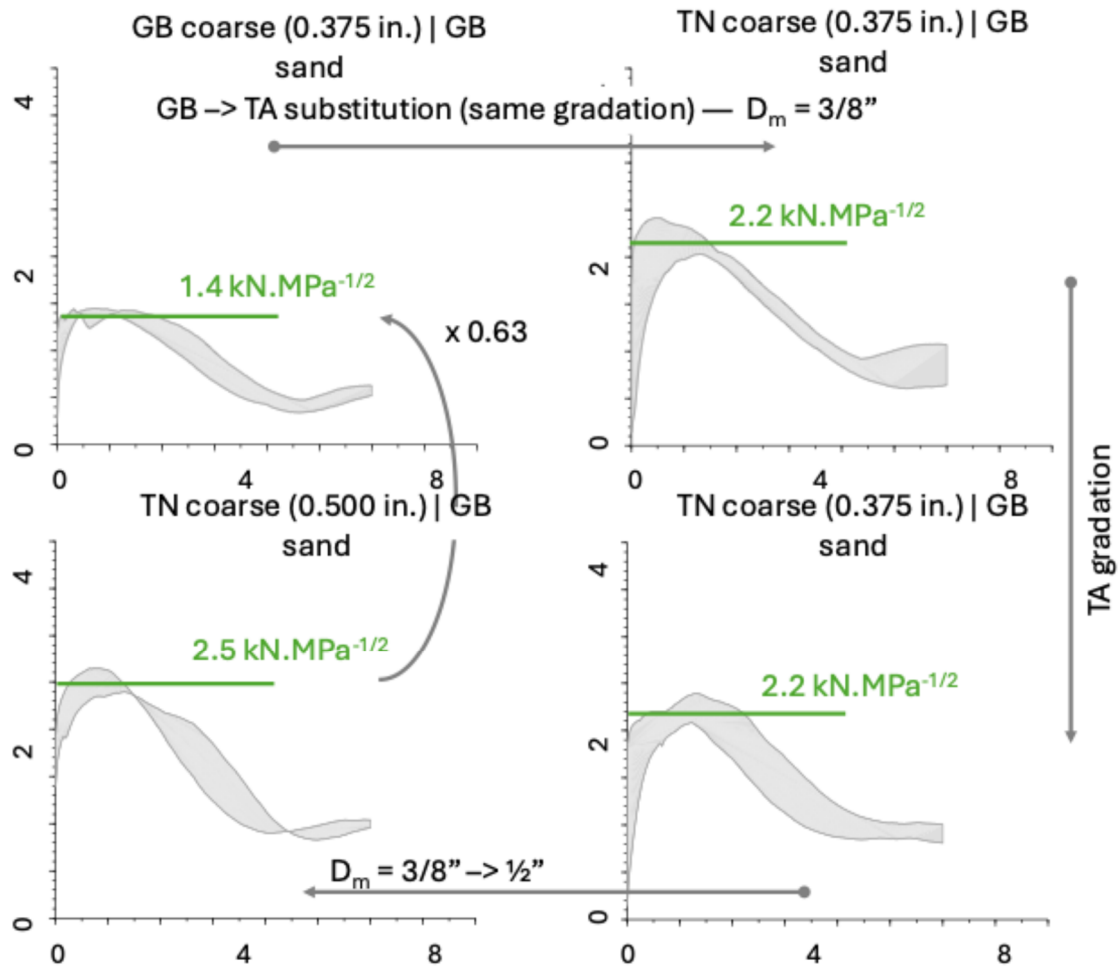
The diameter of the #2 bar is denoted as  $\phi_o$ , and the bonded length for the specimen is denoted as  $l_o$ . Scaling up to #4 ( $\kappa = 2$ ) and #8 ( $\kappa = 4$ ) bar specimens led to an increase in the bonded surface by a multiplying factor of  $\kappa^2$  and an increase in the bonded length by  $\kappa$ . The normalized results are presented as  $F/\kappa^2$  vs.  $\delta/\kappa$ , where  $F$  and  $\delta$  are respectively the measure pulling force and the slippage measured from the displacement difference between the reinforcement and the concrete at the unloaded ends of the specimens. This normalization makes it possible to compare the different test results by eliminating the geometrical characteristics of the specimens and reinforcement. For the sake of visual comparison, the horizontal green bars correspond to  $\frac{F}{\kappa^2} = 16 \text{ kN}$ , and the vertical dashed lines correspond to  $\frac{\delta}{\kappa} = 1 \text{ mm}$ . Axis ranges are identical for all graphs presented as the gray shaded areas between the minimum and maximum forces recorded over three tests for each configuration. Except for one outlier test performed on the #8 specimen with  $\frac{3}{8}$  in. aggregate, the test results for each configuration are

very consistent. The extent of shaded areas is generally quite limited. The possible effect of aggregate size on the normalized force-displacement curves is not clearly apparent in the #4 and #8 specimens. In the #2 specimen, a ~15% increase from ~14 kN to 16 kN is observed between the specimens made of aggregates with  $D_m = \frac{3}{8}$  in. and those made of aggregates with  $D_m = \frac{1}{2}$  in. The most significant scale effect is observed between the #2 and #4 specimens, with an increase in strength of ~6–8 kN (+40%–50%).

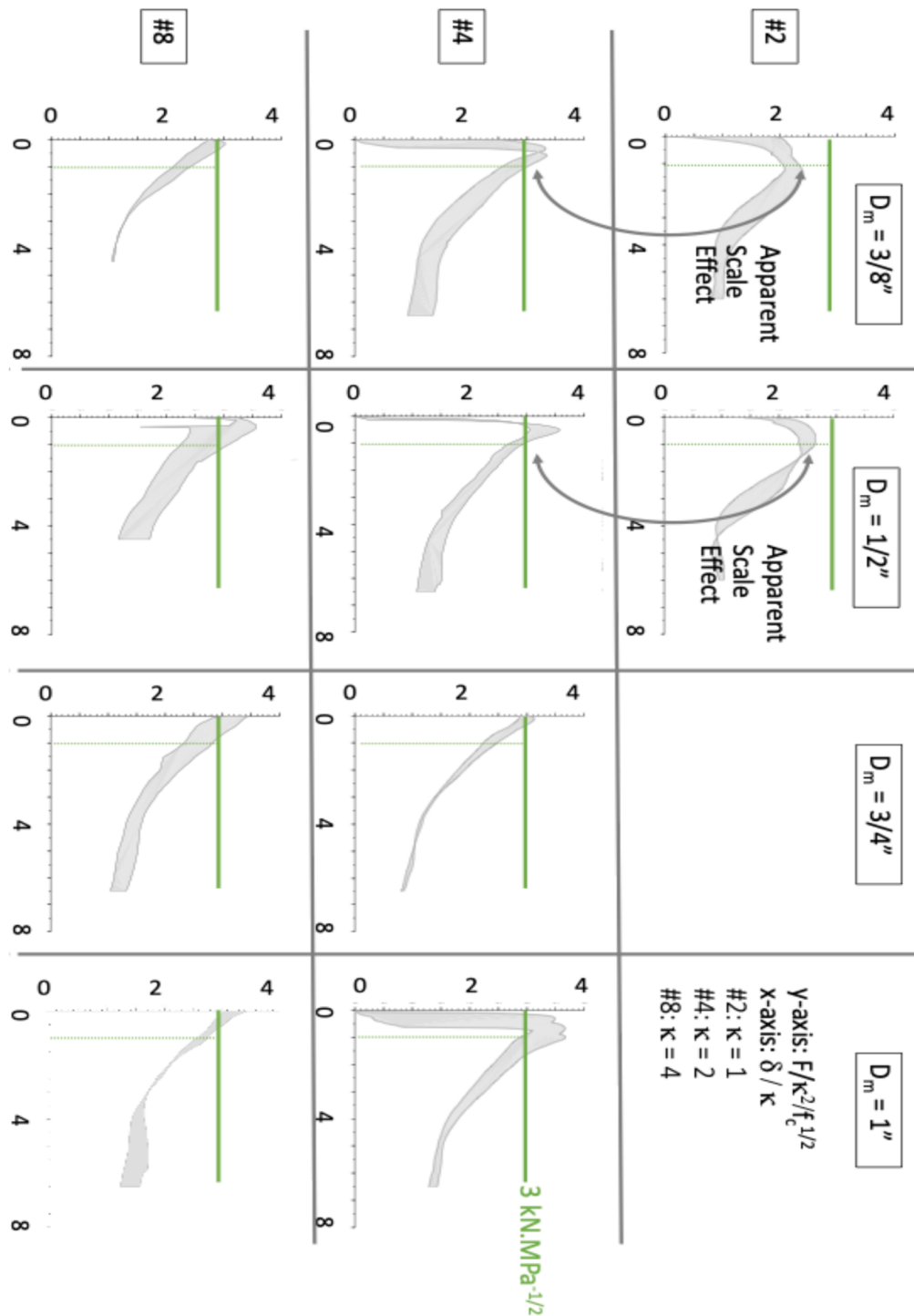
The bond strength of embedded steel reinforcement bars is recognized to be correlated to the square root of the concrete's compressive strength. Hence, the bond test results are reprocessed using the normalized force  $F/(\kappa^2\sqrt{f_c})$ , where  $f_c$  is the average compressive strength of companion concrete cylinders (ASTM C39) on 4 × 8 in. (100 × 200 mm). The compression tests were conducted on the approximate date ( $\pm 1$  day) of the corresponding specimens' bond tests. The normalized force vs. slippage curves are provided in Figure 9-8 and Figure 9-9. The main benefits of this additional normalizing process is reduced curve scattering and unification of all #4 and #8 specimen bond testing data in a set of very comparable curves. The #2 specimens still exhibit a lower normalized bond strength. Substitution of the Japanese aggregates with the Tennessee aggregates still leads to a multiplication factor of approximately 1/0.63 ~ 1.6 on the bond strength. The full-size figures are provided in Appendix A.



**Figure 9-7 Summary of Bond Test Results of the Scale Effect Campaign Showing Normalized Pullout Force  $F/(\kappa^2)$  vs. Normalized Slippage (Detailed Plots are in Appendix A)**



**Figure 9-8 Summary of Bond Test Results of the Scale Effect Campaign Showing Normalized Pullout Force  $F/(\kappa^2 \sqrt{f_c})$  vs. Normalized Slippage for the #2 Specimens (Detailed Plots are in Appendix A)**

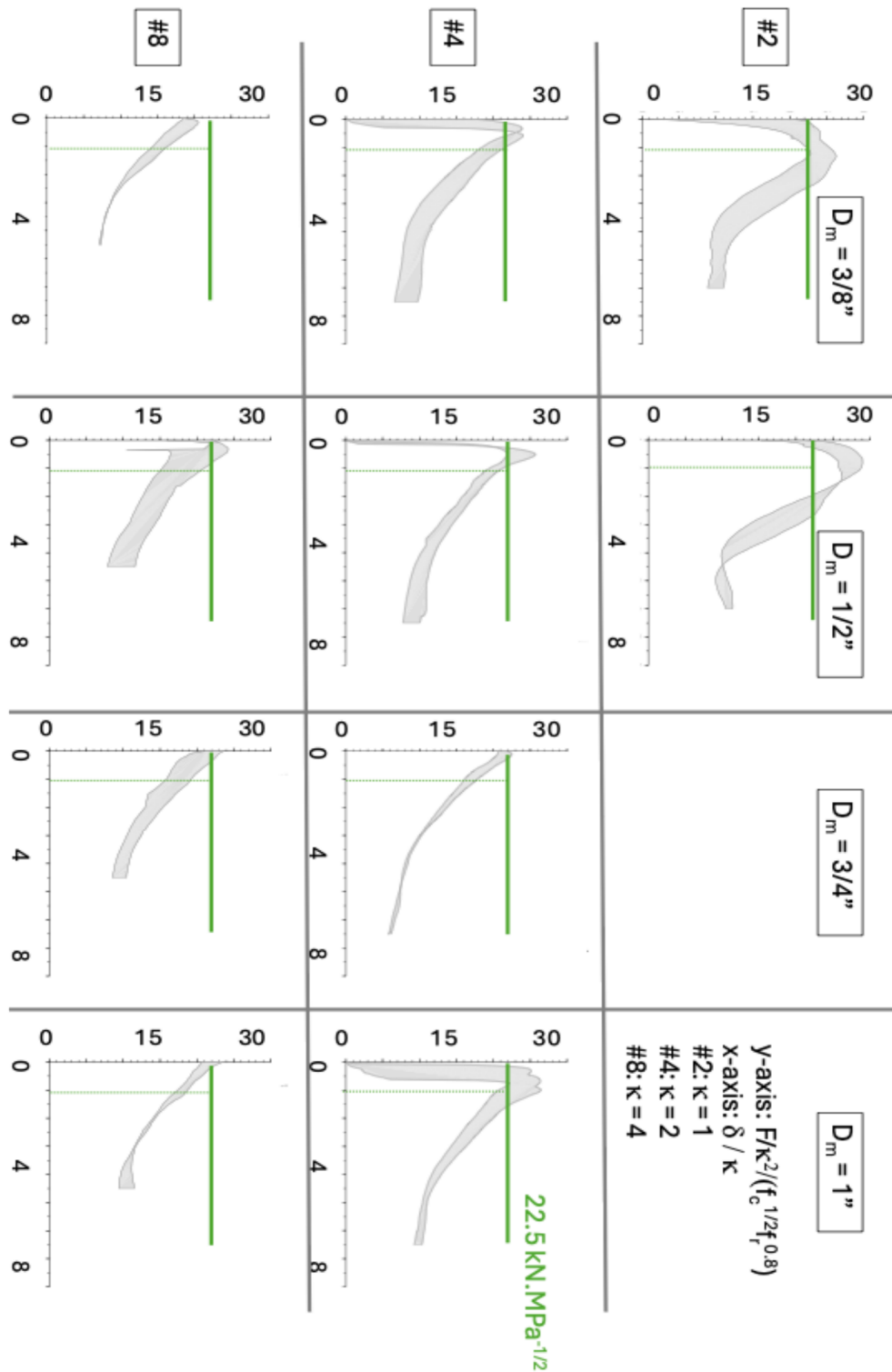


**Figure 9-9 Summary of Bond Test Results of the Scale Effect Campaign Showing Normalized Pullout Force  $F/(\kappa^2 \sqrt{f_c})$  vs. Normalized Slippage (Detailed Plots are in Appendix A)**

The final normalization factor was associated with the geometry of the reinforcement bar ribs. Observations of the fracture surfaces showed that the displaced volume of cementitious materials around the bar was directly associated with the outer diameter of the bar, accounting for rib height. The failure mechanism is illustrated in Figure 11-2 (right). At an early stage of slippage, the localized compression struts in the concrete created by the ribs led to the formation of radial cracks. Those cracks could not propagate towards the lateral surface of the concrete because of the lateral pressure exerted by the jacket. Instead, a shear-like cylindrical fracture along the bar connecting the top of the ribs was the reason for the observed slippage. In this shear zone, friction and small aggregate interlocking effects contributed to the resistance against slippage.

Lettow (2006) proposed that the pullout force is also normalized by a geometrical factor, noted as  $f_r^{0.8}$ , which is calculated as the height of the ribs divided by the center-to-center distance between two consecutive ribs. For the #2, #4, and #8 bars,  $f_r^{0.8}$  is equal to 0.091, 0.139 and 0.147, respectively. The normalized data are presented in Figure 9-10. The full-size figures are provided in Appendix A. The proposed normalization leads to a fair alignment of all bond strength data.





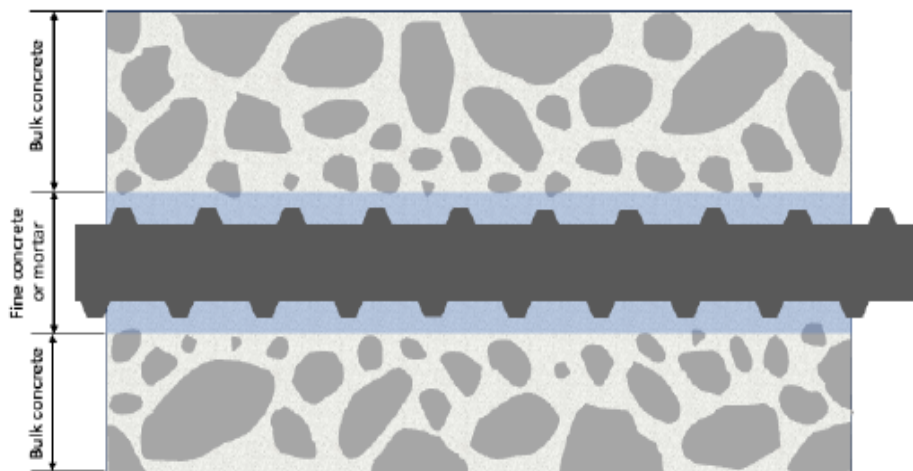
**Figure 9-10 Summary of Bond Test Results of the Scale Effect Campaign Showing Normalized Pullout Force  $F/(\kappa^2 \sqrt{f_c} f_r^{0.8})$  vs. Normalized Slippage (Detailed Plots are in Appendix A)**

## 9.5 Conclusions

The scaling study demonstrated that the bond test data (pullout force vs. slippage) can be interpreted consistently using normalization factors accounting for the compressive strength of the concrete at the time of the test and two geometrical factors accounting for the nominal diameter of the reinforcement bar and the dimensions of the reinforcement ribs. For a given type of aggregate, normalized curves expressed as  $F/(\kappa^2 \sqrt{f_c} f_r^{0.8})$  vs.  $\delta/\kappa$  are very comparable for varied nominal maximum aggregate sizes and specimen geometries except for the specimens fabricated using the #2 bar. In that case, the normalized bond strength is lower than the corresponding bond strengths calculated for the specimens fabricated using the #4 and #8 bars. This additional scaling factor may be attributed to the relative size of the rib height compared to the size of the fine aggregate in the shear region that is mobilized during slippage. Figure 9-11 shows a sketch of the cylindrical shear zone that is pulled out during slippage. The shear strength is affected by the presence of aggregate. The presence of the bar and its ribs creates a wall effect. The aggregate size distribution is not representative of the bulk of the concrete. When approaching the surface of the bar, the fraction of fine aggregate increases, causing a reduction of shear properties.

Nevertheless, the bond test results obtained from small specimens using the #2 bars can be scaled to specimens using higher bar dimensions by calculating the following:

1. The geometry factors  $\kappa$ ,  $f_r$ , and a specific factor of  $\sim 1.3$  to account for the geometry effects associated with the rib height size related to the size of the fine aggregate in the shear region that is mobilized during slippage
2. The square root of the compressive strength



**Figure 9-11 Sketch Showing the Wall Effect Around the Reinforcing Bar**



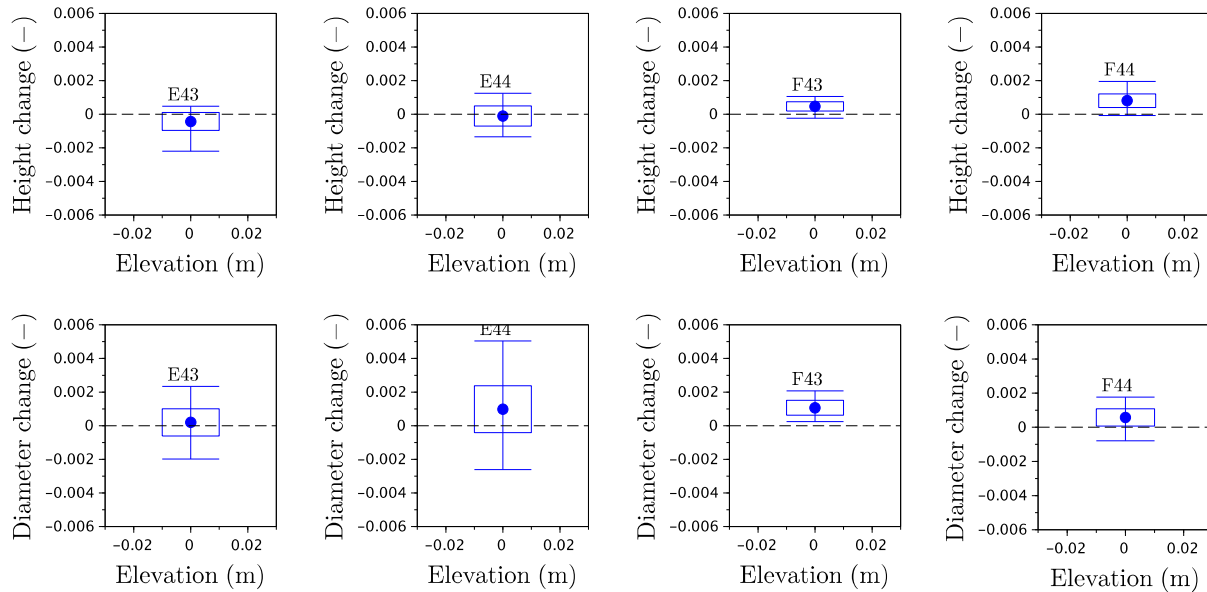
## 10 INTERPRETATION OF TEST RESULTS

Note: In the following section, the term *dimensional change* refers to a length variation of the diameter or the height of the specimens before and after irradiation or before and after heat curing.

### 10.1 Dimensional Change of Irradiated Aggregates

Note: The labeling system used by the JCAMP team varied in their publication. Hence, in this report, a labeling system is adopted which combines the different label forms: GA, F, GA(F), and F/GA correspond to the tested metachert specimens containing 92% quartz, and E, GB, GB(E), and E/GB correspond to the tested sandstone specimens.

Figure 10-1 presents a summary of the dimensional changes measured on two pairs of irradiated aggregates. The top and bottom figures show the changes of heights and diameters. Results are presented from left to right for specimens E43, E44, F43, and F44. Letters E and F refer to aggregates GB(E) and GA(F), respectively, as shown in Figure 6-9. The composition of aggregates is given in Section 2.2.1. The error bars correspond to the minimum and maximum measured values, the box corresponds to the standard deviation, and the filled circle marks correspond to the mean values. When analyzing the mean values, GB(E) aggregates exhibit almost no height expansion with some contraction in specimen E43, as well as some limited diameter expansion. Measurement results are more scattered for specimen E44. The changes of height and diameter are more consistent toward small isotropic expansion ( $< 0.1\%$ , average values). The maximum measured expansion for aggregate GA(F) is approximately  $0.2\%$ .

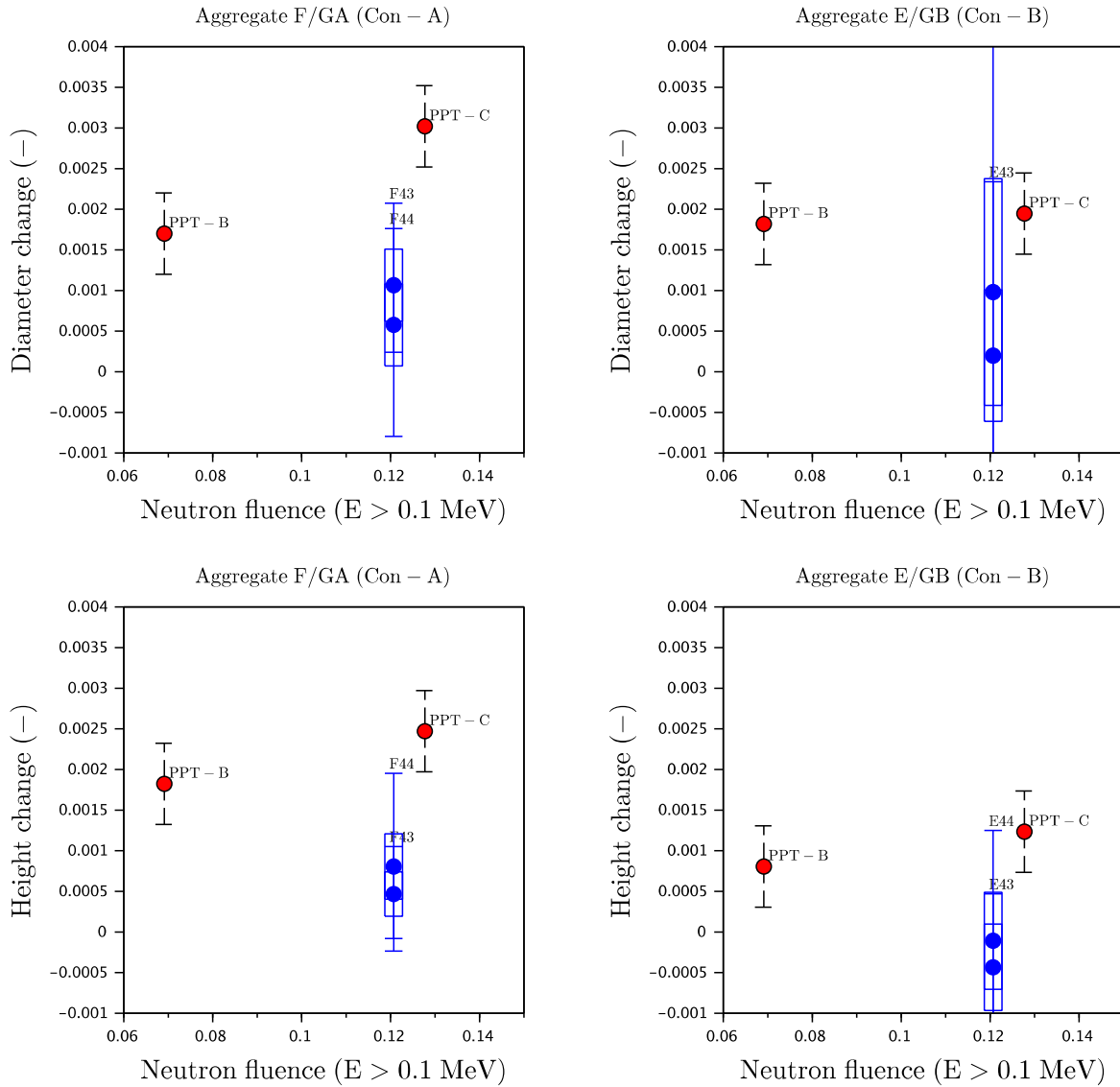


**Figure 10-1 Summary of Post-Irradiation Dimensional Changes of Aggregates**

Figure 10-2 shows the comparison of dimensional changes of aggregates of the same chemical composition after irradiation in the JEEP-II reactor (Maruyama et al., 2017) and in the XK1 position of the LVR-15. The data are presented for fast neutron fluences at energies higher than

0.1 MeV in agreement with Maruyama's presented data. Two JCAMP irradiation experiments—PPT-B and PPT-C—reached  $0.70 \times 10^{19}$  and  $1.28 \times 10^{19}$  n.cm<sup>-2</sup> ( $E > 0.1$  MeV at 53.3 °C), respectively, but during this irradiation experiment, the fast neutron fluence at the end of the fourteenth cycle was  $1.22 \times 10^{19}$  n.cm<sup>-2</sup> ( $E > 0.1$  MeV at irradiation temperatures lower than ~55 °C and higher than ~40 °C using the data provided in Figure 4-4 and Figure 4-5). The radiation-induced dimensional change of rock-forming minerals is temperature dependent: for a given fast neutron fluence, the dimensional change is higher at lower irradiation temperatures (Bykov et al., 1981; Denisov et al., 2012). Therefore, if temperature had been the only governing factor to compare the two experiments, then the dimensional change after the LVR-15/XK1 experiment would be expected to be moderately higher than the changes obtained from the JEEP-II experiment. However, the mean dimensional changes of the aggregates measured after the LVR-15/XK1 experiment are significantly lower than the corresponding changes measured in the JEEP-II experiment.

The changes of diameter (mean values) for aggregates F/GA irradiated in capsule PPT-C (JEEP-II) are ~3–6 times higher than the change of diameter observed after the irradiation experiment in the LVR-15/XK1 position. For aggregate E/GB, the same factor is higher than 2.



**Figure 10-2 Comparison of the Aggregate Dimensional Change Observed on the Aggregate Specimens Irradiated in the JEEP-II Reactor (Red) and the LVR-15 Reactor (Blue). Fluence Given in  $\times 10^{20}$  n.cm<sup>-2</sup>**

The differences in experimental conditions are summarized in Table 10-1. The main differences are (1) the fast flux neutron is 10 times lower in the present experiment than in the JCAMP experiment, and (2) the gamma dose rate is 3–4.5 times higher in the JEEP-II experiment than in the LVR-15 experiment. However, because the duration of the irradiation experiment is much longer in the LVR-15 experiment, the final gamma dose is 3–5 times higher in the LVR-15 experiment, reaching approximately 1 GGy ( $10 \times 10^{10}$  rad).

**Table 10-1 Irradiation Conditions in JEEP-II (Data from Table 22–23 of Maruyama et al., 2017, and this Study’s Experiment in LVR-15/XK1)**

	JEEP-II/PPT-B	JEEP-II/PPT-C	LVR-15/XK1
Fast-neutron flux (n.cm <sup>-2</sup> s <sup>-1</sup> , E > 0.1 MeV)	$\sim 3.6 \times 10^{12}$ ( $\times 10$ )	$\sim 3.6 \times 10^{12}$ ( $\times 10$ )	$\sim 3.6 \times 10^{11}$ ( $\times 1$ )
Fast neutron fluence (n.cm <sup>-2</sup> , E > 0.1 MeV)	$7.0 \times 10^{18}$ ( $\times 0.57$ )	$1.28 \times 10^{19}$ ( $\times 1.05$ )	$1.22 \times 10^{19}$ ( $\times 1$ )
Gamma dose rate (kGy.h <sup>-1</sup> )	330 ( $\times 3.5$ 4.4)	290 ( $\times 3.2$ 3.9)	75.6–93.6 ( $\times 1$ )
Gamma dose (GGy)	0.2 ( $\times 0.15$ 0.22)	0.32 ( $\times 0.25$ 0.35)	0.9–1.3 ( $\times 1$ )
Irradiation temperature (°C)	53.3	53.3	~40–55
Duration (without outages) (days)	~25 ( $\times 0.06$ )	~45 ( $\times 0.11$ )	~392 ( $\times 1$ )

Companion <sup>60</sup>Co gamma irradiation experiments of aggregate GA(F) and GB(E) were conducted by the JCAMP team (Maruyama et al., 2017) at the Takasaki Advanced Radiation Research Institute. The gamma dose and dose rate were 25–100 MGy and 8.6 kGy.h<sup>-1</sup>, respectively (durations 4, 8 and 16 months). The gamma irradiation–induced diameter and height changes of the aggregate specimens did not exhibit distinctive evolution with the gamma dose and were measured at ~0.05–0.15% and 0.1% for aggregates GA(F) and GB(E), respectively. These values are comparable to the measurements obtained from the LVR-15/XK1 post-irradiation data.

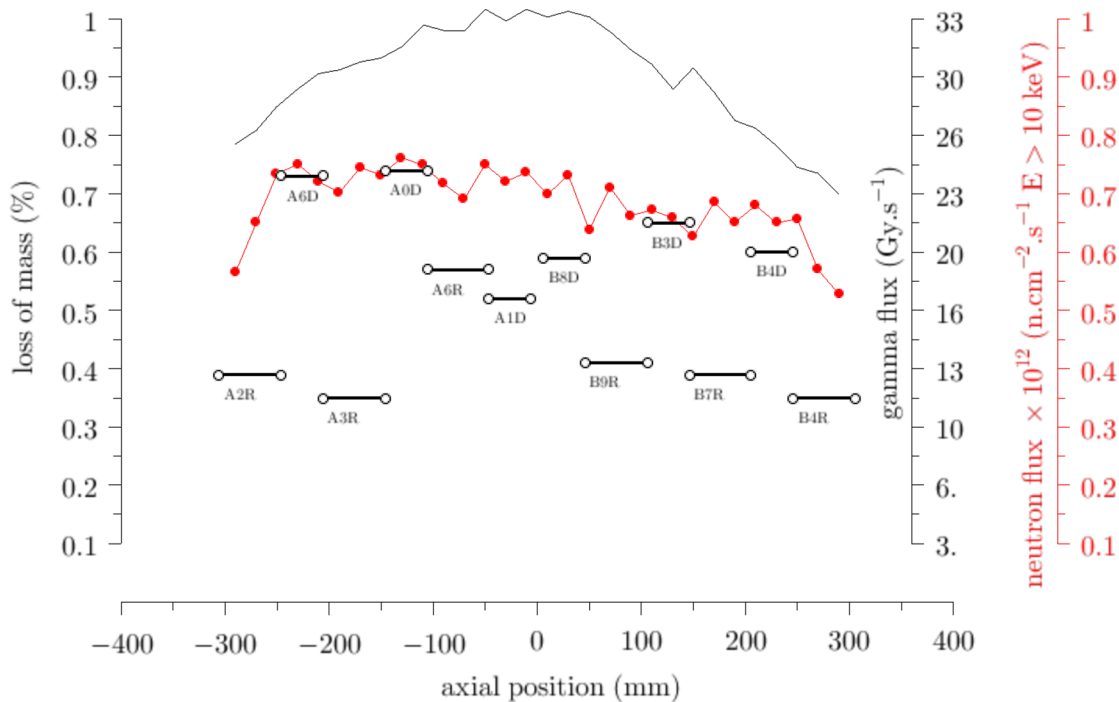
It is unclear whether the observed low irradiation-induced dimensional changes of the aggregate specimens irradiated in the LVR-15/XK1 could be attributed to gamma-irradiation effects. Nevertheless, post-irradiation dimensional data indicate that the fast neutron flux affects the RIVE of aggregates. Observing the neutron and gamma rate effect by comparing the data from experiments using JEEP-II and LVR-15, this result is very significant for in-service irradiated concrete in LWRs because the flux of fast neutrons reaching the surface of the CBS is lower by at least one order of magnitude than the flux at which the LVR-15/XK1 experiment was conducted.

## 10.2 Mass Change of Concrete Specimens

All irradiated specimens exhibit a loss of mass attributed to a loss of water caused by radiolytic effect and gas transport. The mass of the steel bar was assumed constant: visual observation did not identify the presence of corrosion products. Therefore, the relative mass loss in the pullout concrete of the pullout specimens can be obtained by a correction of the total mass loss accounting for the mass of the bar:  $\frac{\Delta m_c}{m_c^0} = \frac{\Delta m}{m^0 - m_s}$ , where subscripts *c* and *s* refer to *concrete* and *steel*, respectively, and the superscript <sup>0</sup> denotes the pre-irradiation condition. The weight per length of #2 bar is ~0.17 lb/ft (0.252 kg/m). The length of the bar in the pullout specimen is 99.7 ± 0.5 mm (allowing for cutting uncertainty).

Hence, the mass of the bar is  $25.2 \pm 0.13$  g. The actual mass loss in the concrete of the pullout specimens is ~15% higher than the total measured loss of mass.

Figure 10-3 presents the mass loss in the concrete of the 12 irradiated concrete specimens plotted against their axial position in the capsule. Because the specimens were pre-dried at  $\sim 60\text{--}62^\circ\text{C}$  for approximately two months, it is expected that the capillary (*free*) water has been completely removed from the specimens. The loss of mass is attributed to chemically bonded water radiolysis and gas transport in the capsule promoted by the He flow. However, the mass losses appear to be uncorrelated to the amplitude of the gamma ray dose rate and the neutron flux. The donut specimens exhibit higher mass loss ( $\sim 0.5\%$ – $0.75\%$ ) than the pullout specimens ( $\sim 0.35\%$ – $0.6\%$ ). This difference could be attributed to the specimen geometry. Whereas radiolytic gas transport is expected to occur mainly along the radial direction of the specimens, the contact surface of the stacked specimens in the capsule is not perfectly sealed. Therefore, additional transport may have occurred through the axial direction (bidimensional *drying* effect) and from the center holes of the donut specimens. Based on the measurement of the TC placed between the steel bar and the concrete in the top pullout specimen, additional heating caused by the presence of the bar is limited.

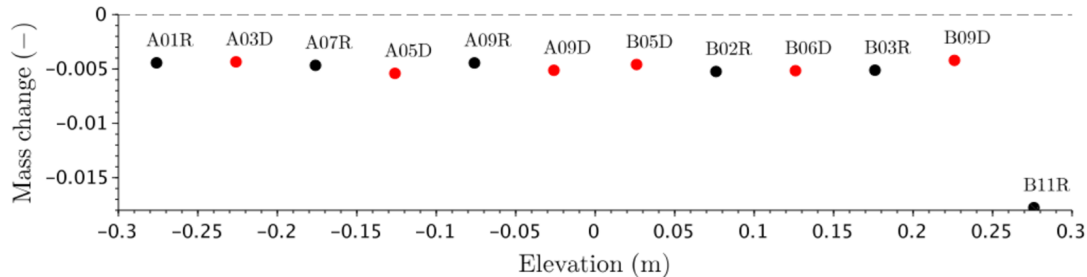


**Figure 10-3 Mass Loss of Irradiated Specimens Against their Axial Positions in the Capsule (Thick Black Solid Lines and Circle Marks; see Figure 2-3 for capsule). Gamma Dose Rate Axial Profile (Thin Black Solid Line) and Fast Neutron Flux Profile (Red Solid Line and Circle Marks)**

Figure 10-4 shows the loss of mass in the heat-cured specimens. Unlike the mass loss in the irradiated specimens, the mass loss in the heat-cured specimens is consistent across those set independently of the geometry with values ranging from  $\sim 0.4\%$  to  $0.55\%$  (the B11R data point is an outlier). In comparison, the loss of mass in the irradiated donut specimens ranges from



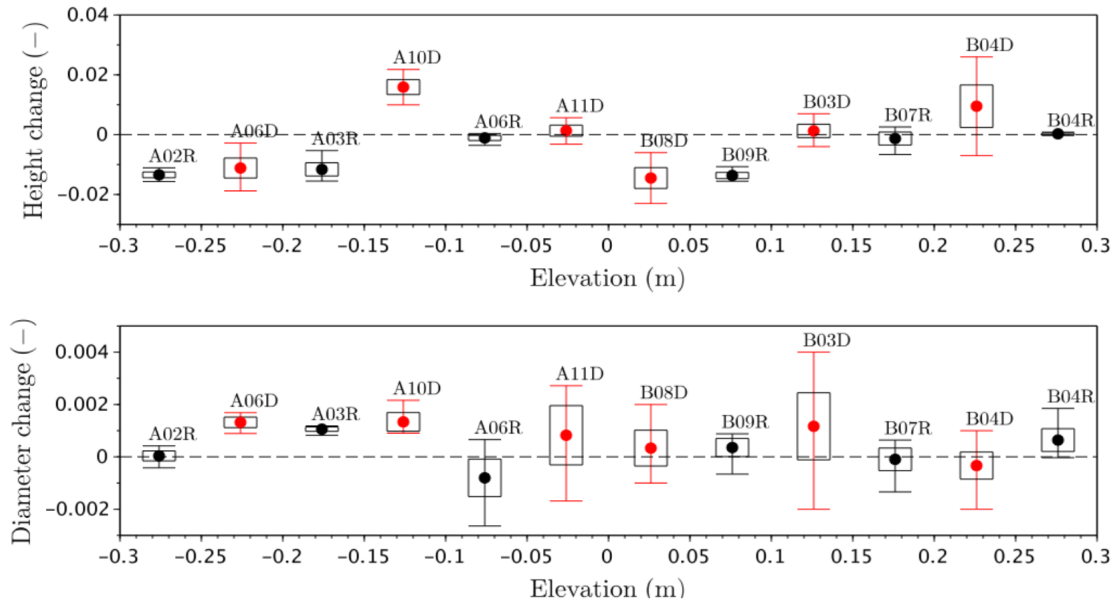
~0.5% to ~0.75%. The helium flow in the irradiation and companion capsules is identical. The temperature histories in both capsules are comparable (average temperature approximately ~45 °C). Therefore, the additional loss of mass can be attributed to radiolytic effects. The loss of mass of the irradiated pullout specimens ranges from 0.35% to 0.4% (0.55% for A6R). These values are slightly lower than the companion heat-cured specimens.



**Figure 10-4 Mass Loss of the Heat-Cured Specimens Against their Axial Position (Mean Value) in the Capsule (See Figure 2-3 for Specimen Positions)**

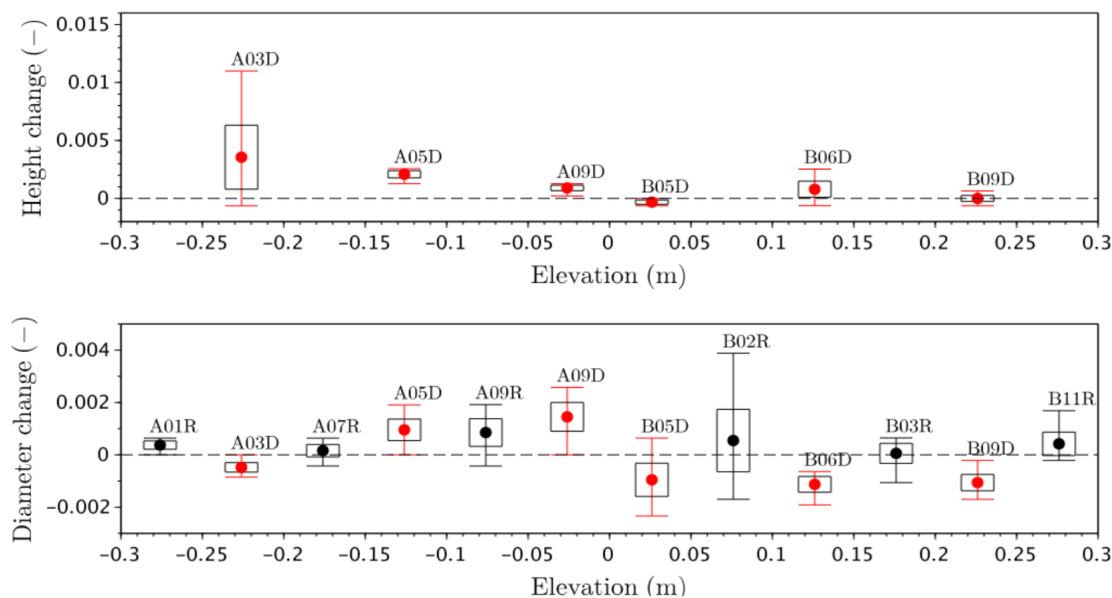
### 10.2.1 Dimensional Changes of Concrete Specimens

Figure 10.5 presents the summary of the dimensional changes of all irradiated concrete specimens. Data are presented as a function of the specimens' positions in the capsule (black represents pullout specimens, and red represents donut specimens). As a first observation, there is no evident correlation between the dimensional changes and the specimen positions, and hence the flux. The range of dimensional changes is approximately one order of magnitude higher for the height changes than the diameter changes: height changes vary between -2% to +2.5%, whereas diameter changes vary between approximately -0.2% and 0.4%.



**Figure 10-5 Summary of Post-Irradiation Dimensional Changes of Concrete Specimens (Black Indicates Pullout Specimens and Red Indicates Donut Specimens)**

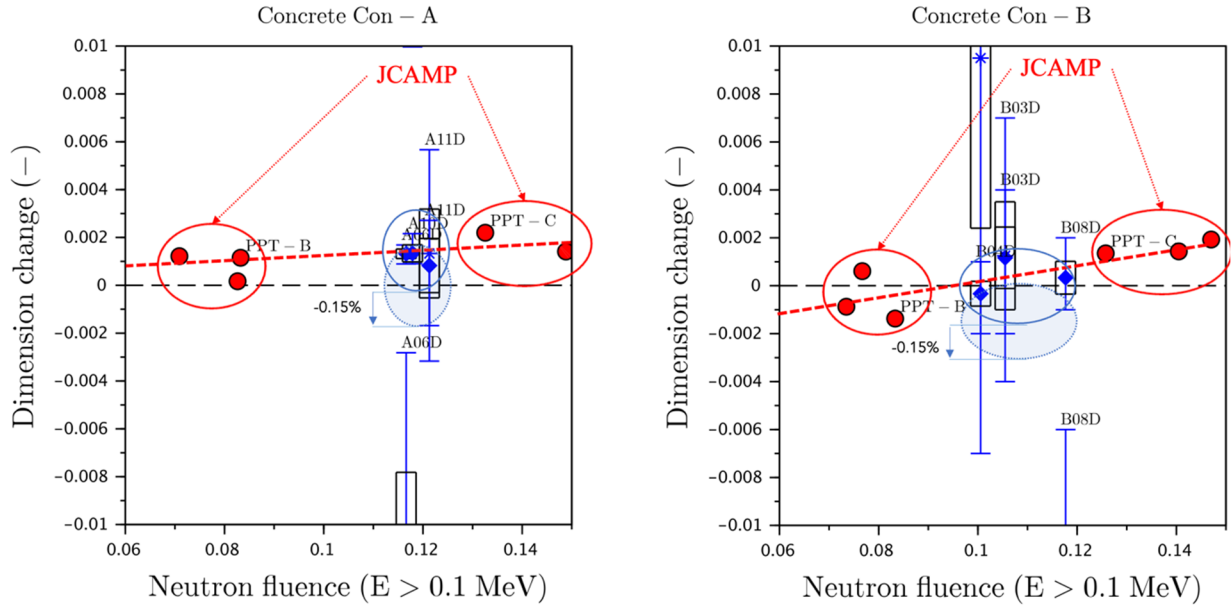
Figure 10.6 shows a comparable plot of the dimensional changes obtained from the heat-cured specimens. The height changes range from  $-0.03\%$  to  $+0.35\%$ , and the diameter changes range from  $-0.1\%$  to  $+0.15\%$ . Thus, the diameter changes are very comparable between irradiation and heat-curing experiments. As mentioned previously, the height change of the irradiated concrete specimens shows higher variations: five specimens exhibit contraction on the order of  $-1\%$  to  $-1.5\%$ , two specimens show expansion of approximately  $+1\%$  to  $+1.5\%$ , and two specimens do not show significant variations. Thus, the height change results of the irradiated specimens are inconsistent and difficult to interpret.



**Figure 10-6 Summary of the Dimensional Changes of the Heat-Cured Concrete Specimens (Black Indicates Pullout Specimens and Red Indicates Donut Specimens)**

Figure 10-7 presents a comparison between the dimensional changes of the concrete specimens irradiated in the JEEP-II reactor, including the JCAMP study—height change, data digitized (from Fig. 17b in Maruyama et al., 2017), and the data obtained from this study, with diamond marks indicating diameter change and stars indicating height change. The diameter changes seen in the irradiation experiment in the LVR-15/XK1 position are consistent with the height change measured from the JCAMP study. Nevertheless, some differences should be highlighted:

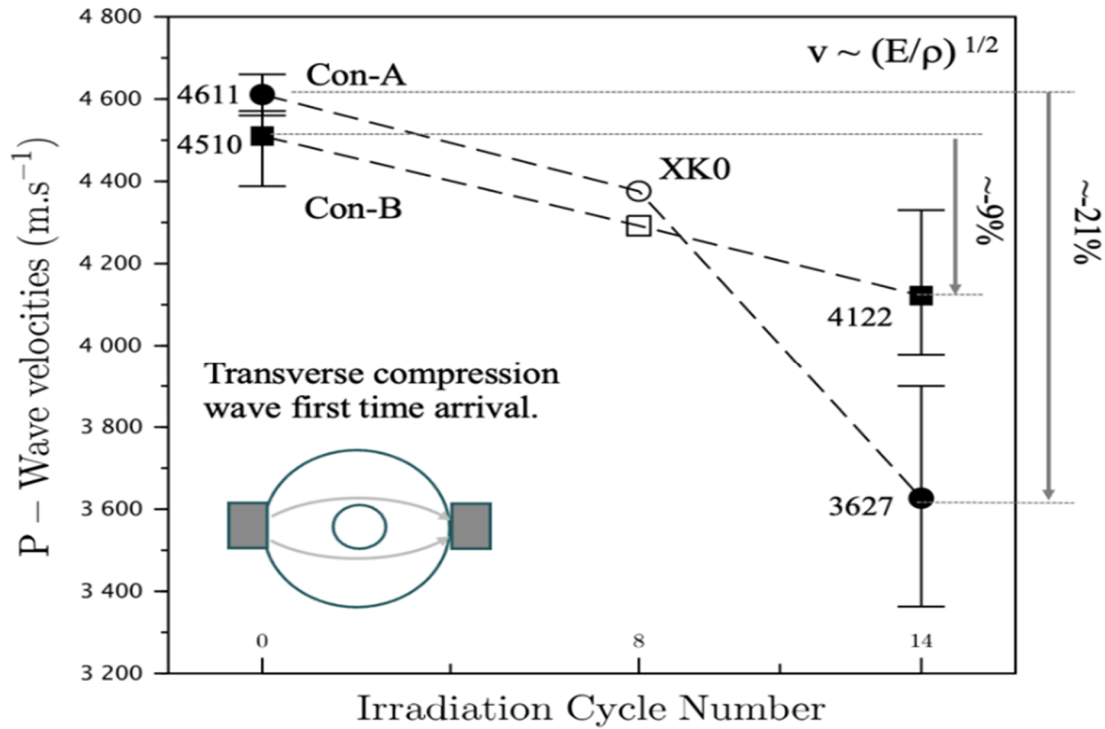
- The loss of mass of the JEEP-II-irradiated specimens ranges between approximately -3% and -4% (Fig. 37a in Maruyama et al., 2017), whereas the loss of mass from the LVR-15-irradiated specimens is always < 0.7%. This discrepancy is explained by the pre-irradiation thermal treatment applied to the specimens in this study. The changes of properties of the LVR-15-irradiated specimens refer to the variations observed between measurements conducted before and after irradiation, but always after pre-irradiation curing.
- The aggregate RIVE is more important for the JEEP-II-irradiated specimens than for the LVR-15-irradiated specimens.
- The total dimensional change results from the contribution of the shrinkage of the cement paste and the expansion of the aggregates. The pre-irradiation curing-induced loss of mass and shrinkage were estimated to range between -0.03% and -0.15% (See Figure 13-2, value at ~50 days). For the sake of comparison, blue shading was added to the figure to show the influence of a -0.15% shrinkage caused by pre-drying on the total diameter changes of the concrete specimens. Then, the diameter changes of the concrete specimens irradiated in the LVR-15/XK1 position are lower than the expected trends derived from the JCAMP data obtained from the irradiation experiment in the JEEP-I reactor. This observation is consistent with the reduction of the aggregates' radiation-induced expansion observed from the comparison of the dimensional changes in the LVR-15/XK1 and JEEP-II irradiation experiment.



**Figure 10-7 Comparison of the Concrete Dimensional Change Observed in the Concrete Specimens Irradiated in the JEEP-II Reactor (Red) and the LVR-15 Reactor (Blue). Diamonds Indicate Diameter Change, and Stars Indicate Height Change. The Distance Between the Unshaded and Shaded Blue Ellipses Corresponds to the Estimated Shrinkage Caused by Pre-Drying Curing**

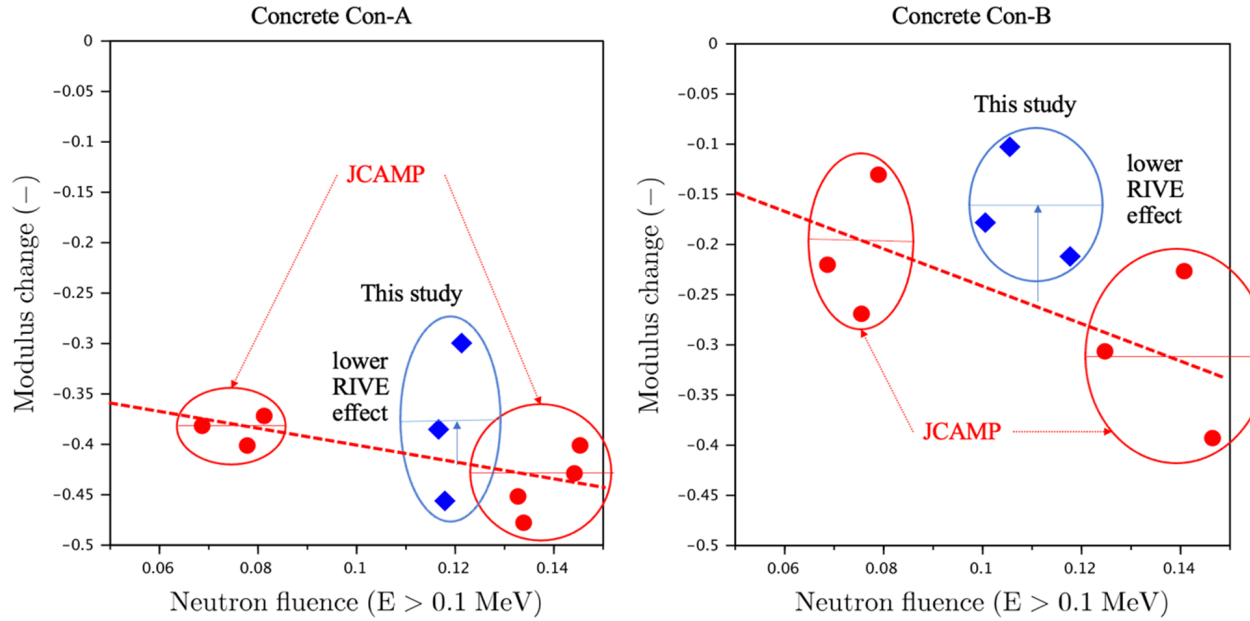
### 10.3 Acoustic Wave Velocities

Figure 10-8 shows the P-wave velocities measured on donut specimens before and after irradiation in the XK1 position (black marks). Post-irradiation (8 cycles instead of 14) measurements obtained from an irradiation experiment conducted in the adjacent position XK0 (data courtesy of CVR) are indicated with white marks. The P-wave velocity of the Con-A and Con-B specimens decreases by an average of approximately 21% and 9%, respectively. Considering that the mass and dimensional changes of irradiated specimens are limited, the dynamic Young's modulus ( $E = \rho v^2$ ) of Con-A and Con-B specimens decreases by an average of approximately 38.1% and 15.7%, respectively.



**Figure 10-8 P-Wave Velocities Measured on Donut Specimens**

Figure 10-9 presents a comparison of the change of elastic modulus obtained from this study (blue marks) and the irradiated JCAMP data digitized from Fig. 37d in Maruyama et al., 2017; static modulus is indicated by red marks. The changes of dynamic modulus obtained from the irradiation experiment in the LVR-15/XK1 position are consistent with the static modulus measured during the JCAMP study. In Figure 10-9, only the JCAMP post-irradiation elastic modulus results are shown. Companion thermally cured specimens at maximum and average irradiation temperatures were also tested by the JCAMP team (Maruyama et al., 2017, Fig. 40c). The corresponding loss of elastic modulus is also consistent with the data presented in Figure 10-9.

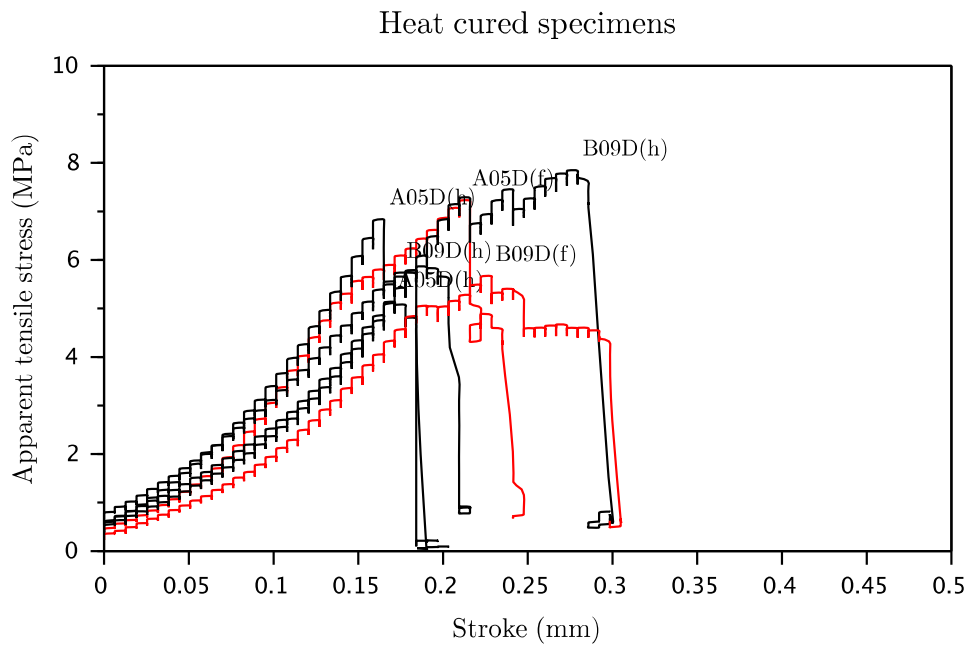
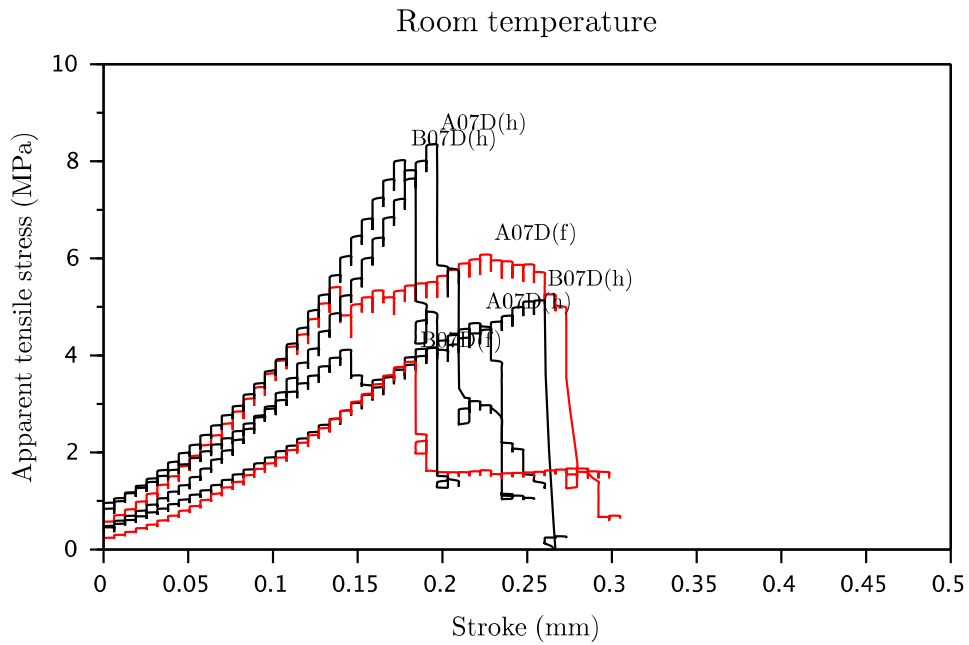


**Figure 10-9 Comparison of the Concrete Elastic Modulus Change Observed in Concrete Specimens Irradiated in the JEEP-II Reactor (Red) and the LVR-15 Reactor (Blue) The Neutron Fluence Values are Provided in  $\times 10^{20} \text{n/cm}^2$**

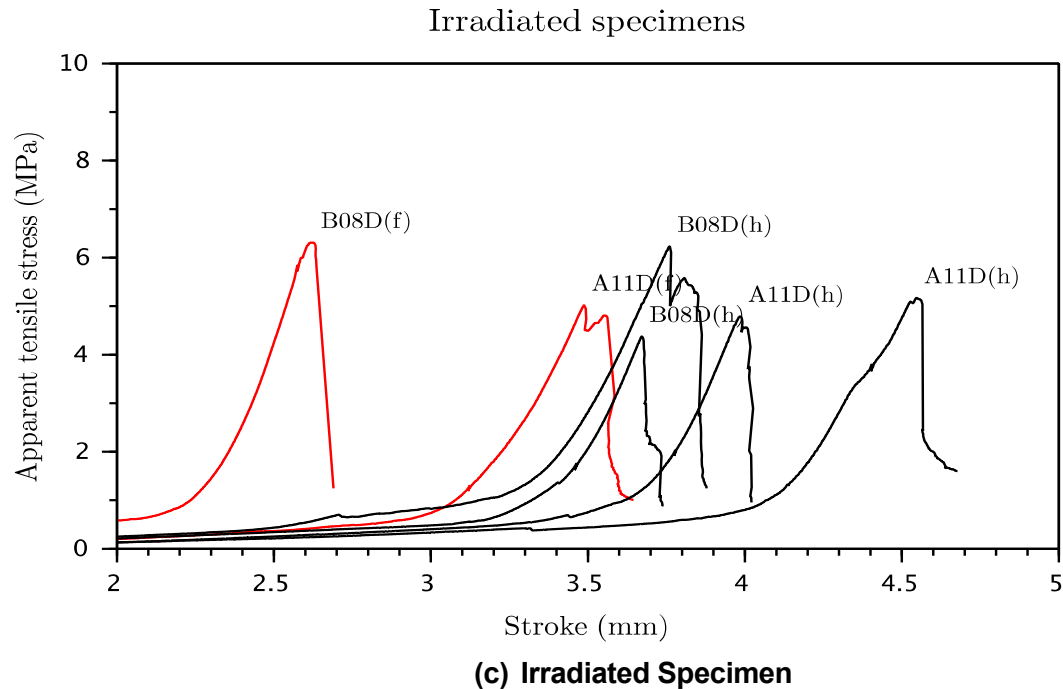
## 10.4 Strength Tests

### 10.4.1 Splitting Strength

Figure 10-10 displays the apparent splitting stress evolution with the machine stroke:  $f$  indicates full specimens (i.e., first splitting tests), and  $h$  is indicative of half specimens (second splitting tests). The apparent tensile stress,  $\sigma_t$ , is calculated as  $\sigma_t = 2F/\pi A$ , where  $F$  and  $A$  are the applied force and the concrete cross-section area ( $1,280 \text{ mm}^2$  for the full donut specimen and  $640 \text{ mm}^2$  for the half donut specimens, respectively) (described in Section 5.4).



**Figure 10-10 Apparent Tensile Stress vs. Press Stroke Measured During Splitting Tests**

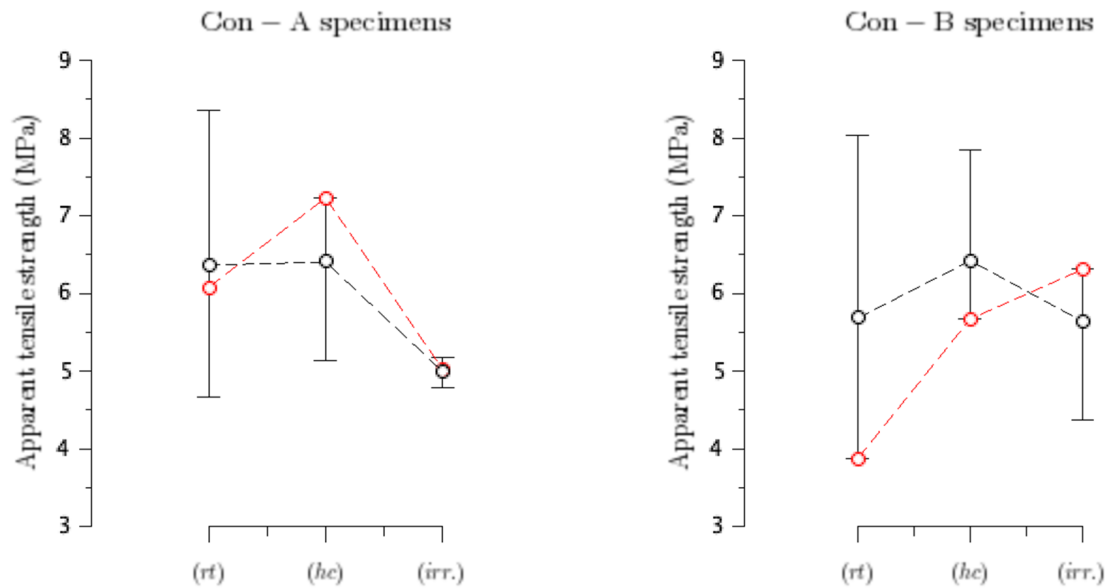


**Figure 10-10 Apparent Tensile Stress vs. Press Stroke Measured During Splitting Tests (Continued)**

Figure 10-11 shows the tensile strengths calculated from one full specimen splitting test (red marks) combined with two half-specimen tests (black marks). Error bars correspond to the minimum and maximum values. The apparent tensile strength of the irradiated specimens is lower than the strength of the specimens cured at irradiation temperature.

Compared to A07D and B07D specimens cured at room temperature, the mean value of the apparent tensile strengths of irradiated specimens A11D and B08D decrease by ~21% and <1%, respectively, for concrete Con-A and Con-B. Compared to the A05D and B09D specimens cured at irradiation temperature, the mean values of the apparent tensile strength of irradiated specimens A11D and B08D decrease by ~22% and ~19%, respectively, for concrete Con-A and Con-B. Splitting strength is governed by the fracture properties of the cement paste, the interfacial transition zone, and the aggregate. The maximum size of the aggregate is approximately 10–13 mm, to be compared to the 16 mm thickness of the concrete wall. Hence, the presence or absence of large aggregates along the fracture surface affects the apparent splitting strength. This effect contributes to the scatter of the results. Qualitative trends can be observed for the irradiated Con-A specimens which exhibit a significant reduction in splitting strength compared to the room temperature and heat-cured specimens. This effect can be attributed to the aggregate RIVE. It is not possible to make a conclusion about any specific trend for the Con-B specimens.

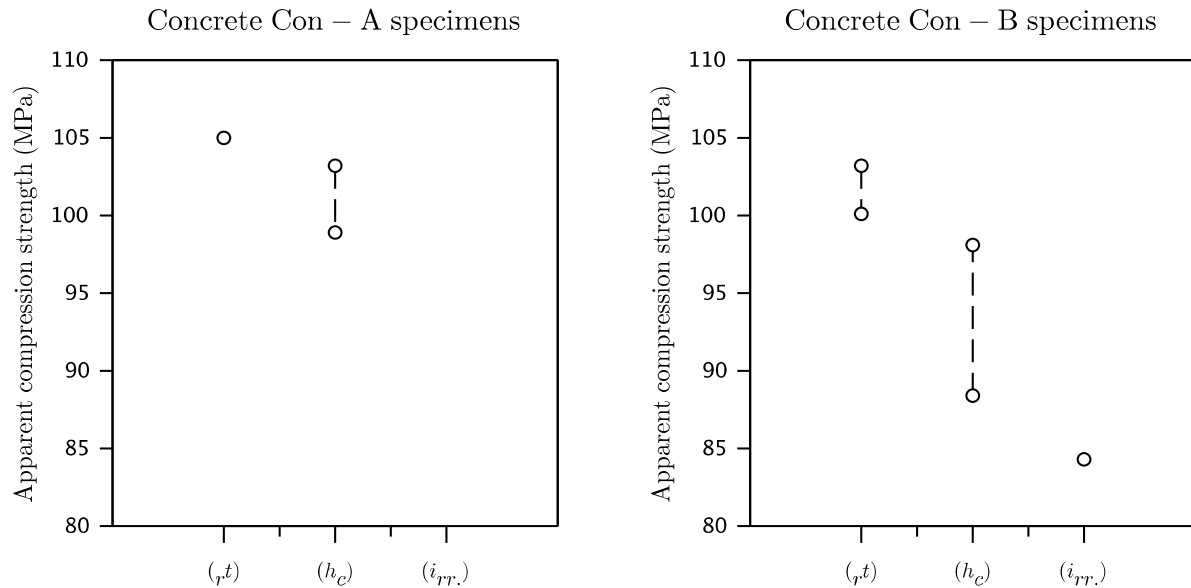




**Figure 10-11 Apparent Tensile Strength (Splitting Tests): *rt* Indicates Specimens Cured at Room Temperature, *hc* Indicates Specimens Cured at Irradiation Temperature, and *irr* Indicates Irradiated Specimens**

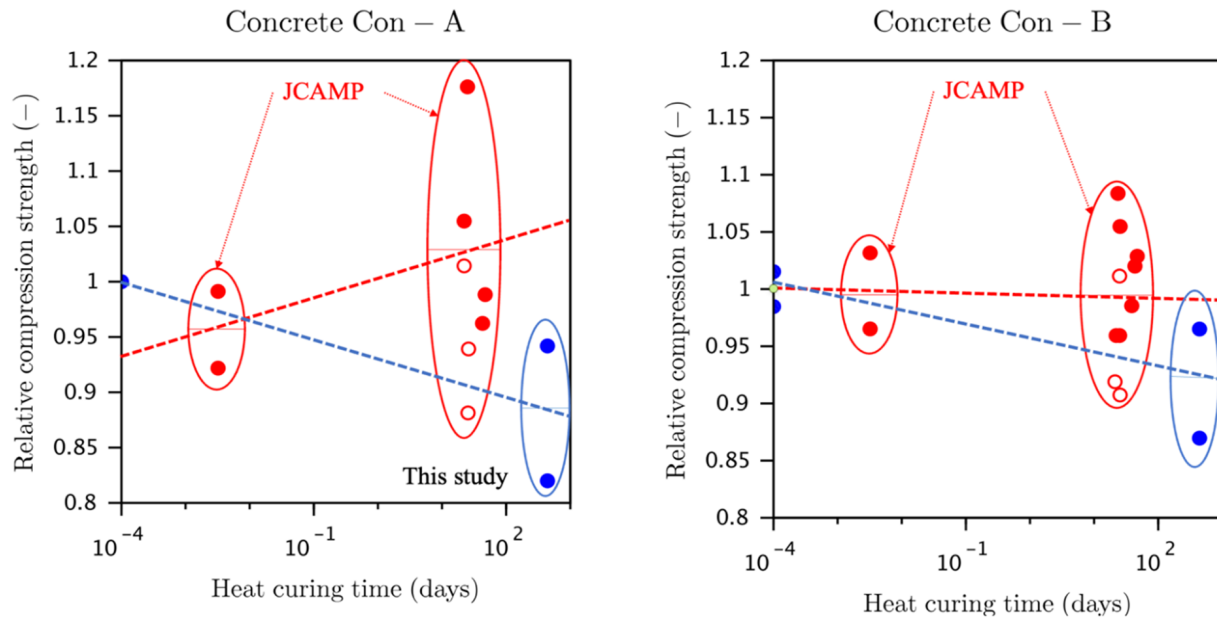
#### 10.4.2 Compressive Strength

Figure 10-12 provides a summary of the compression test data obtained from specimens cured at room temperature (*rt*), those that were heat cured (*hc*), and those that were irradiated (*irr*). The data that were considered unreliable because of experimental issues (e.g., misalignment) were not plotted. Hence, there are no data for the irradiated Con-A specimens. The limited data appear to indicate that heat curing and irradiation caused a reduction of the apparent compressive strength. The effects of heat curing of the compressive strength of concrete were studied by Maruyama et al. (2014c), who found that prolonged exposure at 40–50 °C caused a limited change in compressive strength ( $\pm 10\%$ ) compared to sealed specimens. The gain or reduction in strength appears to be related to the aggregate type: increase was seen with a sandstone aggregate, and decrease was observed with a metachert aggregate. This study's specimens were pre-cured before irradiation and prolonged heat curing. Thus, it is expected that cement hydration was complete at the end of the pre-drying period. Additional drying shrinkage may be the cause of the loss of compressive strength in the heat-cured specimens. However, this compressive strength reduction is not aligned with the evolution of the tensile strength obtained from splitting tests.



**Figure 10-12 Apparent Compressive Strength (Capped Compression Tests)  $rt$  Indicates Specimens Cured at Room Temperature,  $hc$  Indicates Specimens Cured at Irradiation Temperature, and  $irr$  Indicates Irradiated Specimens**

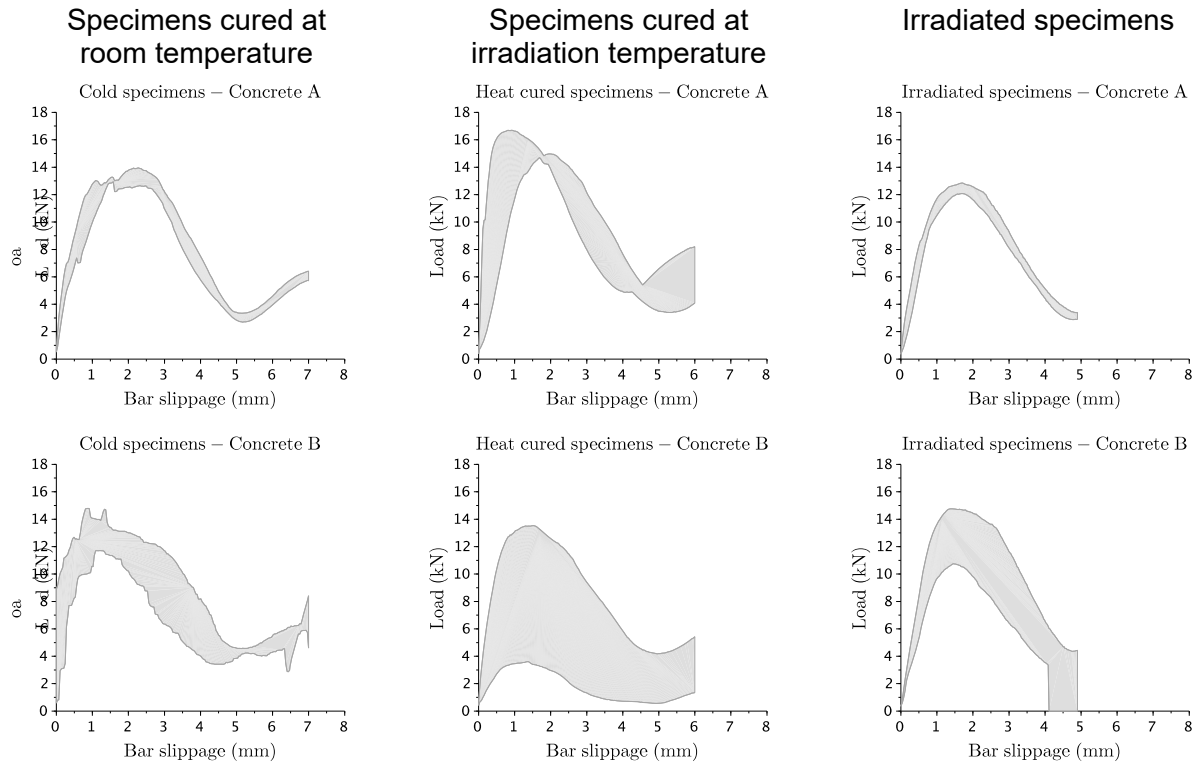
Figure 10-13 provides a comparison between the JCAMP data (Maruyama et al., 2017) and the results obtained from this study for the heat-cured specimens. The JCAMP data were digitized from Fig. 40 of Maruyama's report, providing the uniaxial strength of heat-cured specimens in parallel to the irradiation experiment in the JEEP-II reactor. The JCAMP data are provided as a function of the equivalent fast neutron fluence. For the sake of comparison, the corresponding heat curing durations were obtained assuming a fast neutron flux of  $3.6 \times 10^{12} \text{ n.cm}^{-2} \text{ s}^{-1}$  ( $E > 0.1 \text{ MeV}$ ). Durations are presented using a log-scale axis because the duration of the JCAMP heat curing experiments is estimated to be between 20 and 50 days, whereas the heat curing experiment accompanying the irradiation experiment in the LVR-15 reactor lasted for 441 days after removing the outages. The JCAMP data include heat curing at the average irradiation temperature (empty red marks) and at the maximum irradiation temperature (filled red marks). The results of this study correspond to the blue marks. Compression strength data are normalized by the mean value of the strengths obtained on specimens cured at room temperature. Whereas the JCAMP data do not exhibit a particular trend toward a decrease or increase, the compressive strength of the specimens cured at irradiation temperature at ORNL decreased by  $\sim 10\%$  compared to the strength of the room temperature-cured specimens.



**Figure 10-13 Comparison of the Relative Compression Strength of the Heat-Cured Specimens (JCAMP Data in Red; This Study's Data in Blue)**

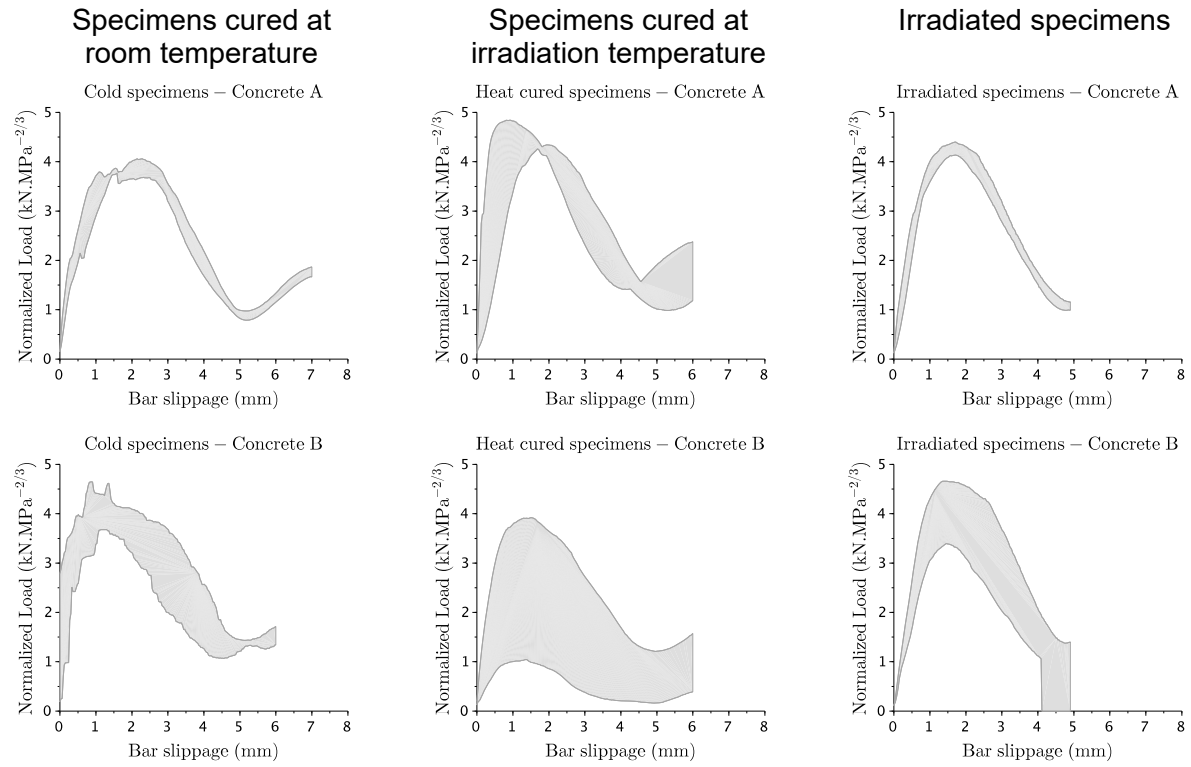
## 10.5 Bond Tests

Figure 10-14 presents a summary of the bond test results conducted on #2 pullout specimens subject to varied curing conditions: at room temperature, at irradiation temperature, and placed in the irradiation position XK1 at the LVR-15 test reactor. The test results are shown as the lower and upper envelopes of the load applied to the reinforcement bar and the differential slippage measured between the free end of the bar and the concrete. Except for results for the concrete Con-B specimens cured at irradiation temperature, the test results are very consistent for each series. For the concrete Con-A specimens, the average maximum load varied from 13.1, 16.0, and 12.2 kN for the specimens cured at room temperature, at irradiation temperature, and irradiated, respectively. For the concrete Con-B specimens, the average maximum load is close to 13.0 kN for the specimens cured at room temperature and irradiated, respectively. It is difficult to interpret the scattered data for the concrete Con-B specimens cured at irradiation temperature; however, none of these data suggest a significant increase of bond force.

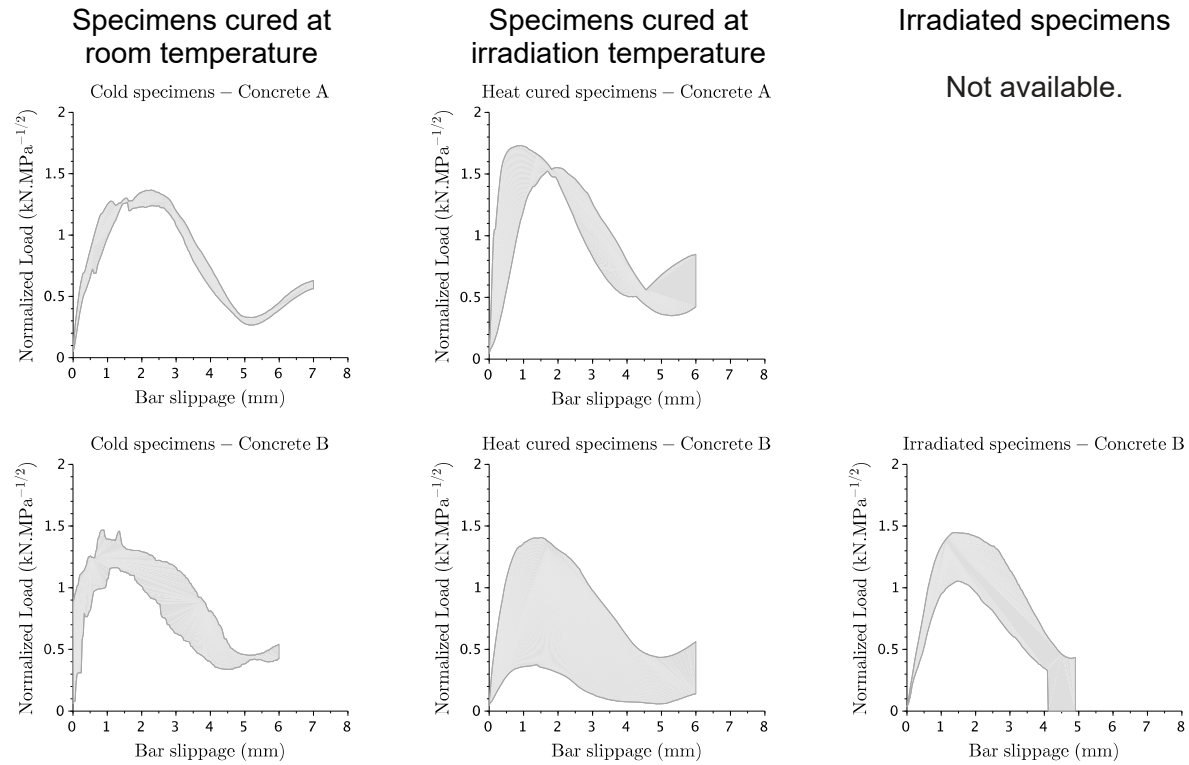


**Figure 10-14 Summary of Bond Test Data on the #2 Pullout Specimens**

In Figure 10-15 and Figure 10-16, the pullout forces were normalized with the apparent average tensile strength to the power of  $\frac{2}{3}$  and the square root of apparent tensile strength, respectively. The compressive strength normalization of the test results for the irradiated Con-A pullout specimens was not possible because of the lack of reliable compression test data. The normalization process aligns well with the bond loads between the room temperature-cured specimens and the irradiated specimens. The normalized bond loads for the Con-A specimens cured at irradiation temperature still exhibit a value that is approximately 20% higher. Given the variability of the strength data measured on non-standard dimensions specimens, this result remains acceptable.



**Figure 10-15 Summary of Bond Test Data on the #2 Pullout Specimens, with Bond Force Normalized by  $f_t^{2/3}$**



**Figure 10-16 Summary of Bond Test Data on the #2 Pullout Specimens, with Bond Force Normalized by  $\sqrt{f_t}$**

## 10.6 Conclusions

Table 10-2 provides a compressive summary of the PIE and test data obtained during this study and a comparison with the data obtained by the JCAMP team (Maruyama et al., 2017). Bond test data are not included in this table.

**Table 10-2 Summary of the Mass and Dimensional Changes and Mechanical Properties Obtained by the JCAMP Team (Maruyama et al., 2017) and Found During this Study (\* Fig. 40 in Maruyama et al. (2017); \*\* Dynamic Modulus; (#) Confined Compression Test; <sup>(a)</sup> Outlier Data)**

	Room temperature		Heat curing		Irradiation	
	JCAMP data	This study	JCAMP data	This study	JCAMP data	This study
<b>Mass change</b>	—	—	(A): 0 to -3.5% (B): 0 to -3.0%	(A): ~0.5% (B): ~ 0.5%	(A): -3.2% – -3.6% (B): -3.3% – -4%	(A): -0.5% – 0.8% (B): +0.3% <sup>(a)</sup> – -0.7%
<b>Dimensional change</b>	—	—	(A): 0 to -0.07% <sup>(*)</sup> (B): 0 to -0.09%	(A): -0.05% – 0.15% (d) (A): 0.1%–0.35% (h) (B): ~ -0.1%(d) (B): -0.03%–0.08%	(A): 0–0.25% (B): ±0.25%	(A): 0.08%–0.13% (B) -0.03%–0.12%
<b>Young modulus (GPa)</b>	(A): 34–37 (B): 33–41	(A): 49–51 <sup>(**)</sup> (B): 45–49 <sup>(**)</sup>	(A): 23–32 (B): 22–30	—	(A): 19–23 (B): 22–32	(A): 25–36 <sup>(**)</sup> (B): 37–44 <sup>(**)</sup>
<b>Compressive strength (MPa)</b>	(A): 62–68 (B): 65–70	(A): 100–103 <sup>(#)</sup> (B): 105 <sup>(#)</sup>	(A): 60–80 (B): 71–75	(A): 86–99 <sup>(#)</sup> (B): 88–98 <sup>(#)</sup>	(A): 56–70 (B): 55–67	
<b>Tensile strength (MPa)</b>	—	(A): 4.6–8.3 (B): 3.9–8.0	—	(A): 5.1–7.2 (B): 5.7–7.8	—	(A): 4.9–5.2 (B): 4.4–6.3

The main conclusions of this research are summarized below:

1. **Fast neutron flux effect:** The dimensional changes of the irradiated aggregates in the LVR-15 do not reach expansion comparable to the changes observed after irradiation in the JEEP-II reactor at comparable fluence and irradiation temperature. For aggregate GA(F), the dimensional changes are 3 to 6 times higher in the JEEP-II irradiation experiment than in the LVR-15 experiment. The main difference between the two experiments in the fast neutron flux, which is ten times lower in the LVR-15 experiment ( $3.6 \times 10^{12} \text{ n.cm}^{-2} \text{ s}^{-1}$ ,  $E > 0.1 \text{ MeV}$ ) than in the JEEP-II experiment ( $3.6 \times 10^{11} \text{ n.cm}^{-2} \text{ s}^{-1}$ ,  $E > 0.1 \text{ MeV}$ ). The mechanism at the origin of this apparent flux effect remains to be identified and characterized to draw effective extrapolations for in-service irradiation in PWRs.
2. **Gamma irradiation effects:** Comparison of the mass changes of the heat-cured and irradiated concrete specimens does not lead to the conclusion that there was a major contribution of significant irradiation-induced radiolysis: the additional mass change is  $<0.2\%$ . It is important to recognize that the specimens tested in this study were pre-dried before irradiation, so water radiolysis was limited to the chemically bonded water of the concrete constituents.
3. **Mechanical properties of concrete:** The tensile strength and dynamic elastic modulus of the irradiated concrete decreased after the irradiation experiment. Concrete Con-A, which was made of 92% quartz aggregate, showed higher loss of mechanical properties than concrete Con-B, which was made of a felsic sandstone containing 47% quartz. The observed losses of the modulus of the specimens irradiated in the JEEP-II reactor and the LVR-15 reactor at comparable fast neutron fluences and irradiation temperature are similar. They are also similar to the losses observed in specimens cured at irradiation temperature. Because of the low radiation-induced expansion of the concrete aggregate, it can be inferred that the loss of mechanical properties can be partly attributed to some shrinkage-induced microcracking caused by water loss.
4. **Steel-concrete bond strength:** The steel-concrete bond strength could be obtained successfully by using an additional jacketing system to ensure a splitting failure mode for all curing and irradiation conditions. It was found that normalizing the pullout force by the square root of the compressive strength provides a reasonable alignment of all the test data given the uncertainties associated with the measurements of the residual strength. The limited space available in the irradiation capsule was incompatible with the placement of standard size specimens. Hence, strength tests were adapted as best as possible. It can be concluded that in the range of  $\sim 0.1\%$  radiation-induced linear expansion of the concrete coarse aggregate, the irradiated bond strength of the #2 steel bar embedded in concrete scales with the square root of the compressive strength of the irradiated concrete. From the scale effect campaign, it can be inferred that the corresponding bond strength of reinforcement bars of diameter higher than 12.7 mm (#4 bar) would be approximately 1.57 times higher than that of the bond strength observed on #2 bar specimens independently of the coarse aggregate size (testing range:  $\frac{3}{8}$  to 1 in.).





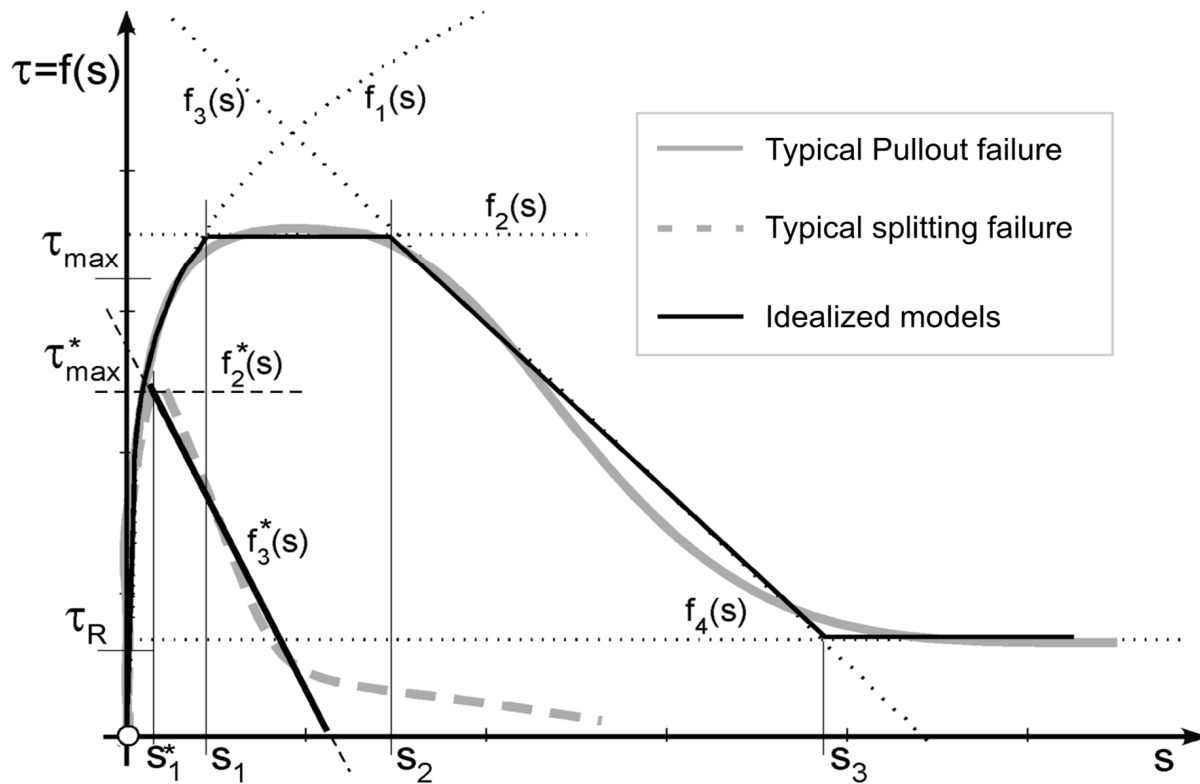
# 11 BOND TEST MODELING

## 11.1 Preliminary Simulation of Bond Test Experiments

The objective of this preliminary set of simulation of the bond strength experiments is to support decision-making regarding the need for adding a confinement jacket prior to testing as described in the previous chapters. The simulations were conducted using a discrete modeling method which shares similarities with the FE method: that is, the lattice discrete particle model (LDPM), which is available through the licensed software Multiphysics Analyses of the Response of Structures (MARS, Pelessone, 2009).

### 11.1.1 Modeling Strategy

The bond strength of steel reinforcement bar, or *rebar*, with concrete depends on multiple factors and includes several reinforcing bar–concrete interaction mechanisms. These mechanisms are associated with the relative displacement between the rebar and the surrounding concrete and the development of forces in the axial, radial, and tangential directions relative to the bar. Along the axial direction, a nonlinear bond-slip behavior is observed. This behavior can be interpreted as the sum of cohesion and frictional forces along the bar's surface. It also exhibits a nonlinear initial elastic behavior up to the bond strength of the bar. Figure 11-1 shows typical bond-slip curves observed during experimental testing for two failure modes: (1) full pullout slipping failure in which the external concrete remains intact as the reinforcing bar pulls out completely, and (2) splitting failure, in which the concrete fractures radially before reaching the maximum bond strength. In the same figure, idealized models are presented for both cases.



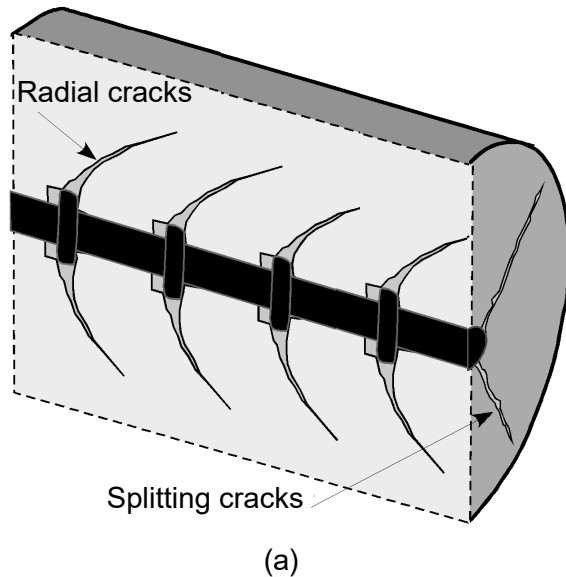
**Figure 11-1 Typical Bond Stress vs. Relative Slippage  $s$  Showing Full Pullout Failure and Splitting Failure with Idealized Model Fits**

When lateral confinement increases, radial stress also rises. Consequently, friction increases, leading to an overall increase in bond-slip resistance. Concurrently, the presence of ribs on the surface of the bar initiates radiating inclined cracks from the tips of these ribs in corrugated bars. The concrete confined between the ribs acts as a strut, generating additional radial stresses. Cracks develop regardless of the concrete cover's thickness. When the cover size is reduced, radial stress from the struts induces splitting cracks, leading to a splitting failure, as seen in Figure 11-2(a). Alternatively, with a sufficiently thick cover, cracks only develop within a limited region around the rebar. The failure mechanism is controlled by the gradual frictional slippage of a cylinder formed by the bar and the locked mortar between the ribs, as seen in Figure 11-2(b). Additionally, when the bar is subjected to torque, the torque-rotation behavior for small rotational angles is expected to follow the same nonlinear pattern as the axial bond-slip relation. However, torsional deformations of rebars are minimal and are not anticipated to significantly affect the overall bond resistance.

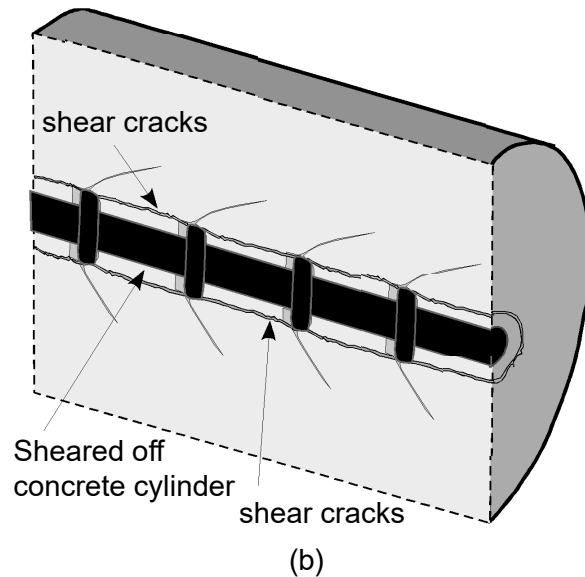
Different modeling scales can be employed to represent these mechanisms. As the modeling strategy progresses from the microscale to the macroscopic scale, physical interactions at lower scales must be integrated into constitutive relations. Although lower scales are essential for expressing and capturing material heterogeneity, bar surface geometry, and potential defects, macroscopic or engineering scales are necessary for simulating large structural elements while maintaining computational efficiency.

In this work, the adopted modeling approach begins from an intermediate level, focusing on main concrete heterogeneity (coarse aggregate mesoscale), subsequently integrating with both macroscopic and microscale considerations.

Splitting failure with limited concrete cover thickness



Bond failure with enough concrete cover thickness

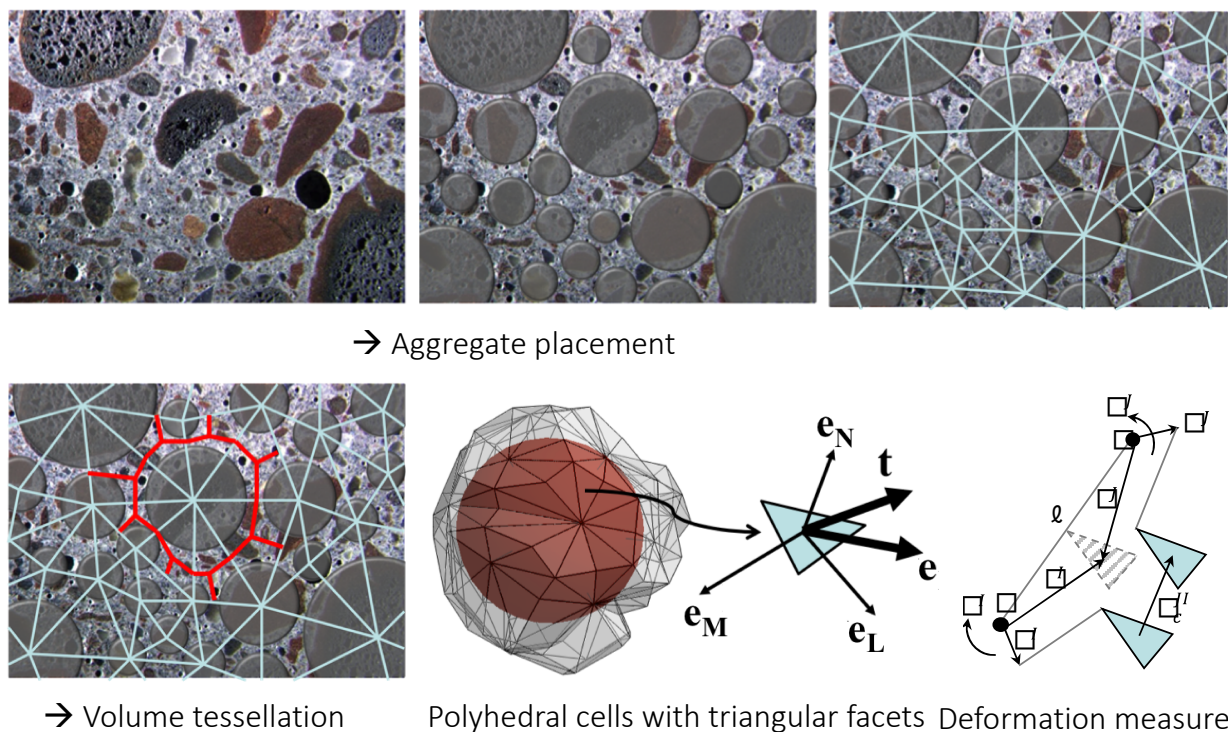


**Figure 11-2 Failure Modes and Crack Development During a Pullout Test: (a) Splitting Failure Mode, and (b) Slipping Failure Mode**

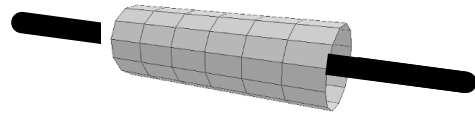
## 11.2 Lattice Discrete Particle Model

At the mesoscale, the LDPM (Cusatis et al., 2011a, 2011b) is utilized alongside bar frame elements (beam elements with both translational and rotational degrees of freedom) interacting with the LDPM concrete model through 2D interface elements. LDPM is a mesoscale discrete model for concrete offering robust capabilities in simulating concrete failure under multi-axial static and dynamic loading conditions. It represents concrete as a collection of interacting large aggregate pieces modeled as spherical particles. These particles are randomly generated and positioned according to the actual concrete particle size distribution. Computational nodes are defined at the centers of these particles, accommodating translational and rotational degrees of freedom. A tetrahedral mesh is created using Delaunay tetrahedralization, followed by a volume tessellation similar to Voronoi tessellation, but with intersections located in the center of the gap between particle pairs rather than at the midpoint between their centroids. These intersections form triangular facets around each particle, composing polyhedral cells that enclose it. Figure 11-3 illustrates a 2D conceptualization of the geometry generation process. Notably, facet centroids serve as locations where vectorial stress-strain relationships are defined. Strain measures are determined based on displacement differences between particle centroids using rigid body kinematics derived from nodal displacements and rotations. Vectorial stresses relate to strains through distinct constitutive relationships representing (1) cohesion and friction during tension and tension-shear deformations, (2) plastic deformation under pure shear, and (3) material compaction and pore collapse under compression and compression-shear. LDPM has been extensively employed to model various concrete behaviors, including the formation of

damage, aging, and deterioration in reinforced concrete. To model reinforcement, one approach involves using 3D elements to represent the actual geometry of the rebar surrounded by LDPM. Although theoretically feasible, this method requires LDPM to simulate the very fine aggregate within the mortar layer surrounding the rebar, necessitating consistent mesh sizes that escalate computational costs. Furthermore, detailed information about the concrete-rebar interface and the mechanical properties of mortar near the rebar is crucial but is often unavailable from current experiments. Therefore, a simplified approach is adopted relying on established bond-slip models from literature as constitutive laws for 2D interface elements generated cylindrically around the rebar. The rebar itself is modeled using 1D frame elements directly connected to these interface elements. Figure 11-4 illustrates the details of these elements and the theoretical constitutive law for the bond model. A short description of the stress-strain relationships for concrete and concrete-rebar interactions in LDPM, as well as the constitutive laws for the rebar, are presented here.

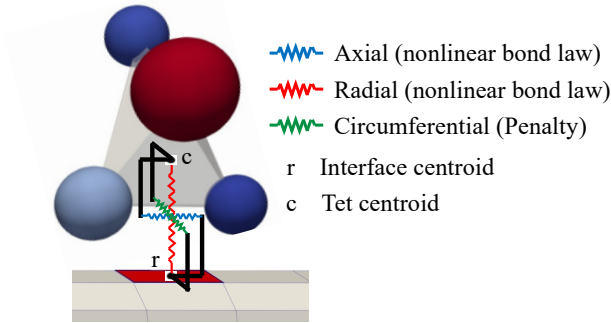


**Figure 11-3 Illustration of Generation Process of the Internal Mesostructure of Concrete Using LDPM Showing Resulting Cells and Discrete Deformation Measure**

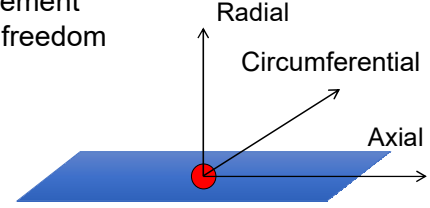


Rebar (1D FE) surrounded by interface elements (2D FEs)

Slippage determined as the relative displacement between points  $r$  &  $c$ .



Interface element degrees of freedom



Nonlinear bond-slip law in the axial direction

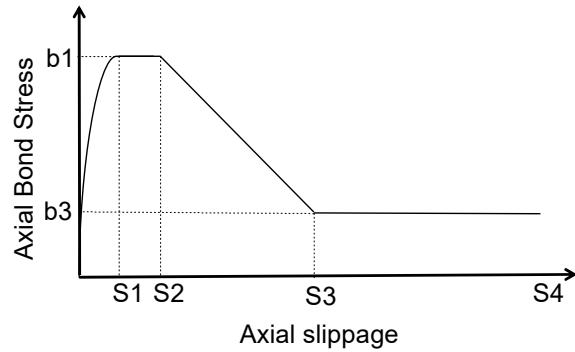


Figure 11-4 Details of the Interface Elements and Bond-Slip Law in the Axial Direction

### 11.2.1 Constitutive Laws for Concrete in LDPM

Strains in LDPM facets are computed from the relative displacement jump of facet centroids that represent the deformation measure based on rigid body kinematics. This displacement jump  $\mathbf{u}_C^I$  between particle/aggregate  $I$  and  $J$  at a facet centroid  $C$  can be calculated as follows (see Figure 11-3):

$$[[\mathbf{u}_C^I]] = \frac{1}{\ell} [\mathbf{U}^J + \boldsymbol{\Theta}^J \times \mathbf{c}^J - \mathbf{U}^I - \boldsymbol{\Theta}^I \times \mathbf{c}^I]$$

The vectors  $\mathbf{U}^K$  and  $\boldsymbol{\Theta}^K$  represent translational and rotational degrees of freedom, respectively, for a particle  $K$ ;  $\mathbf{c}$  is the connecting vector between centroids of facet and particle; and  $\ell$  is the interparticle distance. Facet strain components are defined along normal ( $N$ ) and two mutually perpendicular shear directions ( $M$  and  $L$ ) on a facet plane as  $e_N = \mathbf{n}^T [[\mathbf{u}_C]] / \ell$ ,  $e_M = \mathbf{m}^T [[\mathbf{u}_C]] / \ell$ ,  $e_L = \mathbf{l}^T [[\mathbf{u}_C]] / \ell$ . Using the strain vector  $\mathbf{e} = [e_N \ e_M \ e_L]^T$ , the stress vector  $\mathbf{t} = [t_N \ t_M \ t_L]^T$  is computed with the following constitutive models in elastic and inelastic stages.

#### LDPM Elastic Constitutive Behavior

In the elastic regime, the stress vector is expressed as  $\mathbf{t} = [E_N e_N \ E_T e_M \ E_T e_L]^T$ . Here,  $E_N = E_0$  and  $E_T = \alpha E_0$ , where  $E_0$  is the effective normal elastic modulus at the mesoscale, and  $\alpha$  is the shear-normal coupling parameter. At the mesoscale,  $E_0$  and  $\alpha$  are analogous to macroscale elastic modulus  $E$  and Poisson's ratio  $\nu$ , respectively. The relations between the mesoscale elastic parameters and the macroscale material parameters are  $E_0 = E / (1 - 2\nu)$  and  $\alpha = (1 - 4\nu) / (1 + \nu)$  as presented in Cusatis et al., 2011a.

## Fracture and cohesion under tension and tension-shear

Concrete damage under tension ( $e_N^* > 0$ ) is described in terms of effective strain  $e = \sqrt{e_N^{*2} + \alpha(e_M^{*2} + e_L^{*2})}$  and corresponding effective stress  $t = \sqrt{t_N^2 + (t_M^2 + t_L^2)/\alpha}$ . The stress vector is defined as  $\mathbf{t} = [e_N^* (t/e) \alpha \ e_M^* (t/e) \alpha \ e_L^* (t/e)]$ . The effective stress rate is assumed to be proportional to the effective strain rate ( $\dot{t} = E_0 \dot{e}$ ) and follows the bounding inequality  $0 \leq t \leq \sigma_{bt}(e, \omega)$ , where  $\sigma_{bt}(e, \omega) = \frac{\sigma_0(\omega)}{E_0} \exp[-H_0(\omega)(e - e_0(\omega))/\sigma_0(\omega)]$ . Here,  $\tan(\omega) = e_N^*/\sqrt{\alpha} e_T^* = t_N \sqrt{\alpha}/t_T$ , where  $\sqrt{\alpha} = \sqrt{e_M^{*2} + e_L^{*2}}$ ,  $t_T = \sqrt{t_M^2 + t_L^2}$ , and  $\langle x \rangle = \max\{x, 0\}$ . The limiting strength function  $\sigma_0(\omega) = \sigma_t r_{st}^2 (-\sin(\omega) + \sqrt{\sin^2(\omega) + 4\alpha \cos^2(\omega)})/r_{st}^2 [2\alpha \cos^2(\omega)]$ , where  $r_{st} = \sigma_s/\sigma_t$ , representing the ratio of mesoscale shear strength or cohesion ( $\sigma_s$ ) to tensile strength ( $\sigma_t$ ).  $H_0(\omega)$  defines the post-peak slope for exponential decay of  $\sigma_{bt}(e, \omega)$  for maximum effective strain beyond  $e_0(\omega) = \sigma_0(\omega)/E_0$  as a function of  $\omega$  and expressed as  $H_0(\omega) = H_t(2\omega/\pi)^{n_t}$  and  $H_t = 2E_0/(\ell_t/\ell - 1)$ . Here,  $H_t$  is the softening modulus in pure tension ( $\omega = \pi/2$ ) and  $\ell_t = 2E_0 G_t/\sigma_t^2$ , where  $\ell_t$  = tensile characteristic length, and  $G_t$  = mesoscale fracture energy.

## Friction under compression-shear

Frictional effects under compression are modeled with classical incremental plasticity in LDPM. Incremental shear stress–strain rates are defined as  $\dot{t} = E_T(\dot{e}_M - \dot{e}_M^{*p})$  and  $\dot{t}_L = E_T(\dot{e}_L^* - \dot{e}_L^{*p})$ , where  $\dot{e}_M^{*p} = \lambda \partial \varphi / \partial t_M$ ,  $\dot{e}_L^{*p} = \lambda \partial \varphi / \partial t_L$  with  $\lambda$  as the plastic multiplier for Kuhn–Tucker's conditions  $\varphi \dot{\lambda} \leq 0$  and  $\varphi \dot{\lambda} \geq 0$ . The plastic potential  $\varphi = \sqrt{t^2 + t_L^2} - \sigma_{bs}(t_N)$  for the nonlinear frictional model, where  $\sigma_{bs}(t_N) = \sigma_s + (\mu_0 - \mu_\infty) \sigma_{N0} [1 - \exp(-t_N/\sigma_{N0})] - \mu_\infty t_N$ . Here,  $\mu_0$  and  $\mu_\infty$  denote the initial and final internal friction coefficients, respectively, and  $\sigma_{N0}$  is the transitional normal stress at which transition of friction coefficient occurs.

For compressive loading ( $e < 0$ ), the pore collapse and material compaction behavior are modeled using an incremental strain-hardening formulation. Pore collapse followed by material compaction only initiates at significantly high confinement that can introduce high compressive stresses above 100 MPa. Below this stress level (denoted here as the meso-scale yielding compressive stress  $\sigma_{c0}$ ), the material behaves elastically in compression, with an incrementally elastic normal stress defined as  $\dot{t}_N = E_N \dot{e}_N$ . This is the expected case in the simulations of pullout tests in this work. For further details about the complete formulation under very high confinements that induce pore collapse and compaction, the reader can refer to Cusatis et al. (2011a).

### 11.2.2 Constitutive Laws for Concrete-Rebar Interaction in LDPM

The interaction between concrete and the rebar involves modeling the phenomena described in Section 11.1.1 pertaining to the effects the rebar ribs on the surrounding fine mortar and the concrete layers confining the rebar. This is achieved by using 2D zero-thickness interface elements with vectorial stress-strain relationships (Di Luzio and Cusatis, 2003). The 2D elements surround the rebar and connect its nodes to the nearest LDPM concrete tetrahedron using a line constraint formulation. For a rebar segment of length  $\Delta s$ , the interactive force vector  $\mathbf{f}$  across the interface cylinder (2D elements around the rebar segment) can be expressed as  $\mathbf{f} = K \Delta s \mathbf{u}(x)$ , where  $K$  is a stiffness parameter representative of the local compliance of concrete at the rebar interface, and  $\mathbf{u}(x)$  is the relative displacement vector between the rebar segment and the surrounding concrete. This formulation can be discretized and extended to treat the needed concrete–rebar nonlinear interactions through different constitutive relations. Here, the surface of the rebar is subdivided into finite rectangular interface facets with areas  $a_f$ . The facets divide the rebar surface between two rebar nodes into axial and circumferential

segments (see Figure 11-4). For each facet, the stresses in vectorial form are given as  $\boldsymbol{\sigma} = \{\sigma_a \ \sigma_r \ \sigma_c\}^T$ , where  $\sigma_a$  is axial stress parallel to the rebar axis,  $\sigma_r$  is the radial stress perpendicular to the rebar surface at the center of this facet, and  $\sigma_c$  is circumferential stress tangential to the rebar surface at the center of this interface facet. The slippages in vectorial form are similarly given as  $\mathbf{S} = \{S_a \ S_r \ S_c\}^T$ , where  $S_a$  is axial slippage,  $S_r$  is radial slippage, and  $S_c$  is circumferential slippage. For an interface facet with a normal vector  $\mathbf{n}_f$  to its surface connected to a rebar segment parallel to a direction vector  $\mathbf{n}_r$ , the slippages are related to  $u$  as  $S_a = u \cdot \mathbf{n}_r$ ,  $S_r = u \cdot \mathbf{n}_f$ , and  $S_c = u \cdot (\mathbf{n}_r \times \mathbf{n}_f)$ . Similarly, the forces applied at the concrete nodes and their opposite nodes along the rebar (that are summed over the perimeter and along the segment then lumped at both rebar segment ends) are computed as  $\mathbf{f} = \boldsymbol{\sigma} \cdot a_f$ .

The elastic behavior is given by

$$\begin{bmatrix} \sigma_a \\ \sigma_r \\ \sigma_c \end{bmatrix} = \begin{bmatrix} K_a & 0 & 0 \\ 0 & K_r & 0 \\ 0 & 0 & K_c \end{bmatrix} \begin{bmatrix} S_a \\ S_r \\ S_c \end{bmatrix},$$

where  $K_a$  is axial stiffness,  $K_r$  is radial stiffness, and  $K_c$  is circumferential stiffness.

The inelastic behavior is defined by individually defining constitutive relations for the different stresses and their interactions. Both axial and radial stresses evolve nonlinearly.

#### *Axial Stress Evolution*

The axial stress represents the nonlinear bond-slip relation shown in Figure 11-4 as follows:

$$\sigma_a = \begin{cases} b_1 \left( 1.0 - \left( \frac{S_1 - S_{am}}{S_1} \right)^{n_a} \right) & S_{am} < S_1 \\ b_1 & S_1 \leq S_{am} < S_2 \\ \frac{b_1(S_3 - S_{am}) + b_3(S_{am} - S_2)}{(S_3 - S_2)} & S_2 \leq S_{am} < S_3 \\ b_3 & S_{am} > S_3 \end{cases},$$

where  $S_{am}$  is the maximum absolute axial slippage,  $b_1$  represents the full cohesion and friction bond strength,  $S_1$  is the slippage distance at the end of the elastic regime,  $n_a$  is the exponent defining the order of the elastic part (typically a 2<sup>nd</sup> order elastic part is assumed with  $n_a = 2$ ) which makes the initial axial stiffness  $K_{a0} = n_a b_1 / S_1$ ,  $S_2$  is the slippage at which the cohesion strength starts to degrade and the tunneling behavior is fully developed, and  $b_3$  represents the residual frictional bond strength.

#### *Radial Stress Evolution*

For a plain rebar with no ribs, the radial stress represents the radial contact between the rebar and the surrounding concrete as the rebar moves perpendicular to its axes using a simple penalty formulation  $\sigma_r^{pen} = K_r S_r$  with  $K_r = K_{a0}$ . However, during pullout of ribbed rebars, the rebar ribs initiate radial cracks, as seen in Figure 11-2(a). These cracks subdivide concrete between the ribs into inclined struts. As the rebar is pulled, those struts apply an inclined force on the concrete surrounding the rebar, which in turn causes splitting failure if the cover or confinement is not adequate. With a high enough confinement, the tips of these struts shear off and move with the ribs, thus forming the known tunnel that characterizes bond failure, as seen



in Figure 11-2(a). Therefore, in all cases, an inclined force is initiated first, and then it decays as tunneling progresses. To replicate the radial effect of this force on the radial stress, a rib-induced radial stress  $\sigma_r^{rib}$  is defined a function of  $S_{am}$ , as follows:

$$\sigma_r^{rib} = -\kappa K_r S_{am} \begin{cases} 1.0 & S_{am} < S_2 \\ \frac{S_3 - S_{am}}{S_3 - S_2} & S_2 \leq S_{am} < S_3, \\ 0.0 & S_{am} > S_3 \end{cases}$$

where  $\kappa$  is a rib effect parameter on the radial stress. This expression implies that a compressive rib-induced radial stress  $\sigma_r^{rib}$  increases elastically until cohesion starts to degrade (at  $S_{am} = S_2$ ). Then it decreases toward zero (at  $S_{am} = S_3$ ). By combining the radial contact stress  $\sigma_r^{pen}$  and the rib-induced radial stress  $\sigma_r^{rib}$ , the total radial stress is defined as  $\sigma_r = \sigma_r^{pen} + \sigma_r^{rib}$ .

### Circumferential Stress Evolution

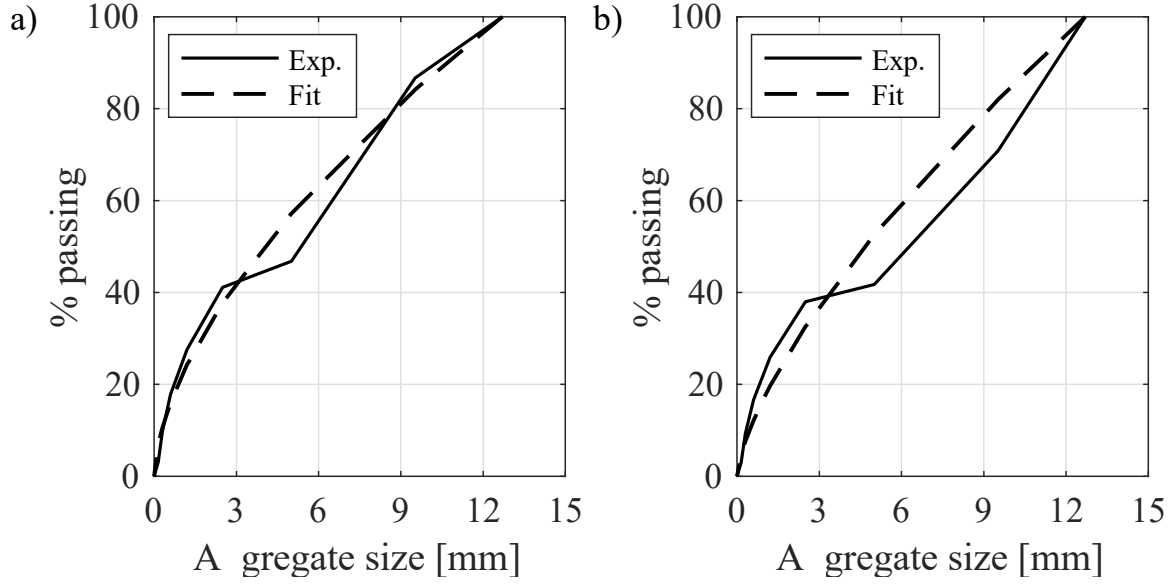
The circumferential stress is induced when the rebar segment is under torque. It is assumed that such torque is very small if it exists. Thus, a simple penalty formulation is also used here, where  $\sigma_c = K_c S_c$  with  $K_c = K_{a0}$ .

### 11.2.3 Model Calibration

LDPM utilizes a set of mix design parameters to generate a realistic mesoscale structure of concrete and another set of material parameters to represent different failure modes. To generate the mesostructure, mixing proportions are essential for determining aggregate volume, and the particle size distribution is crucial for random particle generation. In its simplest form, particle generation in LDPM can be achieved by assuming an idealized Fuller curve. A Fuller curve defines the passing fraction % $p$  of aggregate (sieve) size  $d$  by weight as a power function of the maximum aggregate size  $d_a$  as % $p = 100(d/d_a)^{n_f}$ , where  $n_f$  is the Fuller coefficient. Therefore, based on experimental data,  $n_f$  is calibrated by fitting the particle size distribution using the least squares method. The fitted Con-A and Con-B particle size distributions are depicted in Figure 11-5(a) and (b), respectively. Table 11-1 presents the concrete mix design parameters used for model generation, including the Fuller coefficients obtained from the fitting process.

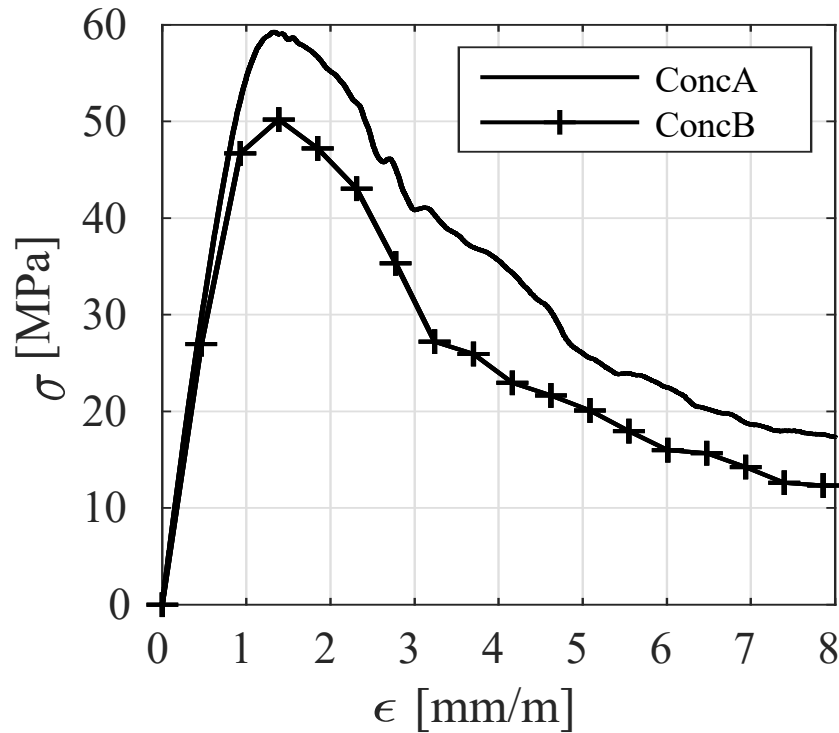
**Table 11-1 Mix Design Parameters Used for the LDPM Mesostructured Generation**

Parameter	Con-A	Con-B
<b>Cement content <math>c</math> (kg/m<sup>3</sup>)</b>	366	354
<b>Water content (kg/m<sup>3</sup>)</b>	183	177
<b>Aggregate content (kg/m<sup>3</sup>)</b>	1794	1814
<b>Water-to-cement ratio <math>w/c</math></b>	0.50	0.50
<b>Aggregate-to-cement ratio <math>a/c</math></b>	4.90	5.12
<b>Aggregate volume fraction</b>	0.70	0.71
<b>Fuller curve coefficient (<math>n</math>)</b>	0.60	0.69



**Figure 11-5 Experimental Particle Size Distribution and Fitted Fuller Curves for (a) Con-A and (b) Con-B**

To reproduce various failure mechanisms in concrete, the mechanical parameters used in the previously defined constitutive relations for LDPM must be calibrated. However, to model concrete under limited confinement, LDPM represent concrete failure by replicating strut-tie effects within its mesoscale structure. These effects are captured by fracture/tension-shear along the ties and compression-shear along the struts. In other words, neither pore collapse nor material compaction is expected, so only elastic, fracture, and shear parameters must be calibrated. As explained earlier, the mesoscale modulus  $E_0$  and the normal/shear coupling parameter  $\alpha$  can be directly computed using their relationships with Young's modulus  $E$  and Poisson's ratio  $\nu$ . Because Poisson's ratio was not measured in this study, a typical value of 0.17 is assumed, leading to  $\alpha = 0.25$ .  $E_0$  can be computed from  $E$  for each concrete mix. It is shown in multiple LDPM publications that only three parameters must be calibrated for low confinement behavior: tensile strength  $\sigma_t$ , tensile characteristic length  $\ell_t$ , and shear strength  $\sigma_s$ .  $\sigma_t$ , and  $\ell_t$ , relative to cohesive fracture behavior. These parameters are linked to the mesoscale fracture energy  $g_t$  of concrete. In LDPM, it was shown that  $g_t$  is equal to the initial fracture energy  $g_f$  (Cusatis and Cedolin, 2007). Thus,  $g_f$  can be estimated following Bažant and Becq-Giraudon (2002) as  $g_f = (f'_c/0.051)^{0.46}(1 + d_a/11.27)^{0.22}(w/c)^{-0.30}$ . Additionally,  $\sigma_t$  closely approximates the splitting tensile strength of concrete  $f_{sp}$ , which is estimated here following ACI-318-19 as given  $\sigma_t = f_{sp} = 0.56\sqrt{f'_c}$  (in MPa units). Finally,  $\sigma_s$  requires calibration from simulations of uniaxial compression tests to match the experimental concrete compressive strength  $f'_c$ . This calibration procedure is detailed in Alnaggar and Bhanot (2018). Figure 11-6 displays simulated stress-strain curves for Con-A and Con-B, along with the experimental values. The calibrated LDPM parameters are listed in Table 11-2.



**Figure 11-6 Numerically Simulated Uniaxial Compression Stress-Strain Curves for Con-A and Con-B**

**Table 11-2 Calibrated LDPM Parameters**

Parameter			
Young's modulus	$E_0$ (GPa)	55.94	51.52
Tensile strength	$\sigma_t$ (MPa)	4.31	3.97
Fracture energy	$g_t$ (N/m)	37.37	33.58
Characteristic length	$\ell_t$ (mm)	224.82	219.34
Shear to tensile strength ratio	$\sigma_s/\sigma_t$ (-)	3.87	3.30

#### 11.2.4 Calibration of the Bond Model Parameters

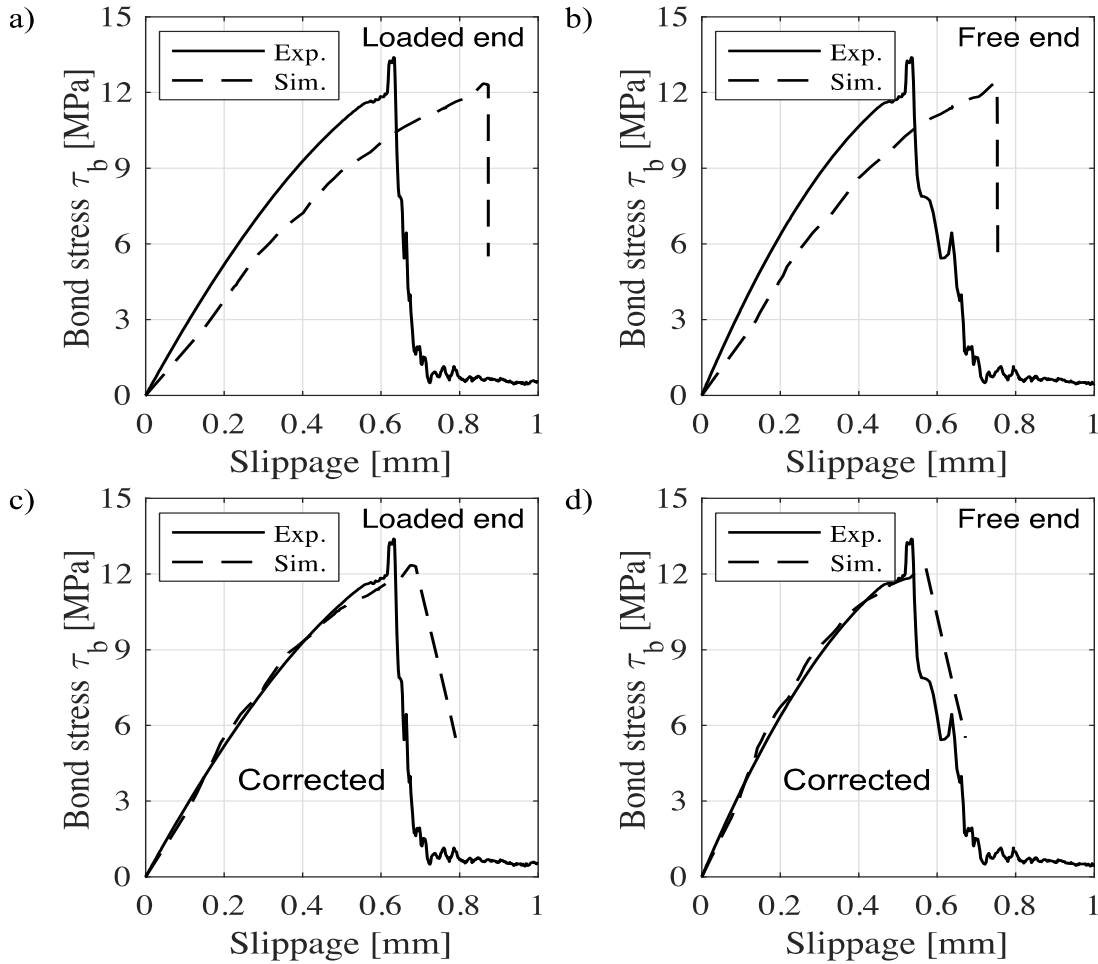
As previously mentioned, only pullout test results for Con-A and Con-B are available using a single rebar size and bond length, with splitting reported as the failure mode in both cases. Consequently, the bond-slip axial behavior cannot be fully calibrated from these experiments. Therefore, the axial stress bond-slip law parameters were calculated based on a similar bond-slip law proposed by Lettow (2006). In Lettow's dissertation, curve fitting relations of the axial

stress obtained from diverse experiments are presented as functions of the rebar diameter  $d_s$ , the rib height  $a_m$ , the rib spacing  $c_m$ , and  $f'_c$ . The computed parameters and the formulas used to compute them from Lettow (2006) are listed in Table 11-3. Note here that the rebar used in this experimental campaign was #2, with a diameter of ¼ in. (6.35 mm). However, in Lettow (2006), the values for  $a_m$  and  $c_m$  were based on standard metric rebars (Table 4.11 in Lettow 2006). Therefore, approximate values of these parameters were taken for the closest rebar diameter (6 mm) in the table, giving  $a_m = 0.25$  mm and  $c_m = 5.0$ . It is assumed also that the elastic part follows a second-degree parabolic curve.

**Table 11-3 Bond-Slip Model Parameters**

Parameter	Formula	Con-A	Con-B
<b>b1 (MPa)</b>	$20(a_m/c_m)^{0.8} (f'_c)^{0.5}$	14	12.86
<b>b3 (MPa)</b>	$0.4b1$	5.6	5.6
<b>S1 (mm)</b>	$b1/[120(a_m/c_m) + 0.23(f'_c)]$	0.725	0.737
<b>S2 (mm)</b>	$S1+0.8$	1.525	1.537
<b>S3 (mm)</b>	$c_m$	5.0	5.0

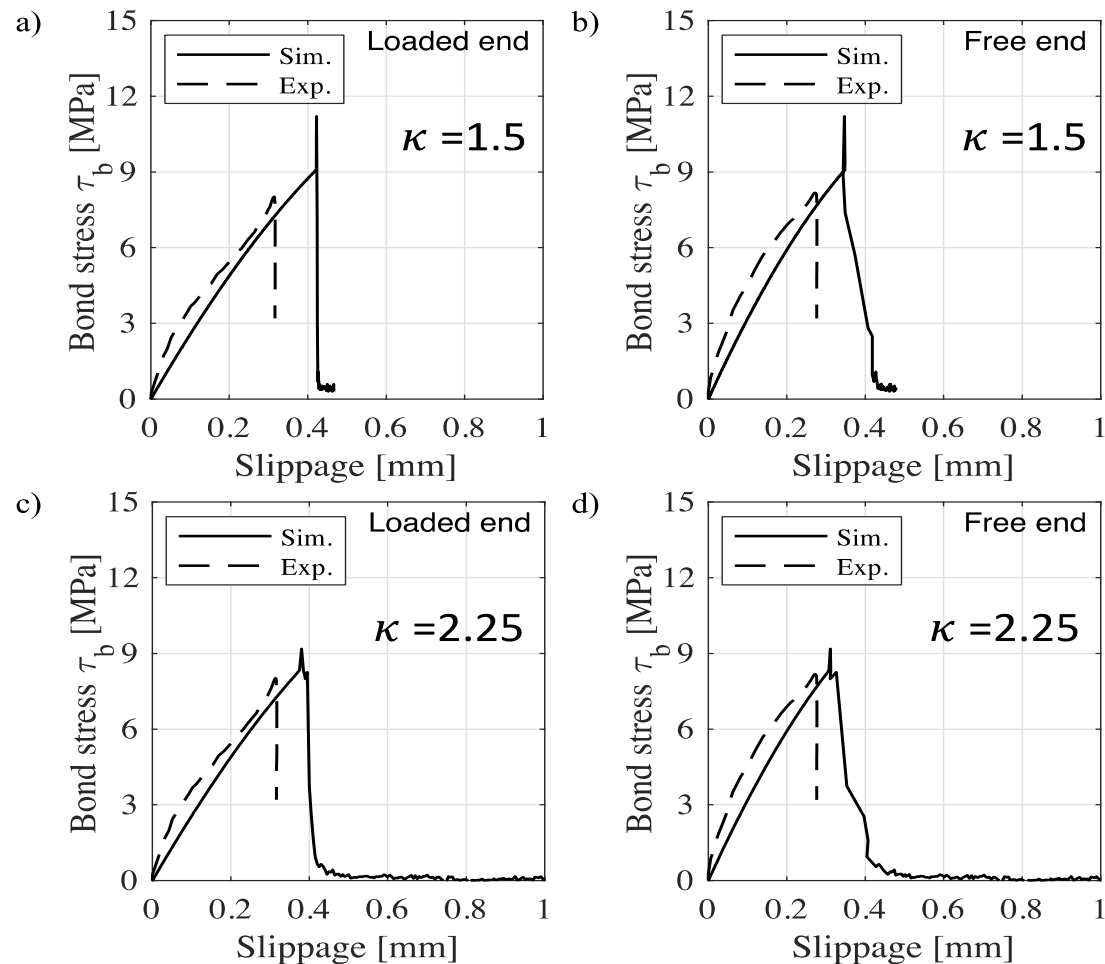
At this stage, the rib effect parameter  $\kappa$  remains for calibration. The Con-A specimen was used for calibration through simulations of the pullout test, resulting in an identified  $\kappa=1.5$ . As depicted in Figure 11-7 (a) and (b), the numerical peak load closely matches the experimental data. Because of elasticity in the testing system and potential imperfections, the initial stiffness in the model is higher than that observed in experiments. Aligning the experimental data to match the initial stiffness from simulations achieves good agreement, as shown in Figure 11-7 (c) and (d).



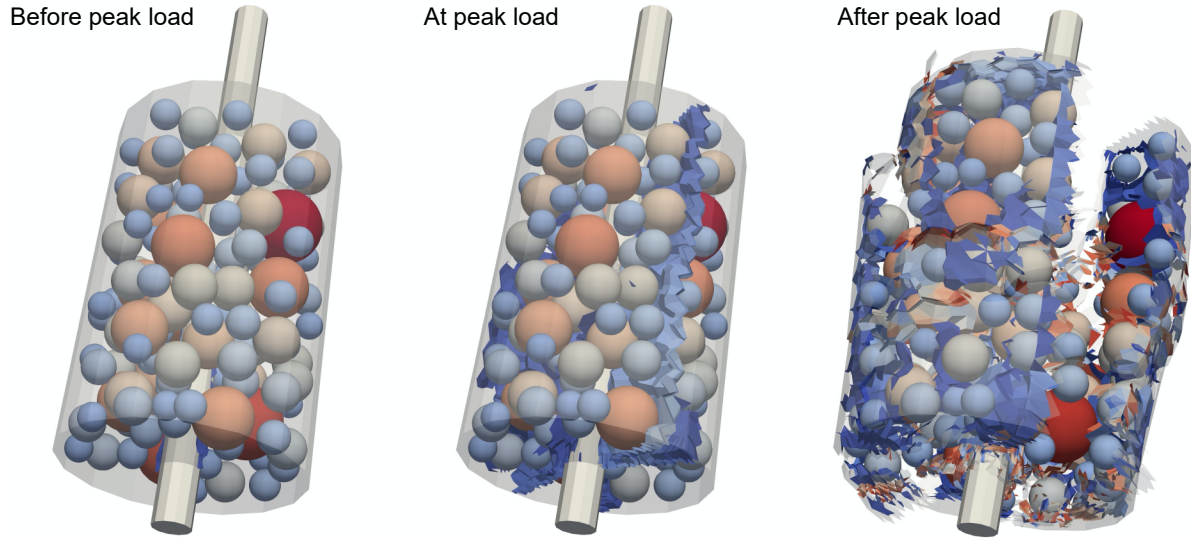
**Figure 11-7 Numerically Simulated Pullout Test Results for Con-A Specimens Showing Bond Stress vs. Experimentally Measured Slippage of the (a) Loaded End, (b) Free End, and Corrected Experimental Slippage of the (c) Loaded End and (d) Free End**

Using these parameters, pullout tests for Con-B specimens were also simulated, and the results are shown in Figure 11-8 (a) and (b). It is worth noting here that pullout test results for Con-B showed a higher peak in the simulations compared to the experiments when the same parameter is used as shown in Figure 11-8. The experiments show 8 MPa for Con-B compared to 12 MPa for Con-A, resulting in a ratio of 66.7%. This contrasts with the ratio of their respective compressive strengths, which is  $50.3/59.3 = 84.8\%$ . However, considering that the failure mode is splitting, one would expect the ratio to align with their respective splitting strength ratio, which is proportional to the square root of the compressive strength ratio and is thus expected to be approximately 92%. This prediction is consistent with the model because it predicts Con-B to fail at 11 MPa and Con-A to fail at 12 MPa, resulting in a ratio of  $11/12 = 91.67\%$ . Given uncertainties in the experiments and challenges in the manufacturing process, this difference may be attributed to imperfections created around the rebar or in the concrete. To investigate further, Con-B was used for calibration instead, resulting in adjusting the parameter  $\kappa$  to 2.25, as shown in Figure 11-8 (c) and (d). Note that the experiments and simulation results are very close. It can be deduced from these results is that  $\kappa$  in Con-B

specimens is higher than in Con-A. Because Con-B has a lower compressive strength, one could expect the opposite. The origin of this observation is unclear. One may hypothesize that possible casting imperfections along the reinforcement of the bond may affect the overall bond strength. Despite this unclarified observation, the calibrated parameters provide reasonable prediction of the splitting failure mode. Figure 11-9 illustrates the evolution of cracking around the internal coarse aggregate.



**Figure 11-8 Numerically Simulated Pullout Test Results for Con-B Using  $\kappa = 1.5$  Showing Bond Stress vs. Experimentally Measured Slippage at (a) the Loaded End and (b) the Free End, and Numerically Simulated Results Using  $\kappa = 2.25$  at (c) the Loaded End and (d) the Free End**



**Figure 11-9 Stages of Crack Formation within the Mesostructure of Concrete as Splitting Failure Develops**

#### *Parametric Study of Pullout Behavior*

As mentioned previously, the values of the fracture energy, the tensile strength, and the bond-slip model were assumed based on literature data. As described in this section, the pullout simulations were performed with different values of these parameters within the reported literature ranges.

#### *Effect of Changing the Rib Effect Parameter*

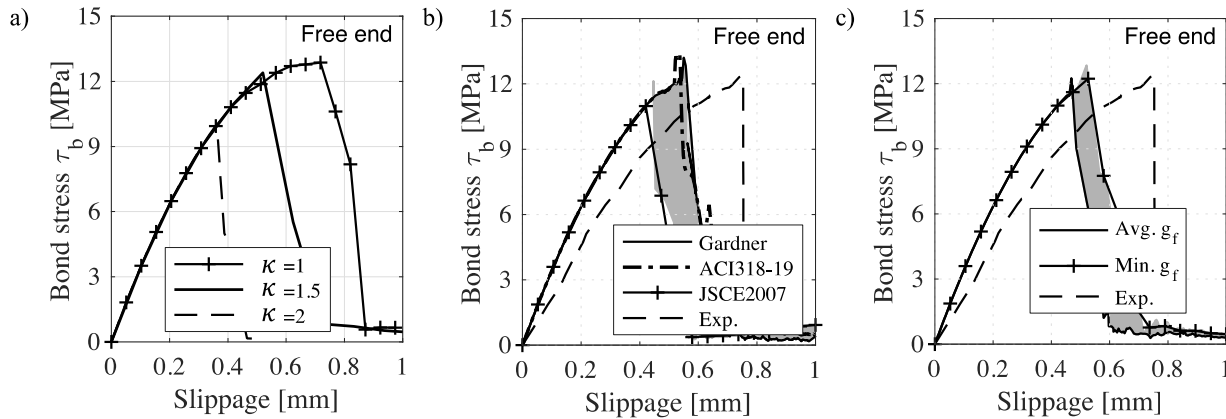
As was shown in the calibrations, the rib effect parameter  $\kappa$  has a significant effect. In fact, if it had been put to zero, then the splitting failure would not have been reproduced. To illustrate the effect of  $\kappa$  on the predicted pullout performance, simulations were performed for Con-A with  $\kappa$  values of 1, 1.5, and 2 which correspond to peak bond stresses of 13, 12, and 10 MPa, respectively, as seen in Figure 11-10 (a). This shows that the higher the value of  $\kappa$ , the faster the induced radial stress accumulates at lower axial slippage, causing the sample to split earlier.

#### *Effect of Changing the Tensile Strength*

As mentioned previously,  $f_{sp}$  predicted using ACI-318-19 is considered a mid-range value of experimental data, as shown in Alnaggar and Bhanot (2018). Therefore, it will be estimated again using a lower fit formula based on the JSCE-2007 Japanese standard ( $f_{sp} = 0.23(f'_c)^{2/3}$ ) and an upper fit using Gardner's model (1990) ( $f_{sp} = 0.33(f'_c)^{2/3}$ ). In this work all other estimated values are kept the same, including the fracture energy  $g_f$ , the bond-slip law, and the calibrated  $\kappa$  of 1.5. Results are shown in Figure 11-10 (b). As expected, a slightly higher peak stress is observed using Gardner's model compared to the ACI-318-19 result. However, the peak stress was lower by approximately 11 MPa in the case of JSCE-2007.

### Effect of Changing the Initial Fracture Energy

Additionally, as presented in Bažant and Becq-Giraudon (2002),  $g_f$  can vary largely for the same concrete parameters—approximately  $\pm 40\%$ . In the present study, only the lower value of  $g_f$  was tested because the mean value of  $g_f$  already gives good results, and it is expected that by increasing it, the predicted peak stress will be higher than experimentally observed. Figure 11-10 (c) shows the results for the mean value of  $g_f$  and a minimum value estimated to that mean value. As illustrated in the figure, the effect of  $g_f$  on the bond strength is limited. In conclusion, the most important parameter governing the bond strength prediction is the rib effect parameter which requires the measurement of radial deformations during pullout.



**Figure 11-10 Parametric Study Results, Including (a) the Effect of Changing the Rib Effect Parameter, (b) the Effect of Changing Tensile Strength, and (c) the Effect of Changing the Initial Fracture Energy**

The LDPM parameters obtained through calibration for the different studied cases are listed in Table 11-4. It must be noted here that elastic parameters  $E_0$  and  $\alpha$  are kept unchanged. For the rib effect parameter study, all LDPM parameters listed in Table 11-2 were kept unchanged.

**Table 11-4 LDPM Calibrated Parameters for the Different Parametric Study Cases**

Parameter	Con-A (reference)	Gardner	JSCE 2007	Minimum $g$
$S_t$ (MPa)	4.31	5.02	3.50	4.31
$G$ (N/m)	37.37	37.37	37.37	22.42
$l_t$ (mm)	224.82	166.02	341.77	134.89
$S_s / S_t$ (-)	3.87	3.33	4.77	4.29

### Conclusions

The LDPM simulations consistently show that the failure mode of the small-size specimens (40 mm diameter) occurs from concrete splitting. To ensure that the failure mode is governed by frictional slipping at the interface between the steel bar and the concrete, it is necessary to add a confining jacket.





## 12 IRRADIATED PROPERTIES OF CONCRETE CONSTITUENTS

The effects of irradiation on the properties of concrete and concrete constituents are driven by varied mechanisms that can be separated based on the understanding that the neutron radiation-induced damage occurs mainly in the well-crystallized aggregate-forming minerals, and gamma radiation-induced radiolytic effects cause further dehydration of water-bearing constituents such as the cement hydrates.

### 12.1 Neutron Irradiation Effect on Concrete Constituents

It is clearly established that neutron irradiation at energies higher than 10 keV is responsible for >99% of the total dpa in rock-forming minerals irradiated in test reactors or in LWR concrete biological shields (Remec, 2015). The damaging threshold energy can also be conventionally taken at 0.1 MeV, which corresponds to approximately >95% of the total dpa under the same irradiation conditions. Note that here, the term *fast neutron* designates neutrons at energies higher than 10 keV, whereas that term often refers elsewhere (e.g., for metal) to energies higher than 1 MeV.

Fast neutron colliding with atom nuclei causes atom ejections (primary knocked out atoms), which in turn may collide and displace adjacent atoms (secondary knocked out atoms). Depending on the nature of the atomic bond in the minerals' crystalline network distortion, voids and bond breakage may occur, thus causing amorphization (or *metamictization*) of the minerals. This process is accompanied by a change in the physical and chemical properties of the minerals. These phenomena also exist beyond amorphization. Note that in this research, the chemical effects—the radiation-enhanced dissolution of minerals and radiochemistry of the interaction between minerals and cement hydrates—are not considered.

#### 12.1.1 Radiation-Induced Volumetric Expansion

##### 12.1.1.1 *Minerals Radiation-Induced Volumetric Expansion (RIVE)*

The most important documented effect in this analysis is the change of density that generally results in RIVE, a mechanism that is mineral dependent:

1. RIVE maximum amplitude is maximum for  $\alpha$ -quartz at 17.8%.
2. Silicates (e.g., quartz, feldspars, micas, pyroxenes, olivine) are generally more prone to RIVE than carbonates (e.g., calcite, dolomite, ankerite). Other oxides (corundum, hematite, periclase) exhibit intermediate RIVE amplitudes (Le Pape et al., 2018).
3. RIVE generally follows a sigmoidal curve with increasing fast neutron fluence. The RIVE rate varies with irradiation temperature. Irradiation conducted at higher temperatures leads to recovering irradiation-induced defects. Thus, the RIVE rate decreases with increasing irradiation temperature (Bykov et al., 1981).
4. RIVE is anisotropic. The volumetric expansion is distributed along the crystallin axis (Denisov et al., 2012).

5. Based on the observations presented in this report regarding the dimensional change of the aggregate specimens irradiated in the LVR-15/XK1 position, it can be hypothesized that the fast neutron flux affects the RIVE rate: lower flux appears to cause lower RIVEs. At this stage of the research, the knowledge of this potential flux effect is too limited to draw a conclusion about how it may affect the RIVE rate of the rock-forming mineral. Therefore, flux effect is ignored in the proposed modeling.

The RIVE of the most common rock-forming minerals can be estimated from empirical expressions available in Le Pape et al., 2018.

#### 12.1.1.2 *Aggregates RIVE*

Aggregates are complex assemblages of minerals. Each forming mineral grain is subject to specific radiation-induced expansions (amplitude and direction). Thus, the overall expansion of the aggregates is the result the assembled contribution of all minerals. In general, distribution of the mineral orientations is random. Thus, the aggregate's RIVE is considered isotropic. Because two adjacent minerals may have different chemical compositions and orientations, incompatible strains can be created when RIVE increases. When these incompatible strains exceed the strength of minerals or the strength of the grain boundary, cracks form, propagate, and widen with increasing fluence.

From a modeling strategy point of view, two situations can be distinguished:

- **Before crack formation**, the aggregate RIVE can be obtained using classical mean field homogenization techniques (e.g., Voigt-Reuss-Hill estimates) or numerical models such as the fast Fourier transform–based code Microstructure Oriented Scientific Analysis of Irradiated Concrete (MOSAIC; Torrence et al., 2021; Cheniour et al., 2022) or the Rigid Body Spring Network models (RBSN, Khmurovska, and Štemberk 2021).
- **After crack formation**, the total volumetric expansion of the aggregates must include the crack volume. The upper bound estimate of the crack volume can be obtained using empirical expressions proposed by Le Pape et al. (2020b). However, numerical models can provide better estimates.

#### 12.1.1.3 *Cement Hydrates*

Cement hydrates include hydrogen bonds (weak ionic bonds). Covalent bond–structured minerals are necessary to develop RIVE. There is no experimental evidence showing that neutron RIVE is a predominant mechanism in cement hydrates. Neutrons are unlikely to develop significant damage in the cement paste because the paste's poor crystallinity and high porosity prevent any defect accumulation (Kontani et al., 2013). However, irradiated hardened cement waste and cement grout exhibit shrinkage caused by dehydration (Gray, 1971).

### 12.1.2 **Irradiated Elastic Properties**

#### 12.1.2.1 *Irradiated Minerals Elastic Properties*

Irradiation-induced amorphization—the disordering of the crystalline structure—leads to the *isotropization* of the minerals. Data on the evolution of the varied elastic constants with increasing neutron fluence are very limited in the literature.

These data are limited to quartz and vitreous silica (Mayer et al., 1956, 1960). Each constant evolves differently: some increase, some decrease, and some evolve nonmonotonically.

Whereas the notion of Young's modulus is evidently inadequate to describe the elastic properties of pristine minerals because of their anisotropic structures, the Young's modulus of a randomly oriented polycrystalline assemblage made of a single mineral (with the same chemical composition) is a property that makes it easier to understand the evolution of the elastic properties of irradiated minerals. Molecular dynamics (MD) simulations make it possible to estimate the pristine and irradiated Young's modulus of minerals. Table 12-1 reproduces the results obtained by Krishnan et al. (2018) for a selection of silicates. It can be observed that irradiation-induced amorphization does not always cause a loss of elastic modulus. For example, the modulus of quartz exhibits a gain of ~20%, whereas the moduli of albite and anorthite, which are feldspar minerals commonly found with quartz, decrease by -5% to -20%. These changes are accompanied by radiation-induced expansions which are much higher in quartz than in feldspars.

**Table 12-1 Pristine and Irradiated Density and Young's Modulus of Minerals (Krishnan et al., 2018)**

Minerals		Density (g.cm <sup>-3</sup> )		Young's modulus (GPa)	
Name	Composition	Pristine	Irradiated	Pristine	Irradiated
<b>Albite</b>	NaAlSi <sub>3</sub> O <sub>8</sub>	2.61 (2.62)	2.45 (2.46)	111.20 (104.3)	91.02
<b>Almandine</b>	Fe <sub>3</sub> I <sub>2</sub> Si <sub>3</sub> O <sub>12</sub>	4.20 (4.30)	3.42	179.79	104.54
<b>Anorthite</b>	CaAl <sub>2</sub> Si <sub>2</sub> O <sub>8</sub>	2.73 (2.76)	2.81	113.01 (116.7)	107.62
<b>Diopside</b>	MgCaSi <sub>2</sub> O <sub>6</sub>	3.21 (3.27)	2.85 (3.09)	176.85 (167.6)	96.11
<b>Enstatite</b>	MgSiO <sub>3</sub>	3.04 (3.20)	2.79 (2.98)	142.57 (186.1)	106.14
<b>Jadeite</b>	NaAlSi <sub>2</sub> O <sub>6</sub>	3.26 (3.34)	2.65	200.73 (212.8)	86.374
<b>Nepheline</b>	NaAlSiO <sub>4</sub>	2.48 (2.57)	2.49	74.61	83.49
<b>Quartz</b>	SiO <sub>2</sub>	2.66 (2.64)	2.19 (2.20)	104.77 (96.6)	125.97 (118.1)

*Numbers in italic font correspond to experimental data.*

Based on the MD simulation results, Krishnan (2018) suggests an empirical expression to estimate the Young's modulus of an equivalent polycrystalline assemblage for a single mineral with randomly distributed orientation using a cubic function of the density change (Krishnan et al., 2019).

#### 12.1.2.2 Irradiated Aggregates Elastic Properties

Similar considerations regarding aggregate RIVE also apply to the elastic properties of irradiated aggregates which are affected both by the change of elastic properties of the irradiated constitutive minerals and the formation of cracks caused by incompatible mineral RIVEs.

Post-neutron irradiation measurements of the residual Young's modulus of varied rocks show that Young's modulus and RIVE are correlated (Denisov et al., 2012). This observation may seem contradictory with the data presented in Table 12-1, which provide theoretical estimates of the Young's modulus of uncracked irradiated polycrystalline system made of a single mineral type. When rocks are irradiated, the mismatch strains between the varied forming minerals cause cracking which is responsible for the loss of Young's modulus observed in irradiated rocks. In summary, the main reason for this correlation is that although the elastic properties of irradiated aggregate-forming minerals may not always decrease, the evolution of the effective Young's modulus of irradiated aggregates is dominated by irradiation-induced cracking. Figure 12-1 contains the data presented by Denisov et al. (gray marks) and data obtained by ORNL on aggregates provided by JCAMP (JEEP-II irradiation, colored marks). The data are presented as the ratio of the irradiated Young's modulus to the unirradiated modulus (y-axis) against the total RIVE of the corresponding aggregates (x-axis).

The data collected by Denisov et al. (2012) are represented using the following marking system:

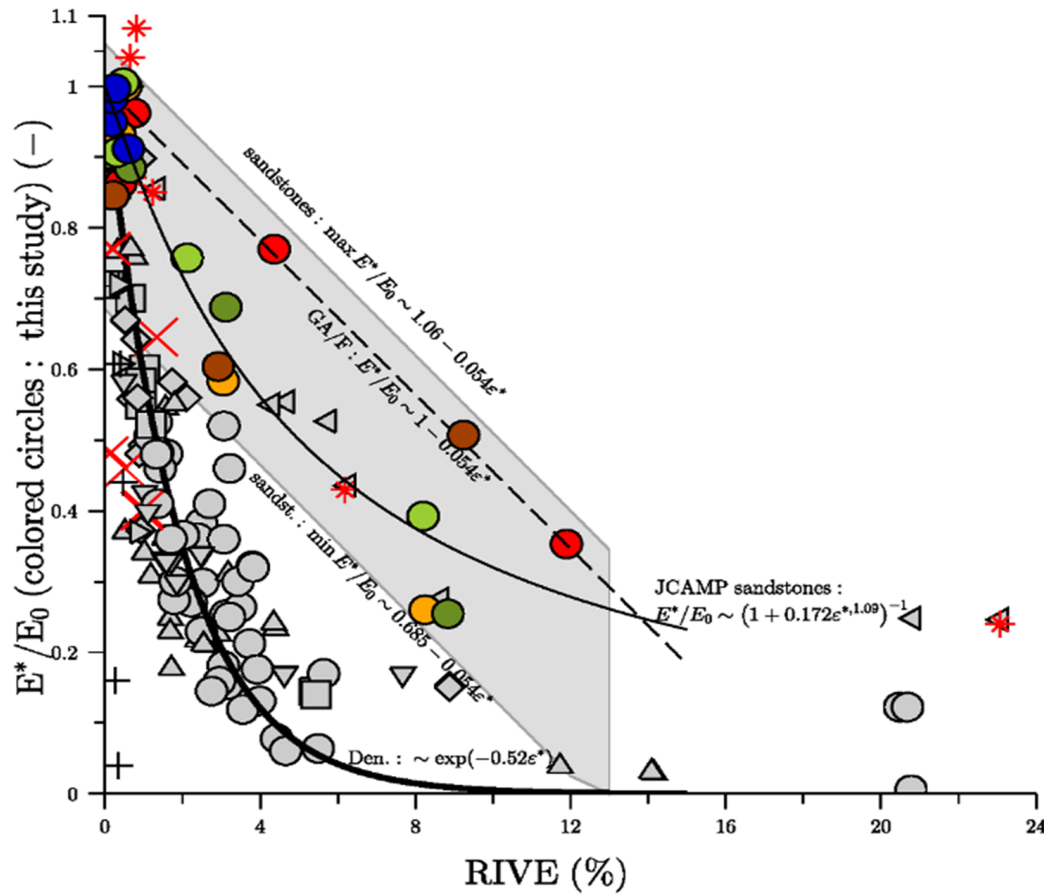
Upward pointing triangles: albitite, gabbro, labradorite, urtite  
 Left-pointing triangles: auleurolite  
 Diamonds: basalt, diabase  
 Circles: granite, graniodorite, diorite, andesite  
 Squares: hornblendite  
 x: dolomite, limestone  
 Right-pointing triangles: magnesite  
 Downward pointing triangles: pyroxenite, peridotite, olivinite, dunite  
 \*: sandstone  
 +: siderite

The general trend that the relative modulus exhibits is an exponential decrease with the RIVE:

$E^*/E_0 \sim \exp(-0.528\varepsilon^*)$ , with  $\varepsilon^*$  the RIVE expressed in percent.

The color marks (JCAMP aggregates analyzed by ORNL) correspond to one metachert aggregate GA(F) in red, four felsic sandstones including aggregates GB(E) in brown, and one calcic limestone as indicated by blue marks. It can be observed that these five sedimentary aggregates exhibit a trend that differs from Denisov's data, which are mostly obtained from igneous rocks. Aggregate GA(F) follows a linear trend:  $E^*/E_0 \sim 1 - 0.054\varepsilon^*$ , whereas the felsic sandstones show a faster drop of modulus with RIVE that is approximated by the fitting function  $E^*/E_0 \sim [1 + 0.172(\varepsilon^*)^{1.09}]^{-1}$ . This fitting function appears to be applicable for  $\varepsilon^* < \sim 4\%$ . The sandstone data collected by Denisov, as indicated by red stars, also appear to follow that trend. Hence, the data plotted in Figure 12-1 suggest that the elastic properties of igneous rocks and sedimentary rocks are affected differently by RIVE, even though they all contain silicates. It can be hypothesized that this difference may be attributed to the grain boundary properties because the rock formation processes differ.

For the data analysis obtained from the irradiation experiment conducted in the LVR-15 reactor, it was assumed that the empirical equations presented above are applicable to aggregate GA(F) and GB(E).



**Figure 12-1 Young's Modulus of Irradiated Aggregates (Relative to the Pristine Value) and Aggregate RIVE**

## 12.2 Gamma Irradiation Effect on Concrete Constituents

### 12.2.1 Cement Hydrates

C–S–Hs (calcium silicate hydrates) are the main binding hydrates found in ordinary Portland hardened cement paste. Pre-dried synthesized C–S–Hs were irradiated at a dose rate of 30 Gy/s at the Gamma Irradiation Facility (GIF) at SNL to reach gamma doses of 24 and 189 MGy (Baral et al., 2022).

The post-irradiation Young's modulus increases from 23.5 GPa (pristine) to ~27 GPa at 189 MGy. This gain is attributed to the decrease in basal spacing and removal of interlayer water.

### 12.2.2 Cement Paste

Hardened cement paste specimens subject to combined neutron and gamma irradiation in the Herald reactor at the Atomic Weapons Research Establishment, Aldermaston, UK, did not show a change in Young's modulus and tensile strength (Gray, 1971).

### **12.2.3 Concrete**

Co<sup>60</sup> gamma irradiation conducted at the Japan Atomic Energy Agency (JAEA) Takasaki Advanced Radiation Research Institute concluded that the increase of concrete compressive strength was caused by irradiation-induced heating and drying (Maruyama et al., 2017). Hence, the properties of gamma-irradiated concrete are governed by the loss of mass (dehydration). During combined neutron and gamma irradiation, aggregate RVE and cement paste shrinkage cause incompatible strains, resulting in microcracking.

## 13 INTERPRETATION OF IRRADIATED AGGREGATE AND CONCRETE DATA

In this section, the properties of aggregates and plain concrete specimens irradiated in the LVR-15/XK1 position are interpreted using various models.

### 13.1 Aggregate Expansion

#### 13.1.1 Analytical Model

The aggregate RIVE is calculated using two bounding equations:

1. The cumulative contribution of the mineral expansion using mean field homogenization theory can be calculated by using equations from Le Pape et al., 2020b. The input data are the weight fractions of minerals obtained from x-ray diffraction (XRD) Rietveld analysis (Maruyama et al., 2017). The RIVE are modeled using empirical equations (Le Pape et al., 2018) fitted on Denisov's data (2012). Note that the stiffness tensors are assumed to be unchanged by irradiation in this model. Because RIVE is obtained from Voigt-Reuss-Hill estimates, this assumption leads to acceptable approximations.
2. The additional crack volume is caused by incompatible strain in the aggregate assemblage. The analytical model can only provide an upper bound estimate based on the analysis of Denisov's data. For both aggregates GA(F) and GB(E), that upper bound estimate is  $\sup(\Delta\phi) \sim 1.86\varepsilon^*$ , where  $\Delta\phi$  is the additional voids / cracks volume, and  $\varepsilon^*$  is the expansion of the uncracked aggregate (Le Pape et al., 2020b). This upper bound is quite inadequate to describe aggregates irradiated at low damaging fluence of approximately  $10^{19}$  n.cm<sup>-2</sup>,  $E > 10$  keV. This bound is more effective for describing the cracking regime closer to  $10^{20}$  n.cm<sup>-2</sup>,  $E > 10$  keV.

Table 13-1 provides a summary of the post-irradiation volumetric changes measured on the GA(F) and GB(E) aggregate specimens irradiated in capsules PPT-B and PPT-C in the JEEP-II reactor (Maruyama et al., 2017) and the specimens irradiated in the XK1 position in the LVR-1r5 reactor. Only the mean volumetric change values are reported in this table. Voigt and Reuss estimates for the uncracked aggregates are designated by (V) and (R), respectively. It can be observed that the theoretical estimates are comparable to the measured volumetric changes for the specimens irradiated in the JEEP-II reactor. However, the theoretical volume changes largely overestimate the post-irradiation change of volume measured on the specimens irradiated in the LVR-15 reactor. Note that the lowest estimates correspond to the Voigt bound assuming an irradiation temperature of 55 °C. The actual average irradiation temperature in this study is closer to 45 °C.

This finding is not surprising because (1) the difference of RIVE between specimens irradiated in similar fast neutron fluence and temperature conditions in the JEEP-II and LVR-15 reactors is reported in this document, and (2) the minerals' RIVE empirical models were developed from literature data obtained mainly from Russian reactors operating at fast neutron flux comparable to that of the JEEP II reactor. The fast neutron flux appears to be determinant of the RIVE rate of rock-forming minerals.



**Table 13-1 Post-Irradiation Volumetric Change of Aggregate GA(F) and GB(E) Irradiated in the JEEP-II Reactor (Maruyama et al., 2017) and the LVR-15 Reactor (XK1 Position): Comparison Between Post-Irradiation Measurement and Theoretical Estimates**

Irradiation conditions			Volumetric changes (mean)	
Reactor/position or capsule	Fluence ( $\times 10^{19}$ n.cm <sup>-2</sup> , E > 10 keV)	Temperature (°C)	Post-irradiation measurement (%)	Theoretical Estimates (-)
<b>Aggregate GA(F)</b>				
<b>JEEP-II/PPT-B</b>	1.14	53.3	0.57%	0.55% (R) 0.52% (V)
<b>JEEP-II/PPT-C</b>	2.09	53.3	0.91%	1.15% (R) 1.08% (V)
<b>LVR-15/XK1</b>	1.50	40–55	0.20%–0.25%	1.22% (R) 0.68% (V)
<b>Aggregate GB(E)</b>				
<b>JEEP-II/PPT-B</b>	1.14	53.3	0.43%	0.32% (R) 0.25% (V)
<b>JEEP-II/PPT-C</b>	2.09	53.3	0.49%	0.66% (R) 0.52% (V)
<b>LVR-15/XK1</b>	1.50	40–55	-0.04%–0.185%	0.67% (R) 0.33% (V)

### 13.1.2 Mosaic

The simulations of the irradiation experiments of aggregate GA(F) and GB(E) in the JEEP-II reactor is detailed in Cheniour et al. (2022). The main features and characteristics of the model are discussed below. Simulations are conducted in 2D only.

The microstructures are obtained using a combination of characterization techniques conducted on unirradiated specimens provided by the JCAMP:

1. XRD Rietveld analysis as provided in Table 12 in Maruyama et al., 2017): This analysis provides the target weight fractions of the varied types of minerals present in the aggregate.
2. Thin section petrography and image analysis: Not only does petrography makes it possible to confirm the nature of the mineral present, but thin section image analysis is also necessary to obtain the mineral grain size distributions. The mean (and variance) mineral grain sizes for GA(F) and GB(E) aggregates are 72(1)  $\mu\text{m}$  and 136(5)  $\mu\text{m}$ , respectively.
3. Micro x-ray fluorescence (m-XRF) and scanning electron microscopy (SEM), combined with energy dispersive x-ray spectroscopy (SEM/EDS) elemental maps: the m-XRF

elemental maps (elements heavier than sodium) are  $400 \times 400$  pixels, with each pixel representing a  $15 \times 15 \mu\text{m}^2$  area. Only one mineral is attributed to a single pixel. The SEM analysis provides complementary information on lighter element concentrations. Sodium is notably found in albite, an endmember for both plagioclase and alkali feldspars present in aggregate GB(E).

The phase maps reconstruction follows the methodology presented in Li et al. (2020). The crystalline mineral properties are highly anisotropic. Their elastic constants, the coefficients of thermal expansion, and radiation-induced expansion vary along the crystallographic axis. These properties have been collected in the Irradiated Minerals, Aggregates and Concrete (IMAC) database.

Each mineral grain, referred to as a *particle* in MOSAIC, includes several contiguous pixels, depending on the size of the grain. The crystal is randomly oriented. Each grain is surrounded by an artificial one-pixel layer called the *inter-particle interface* (IPI). This artificial interface is introduced to account for possible grain boundary cracking. Because the thickness of the IPI is finite, it introduces a volume fraction bias. Thus, the IPI's elastic properties, thermal expansion coefficients, and radiation-induced expansion are assumed to be equal to the average properties of the aggregate to correct this bias.

The strength properties of the IPI are not experimentally determined. Hence, it is simply assumed that the IPI strength is independent of the adjacent minerals' properties. The IPI strength is calibrated on the irradiated Young's modulus of the aggregates.

Irradiation simulations are conducted assuming an irradiation temperature of  $53.3^\circ\text{C}$  (JEEP-II experiment). This temperature is close to the maximum temperature in the aggregate holder elevation during the LVR-15 irradiation experiment. Because RIVE rate is influenced by irradiation temperature, the simulated expansions can be considered as a lower bound for the range of temperature experienced by the aggregates during the LVR-15 irradiation experiment.

The volumetric change estimated by MOSAIC for aggregate GA(F) is 0.87% at  $1.2 \times 10^{19} \text{ n.cm}^{-2}$  ( $E > 10 \text{ keV}$ ). This value is in the range of the Voigt–Reuss bounds presented in Table 13-1. The post-irradiation volumetric change ranges between 0.20% and 0.25% and thus is  $\frac{1}{4.4}$  to  $\frac{1}{3.5}$  times lower than the simulated value. Once again, this result stresses the effects of the fast neutron flux in combination with the defects recovery rate.

The volumetric change estimated by MOSAIC for aggregate GB(E) is 0.47% at  $1.2 \times 10^{19} \text{ n.cm}^{-2}$  ( $E > 10 \text{ keV}$ ). The same conclusions that were drawn for aggregate GA(F) can be drawn for aggregate GB(E).

## 13.2 Aggregate Young's Modulus

Because the theoretical and simulated radiation-induced expansions overestimated the post-irradiation measurements, the simulated loss of Young's modulus is also overestimated. Instead of using models, the loss of modulus can be estimated from the empirical equations provided in Figure 12-1 and obtained from ultrasonic wave velocity measurements conducted on specimens irradiated in the JEEP-II reactor.

The estimated losses of modulus of aggregate GA(F) and GB(E) are estimated at <2% and <3%, respectively.

### 13.3 Mesoscale Modeling of Concrete Dimensional Changes and Damage

The observed dimensional changes and damage have origins in both aggregate and paste because the concrete is exposed to the different conditions over the project period. These conditions are: (1) temperature changes both in the heat-cured and irradiated concrete specimens, (2) moisture loss caused by pre-drying and continued drying for all concrete samples, and (3) gamma-induced radiolitic effects. These exposure conditions are highly coupled and produce volumetric deformations (expansions and contractions), as well as changes in elastic properties of the aggregate as explained before. Volumetric deformations are represented in LDPM as imposed strains  $\mathbf{e}^{imp}$  (eigen strains). Assuming strain additivity, the LDPM total strain vector  $\mathbf{e}$  is defined as  $\mathbf{e} = \mathbf{e}^* + \mathbf{e}^{imp}$  and so the stress vector is computed using only the mechanical strain vector  $\mathbf{e}^*$ , which is computed by subtracting  $\mathbf{e}^{imp}$  from  $\mathbf{e}$ . The imposed strain can simulate various volumetric deformation-inducing phenomena. In this work, it is used to simulate thermal shrinkage and RIVE-induced strains, which reads as  $\mathbf{e}^{imp} = \mathbf{e}^T + \mathbf{e}^S + \mathbf{e}^R$ . Because the LDPM formulation is based on incremental stress evolution, any imposed strain is applied as an increment during each time step. In the following analysis, the aforementioned conditions and their modeling in LDPM (imposed strain increments) are explained.

#### 13.3.1 Thermal Deformation

In its simplest form, thermal deformation is assumed to vary in proportion to temperature changes with a constant coefficient of thermal expansion (CTE). However, CTE of any material is usually a nonlinear function of temperature, especially for large temperature changes. The CTE of the aggregate is close but different from that of the paste, so such a difference can introduce internal self-equilibrated stresses. Under high thermal gradients, these stresses alone can lead to concrete damage in a phenomenon called *thermal spalling* (Chen et al., 2020). Nevertheless, in this campaign, the temperature range was limited between room temperature and approximately 65 °C. Therefore, assuming a constant CTE that is a homogenized average of aggregate and paste CTE is acceptable. A typical value of  $10 \times 10^{-6} / ^\circ\text{C}$  is assumed. It is important to mention here that in most of the experiments, constant temperature was maintained over long periods of time. However, to simulate changes of temperature between each fixed temperature point, the multiphysics module of LDPM (MP-LDPM) is utilized which can evolve temperature in time and space using a general heat diffusion formulation as  $\nabla \cdot (\lambda_t \nabla T) - \rho c_t \frac{\partial T}{\partial t} + \dot{\alpha}_c c \tilde{Q}_c^\infty = 0$ , where  $\lambda_t = 2.3 \text{ W/m}^\circ\text{C}$  is the thermal conductivity,  $c_t = 1100 \text{ J/kg}^\circ\text{C}$  is the heat capacity,  $\rho = 2400 \text{ kg/m}^3$  is the material density, and  $\tilde{Q}_c^\infty \approx 450 \text{ kJ/kg}$  is the cement hydration enthalpy. Note that the last term,  $\dot{\alpha}_c c \tilde{Q}_c^\infty$ , represents a heat source that accounts for cement hydration as a function of the rate of its hydration degree  $\dot{\alpha}_c$ , which is defined in the next section. Therefore, for transient thermal conditions, MP-LDPM can predict the temperature distribution evolution. Given the temperature changes, the thermally imposed strain increment  $\Delta \mathbf{e}^T$  (note that T denotes *thermal*, not *transpose*) that represents thermal deformation of the material between any two aggregate centers in LDPM sharing the same facet is represented by

$$\Delta \mathbf{e}^T = \begin{bmatrix} \Delta \varepsilon_N^T \\ 0 \\ 0 \end{bmatrix}, \quad \Delta \varepsilon_N^T = CTE \cdot \Delta T,$$

where  $\Delta T$  is the change in temperature during the time step. Note here that the shear strain components are both set to zero assuming that thermal strains are purely volumetric. This assumption also applies to the following cases.

### 13.3.2 Shrinkage

Shrinkage of concrete is related to the loss of moisture content caused by continued chemical reactions (hydration of cement paste) or environmental exposure such as lower ambient air humidity and radiolysis. Using MP-LDPM, shrinkage is assumed to be proportional to the total change of the moisture content (specifically the evaporable water content,  $w_e$ ) represented as relative humidity ( $h$ ) changes. Predicting the spatial and temporal evolution of humidity in MP-LDPM requires the calibration of multiple parameters. These parameters are involved in three main chemo-physical processes detailed in Alnaggar et al., 2017.

1. Chemical hydration: defines the rate of hydration reaction (hydration degree  $\alpha_c$ ) as  $\dot{\alpha}_c = \frac{A_{c1} e^{-\eta_c \alpha_c / \alpha_c^\infty} e^{-E_{ac}/R(T-T_0)}}{1 + (5.5 - 5.5h)^4} \left( \frac{A_{c2}}{\alpha_c^\infty} + \alpha_c \right) (\alpha_c^\infty - \alpha_c)$ , where  $E_{ac}$  is the hydration activation; Energy ( $E_{ac}/R \approx 5000/^\circ K$ ),  $T_0 = 296^\circ K$  is the reference temperature assumed to be room temperature;  $\alpha_c^\infty = (1.031w/c)/(0.194 + w/c)$  is the asymptotic hydration degree; and  $A_{c1}$ ,  $A_{c2}$ , and  $h_c$  are chemical affinity parameters.
2. Sorption/desorption isotherm and moisture capacity are phenomena that control the relative amounts of different water phases in the material based on its hydration degree and relative humidity. Thus the evaporable water is given by  $w_e(h, \alpha_c) = G_1(\alpha_c) \left[ 1 - \frac{1}{e^{10(g_1 \alpha_c^\infty - \alpha_c)h}} \right] + K_1(\alpha_c) [e^{10(g_1 \alpha_c^\infty - \alpha_c)h} - 1]$ , where  $G_1(\alpha_c) = g_2 \alpha_c$ ,  $K_1(\alpha_c) = \frac{w_0 - 0.188 \alpha_c G_1(\alpha_c) [1 - e^{-10(g_1 \alpha_c^\infty - \alpha_c)}]}{e^{10(g_1 \alpha_c^\infty - \alpha_c)} - 1}$  and  $w_0$  is the initial water content. In its simplest form (assumed to be used here), the sorption isotherm can be defined using two material parameters  $g_1$  and  $g_2$ .
3. Nonlinear moisture diffusion in the pore system holds that moisture diffusion within the concrete pore structure is a nonlinear process. In MP-LDPM, it is simulated as a function of the change in relative humidity using a Fickian diffusion model as  $\nabla \cdot (D_h \nabla h) - \frac{\partial w_e}{\partial h} \frac{\partial h}{\partial t} - \frac{\partial w_e}{\partial \alpha_c} \dot{\alpha}_c - \dot{w}_n = 0$ , where  $\dot{w}_n = 0.253 \dot{\alpha}_c$  is the nonevaporable water content formulated as a sink term to account for the time evolution of water consumption by hydration, and  $D_h(h, T) = \exp\left(\frac{E_{ad}}{RT_0} - \frac{E_{ad}}{RT}\right) D_1 \left[ 1 + \left(\frac{D_1}{D_0} - 1\right)(1 - h)^n \right]^{-1}$  is the temperature- and humidity-dependent nonlinear moisture diffusion coefficient. The parameters that control  $D_h$  include the diffusion activation energy  $E_{ad}$ , the diffusion exponent  $n$ , and diffusivities under fully dry and fully saturated conditions  $D_0$  and  $D_1$ , respectively.

These parameters require additional experiments not performed in this campaign because of the difficulties associated with placing instrumentation inside the irradiation capsule and the dimensions of the specimens. Therefore, typical values of these parameters were assumed based on previous MP-LDPM simulations performed on similar concrete composition. These parameters are listed in Table 13-2.

**Table 13-2 MP-LDPM Parameters for Cement Hydration and Moisture Transport**

Parameter	Value	Parameter	Value
$E_{ac}$ (J/mole)	41,572	$g_1$	1.25
$A_{c1}$ (1/hr)	$15 \times 10^6$	$\kappa_{vg}$	0.2
$A_{c2}$ (-)	$1 \times 10^{-4}$	$E_{ac}$ (J/mole)	40,000
$\eta_c$	5	$n$	3.5
$a$	5.5	$D_0$ (kg/mm/hr)	$2 \times 10^{-10}$
$b$	4	$D_1$ (kg/mm/hr)	$4.9 \times 10^{-7}$

Using these parameters, the spatial and temporal distributions of the internal relative humidity ( $h$ ) can be simulated. Shrinkage deformation is modeled as a linear function of the change in relative humidity governed by a single concrete shrinkage coefficient noted as  $\kappa_{sh}$ . Thus, the imposed shrinkage strain increment  $\Delta \mathbf{e}^S$  reads

$$\Delta \mathbf{e}^S = \begin{bmatrix} \Delta \varepsilon_N^S \\ 0 \\ 0 \end{bmatrix}, \quad \Delta \varepsilon_N^S = \kappa_{sh} \cdot \Delta h,$$

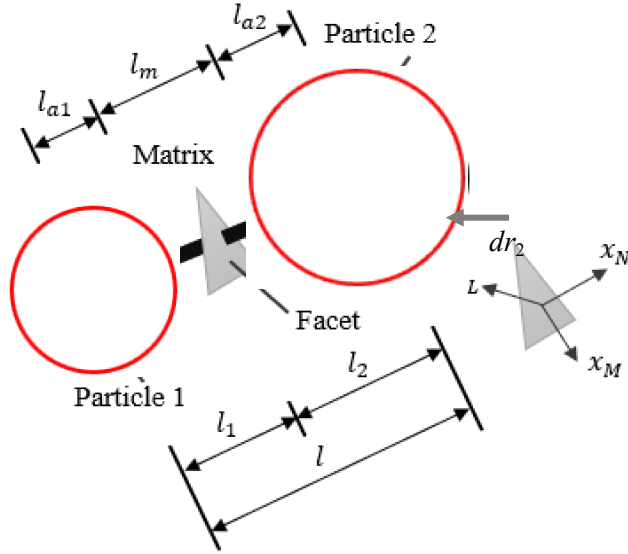
where  $\kappa_{sh}$  is defined over the entire LDPM edge linking the centroids of the two interacting aggregate pieces, which implies that shrinkage is smeared within the paste. This is an approximation.

The explicit determination of  $\kappa_{sh}$  requires microscale simulation of the paste. However, in previous MP-LDPM publications, the average  $\kappa_{sh}$  assumption was used with very acceptable results, especially when humidity variation rates are low. In this project, the same simplification was utilized. Here, two bounding values of  $\kappa_{sh}$  are used to estimate the possible range of shrinkage deformations.

### 13.3.3 Radiation-Induced Volumetric Expansion (RIVE)

RIVE was extensively studied during this campaign. MP-LDPM was adopted to model RIVE. Implementation within the framework of MP-LDPM is detailed here. Neutron irradiation causes both aggregate expansion and degradation of aggregate mechanical strength. Therefore, both effects need to be taken into account. As depicted in Figure 13-1, expansion of two adjacent particles increases the initial length of the strut,  $\ell$ , by  $dr_1 + dr_2$ , representing the dimensional changes of the two particles, respectively. The total length of the strut is the sum of the two particles radii,  $\ell_{a1}$  and  $\ell_{a2}$ , and the length,  $\ell_m$ , of the mortar placed between the two particles. The mortar includes fine particles that are also subject to RIVE. Their expansion is calculated from the volume fraction  $V_{fa}$  of aggregates relative to the mortar's volume fraction  $V_m$ . The total contribution of aggregate to the change  $d\ell$  of the strut length  $\ell$  reads as follows:

$$d\ell = dr_1 + dr_2 + d_{fa} \quad , \quad d_{ri} = \Delta RIVE_i \cdot r_i \quad (i = 1,2) \quad , \quad d_{fa} = \Delta RIVE_{fa} \cdot \frac{V_{fa}}{V_m} \cdot \ell_m.$$



**Figure 13-1 Schematic Representation of LDPM Modeling of Aggregate RIVE Effects**

From this length change, one can compute the increment of the imposed RIVE strain  $\Delta \mathbf{e}^R$  as

$$\Delta \mathbf{e}^R = \begin{bmatrix} \Delta \varepsilon_N^R \\ 0 \\ 0 \end{bmatrix}, \quad \Delta \varepsilon_N^R = d\ell/\ell.$$

As for the elastic modulus degradation, the model uses the initial homogenized elastic modulus and the provided aggregate elastic moduli to compute the equivalent normal modulus of the paste between them, as follows:

$$\frac{\left(1 - \frac{Vfa}{Vm}\right) \ell_m}{E_N^p} = \frac{\ell}{E_N} - \frac{\ell_{a1}}{E_N^{a1}} - \frac{\ell_{a2}}{E_N^{a2}} - \frac{\frac{Vfa}{Vm} \cdot \ell_m}{E_N^{fa}}.$$

Then, at each time step, aggregate elastic moduli are computed based on the degradation formula provided. These degradations are functions of RIVE. Examples of such fitted formula are presented in Figure 12-1. It remains to compute RIVE for each aggregate and for the fine aggregate. Here, the RIVE models detailed in the IMAC database are utilized (Le Pape, 2016; Le Pape et al., 2018). The inputs to these RIVE models are the temperature and fluence at the aggregate location. For the reduced size specimens tested in this project, the variations of the fluence are assumed to be negligible in the specimens. Thus, only the temporal evolution of fluence was considered. The spatial evolution of fluence is considered when modeling the CBS using fluence profile produced by VERA-Shift (Cheniour et al., 2023). Thus, one can compute  $\Delta RIVE$  at each time step based on the values of temperature and fluence  $\phi$  at this time step  $t$  and the previous time step  $t - \Delta t$  as follows:

$$\Delta RIVE^t = RIVE(\phi, T)^t - RIVE(\phi, T)^{t-\Delta t}.$$

It is important to note here that RIVE is the most detailed phenomenon in the model because its information is the most detailed in the experimental campaign. With these data, it is possible to

estimate not only both fine and coarse aggregate expansion, but also the effects of this expansion on the elasticity and cracking. Please note that predicted cracking is the result of the fracture of the mortar matrix under nonhomogeneous aggregate expansion. In this work, it is assumed that LDPM can predict the degree of mechanical damage without postulating additional phenomenological damage to its constitutive laws. This means that the cracking induced as a result of RIVE already degrades the mesoscale strength of the system by reducing the strength along the struts and ties that have been cracked. Thus, any further mechanical loading will be resisted by an already cracked, weaker lattice system. This MP-LDPM capability was previously proven to be successful in the very similar case of ASR, in which MP-LDPM was able to predict ASR damage in various experimental campaigns (Alnaggar et al., 2017). However, such a prediction is mainly based on the assumption that aggregate remains more resistant than the interfacial transitional zone (ITZ) between the aggregate and the bulk mortar. Thus, it is assumed that the ITZ remains the weakest link in the composite. Such an assumption should be assessed and possibly revisited if RIVE causes extensive aggregate cracking that leads to a dramatic loss of its mechanical strength. To test these assumptions, an extensive experimental campaign testing varied RIVE amplitudes would be required.

#### **13.3.4 Effects of Other Exposure Conditions**

As explained above, gamma irradiation dose was high in this project. The main effects of gamma irradiation are expected to induce more drying (shrinkage), C-S-H densification (strength gain), and increased viscoelastic/viscous deformations (creep). As detailed above, data are not adequate at this writing regarding the quantitative assessment of these effects. However, if creep deformations occur, they are expected to be very small because the samples were free to deform, and the only source of confinement or constraints would result from the bond between the rebar and the concrete. Furthermore, a high-strength cement was used that minimizes the chance of a significant strength gain. Finally, pre-drying significantly reduced further shrinkage, as explained below. Therefore, it is assumed that the effects of these phenomena are of a second order.

### **13.4 Interpretation of Concrete Dimensional Changes Results**

Mass loss and RIVE are simulated separately to evaluate their possible combined effects on the observed dimensional changes. Note that because all measurements were performed at room temperature, thermal deformations did not contribute to the measured deformation differences. However, as explained above, thermal conditions were considered in both hygral deformations and RIVE.

#### **13.4.1 Simulation of Shrinkage Deformations**

Very limited experimental data were available in this project regarding the identification of hygro-thermo-chemical behavior of the material. Therefore, the only option is a parametric study using the upper and lower limits of MP-LDPM parameters as identified in previous extensive MP-LDPM calibrations.

In this project, it is assumed that the initial curing stage during the first 28 days was enough to achieve a very high degree of hydration because the cement used was the high early strength cement that would result in a hydration degree of approximately 95% to 99% of the asymptotic hydration degree at 28 days. With this simplifying assumption, the mass loss during the pre-drying stage and the final mass loss after irradiation were simulated. The assumed MP-LDPM parameters are listed in Table 13-2. With these parameters, theoretical amounts of water

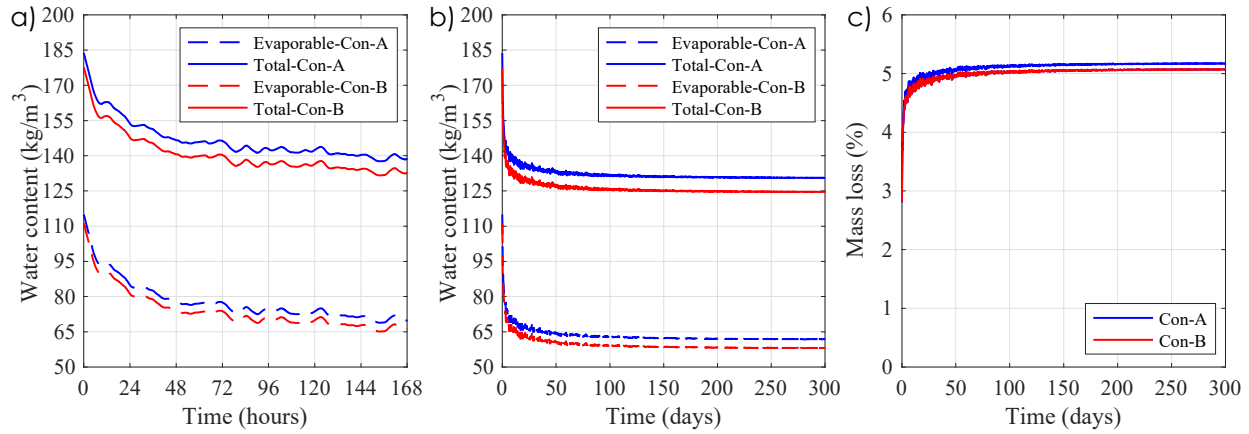
phases can be calculated for both Con-A and Con-B, as listed in Table 13-3, based on the formulations in Alnaggar et al., 2017 and an asymptotic relative humidity value of 10% because the irradiated and heat-cured specimens were placed in capsules swept by a constant inert gas flow.

**Table 13-3 Initial Water Content in Concrete Con-A and Con-B**

Water forms	Water content (kg/m <sup>3</sup> = L/m <sup>3</sup> )	
	Con-A	Con-B
Total	183	177
Non-evaporable	69	67
Evaporable	114	110
Remaining evaporable	69	65
Remaining total	138	132

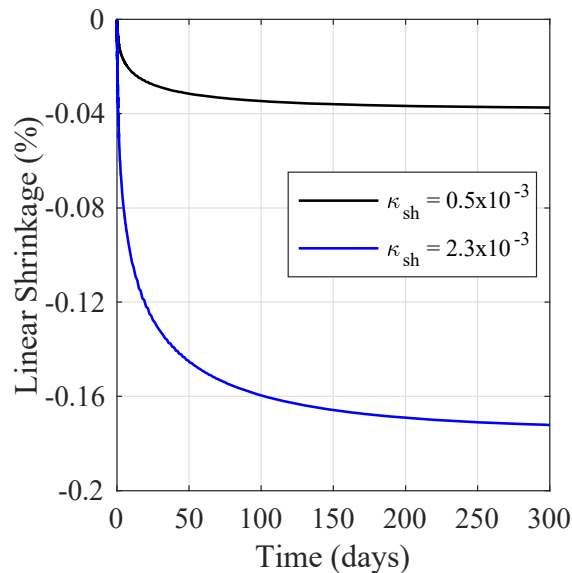
Using the same parameters, mass loss was simulated over the first 300-day period of the project, starting with casting and including curing, pre-drying, and part of the irradiation cycles. Simulations were limited to the first 300 days because the mass changes had nearly plateaued after 200 days. In these simulations, only hygric deformations were computed. The specimens were cured at room temperature during the first 28 days. Then the temperature was raised to the pre-drying temperature of ~60 °C, which was kept constant for the following 300 days. The relative humidity was maintained at 95% for the first 28 days of curing and was then reduced to an assumed value of 10% to represent the dry conditions of forced gas flow. The simulated water content evolutions are presented in Figure 13-2(a). Figure 13-2(b) shows the same data during the pre-drying period only. It is important to note here that this is a limiting case simulation in which various material parameters were assumed given the limited experimental data. However, by using changes in water content, along with mix design proportions, the expected mass loss can be calculated as presented in Figure 13-2(c). This simulated mass loss at the end of the pre-drying (approximately 4.5%) is close to the observed experimental value. Therefore, it can be assumed that drying during irradiation will result in an asymptotic shrinkage of approximately 5%.





**Figure 13-2 Effects of Relative Humidity Conditions: (a) Water Content Changes During Pre-drying Stage (168 Hours = 7 Days), (b) Water Content Changes for the First 300 Days After Initial Curing (Includes Pre-Drying), and (c) Mass Loss % for the First 300 Days After Initial Curing (Includes Pre-Drying)**

Using these simulated mass losses, total shrinkage can be estimated. Again, no specific shrinkage experiments were performed, so total shrinkage was computed using the minimum and maximum shrinkage coefficients identified for similar concrete mixes in di Luzio, 2009a, 2009b. These are  $\kappa_{sh} = 0.5 \times 10^{-3}$  and  $\kappa_{sh} = 2.3 \times 10^{-3}$ . The results are shown in Figure 13-3. Using these two values for  $\kappa_{sh}$ , total drying shrinkage estimates range between 0.04% and 0.17%.



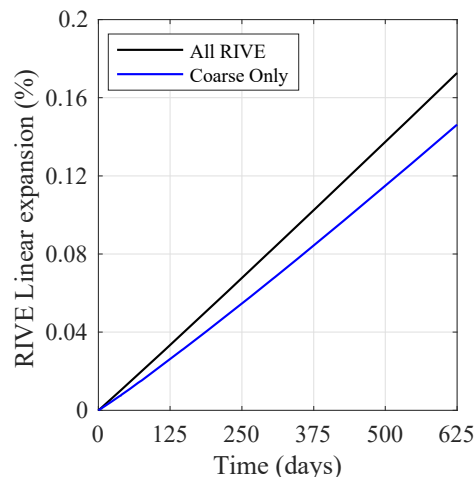
**Figure 13-3 Predicted Linear Shrinkage of the Donut Specimens for the First 300 Days Caused by Water Loss – Upper and Lower Bounds are Based on Shrinkage Coefficient Values from the Literature (Adbellatef et al., 2019, Di Luzio and Cusatis, 2013)**

### 13.4.2 Simulation of RIVE Deformations

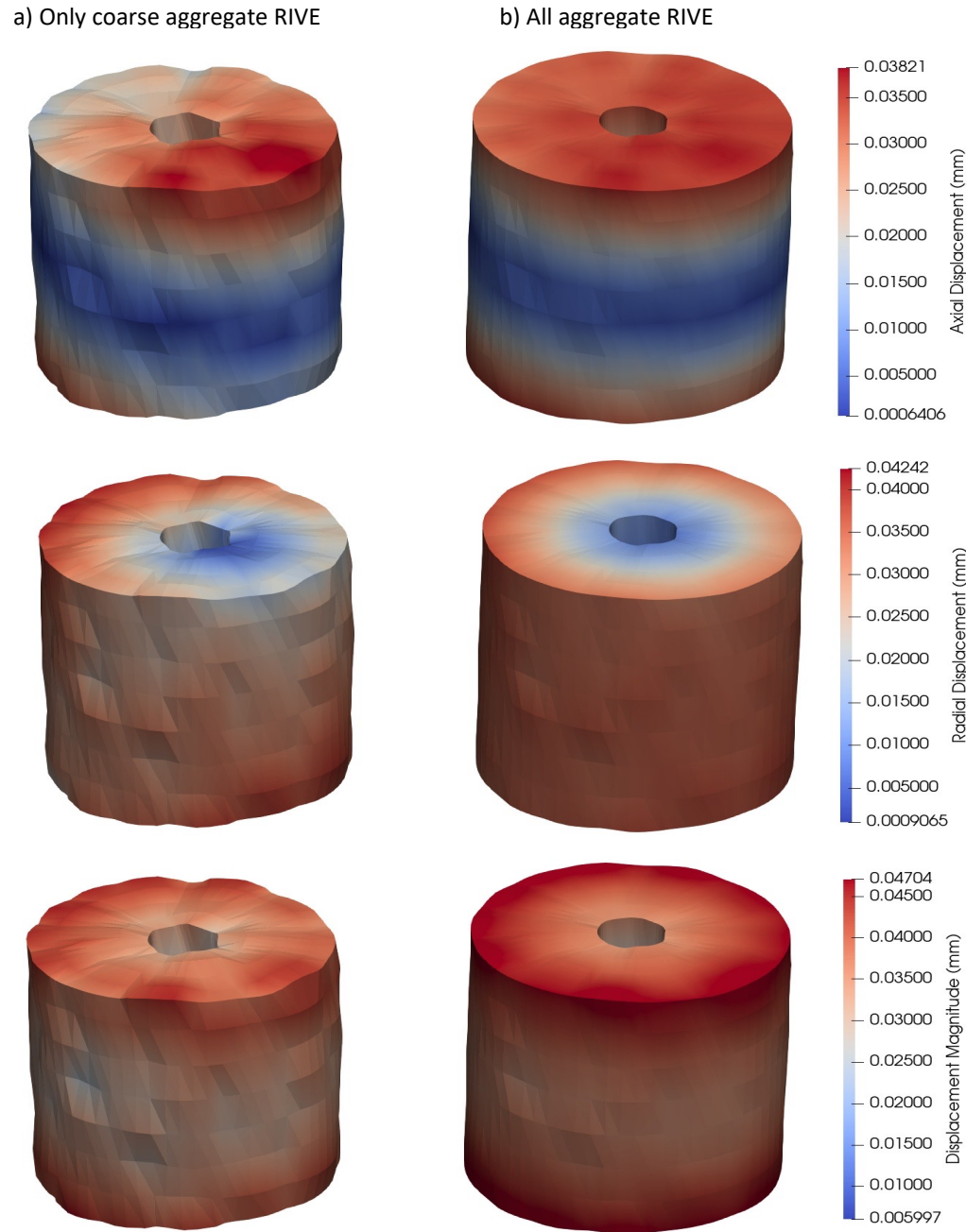
The PIE provided RIVE data on aggregate and concrete specimens. The evolution of aggregate RIVE deformations were simulated based on the assumptions presented in Section 13.3.3. According to the PIE results, the final aggregate expansion is estimated to be limited to ~0.2% or less. Hence, instead of simulating RIVE using the integration of mineral-specific RIVE models, aggregate RIVE is approximated by a linear expansion up to 0.2% over the duration of the irradiation experiment.

In this work, the contribution of fine and coarse aggregate of the expansion of irradiated concrete was examined. Neglecting the fine aggregate RIVE evidently results in a lower total volume change, as shown in Figure 13-4. However, fine aggregate RIVE reduces the spatial variability within the concrete. Hence, less distortion can be expected when all aggregates contribute to the RIVE. This is illustrated by the simulated deformations in Figure 13-5 (a) and (b), colored by axial (vertical), radial, and total displacement of the donut. Note that the donuts were simulated assuming free expansion in all directions and that the reference point (zero displacement) is the donut center of mass. Figure 13-5 (a) shows a more distorted donut, although its total expansion is smaller than that shown in Figure 13-5(b), which appears to have more uniform expansion. Such a difference has pronounced effects on the loss of mechanical strength, as detailed below. Nevertheless, the total expansion from RIVE ranges between 0.15% and 0.17%, which is comparable to the estimated shrinkage.

Thus, the cumulative effects of shrinkage and RIVE deformations explain the limited and scattered dimensional changes observed experimentally. Basically, by subtracting the maximum shrinkage deformation (0.17%) from the nonuniform RIVE expansions that are on the order of 0.15% to 0.17%, one expects no expansion at all, and only shrinkage. Then, by subtracting the minimum shrinkage of 0.04%, a small expansion could be observed. This also explains why some specimens have experienced a minor decrease in volume rather than expansion. Note that these predictions are based on multiple simplifying assumptions, including the assumed MP-LDPM parameters, uniformity of the fluence over the volume of the specimen, and use of the maximum value of the fluence at the capsule center, not at each donut.



**Figure 13-4** Predicted Linear Expansion of the Irradiated Donut Specimens Caused by Aggregate Expansion up to 0.2%: (Blue) Accounting Only for Coarse Aggregate Expansion; (Black) Accounting for Fine and Coarse Aggregates



**Figure 13-5** Simulated Deformations of the Donut Samples Under Predicted RIVE from Aggregate Expansion Measurements (0.02%) Showing the Difference Between (a) Considering Only Coarse Aggregate vs. (b) Considering All Aggregates to Expand. The Top Row Shows Axial (Vertical) Displacement, the Middle Row Shows Radial Displacement, and the Bottom Row Shows Displacement Magnitude; All Displacement was Measured from the Center of Mass of the Donut.

## 13.5 Interpretation of Concrete Mechanical Strength Results

### 13.5.1 Interpretation of Difference Between Donut and Cylinder Compressive Strength

As mentioned before, LDPM predicts concrete mechanical strength by explicitly representing its aggregate interactions under tension, compression, and shear. Tensile failure is physically represented based on quasi-brittle fracture mechanics utilizing a constitutive law that resembles the cohesive crack model (see Section 11.2.2). Therefore, LDPM can predict the evolution of macroscopic damage as a function of the growth of inter-aggregate crack networks that grow, coalesce, and unload, depending on complex aggregate interactions. Hence, by imposing internal aggregate expansion on the LDPM system as imposed volumetric strains, this expansion introduces inter-aggregate forces that are very similar to those predicted during mechanical loading. Therefore, the main assumption here is that LDPM can predict RIVE-induced damage just as it predicts damage under loading without changing its constitutive laws. In other words, LDPM simulates RIVE as a forced internal displacement (the imposed RIVE strain) within its mesostructure, which is comparable to imposing displacement as a result of mechanical loading. Furthermore, if RIVE-induced damage in aggregate does not result in a residual strength weaker than the strength of the ITZ, then LDPM is expected to predict RIVE-induced damage correctly.

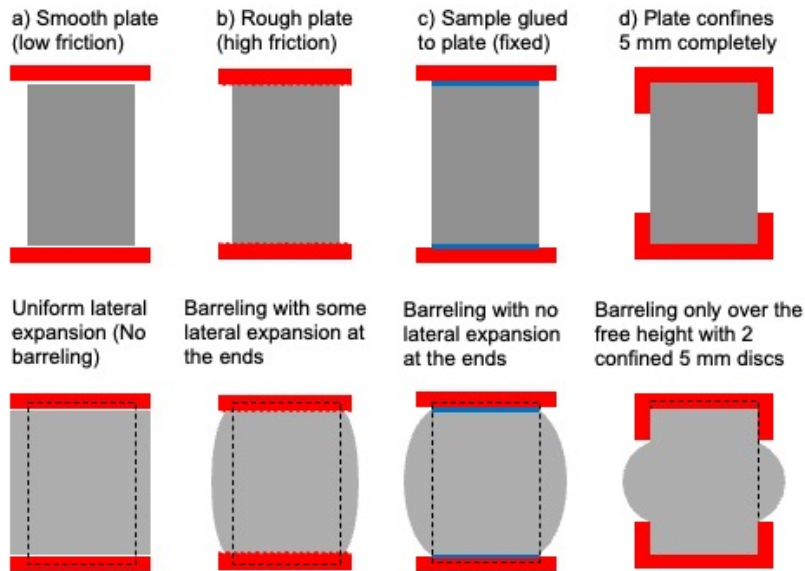
Using LDPM-calibrated parameters, the uniaxial compression tests of 2 in. × 4 in. cylinders cured at room temperature were simulated assuming low friction (LF) because the samples were tested using rubber pads on both sides. Low friction simulations utilize a stick-slip friction law between the simulated donut and the simulated compression caps. In this model, at any given slip displacement  $d$  between the cap and the concrete surface nodes, the force resisting the slippage is formulated using a friction factor  $f_f$  that is a function of a kinematic friction factor  $f_k$ , a static friction factor  $f_s$ , and a characteristic length  $A$  that is calibrated using available experimental data. This friction factor  $f_f$  is given by

$$f_f = f_k + (f_s - f_k) \frac{A}{A + d}.$$

This stick-slip law has been used in various LDPM publications and shows very good agreement with uniaxial compression of concrete samples with and without friction-reducing end preparation. Low friction parameters are listed in Table 13-4.

To ensure accuracy of results accounting for LDPM mesostructure generation variability, 20 numerical samples were created and simulated. The range and average values of the predicted compressive strength are in good agreement with the experimental ranges, as shown in Figure 13-6(a). Because of irradiation constraints described in Section 2.32.3 only donut specimens were irradiated. These samples were tested in uniaxial compression. As a result of aspect ratio, loading boundary conditions, and geometric features, donut samples experience more confinement during compression than cylinders. Therefore, they fail at a higher compressive stress. During the test, the rubber caps tend to deform around the donut edges. Because it is difficult and time consuming to precisely simulate this boundary condition, four different limiting cases were simulated to show the effect of confinement degree on the predicted compressive strength. The four cases illustrated in Figure 13-6 include (a) LF between the donut and rubber, (b) high friction (HF) between the donut and rubber using the same aforementioned stick-slip formulation with HF parameters listed in Table 13-4, (c) no lateral displacement of donut points in contact with rubber (fixed), and (d) no displacement of the top and bottom 5 mm zones of the donut as a result of rubber curling (5 mm Conf.). As shown, LDPM predicts the confinement

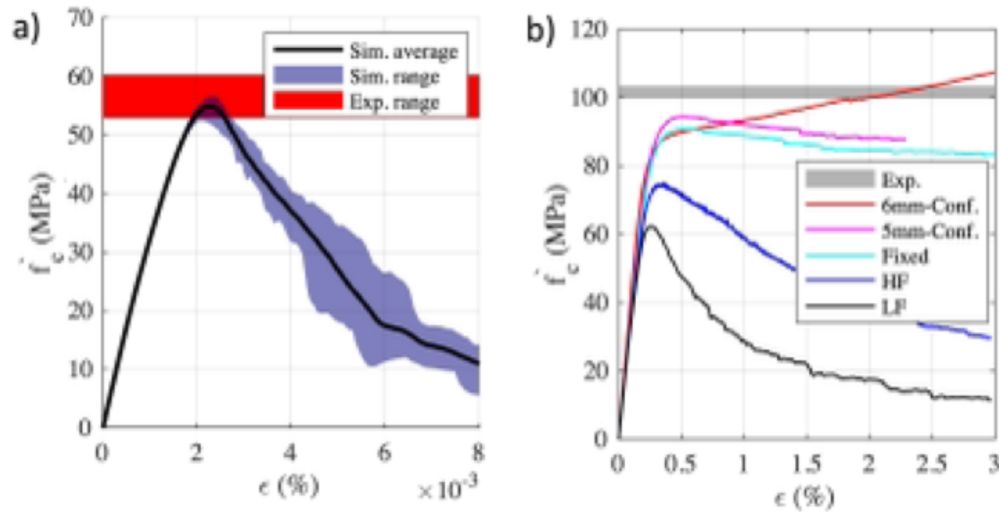
effects, showing confined compressive strengths of 90 MPa and 95 MPa for the fixed and 5 mm confinement cases, respectively. These increases are very close to the observed experimental results (100–103 MPa). Therefore, although irradiated samples were only donuts, LDPM can be used to simulate the irradiated donut results and then predict the corresponding effects of irradiation on the cylinder's compressive strength. In conclusion, the predicted change in compressive strength using LDPM can be used as an accepted prediction of the test data.



**Figure 13-6 Four Boundary Conditions Used to Model the Compression Tests**

**Table 13-4 Compression Test Friction Parameters**

Parameter	Low friction	High friction
$f_s$ (-)	0.03	0.13
$f_k$ (-)	0.0084	0.015
$A$ (mm)	0.0195	1.3

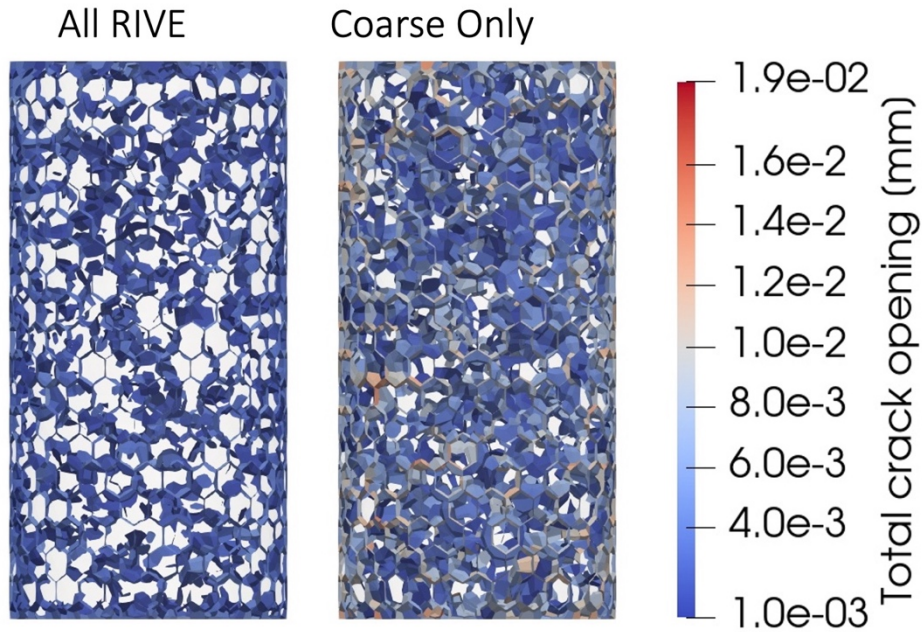


**Figure 13-7 Simulation Results Showing LDPM Prediction of Compression Tests for Different Conditions: (a) Prediction of 2 in.  $\times$  4 in. Cylinders Showing Numerical Average and its Range Compared with Experimental Average, (b) Donut Uniaxial Compression with Different Boundary Conditions Based on 2 in.  $\times$  4 in. Cylinder Calibrations of Room Temperature–Cured Specimens**

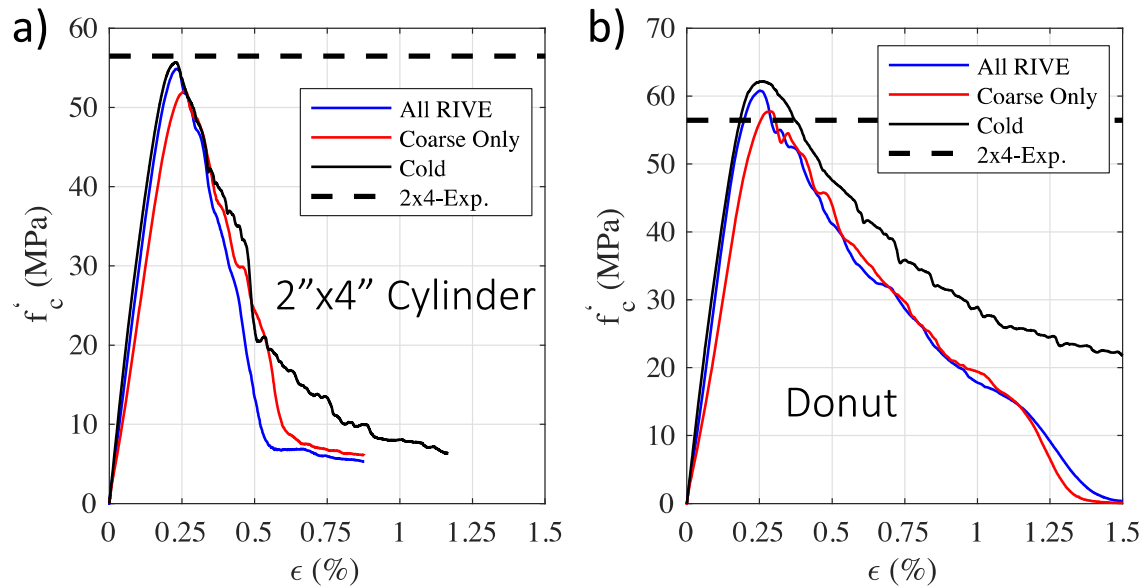
### 13.5.2 Simulation of RIVE Effects on Donut and Cylinder Compressive Strength

For the irradiated samples, the same two RIVE scenarios assumed in expansion interpretations were simulated: namely, assuming all aggregates to expand, and assuming only coarse aggregates to expand. Note here that the random variability in aggregate mineralogy between each aggregate piece and the other is neglected because it would require further probabilistic analysis at the scale of the aggregate distribution. Nevertheless, because the mortar expansion is uniform and each coarse aggregate piece expands differently depending on its diameter, the imposed RIVE strain is more homogeneous when all aggregates are expanding, and it becomes more heterogeneous only if coarse aggregates expand. The more heterogeneous expansion results in larger scatter in crack openings and thus higher reduction in compressive strength. This is expected because purely uniform expansion would not create internal stresses, just like expansion of concrete under uniform temperature. This difference is captured by LDPM; as shown in Figure 13-7, the case for coarse aggregate expansion only shows larger crack openings scattered all over the sample (orange-colored cracks), whereas in the other case, cracks tend to be smaller. The result of such differences is that there is more loss in compressive strength for the *coarse only* case compared to the *all RIVE* case, as shown in Figure 13-8 (a) and (b). The predicted residual compressive strength for both cases is presented in Table 13-5. Note that donut simulations assume LF boundary conditions. This is because confined compression includes triaxial effects, and although LDPM is capable of simulating these effects, it would require additional experimental data, including a hydrostatic test and two triaxial tests at low and high confining pressures. Those test results were not made available in this campaign.





**Figure 13-8** Difference in RIVE-Induced Cracking When Considering All Aggregates to Expand (Left) vs. Considering Only Coarse Aggregates to Expand (Right)



**Figure 13-9** Simulated Uniaxial Compressive Strength Tests for Irradiated and Room Temperature (Cold) Cases Compared with the Reference  $2 \times 4$  Cylinder Strength at Room Temperature: (a)  $2 \times 4$  Cylinder Results, and (b) Donut Results

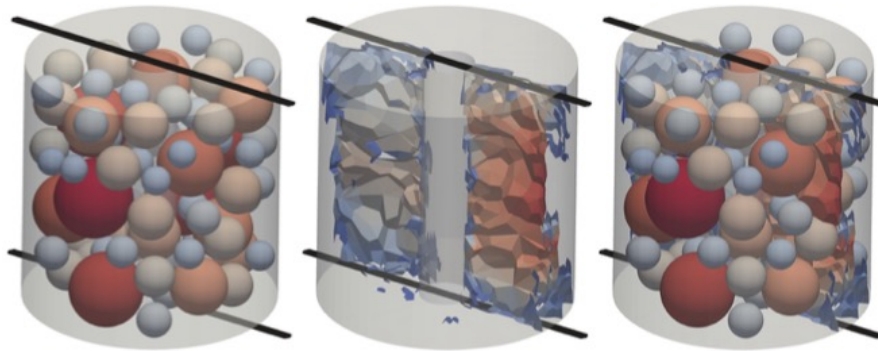
**Table 13-5 Predicted Compressive Strength Reduction in Concrete Con-A Caused by Aggregate RIVE under the Irradiation Conditions Tested in the XK1 Position (LVR-15 Reactor)**

Sample type	All RIVE	Coarse aggregate only
2 in. × 4 in. cylinder	99%	94%
Donut	98%	93%

As can be seen from the predictions in Table 13-5, both the 2 in. × 4 in. cylinder and donut samples have similar results in terms of strength reductions, making it acceptable to use LDPM to infer the effects of RIVE on strength reduction. It must be also mentioned here that the small reduction in strength for the *all RIVE* case is reasonable and matches the experimental results. Finally, because the observed RIVE is very small, as discussed above, the assumption that the ITZ is still the weakest link is reasonably valid. Thus, it can be concluded that LDPM results are reasonably predictive within the calibrated RIVE range.

### 13.5.3 Simulation of Donut Splitting Strength

As in the simulations for compressive strength, donut samples for the room temperature (rt) and irradiated (irr) cases were simulated. For each curing case, 20 samples were generated to obtain a statistically relevant set of outputs. It is important to mention that the splitting test results are highly scattered because of the size of the samples and the relative size of the maximum aggregate diameter to the sample itself. This effect can be observed from the simulated test shown in Figure 13-8: the sample realization is shown with a transparent donut outline so that the internal coarse aggregate can be visible. Because LDPM currently assumes that cracks only form between aggregate particles, the presence of a large aggregate diverts the crack propagation around it, thus creating a tortuous crack path, as can be seen in Figure 13-9 (middle and right.) This explains the scatter observed in simulation results.

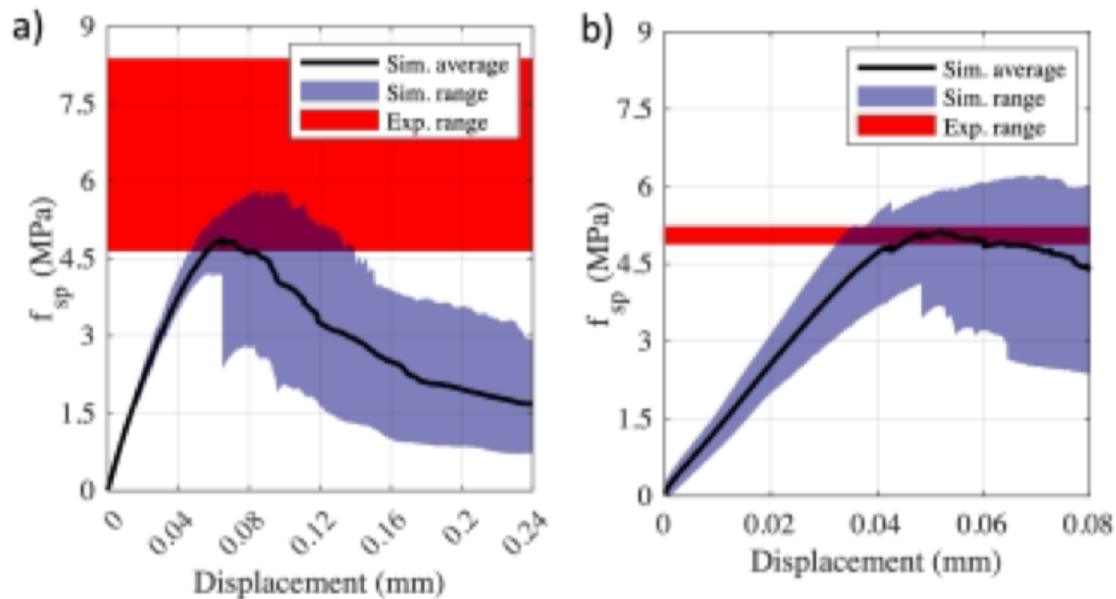


**Figure 13-10 Simulation of Donut Splitting Test Showing the Loading Rods and Internal Aggregate Structure (Left), the Simulated Splitting Crack (Middle), and the Crack Location Around the Aggregate (Right)**

The simulation results are shown in Figure 13-10 for the rt cured specimens (left) and the irr specimens (right), respectively. Note that for both cases, the numerical simulations overlap with the experiments. However, the experimental scatter for the rt case is significantly high, but



LDPM simulations are closer to the lower limit. For the irr case, the LDPM simulations are more scattered than those in the experimental range. However, the average strength agrees well with that seen in the experiments.



**Figure 13-11 Prediction of Donut Splitting Strength and Comparison with Experimental Ranges: rt Samples (a), irr Samples (b)**

### 13.6 Interpretation of Bond Test Results

After validating the capabilities of LDPM to predict RIVE-induced damage to the concrete strength, LDPM is used here to simulate the effects of RIVE on bond strength.

As mentioned above, all pullout samples were jacketed to ensure the formation of a bond failure by replicating confinement conditions. The jacket is attached to the specimen using an epoxy filler. Figure 13-11 presents the LDPM model of the pullout sample showing all model components. The rebar (red element) is simulated using 1D beam elements and is connected to the concrete with 2D interface elements (blue elements). The concrete (gray transparent volume showing coarse aggregate inside) is modeled using LDPM. The epoxy (orange) and the steel jacket (black) are modeled using hexahedral FEs. The constitutive models of the rebar, epoxy, and steel jacket material are elastic—perfectly plastic—with parameters listed in Table 13-6, to ensure that a possible yielding failure is correctly captured by the model. LDPM parameters are the same as those listed previously; however, the bond model parameters were fine tuned to best fit the rt pullout response. The final bond model parameters are listed in Table 13-7 (rt column).

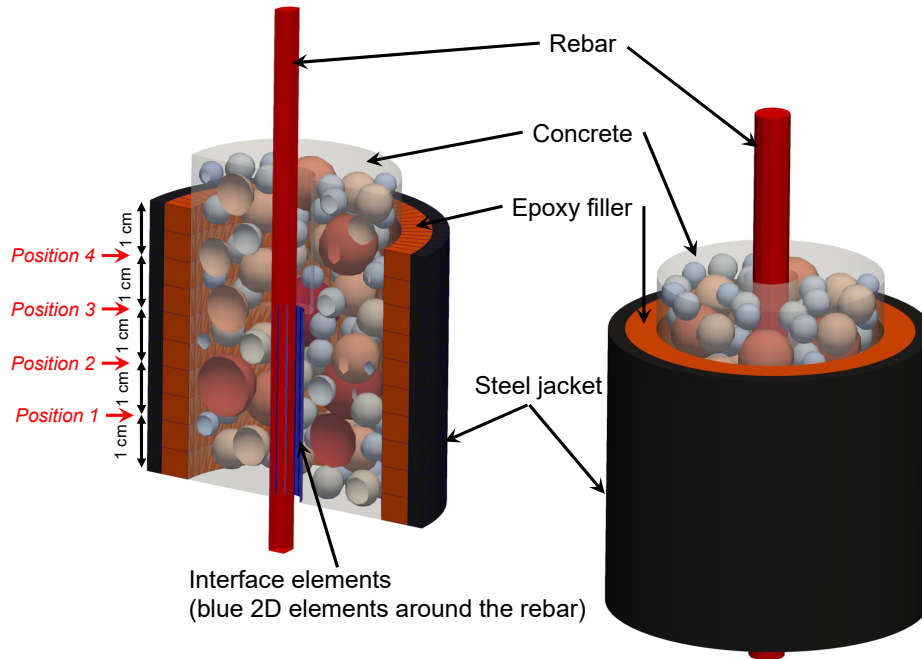
**Table 13-6     Elastoplastic and Density Parameters for Epoxy, Steel Bar, and Steel Jacket**

Parameter	Rebar	Epoxy	Steel jacket
Density (g/cm <sup>3</sup> )	7.8	1.1	7.8
Elastic modulus (GPa)	200	2.0	200
Yield strength (MPa)	483	48.3	220
Poisson's ratio (-)	0.3	0.3	0.3

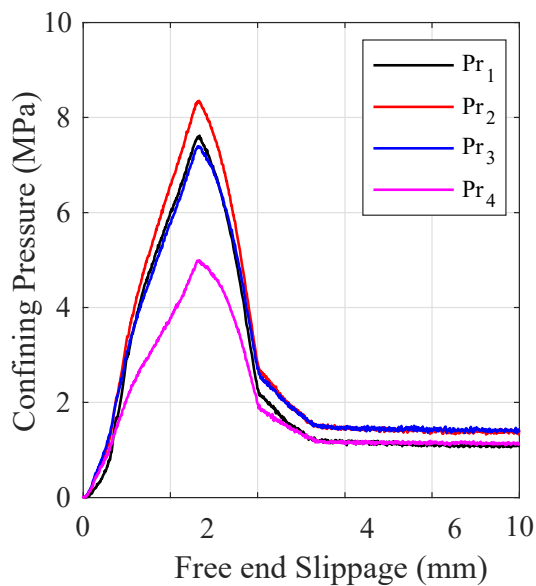
To accurately replicate the boundary conditions of the experiments, two stages must be simulated: first, the irradiation stage in which the sample is not jacketed, and second, the pullout test, which is conducted after jacketing the sample. During simulation, the first stage is replicated by deactivating the epoxy FEs. This approach prevents stress transfer between the concrete and the jacket, thus allowing for development of RIVE-induced damage without any constraints.

Before applying the pullout force to the loaded end of the rebar, the epoxy FEs are activated. To assess the effectiveness of this method, the average hoop stress in the steel jacket is measured at four locations: 1 cm, 2 cm, 3 cm, and 4 cm from the edge of the jacket as measured from the free end side. At these four positions, indicated in Figure 13-11, the tension in the steel ring elements (hoop stress,  $S_t$ ) is averaged around the circumference. This average tension is then used to calculate the confining pressure on the epoxy, which is subsequently applied to the concrete specimen. The confining pressure is calculated using the thin cylinder equations ( $Pr = S_t t_c / r_c$ ), where  $t_c$  is the cylinder wall thickness, and  $r_c$  is the cylinder average radius (radius to the middle of its wall thickness).

The evolution of the confining pressures is plotted against free-end displacement during the pullout test in Figure 13-12. Note that the simulated irradiation-induced lateral stresses are nearly zero, so all pressure curves start from zero during the irradiation simulation period. The maximum confining pressure is approximately 8 MPa, which is significantly higher than the tensile strength of the concrete. Therefore, failure occurs from bond failure.



**Figure 13-12 Cross View and External View of the Bond Test Model**



**Figure 13-13 Lateral Pressure Applied by the Steel-Epoxy Jacketing During the Bond Test Where  $Pr_i$  is the Pressure at  $i$  cm from the Free End Side of the Steel Jacket**

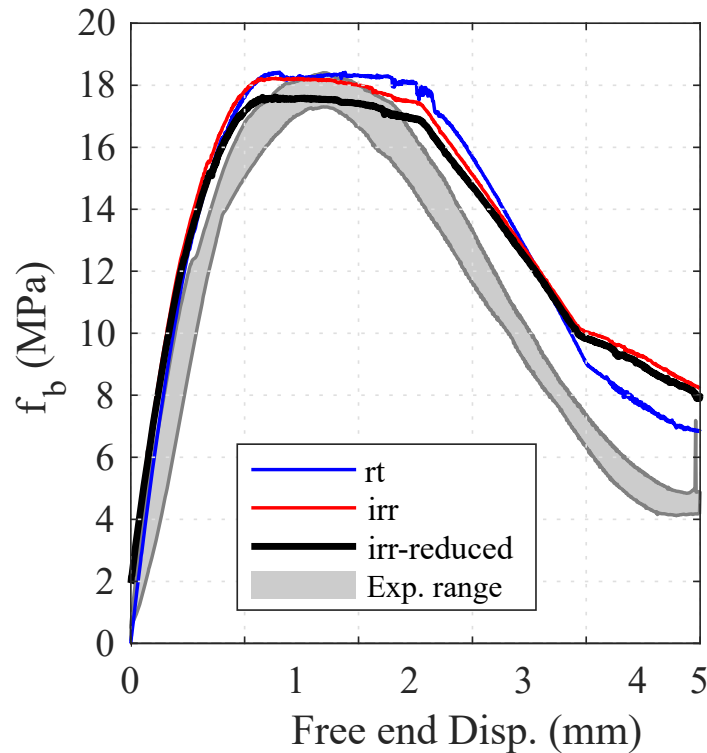
These simulations are analyzed to understand the effects of RIVE on bond strength. Three cases are compared: rt, irr, and irradiated reduced (irr-reduced). The rt case uses the LDPM and bond model parameters without any modifications and without any imposed RIVE. The irr case also uses the same parameters, but with RIVE imposed. The irr-reduced case is used to test the hypothesis that the bond strength is proportional to the square root of the concrete

compressive strength. It is assumed that this hypothesis holds true even under moderate RIVE-induced damage if the aggregate is not severely damaged. This implies that there will be a limit beyond which the aggregate will be significantly damaged, and the assumption will no longer hold.

For the irr-reduced case, the same LDPM material parameters are used, but all bond stress boundaries of the bond law are scaled by the square root of the ratio between the  $r_t$  and irr concrete compressive strength, as shown in Table 13-5 for the coarse aggregate case only. In this worst-case scenario, with a concrete strength ratio of 93%, the modified bond law parameters are listed in Table 13-7 (irr-reduced column). The simulated pullout test results for the three cases are plotted in Figure 13-13. As observed, the  $r_t$  case is outside the experimental range but approaches the upper bound. The irr case, however, has almost the same peak bond strength as the  $r_t$  case. It is postulated that the irr case is very close to the  $r_t$  case because of three main conditions:

1. The jacket and epoxy are providing enough confinement
2. At such low RIVE, the confined concrete is still capable of providing confinement and shear resistance during most of the pullout stage
3. The bond law parameters are kept independent of RIVE-induced damage in concrete

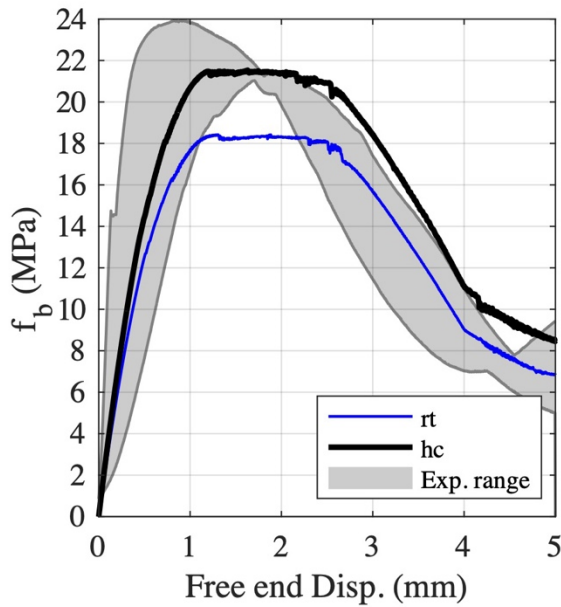
Nevertheless, because of the slight damage in concrete induced by RIVE, a small deviation is observed between the irr and  $r_t$  cases, particularly in the post-peak response. The cohesion plateau is shorter for the irr case compared to the  $r_t$  case. Further analysis reveals that the irr-reduced case falls within the experimental data range, confirming that the bond law parameters should indeed be a function of the RIVE-induced damage in concrete, as hypothesized. Moreover, because the irr-reduced case is based on the worst-case scenario for strength reduction (93%), it is close to the lower bound of the experimental data. This suggests that if other reduction ratios were simulated, then the resulting curves would lie between the irr and irr-reduced curves, thus falling within the experimental range, as well. It is also important to note that this model overestimates the post-peak frictional component. This issue could be addressed by further calibrating the frictional component independently or by recalibrating the entire bond-slip model. The radial stress coefficient is expected to decrease if the concrete is damaged as a result of RIVE. However, this further calibration would require additional experimental data which is beyond the scope of this study.



**Figure 13-14**     **Simulation of the Bond Tests Assuming No Effects of the Concrete Strength on the Steel-Concrete Bond Constitutive Model. rt: Room Temperature, irr: Degradation of the Concrete Caused by Irradiation, irr-reduced: Same as irr with a Degradation of the Steel-Concrete Bond Strength**

To further test this hypothesis, the pullout test results of the hc samples are also simulated. However, given that the compressive strength data from donuts include triaxial effects, it is not easy to calibrate LDPM parameters or use these data to scale the bond strength, but the splitting tensile strength could be used instead. Furthermore, the rt splitting tensile strength experimental results are significantly scattered. Therefore, the irr splitting tensile strength data are used instead. Concrete splitting tensile strength is typically estimated as a function of its compressive strength. Following ACI-318-19, the splitting tensile strength is assumed to be proportional to the square root of the compressive strength. Thus, the splitting tensile strength ratio can be used directly for scaling the bond strength. Using this scaling provides a set of bond law parameters. The irr splitting tensile strength average is 5.05 MPa, and the hc splitting strength average is 6.15 MPa, so  $f_{tr} = 1.22$ . Thus, the scaling factor is 1.22.

The scaled parameters are listed in Table 13-7 under hc. The results again confirm the validity of this assumption, as shown in Figure 13-14 for the rt case and the increased hc cases. The notable very high peak in one of the experiments is thought to be the result of the presence of a large aggregate directly touching one of the rebar ribs. Also, in this case, not only the hc cases are close to the peak bond strength; the frictional part is also within the experimental results envelope or very close to it. This indicates that RIVE has an additional effect on the frictional part that was not well captured by simply scaling based on the square root of the compressive strength.



**Figure 13-15** Simulation of the Bond Tests Assuming Effects of the Concrete Strength on the Steel–Concrete Bond Constitutive Model

**Table 13-7** Bond-Slip Model Parameters for Con-A at Different Exposure Conditions

Parameter	rt	irr-reduced	hc
<b>b1 (MPa)</b>	19.2	18.5	22.5
<b>b3 (MPa)</b>	6.00	5.78	7.00
<b>S1 (mm)</b>	1.20	1.20	1.20
<b>S2 (mm)</b>	2.60	2.60	2.60
<b>S3 (mm)</b>	4.00	4.00	4.00
<b><math>\kappa</math> (-)</b>	1.50	1.50	1.50

### 13.7 Case Study for Higher RIVE Expansions

Based on the LDPM results obtained at this study, it is possible to assume an acceptable level of prediction and explanation of the mechanisms affecting bond degradation. This section describes how LDPM is used to further analyze the impact of higher RIVE expansions. A 1% RIVE limit is assumed because the LDPM formulation used in this study is based on linear strain assumptions and does not account for large displacement effects. Figure 13-15 presents a comparison between the rt case and two irr cases at 0.2% (average attained RIVE) and 1% RIVE. These simulations use the reference bond parameters from the RT case. Even at 1% RIVE, bond degradation remains minimal. This outcome is expected because the LDPM is utilized to model the bulk concrete surrounding the rebar zone, whereas the fine mortar around it is modeled using interface element constitutive laws. Because the bond law parameters were not altered, the bond properties appear unchanged, even at 1% RIVE.

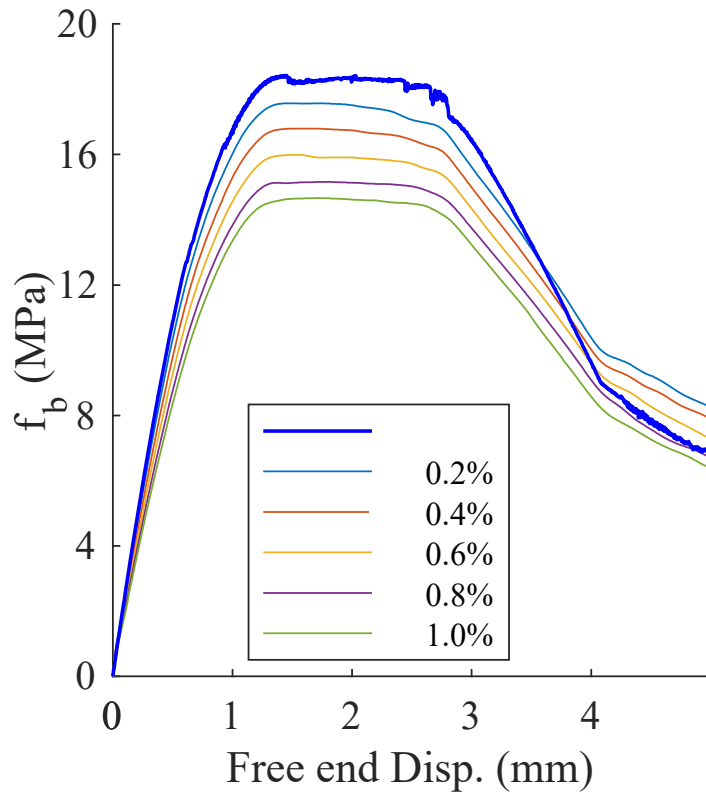
To account for the effect of compressive strength reduction on bond strength, simulations of the compressive strength of donuts with only coarse aggregate RIVE were performed for 0.4%, 0.6%, 0.8%, and 1.0%. The peak compressive strengths for all cases are listed in Table 13-8. It can be observed that at 1%, the compressive strength drops down to 35.57 MPa, so the bond strength ratio is expected to drop according to the square root ratio, which should be approximately 0.8. Using the listed ratios, the bond law parameters are scaled as listed in Table 13-9. Pullout simulation results are presented in Figure 13-16 and Figure 13-17. As can be seen from the results, a noticeable change in the bond strength can be observed.

**Table 13-8 Prediction of the Effect of Extended Irradiation on Concrete Compressive Strength**

<b>RIVE</b>	<b>Peak strength</b>	<b><math>cr</math></b>	<b><math>(cr)^{0.5}</math></b>
<b>Reference</b>	55.69	1.00	1.00
<b>0.2%</b>	52.12	0.94	0.97
<b>0.4%</b>	46.88	0.84	0.92
<b>0.6%</b>	42.43	0.76	0.87
<b>0.8%</b>	38.24	0.69	0.83
<b>1.0%</b>	35.57	0.64	0.80

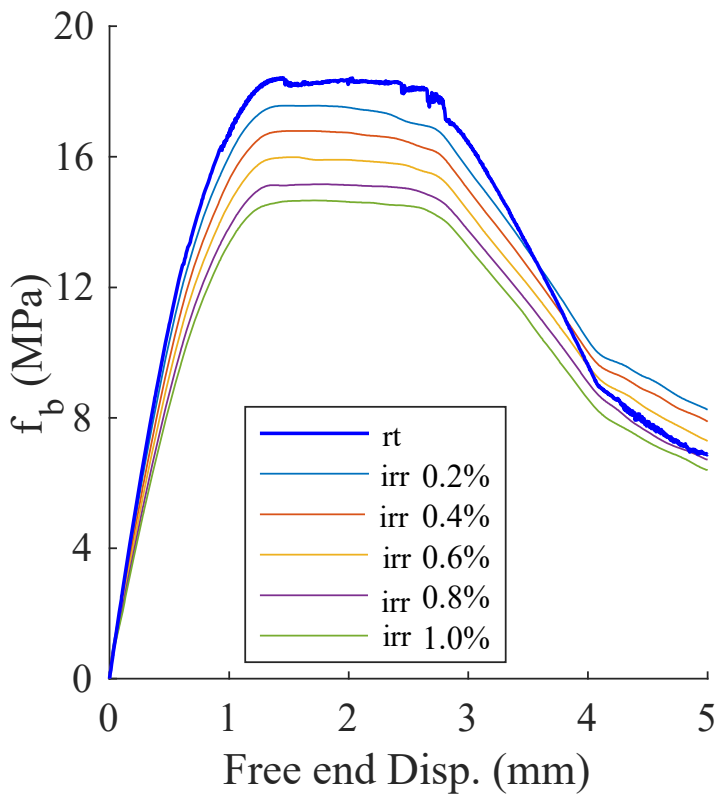
**Table 13-9 Scaled Bond Law Parameters for the Extended Radiation Cases**

<b>Parameter</b>	<b>0.4%</b>	<b>0.6%</b>	<b>0.8%</b>	<b>1.0%</b>
<b>b1 (MPa)</b>	17.62	16.76	15.91	15.35
<b>b3 (MPa)</b>	5.50	5.24	4.97	4.80
<b>S1 (mm)</b>	1.20	1.20	1.20	1.20
<b>S2 (mm)</b>	2.60	2.60	2.60	2.60
<b>S3 (mm)</b>	4.00	4.00	4.00	4.00
<b><math>\kappa</math> (-)</b>	1.50	1.50	1.50	1.50



**Figure 13-16 Prediction of Bond Strength Reduction Caused by Extended Irradiation Not Accounting for the Effect of Irradiated Concrete Compressive Strength Reduction**





**Figure 13-17 Prediction of Bond Strength Reduction Caused by Extended Irradiation Accounting for the Effect of Irradiated Concrete Compressive Strength Reduction**

## 14 STRUCTURAL PERFORMANCE OF IRRADIATED REINFORCED CONCRETE

### 14.1 Introduction

In LWRs, the CBS directly facing the RPV performs an important support function for the RPV and other structures and components. The CBS's primary function is to protect equipment and personnel from the radiation exiting the RPV, including neutron and gamma irradiation. Concrete contains a large amount of high-cross section hydrogen from the constitutive water ( $\sim 150\text{--}200 \text{ L}\cdot\text{m}^{-3}$ ), thus conferring excellent shielding properties to concrete (Kaplan, 1971, 1989). Hence, and unlike the Water-Water Energetic Reactor (WWER–VVER) design (Khmurovska et al., 2019), in general, the CBS in PWRs does not include a specific heavy-aggregate concrete shield (e.g., using hematite, ilmenite, or magnetite) but is made of natural aggregate structural concrete (Hookham, 1991) like the structural concrete used for the construction of other parts of the NPP (e.g., the containment building). Only natural aggregate concrete is considered in this report. The CBS tends to be more massive in PWRs than BWR designs because it typically supports the RPV and other large equipment. Nevertheless, this is not a generality because the RPV may also be supported by steel columns embedded in the CBS in some designs. The structural function of the RPV supporting structure is to transfer the static or seismic load of the reactor to the foundation system. The thickness of the biological shield wall varies with the nuclear steam supply system (NSSS) design (Verrall and Fitzpatrick, 1985). It typically ranges between 1.5 and 2.2 m (4.9–7.2 ft.) for PWRs and 0.60 and 1.20 m (2–4 ft.) for BWRs. The most common form of RPV support comprises shoes resting directly on the concrete, short columns, support beams, and pedestals embedded in the CBS below the nozzles. A comprehensive review of the RPV support systems can be found in Biwer et al., 2021, NUREG/CR-7280.

The assessment of the long-term structural integrity of the CBS involves addressing several questions. The first question is associated with the structural integrity of the RPV support system, including the effects of irradiation on the steel structures and components. This specific question is not addressed in this report. The three other questions are associated with the structural capacity of the CBS to transfer in-service passive loading and accidental loading during an accident such as an earthquake or a loss of coolant accident. Subject to prolonged irradiation over extended operation, it is expected that the region of the CBS exposed to a high level of irradiation near the core mid-elevation may be subject to irradiation-induced degradation. The possible damage extent depends on the irradiation fields and the structural response of the CBS to irradiation-induced damage. Both aspects are important for a correct structural assessment. Irradiation transport is the subject of previous research. The reader is referred to the report entitled *Radiation Evaluation Methodology Guidance of Concrete Structures* (NUREG/CR-7281), which describes state-of-the-art hybrid methods for calculating 3D neutron fluence and gamma dose fields in concrete. The purpose of the research presented in this report is focused on the second aspect: the structural simulation of irradiated concrete.

### 14.2 State of the Art

**Early approach using shell theory:** The effects of irradiation on the structural performance of LWR reinforced concrete biological shield have been the subject of research since the early 2010s. Mirhosseini et al. (2014) developed a reinforced concrete (RC) membrane model accounting for the concrete strength reduction resulting from the irradiation. The finite element model uses the modified compression-field theory developed by Vecchio et al. (1982, 1986)

from an extensive set of unirradiated structural experiments on RC panels subjected to varied combined compression and shear in-plane loading. The behavior of RC membrane elements, viewed as scale models for RC walls and shells in NPPs, under shear, and in a combination of shear and tension and compression, is analyzed in terms of strength (in-plane loading), ductility, and failure mode. The irradiated concrete compressive and tensile strength reductions are derived from a direct interpretation of Hilsdorf's curves (1978), including Dubrovskii's debatable data in particular (Dubrovskii et al., 1966; Fujiwara et al., 2009) obtained at very high fluences ( $> 10^{20}$  n.cm<sup>-2</sup>). As noted by Field (2015), Hilsdorf compiled irradiated properties for a large range of concrete mixes made by a wide range of aggregates' chemical compositions, mostly unspecified fast neutron energies, and varied test conditions. The possible irradiation effect on carbon steel reinforcement is not taken into account.

This assumption for fluence below  $10^{20}$  n.cm<sup>-2</sup> is based on the ACI 349.3R-03 report, which states, "Neutron irradiation produces changes in the mechanical properties of carbon steel (increase in yield stress and rise in the ductile-brittle transition temperature). As a consequence, steel reinforcement exposed to high cumulative neutron fluence (above  $10^{20}$  n.cm<sup>-2</sup>) may experience reduced ductility."

Mirhosseini's approach is to conduct structural failure analysis of NPP reinforced concrete components using nonlinear FEA. However, the use of membrane elements for modeling the effects of irradiation of a thick structure such as the CBS is highly debatable. First, the actual thickness-to-height ratio of such a component is approximately 1 to 5. Second and more importantly, the radiation fields (Field et al., 2015) through the member thickness are characterized by a high gradient: a high-neutron flux drop by one order of magnitude over a short distance of ~10–20 cm. Accounting for this gradient, along with possible moisture transport, implies modeling nonuniform thermo-hygro-radiological effects in the CBS. If a shell model were created for this purpose, then it would require either the use of multilayered shell elements or 3D-volume elements, or a 2D-surface element  $r - z$  in a cylindrical model, or a 1D- $r$  segment element in a radial-cylindrical model.

Finally, although Mirhosseini (2014) acknowledges that "Deterioration of shielding concrete is mostly due to volume changes of concrete. Aggregate expansion is the main factor of radiation deterioration in concrete in NPPs," it is possible that RIVE-induced stresses are not accounted for in their modeling work.

***Coupled thermo-hydro-mechanics:*** The approach followed by the research team of the University of Padova (Pomaro et al., 2011; Salomoni et al., 2014) was developed based on an existing coupled nonlinear thermo-hygro mechanical (TH→M) model initially developed by Schrefler et al. (1989), Baggio et al. (1995) and Majorana et al. (1998). Heat transfer and moisture transport are coupled following a scheme developed by Schrefler et al. (1989), derived from the pioneering work of Luikov (1975). Radiation effects are assumed to be uncoupled from thermal and moisture transport in these early works. Note that a fully coupled transport model has been recently published by the University of Padova (Zhang et al., 2024).

The concrete mechanical model includes thermal expansion, autogenous shrinkage, creep, load-induced thermal strain rate, damage, and plasticity effects. The incremental isotropic damage formulation follows Mazars's theory combining tensile and compression strain effects on damage (Mazars and Pijaudier-Cabot, 1989). An equivalent damage index is assumed to result from a cumulative (multiplicative effect in the sense of the Gérard et al., 1998) effect of mechanical, thermo-chemical, and radiation damage:  $\tilde{d} = 1 - (1 - d_m)(1 - d_T)(1 - d_\phi)$ , where  $\tilde{d}$ ,  $d_m$ ,  $d_T$  and  $d_\phi$  are respectively the overall, mechanical, thermal, and irradiation-induced

damage. Concrete radiation damage is determined assuming a lower bound exponential fit of Hilsdorf's data showing a gradual decrease of the elastic modulus to what is interpreted as an asymptotic value of 50% of the initial elastic modulus with increased neutron fluence. The 1D simulation of a biological shield is performed on a 3.5 m thick prism to obtain a damage profile within the thickness of the concrete shield. The model simulations predict that the irradiation effects are the only source of damage in the concrete shield and that damage progresses inward into the shield with the accumulated fluence. The calculated stress levels are particularly low ( $< 1$  MPa), even in the presence of radiation. The maximum estimated damage after 50 years of operation is equal to the threshold chosen by the author for radiation damage in concrete (here assumed at 0.5). Maximum damage is observed at the surface of the CBS, where the fluence reaches its peak value. For an ordinary concrete, the damage profiles appear to decrease almost linearly from the surface with an approximate gradient of  $\sim 0.8 \text{ m}^{-1}$  depth for fast neutrons and  $\sim 1.2 \text{ m}^{-1}$  depth for thermal neutrons. After sufficient irradiation exposure time, the damage profile exhibits a plateau caused by damage saturation resulting from the interpretation of Hilsdorf's plot of elastic modulus vs. neutron fluence.

Depending on the energy level used for the interpretation of Hilsdorf's data, the maximum damage depth, defined by  $\tilde{d} > 0$  after 50 years of operation, is estimated to be approximately 1 m and 0.7 m, respectively, for fast neutrons and thermal neutrons.

This rather deep damage penetration is the result of the very high total fluence exposure assumed— $10^{12} \text{ n.cm}^{-2} \text{ s}^{-1}$ —which leads to a total fluence of approximately  $1.6 \times 10^{21} \text{ n.cm}^{-2}$  after 50 years of operation. Such a flux is one-to-two orders of magnitude higher than the estimated bounding value for PWR CBS (Esselman and Bruck, 2018; Remec et al., 2013).

Pomaro's approach contains several important features for modeling the effects of coupled TH→M effects on irradiated concrete. Interestingly, however, the effects of moisture transport and temperature on the cumulated damage appear to be negligible because of the low temperature and small induced stress found in Pomaro's simulation. At the time that this research was performed, the understanding of the dominant role of RIVE on damage development was not clearly identified. Thus, the proposed model initially ignored the potential effects of RIVE which can potentially develop large stresses and subsequent mechanical damage. Follow-on works produced by the same institution (Pomaro et al., 2022, Zhang et al, 2024) included RIVE in their models to obtain convincing validation against experimental data.

**Analytical and semi-analytical methods:** Andreev and Kapliy (2014) established the first 1D-radial analytical model explicitly accounting for the effects of RIVE in a thick, hollow concrete cylinder. Considering a theoretical attenuation profile of the fast neutron fluence, they found that the structural constraints preventing the RIVE in the area adjacent to the reactor cavity cause large biaxial compression in the vertical and orthoradial (or hoop) directions. Their calculations also showed important tensile stresses toward the back of the wall to balance the compressive forces occurring near the reactor cavity. However, the operational conditions (fluence up to  $5 \times 10^{24} \text{ n.cm}^{-2}$  and temperature  $\sim 500^\circ \text{C}$ ) and the geometry (inner radius at 3.3 m) considered by these authors are not representative of LWR conditions. The model developed by Andreev and Kapliy qualitatively captures the structural response of a thick concrete structure exposed to high fast neutron fluences. Subsequently, Le Pape (2015) improved Andreev's 1D-model of a prototypical unreinforced CBS at the elevation of the mid-fuel core assembly by introducing irradiated concrete's mechanical properties based on the data collected in Field et al. (2015) and irradiation fields representative of PWRs. Young's modulus, the tensile strength, and the compressive strength were considered as empirical functions of the fluence exposure: degradation of the irradiated concrete properties occurred for fluence levels higher than to  $10^{19}$

n.cm<sup>-2</sup>. The same criticisms drawn against the use of Hilsdorf's data by Mirhosseini can be made here. The proposed empirical equations do not distinguish between the varied types of concrete compositions; they simply consider the entire available dataset as a statistically representative set of irradiated data. The model does not include mechanical damage. This implies that cracking induced by excessive stresses is not accounted for in this model and that no stress redistribution occurs. The simulations confirm Andreev's conclusions for long-term fluence exposure in PWRs. The portion of the CBS located in the vicinity of the reactor cavity is subject to high compressive stresses caused by restrained RIVE. Those biaxial compressive stresses in the vertical and circumferential directions largely exceed the residual irradiated compressive strength. Simultaneously, important radial strains occur in the same region. This stress state is qualitatively analogous to submitting a thick cylinder to a thermal shock increasing the temperature in the cavity. The amplitude of these irradiation-induced compressive stresses increases with the thickness of the CBS: the increase of structural stiffness prevents the irradiation-induced expansion in the vertical and orthoradial directions. A probabilistic analysis was also conducted (Le Pape, 2015). It was determined that the extent of degradation found in this study is on average 5% of the CBS thickness, with a maximum value close to 20%. To balance the high compression zone, the back of the CBS appears to be subjected to tension. The significance of this tension could not be addressed in the proposed model, which does not account for energy dissipation caused by cracking or relaxation.

**Finite element analysis:** Using the irradiated concrete properties modeled in Le Pape (2015), Bruck et al. (2019) developed a finite element model accounting for the presence of the reinforcement and the considered concrete failure caused by overstresses. The structural model represents a “piece of pie” or a wedge, a representative sector of the CBS assuming axisymmetric conditions. Whereas the radiation fields are not axisymmetric because of the reactor core geometry, sector models generally assume the highest azimuthal flux as an input. The boundary conditions assume the absence of orthoradial displacement (axisymmetry). The boundary condition in the vertical direction is more difficult to estimate. Limited vertical deformation is limited but is possible because of the geometry of the CBS. Sector models usually assume the absence of vertical displacements which lead to overestimating the structural constraints, and thus the compression stresses in the most irradiated region. In Bruck's model, microcracking caused by irradiation damage is caused by the loss of elastic modulus and strength—both considered as functions of fluence as in Le Pape (2015). The results of this study show compression damage of the concrete most exposed to irradiation and tension damage at the back of the CBS. Damage depth extents are not provided.

More recently, Khmurovska et al. (2019) studied the long-term effects of irradiation on a VVER-440/213 CBS using a finite element model. The VVER CBS includes a 70 cm thick serpentine shield facing the reactor cavity and a 2.5 m structural concrete. Irradiation-induced, thermal, and mechanical damages are cumulated using an approach like Pomaro's (2011). Irradiated concrete properties follow the suggestion from Le Pape (2015). Mazars's model is assumed to account for mechanical damage, and the B3 model is assumed to account for creep (Bažant and Jirásek, 2018). The simulation results show the formation of vertical cracks propagating from the top of the CBS, where the thickness is reduced. These cracks are caused by the gradual vase-shaped deformation induced by the expansion of the serpentine shield. In the United States, PWR CBSs that support RPVs have many variations in design, and that should be included in the plant-specific evaluation.

**Discrete models:** As an alternative to FEA, Kambayashi et al. (2020) developed a lattice-based discrete meso-scale model of a portion of a prototypical CBS. The model uses the RBSM approach. The advantage of discrete modeling of quasi-brittle materials is the explicit

representation of crack opening in the constitutive model. This inherent characteristic of discrete models makes them suitable to represent both diffused microcracking and fracture. This feature is beneficial to irradiated CBS modeling because intrinsic irradiation damage of concrete causes microcracking, and structural constraints result in mechanical damage.

Using RBSM, aggregates and reinforcing bars are explicitly represented. Cracking and creep occur in the mortar phase surrounding the aggregates subject to RIVE. Thermal strains are also taken into account. This study once again confirms the occurrence of large compressive stresses near the reactor cavity causing cracking parallel (spalling effect) to the inner surface of the concrete wall. Cracking extends beyond the location of the inner vertical and circumferential rebars, reaching a depth of about 200 mm, although a crack opening is considerably reduced beyond the rebar when compared to cracking in the concrete cover (distance to rebar center: 100 mm).

Using a comparable meso-scale finite element model, Giorla et al. (2016) concluded that the penetration of damage reached approximately 150 mm after 80 years of operation. This study did not find detrimental tensile stress at the back of the CBS as the result of mortar's relaxation and stress redistribution in the reinforcement.

In conclusion, the literature analysis determined that irradiation-induced damage in a PWR CBS combines two forms of damage: (1) direct degradation resulting from irradiation-induced damage causing micro-cracking in the concrete constituent, and (2) mechanical damage caused by large vertical and circumferential stresses resulting from the structurally restrained RIVE.

In an effort to pursue this research sponsored by the U.S. DOE LWRS Program and the U.S. Nuclear Regulatory Commission (NRC), two modeling strategies were developed. The first uses the finite element code Grizzly developed under the MOOSE platform, and the second uses the LDPM. Using two different modeling strategies allows for comparison of the irradiation damage profile and extent. Because LDPM does not arbitrarily separate damage caused by irradiation and structural effects, LDPM is expected to better represent cracking in the biological shield. However, Grizzly modeling can be more representative of industry standards for structural analysis. The following discussion uses some information published in Cheniour et al., 2022.

### **14.3     Finite Element Model**

#### **14.3.1     Model Geometry and Mesh**

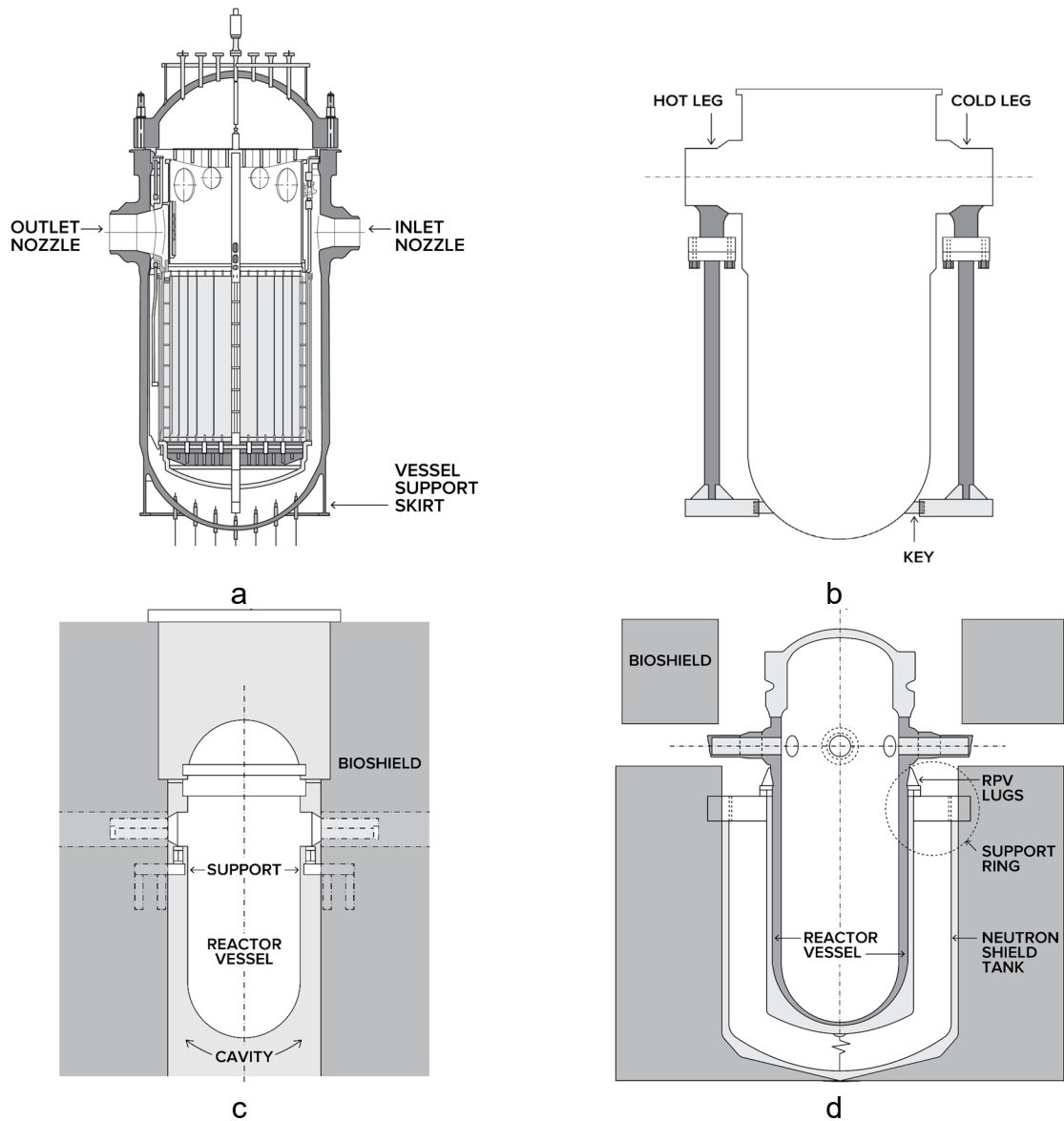
##### **14.3.1.1     Geometry**

The design of LWR CBS varies across the U.S. commercial nuclear fleet. First, in this study that focuses on the effects of neutron irradiation, BWRs are not considered because the following was established

*The estimated bounding (maximum) fluence at the reactor vessel support pedestals was conservatively determined to be  $\sim 1.8 \times 10^{18} \text{ n.cm}^{-2}$  at 80 years of operation, which is almost an order of magnitude lower than threshold value for concrete degradation defined previously. As such, it is unlikely that chronic radiation exposure will appreciably affect the structural margin in the reinforced concrete BWR vessel support pedestals (Wall, 2016).*

However, a plant-specific evaluation should be performed. For example, the effects of secondary gamma-induced heating in a metal-bearing heavy concrete shield may need further examination. The proposed work intends to use a generic methodology using a modified prototypical reactor geometry for a modified Westinghouse 4-loop PWR. These methodological guidelines are provided to support performance of future structural assessment of irradiated CBSs. This is not a bounding example: 2-loop and 3-loop PWRs may have higher fluence than 4-loop reactors.

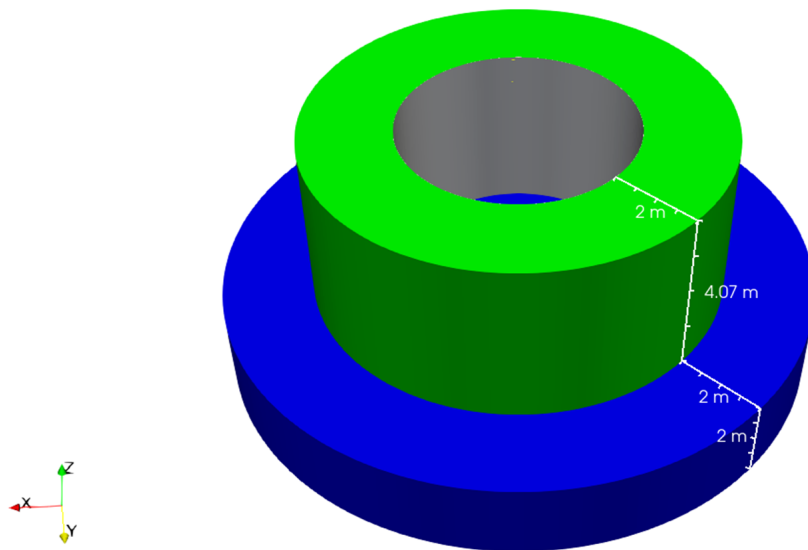
The concrete model geometry consists of two main entities: (1) a thick hollow cylinder representing the CBS (inner concrete radius: 258.2 cm, outer radius: 458.2 cm, height: 407.1 cm) and (2) a thick circular basemat (height: 2 m, outer radius: 648.2 cm). A ½ cm thick steel liner is also modeled. For the sake of simplicity, this geometry does not include ex-core detector wells embedded in the concrete. The liner's outer radius corresponds to the concrete's inner radius. The liner and the concrete interface are assumed to be perfectly bonded, and connectors are not represented because the details were not available from ORNL, and this also allows for simplicity. The basemat geometry is not represented to its full extent because appropriate boundary conditions are introduced at the lateral extremities of the basemat (absence of radial displacement). Modeling the basemat is critical to account for the lateral structural restraint occurring at the junction between the CBS and the basemat.



**Figure 14-1 Illustration of Varied Supporting System for the RPV (Biwer et al., 2021): (a) PWR RPV with a Support Skirt, (b) PWR RPVs Supported on Columns and Anchored to CBS for Lateral Support ( for Seismic, Accident, Stability, etc.) (c) PWR Supported on Cantilevered Beams or Extended Supports, and (d) PWR RPV Supports Mounted on a Neutron Shield Tank**

The proposed geometry is not intended to fully replicate a specific 4-loop PWR design, but instead it provides representative dimensions. However, it must be recognized that the geometry affects the stress and damage fields. Notably, as discussed in Section 14.2, the thickness of the CBS plays an important role in the irradiation-induced stress profile along the radial direction resulting from the force equilibrium between the irradiated portion subject to compression and the back of the wall subject to tensions. The chosen thickness of 2 m is close to the thickness of 1.75 m used in Matijević et al. (2015) for the H.B. Robinson-2 unit and matches the thickness used in Kambayashi's work (2020).





**Figure 14-2 3D View of the Mesh Showing the Main Structural Elements in the Model: Blue Basemat, Green Concrete Shield, and Gray Liner**

#### 14.3.2 Mesh

The CBS mesh employs first-order hexahedra to represent the 3D solid, together with truss elements for the rebar. The solid mesh was generated using built-in tools provided by MOOSE which allow for meshing primitive geometries and combining meshes that share nodes at common locations. For the CBS wall, an annular mesh was generated and extruded, with elements being progressively refined towards the inner surface. Gradual mesh refinement of the concrete near the reactor cavity is necessary to capture the gradient of fast neutron flux (approximately one order of magnitude loss over  $\sim 15$  cm). Ideally, mesh refinement in the vertical and hoop directions would be needed to avoid creating distortion of the finite elements and reducing the accuracy of the elements' shape functions. However, refining the mesh in all directions would result in creating very computationally expensive mesh. The CBS liner mesh, which is connected to the CBS wall mesh via common nodes, has the same height as the concrete wall and a thickness of 5 mm represented by a single-element layer.

The basemat mesh was generated as a separate mesh to ensure that the nodes located on the top surface coincide with those on the CBS wall. The main purpose of modeling the basemat is to generate structural stiffness. Possible degradation of the basemat is not considered. Hence, the element's size is gradually increased toward the outer surface of the basemat. The elements are mostly first-order hexahedra except for in the center of the cylinder, where they are first-order tetrahedra.

Following the specifications provided in Risner et al. (2020), the reinforcement consists of vertical and hoop steel bars #8 (dia. 1 in., 2.54 cm) located with a 3 in. cover near the inner diameter and the outer diameter of the concrete shield. The bars are spaced every 10 in. (25.4 cm) center-to-center.

The bars' mesh is generated using *Gmsh* (Geuzaine and Remacle, 2009). The bars are represented as 1D line elements embedded in the concrete solid elements. The bars are

meshed independently from the 3D solids. The bar node displacements are associated with the surrounding concrete nodes using kinematic constraints to enforce that the displacements of the concrete and bar are equal at the line element nodes through a penalty method.

### **14.3.3 Boundary Conditions**

The bottom surface of the basemat is fixed (no vertical displacement). Hence, potential basemat curvature is prevented because of the thickness of the basemat conferring at a high bending stiffness. This infinite bending stiffness effect is also augmented by adopting a no-radial displacement boundary condition at the lateral surface of the basemat. The other surfaces of the model are not kinematically constrained.

### **14.3.4 In-Service Conditions and Loading**

#### *14.3.4.1 Permanent Loading*

The PWR RPV can weigh as much as 427,000 kg (941,600 lb) (Mager et al., 1999) without the core and the refueling cavity elements. Such a weight leads to an average vertical pressure in the section of the biological shield of < 0.1 MPa. The self-weight of the concrete over a 4 m height accounts for another 0.1 MPa. Because the objective of the proposed model is to characterize the effects of irradiation on damage formation over the entire CBS, those permanent-loading induced stresses are negligible compared to the RIVE-induced stresses. They are thus not accounted for in the model.

#### *14.3.4.2 Operating Radiation Conditions*

The fast neutron irradiation fields are calculated using the irradiation transport code VERA (Kochunas et al., 2017), a software suite that enables neutron transport calculations using both deterministic and hybrid deterministic / Monte Carlo methods. High-fidelity in-core radiation transport calculations with temperature feedback are performed using MPACT (Collins et al., 2016), a deterministic neutron transport code, and CTF (Avramova, 2009), a subchannel thermal hydraulics code.

### **14.3.5 Concrete Constitutive Model**

The proposed constitutive model is analogous with an ASR model implemented in Grizzly. RIVE as function of fast neutron fluence can be modeled using sigmoidal curves with a mathematical expression similar to ASR expansion as a function of time. The *intrinsic* damage, or the loss of mechanical properties during unconstrained swelling experiments, is directly derived from the concrete expansion. Note that in this study, the presence of a liner prevents moisture transport. Hence, the effects of moisture content on concrete properties are not considered. In the absence of a liner, moisture transport simulations should be included in the analysis to accurately model shrinkage and creep, and all other concrete properties are subject to changes with the moisture content.

#### *14.3.5.1 Strength and Mechanical Damage Model*

Two damage models are employed simultaneously. Irradiation-induced intrinsic damage captures the loss of elastic modulus of irradiated concrete: micro-cracking caused by incompatible radiation-induced expansion. Structural damage caused by the formation of restrained stresses is model using a classical Mazars' isotropic model for lack of a better

available option. As discussed previously, expansion in the most irradiated region of the CBS occurs mainly in the radial directions as a result of the confined RIVE-induced biaxial compression stresses in the vertical and hoop directions. Hence, structural cracking is expected to develop parallel to the inner surface of the CBS (mainly radial openings as illustrated in the meso-scale lattice discrete particle model presented in Section 14.4). Thus, it would be more representative to use an anisotropic damage model to account for the cracking-induced loss of stiffness in the radial direction, whereas the vertical and hoop directions maintain higher stiffnesses.

#### 14.3.5.2 *Radiation-Induced Volumetric Expansion (RIVE) and Damage*

The RIVE of concrete is caused by the change of density of irradiated aggregates. The kinetics and amplitude of aggregate RIVE depends on several factors:

1. **The aggregate mineralogy.** The RIVE of rock-forming minerals are subject to important variations depending on their chemical composition and crystalline structure. Detailed studies can be found in the literature (Denisov et al., 2012; Le Pape et al., 2018). In summary, the nature of the atomic bonds governs the RIVE amplitude. The more covalent bonds that are present, the higher the RIVE. The more ionic bonds that are present, the lower the RIVE. Hence, quartz is the mineral which exhibits the highest RIVE up to 17.8%, among all other silicates. When the ratio of ionic to covalent bonds increases, RIVE decreases. Carbonates exhibit low RIVE <0.5%.
2. **The fast neutron fluence.** Aggregate RIVE increases gradually with increasing fast neutron fluence. In the context of concrete studies, fast neutrons are conventionally characterized by energies higher than 10 keV or 0.1 MeV. Both energies can be adopted because they respectively cause close to 100% and >95% of the dpa occurring in irradiated minerals in LWRs. Mineral RIVEs are empirically described by a sigmoidal curves function of the fast neutron fluence and the irradiation temperature (Le Pape et al., 2018). A simplified method to estimate the RIVE of aggregate is to apply a rule of mixtures (weighted averaging method) using the volume fraction of the minerals present in the aggregates (Le Pape et al., 2020b).
3. **The irradiation temperature.** When the irradiation temperature increases, the RIVE rate decreases as a result of defects recovery. RIVE equations accounting for temperature are provided in Le Pape et al., 2018. These equations were derived from irradiated data obtained from test reactor experiments.
4. **The fast neutron flux.** This concept is still not fully elucidated at this writing. In the experimental study presented in this report, the first evidence of fast neutron flux effect is observed. In the case of aggregate GA(F) containing 92% quartz, the dimensional change of the specimens irradiated in the LVR-15 reactor is approximately  $\times \sim 4$  to  $\times \sim 5$  lower than the same composition aggregates irradiated at comparable fast neutron fluences in the JEEP-II reactor. The fast neutron fluxes in the LVR-15/XK1 and JEEP-II reactors are  $\sim 3.6 \times 10^{11} \text{ n.cm}^{-2} \text{ s}^{-1}$  and  $\sim 3.6 \times 10^{12} \text{ n.cm}^{-2} \text{ s}^{-1}$  ( $E > 0.1 \text{ MeV}$ ).

In this simulation study, aggregate GA(F) was adopted because of its high content in quartz (92%), causing significant RIVE. The contribution of the 8% remaining minerals is neglected.

The RIVE model for quartz is given in Le Pape, 2018 and is available in the IMAC database (Le Pape et al., 2018, 2020). It follows a Zubov-type expression (Zubov and Ivanov, 1966) as a function of the neutron fluence and temperature. The RIVE model is expressed as follows:

$$\varepsilon^*(\Phi, T = T_{ref}) = \varepsilon_{max} \frac{1 - e^{-\frac{\Phi}{\Phi_c}}}{1 + e^{-\frac{\Phi - \Phi_L}{\Phi_c}}}$$

where  $\varepsilon^*$  is the radiation-induced expansion, which has a maximum value  $\varepsilon_{max}$ ;  $T$  is temperature;  $T_{ref} = 45^\circ \text{C}$  is the reference temperature,  $\Phi$  is the fast neutron fluence ( $E > 10 \text{ keV}$ ), and  $\Phi_c$  and  $\Phi_L$  are the characteristic fluence and the latency fluence, respectively. An Arrhenius activation function describes the evolution of the latency fluence and the characteristic fluence in Zubov's model. Refer to Table 1, ZA model in Le Pape et al., 2018 for values.

Using the law of mixture, the GA(F)—92% quartz content—aggregate RIVE is approximated to 0.92 times the RIVE of quartz. Then the estimates of the corresponding concrete expansion can be derived by the analytical expressions provided in Le Pape et al. 2015b, Eq. {20}. The upper bound equation depends only on the volume fraction of aggregates ( $f_a$ ). The concrete RIVE can be estimated by multiplying the aggregate RIVE by a factor of  $2f_a/(1 + f_a)$ , which ranges from 0.75 to 0.85 for ordinary concrete. Thus, Con-A concrete RIVE reads:  $\varepsilon_{concrete}^* \sim 0.74 \times \varepsilon_{quartz}^*$ .

The engineering properties of concrete are affected by fast neutron irradiation (Hilsdorf et al, 1978; Field et al., 2015). The changes of properties are generally reported in the literature as functions of the neutron fluence. However, the loss of engineering properties results from the formation of microcracking caused by incompatible strains between the concrete constituents (e.g., between adjacent aggregate-forming minerals, between an aggregate and the surrounding cement paste). Hence, the loss of engineering properties caused by neutron irradiation can be alternatively described as a function of its RIVE. The advantage of this formulation is an explicit description of the irradiated concrete microcracking in the constitutive model. This is referred to as *intrinsic micromechanical damage* hereafter.

The intrinsic micromechanical damage is obtained by fitting the evolution of the irradiated Young's modulus of concrete against the RIVE assuming a rational function comparable to the one used to model ASR in Black Bear (Giorla, 2016b). This choice for the fitting mathematical function is arbitrary. Other fitting functions could be adopted (e.g., Spencer et al., 2021).

#### 14.3.5.3 Thermal Expansion

The coefficient of thermal expansion (CTE) of aggregate also varies with its mineralogy in an approximate range of  $5\text{--}15 \mu\text{m.m}^{-1} \text{ }^\circ\text{C}^{-1}$ . A common estimate of CTE in concrete is approximately  $10 \mu\text{m.m}^{-1} \text{ }^\circ\text{C}^{-1}$ . Thus, at a temperature below  $65^\circ \text{C}$  (ACI prescription), the corresponding volumetric expansion is less than 0.135%. In comparison with the assumed amplitude of RIVE (several percent), the thermal expansion is quite negligible and is not considered in this model. This assumption is specific to this study and shall not be generalized.

#### 14.3.5.4 Creep

It may seem surprising to discuss the effects of creep on the structural behavior of the CBS. The CBS is not post-tensioned, and it transfers limited permanent loading causing vertical stresses <

0.1 MPa. However, creep contributes greatly to the dissipation of RIVE-induced stresses. This effect has been studied as discussed in Giorla et al., 2017. In summary, when RIVE is confined, it causes important compressive stresses and elastic energy. When these stresses exceed the material's resistance, it leads to cracking. However, RIVE increases at a rather slow rate. Hence, the RIVE-induced stress relaxation caused by a viscous mechanism may occur. Thus, two dissipation mechanisms occur concurrently: the formation and propagation of damage (cracks), and relaxation. The term *relaxation* refers here to the dual mechanism of creep. In the simulations conducted by Giorla et al. (2017), it was shown that accounting for creep properties delays damage formation when RIVE increases.

Creep properties depend on moisture content and temperature. In this study, the question of drying creep or the effects of moisture content on basic creep properties are not addressed because the presence of the liner maintains the moisture content close to 100%. When temperature increases, creep rate increases.

The effects of irradiation of concrete creep properties are still poorly understood. Based on the limited experiment conducted on cement grout by Gray (1971) and further analyzed by Giorla et al. (2017), neutron irradiation appears to significantly accelerate the creep rate. To the best knowledge of the authors, no other experiment was published on the effect of neutron irradiation of the creep properties of cement constituents. When subject to gamma irradiation, the creep rate of concrete specimens that are sealed to prevent moisture migration but permitting radiolitic gas venting (McDowall, 1971) is lower than the creep rates observed in the absence of gamma irradiation. The creep rate decrease is attributed to radiolysis-induced drying of the cement paste. At this stage of the research, it is not possible to provide definitive conclusions on the effects of irradiation on concrete creep properties.

One can opt for ignoring the creep effect in the CBS model. This hypothesis will lead to increasing irradiation-induced damage.

In this methodological study, creep was included in the constitutive law of concrete using the B3 model developed by Bažant and Jirásek (2018). The creep compliance function is taken from Torrenti and Le Roy (2018) using the creep data provided by Kommendant et al. (1976). These parameters do not account for the possible effects of irradiation.

#### 14.3.5.5 *Mechanical Damage*

The loss of engineering properties of irradiated concrete is derived from post-irradiation characterization of specimens placed in irradiation capsules. Unless unwanted confinement occurred because of underestimated expansion, the concrete specimens are free to expand during the neutron irradiation reported in the literature. The irradiated concrete Young's modulus and strength properties decrease when incompatible strains occur in the concrete constituents, thus creating *microcracking* (See Section 14.3.5.2). The corresponding damage is referred to as *intrinsic microstructural damage*.

However, a second source of damage must be considered when modeling a CBS: that is, *mechanical or structural damage*. This is caused by excessive stresses and strains resulting from structural constraints that prevent RIVE from developing freely. In the context of this study, an isotropic damage model was adopted (Mazars and Pijaudier-Cabot, 1989) because of its simplicity and its availability in the code Black Bear. Constitutive parameters can be found in the literature (Pijaudier-Cabot and Mazars, 2001; Hamon, 2013).

Because the stress state in the irradiated region of the CBS near the reactor cavity is highly directional (tension in the radial direction and compression on the two other direction), it is recommended that the use of anisotropic damage models in future work be considered (e.g., using microplane models).

The microstructural and structural damage are cumulated assuming that the total damage is equal to the maximum value of the two. As noted in the *State-of-the-Art* section, several authors have adopted a cumulative damage rule assuming multiplication factors:  $\tilde{d} = 1 - (1 - d_1) \times (1 - d_2)$  instead of  $\tilde{d} = \max(d_1, d_2)$ . The multiplicative rule tends to increase the cumulative damage.

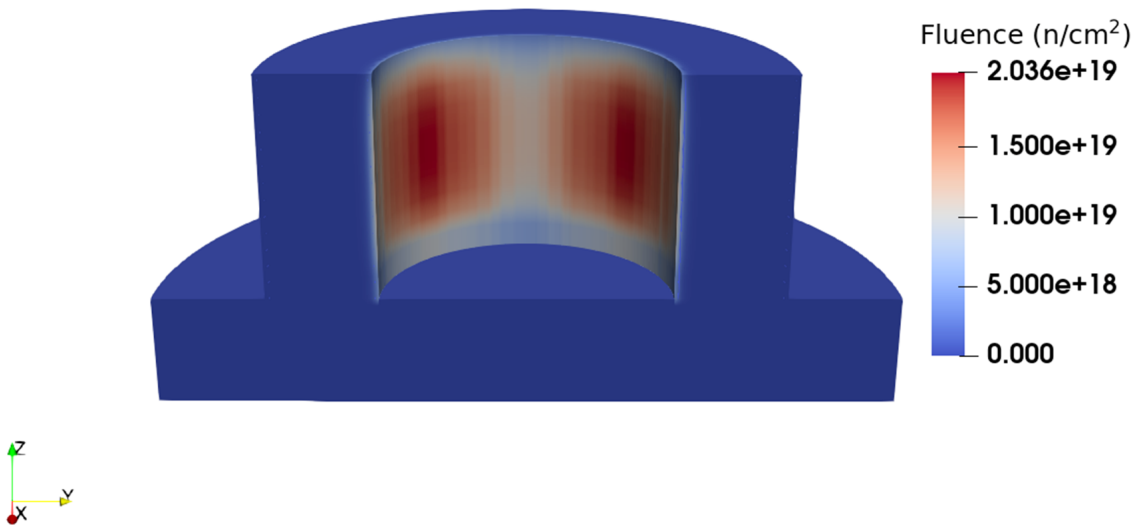
### 14.3.6 Steel Constitutive Model

The metal liner and the reinforcement are made of construction-grade mild steel properties. The yield stress and elastic properties are of crucial importance for the structural behavior of reinforced concrete. Nevertheless, at the considered operational temperature ( $< 65^\circ\text{C}$ ), these properties are not affected (Graves et al., 2014, Section 4.3.2.2). The Young's modulus and Poisson ratio of mild steel are assumed to be equal to 200 GPa and 0.3. During this study, it was found that the liner and the reinforcement remain in the elastic regime under the considered in-service condition, as only the weight of the RPV without the core and other refueling elements (Section 14.3.4.1) and radiation (Section 14.3.4.2).

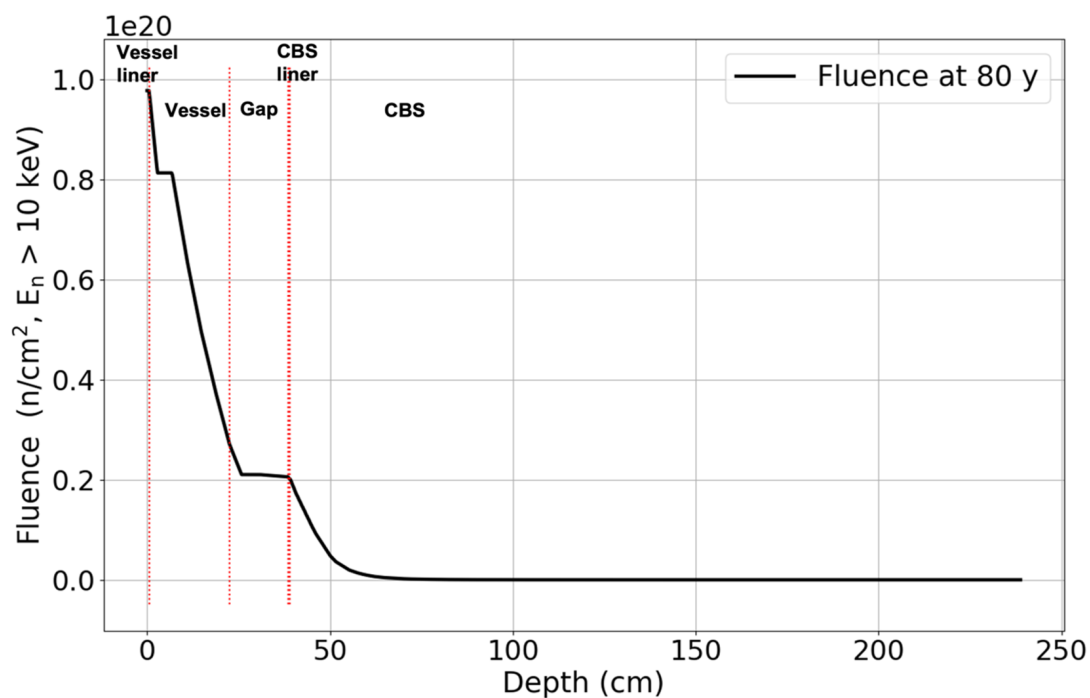
### 14.3.7 Simulation Results

In the conducted simulation using VERA, the maximum fluence at the surface of the concrete is equal to  $2 \times 10^{19} \text{ n.cm}^{-2}$  ( $E > 10 \text{ keV}$ ) at 80 years of operation. Such a fluence is consistent with the estimates provided by Esselman and Bruck (2018) for 4-loop PWRs for 80 years of operation. Note that higher fast neutron fluence approaching  $7 \times 10^{19} \text{ n.cm}^{-2}$  ( $E > 0.1 \text{ MeV}$ ) could be expected for a number of 2-loop and 3-loop reactors. Thus, the results presented hereafter do not pretend to address a bounding case scenario. However, the methodologies are expected to provide guidance for future simulations.

Irradiation transport results in a non-uniform fast neutron flux field. Figure 14-3 shows the fast neutron fluence calculated using the code VERA and projected on the Grizzly finite element mesh (concrete). At the surface of the CBS, the fast neutron fluence ranges between  $\sim 5 \times 10^{18} \text{ n.cm}^{-2}$  and  $2 \times 10^{19} \text{ n.cm}^{-2}$ . At approximately the mid elevation of the CBS, the azimuthal variation of fast neutron fluence ranges between  $\sim 1 \times 10^{19} \text{ n.cm}^{-2}$  and  $2 \times 10^{19} \text{ n.cm}^{-2}$ . These variations are caused by the core design geometry. At the location where the fast neutron fluence is the highest, the radial profile of fast neutron fluence is presented in Figure 14-4. Resulting mainly from the presence of hydrogen (high-cross section element), the fast neutron fluence drops rapidly with increasing radius. At  $\sim 7.5 \text{ cm}$  from the surface, the fast neutron fluence reaches  $1 \times 10^{19} \text{ n.cm}^{-2}$ ; at a depth of  $\sim 12.5 \text{ cm}$ , the fast neutron fluence reaches  $0.5 \times 10^{19} \text{ n.cm}^{-2}$  at 80 years of operation. Hence, it can be inferred that the neutron-induced *intrinsic microstructural damage* causing a reduction of concrete properties will reach approximately 7.5 cm for this case study. Note that in this simulation, the reinforcement center is located at  $\sim 7.5 \text{ cm}$  (3 in.) from the surface. The question to be addressed is: Does the contribution of the *structural damage* increase the damage depth beyond the *intrinsic microstructural damage* depth? In other words, is a structural simulation necessary to infer the irradiation-induced damage, or can the damage depth be evaluated with a simple analysis of the fast fluence field using a cut-off fluence of  $10^{19} \text{ n.cm}^{-2}$ ?



**Figure 14-3** Calculated Fast Neutron Fluence ( $E > 10 \text{ keV}$ ) Field at 80 Years of Operation



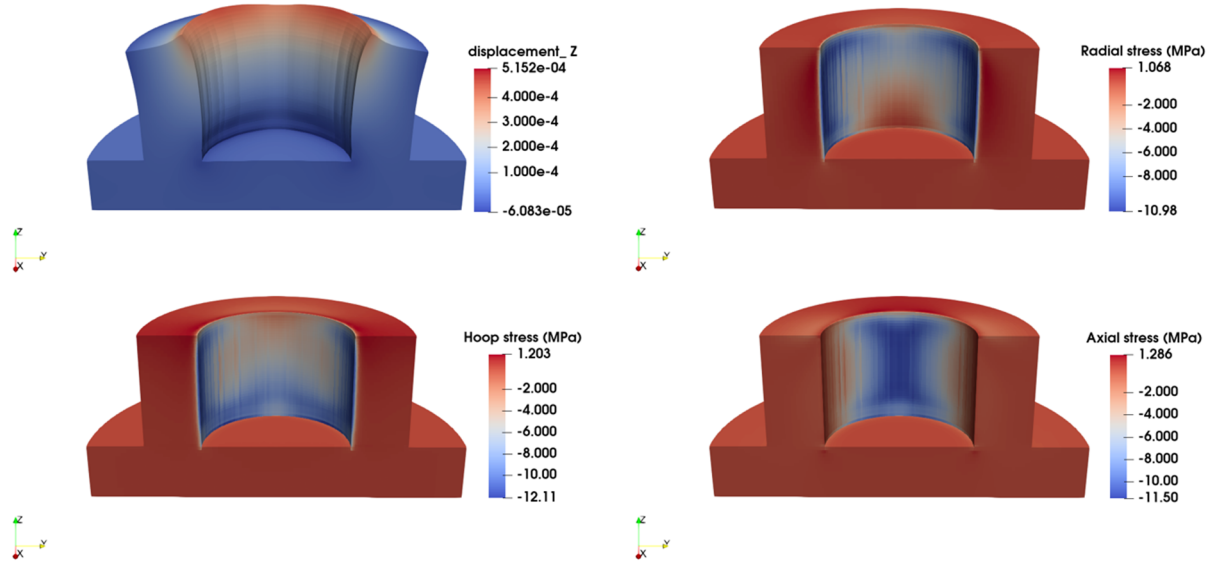
**Figure 14-4** Fast Neutron Profile ( $E > 10 \text{ keV}$ ) Across the RPV, the Reactor Cavity, and the CBS at 80 Years

The general in-service structural behavior of the CBS can be summarized as follows. The CBS deformation exhibits a vase-shape. RIVE mainly occurs near the reactor cavity, creating an

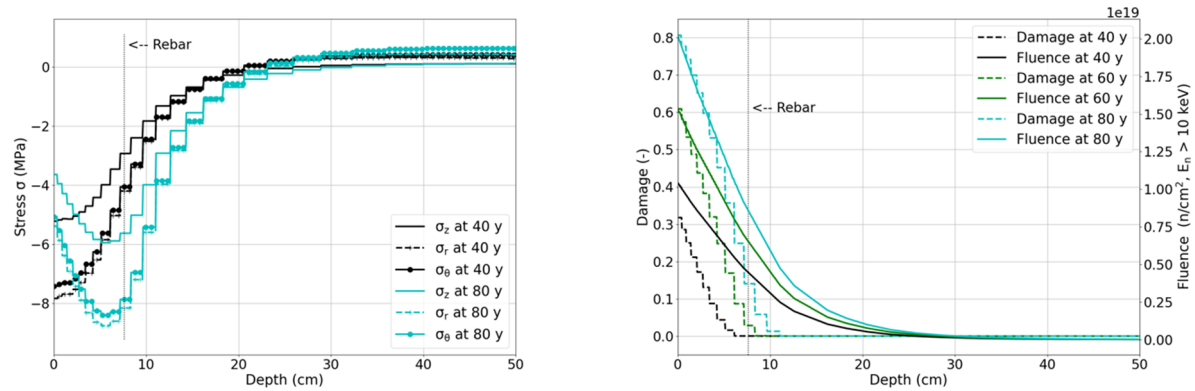
upward push and bending (Figure 14-5, top left). The bending effect is more prominent at higher elevation because of a decrease of structural restraint. At lower elevations, the basemat prevents the rotations and vertical displacements of the CBS. Note that the deformation shown does not account for the interactions with the RPV, the RPV nozzle, and the nozzle support. Such a vase-shaped deformation was observed from the finite element simulation results of a prototypical VVER-440 CBS (Khmurovska et al., 2019). The cross-section of the VVER-440 CBS is reduced toward the back of the wall at the top elevation, causing the vase shape's bending to form structural cracks along regularly distributed  $r$ - $z$  planes. The formation of such structural cracks in the proposed model is prevented by keeping the CBS thickness constant up to the highest elevation. For plant-specific evaluation, geometrical variations should be included in the model for assessment of the structural responses such as deformation, strain, stress, and deformation.

The gradual structural restraining effect going down in elevation toward the basemat is well illustrated by the hoop stress map. Depending on the azimuth, the hoop (circumferential / orthoradial) stress at the concrete surface varies vertically from approximately 12 MPa in compression at the lowest elevation to close to zero at the highest elevation, or it is quite constant at approximately 10 to 12 MPa in compression (Figure 14-5, bottom left). The corresponding vertical (axial) surface stress does not show significant variation vertically, but it shows important variation azimuthally, also ranging between 0 and 12 MPa in compression (Figure 14-5, bottom right). It is important to recognize that the surface stresses discussed above correspond to values calculated at 80 years of operation. These stresses have already relaxed because of irradiation-induced damage. This phenomenon is explained in Figure 14-6 (left) showing the radial, orthoradial, and vertical stress profiles along the radial direction at 40 and 80 years of operation. The location of the origin of these profiles corresponds to the point of maximum surface damage. The stresses increase gradually from the surface of the biological shield (maximum compressive stress) toward the back of the CBS (maximum tension) (Le Pape, 2015). In Figure 14-6 (left), it can be observed that the stresses at 40 years of operation have already relaxed in the first ~5 cm because of radiation-induced damage. At 80 years of operation, the relaxation effect is even more prominent. The maximum compressive stresses are located at a distance of approximately ~5 cm from the surface of the CBS. In that region, compression stresses decrease. The tensile stresses toward the back of the CBS remain under ~1 MPa. Hence, damage is only created in the region exposed to the higher fast neutron fluence near the reactor cavity.





**Figure 14-5 Simulation Results at 80 Years of Operation. (Clockwise from Top Left Figure): Amplified ( $\times 1500$ ) Structural Deformation (m); Radial Stress Field; Axial (Vertical) Stress Field; and Hoop (Orthoradial) Stress Field**



**Figure 14-6 (Left) Radial Profiles of the Radial (r), Hoop ( $\theta$ ) and Vertical (z) Stress Across the Depth of the CBS at 40 and 80 Years of Operation. (Right) Radial Profiles of the Fast Neutron Fluence ( $E > 10$  keV, Solid Lines) and Cumulative Damage (Dashed Lines) Across the Depth of the CBS at 40, 60 and 80 Years of Operation**

Figure 14-6 (right) shows the radial profile of the fast neutron fluence and the cumulative damage. Note that the cumulative damage is a scalar, the value of which is always lower than 1 (maximum damage). The damage profiles decrease from the maximum value at the surface of the concrete. The maximum damage values at the surface on the CBS are 0.32, 0.6, and 0.8 at 40, 60 and 80 years of operation, respectively. It is observed that the damage zone (i.e., where

the value of damage is higher than 1) increases with time. At 40, 60, and 80 years of operation, the damaged depth reaches approximately 6, 9, and 11 cm, respectively. Simulation results also show that initial damage is caused by the *intrinsic microstructural damage*, whereas at a later stage, damage corresponds to the *structural damage* caused by the constrained RIVE-induced stresses.

In the presented simulation results, the steel liner and reinforcing bars are subject to compression stresses lower than 40 MPa, thus remaining in the elastic regime.

## **14.4    Meso-Scale Structural Models**

### **14.4.1    Irradiation-Induced Damage Depth**

In the previous section, a methodological example of a finite element simulation of the effects of in-service irradiation of a CBS is presented. This section provides the results of simulation obtained using a different modeling approach using the LDPM. The LDPM approach is comparable to the RBSM developed by Kambayashi et al. (2020). Both discrete models present the advantage of modeling concrete cracking explicitly in the form of displacement jumps between *particles*. Hence, crack opening can be quantified. An additional feature of the RBSM and the LDPM is that they do not require artificial separation of the intrinsic microstructural damage and the structural damage, unlike the finite element models proposed in the previous section or in the literature (e.g., Pomaro et al., 2011; Khmurovska et al., 2019). In LDPM, intrinsic microstructural damage occurs because of microstructural heterogeneity: shrinkage and RIVE vary between adjacent particles of different geometries. Thus, the loss of mechanical properties caused by neutron irradiation result from the formation of microcracking. The structural damage also corresponds to the formation, growth, and coalescence of microcracks to form fracture under the action of external loading or constrained deformation. Both forms of damage are governed by the same cracking mechanism.

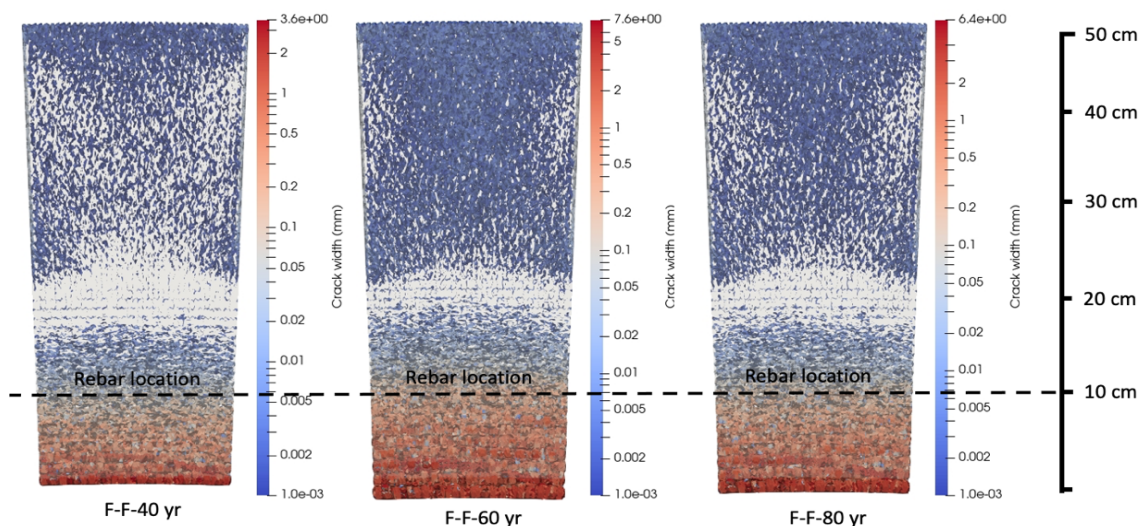
Nevertheless, RBSM and LDPM techniques are currently inadequate to model the entire CBS because of computational cost. Hence, the model is limited to a representative structural volume of the CBS, represented by a limited sector or wedge cut out from the CBS around the location of highest neutron flux at the surface of the concrete. Such a wedge model can be viewed as a numerical simulation extension of the analytical 1D models published by Andreev and Kapliy (2014) or Le Pape (2015). The wedge model applied to the in-service irradiation effects on the CBS was first introduced by Bruck et al. (2019) using a finite element model. The dimensions of the wedge are constrained by the thickness of the CBS, the maximum aggregate size, and if represented, the spacing between the reinforcements. The last two parameters control the dimensions of the wedge in the orthoradial (hoop) and vertical directions. In the LDPM model, it is assumed that those dimensions are higher than 8 times the maximum aggregate size. Because irradiation-induced damage is expected to occur in the concrete region directly facing the reactor cavity, it is not necessary to model the entire domain using a mesoscale model.

Hence, two concrete domains are distinguished: (1) the *meso-scale model domain* (MSMD) and (2) the continuum model domain (CMD). The MSMD is applied in the region subjected to irradiation-induced damage. Kambayashi et al. (2020) assumed a dimension of 350 mm for the MSMD. In the LDPM, the radial dimension of the MSMD is taken equal to 500 mm as a conservative value. The CMD radial dimension is 1.5 m. The height of the model is 10 cm, and the shortest dimension in the orthoradial direction is ~20 cm.

Wedge models assume axisymmetric boundary conditions: the lateral cut-out faces of the wedge are prevented from displacement in the orthoradial direction, but they allow local displacements in the radial and vertical directions (frictionless lateral surfaces). The boundary conditions on the top and bottom surfaces assume that the average vertical strain is zero. Such a boundary condition is only an approximation of the displacement field calculated by the Grizzly finite element full model of the CBS presented in the previous section. Vertical deformations and bending can be observed in Figure 14-5. Hence, assuming no vertical deformation in the wedge model leads to increasing the structural constraints and thus the RIVE-induced stresses near the reactor cavity.

The model is subject to the same neutron flux, varying only in the radial direction. The radial profile is extracted from the previous VERA-Shift simulation results at the location of the maximum neutron flux at the surface of the CBS.

The main output of this model is the spatial distribution of crack opening at varied operation time (see Figure 14-7). The cracking pattern is characterized by different preferential orientations in the wedge model. Near the reactor cavity, in a region that can extend to about 200 mm, cracks open along the radial direction. These cracks are caused by significant radiation-induced expansion which are structurally constrained in the vertical and the orthoradial directions, thus causing bi-axial compression stresses. Hence, expansion can only occur in the radial direction causing the formation of cracks. Crack opening width (in the radial direction) is at its highest near the surface of the CBS, and it decreases when penetrating inside the CBS. The minimum crack volume occurs at a distance of ~200 mm. Beyond that distance, the cracks' preferential openings occur perpendicularly to the radial direction (Figure 14-7). These cracks result from tension stresses balancing the compression stresses occurring in the high irradiated region. These tensile stresses remain low, and the resulting microcracking is structurally insignificant.

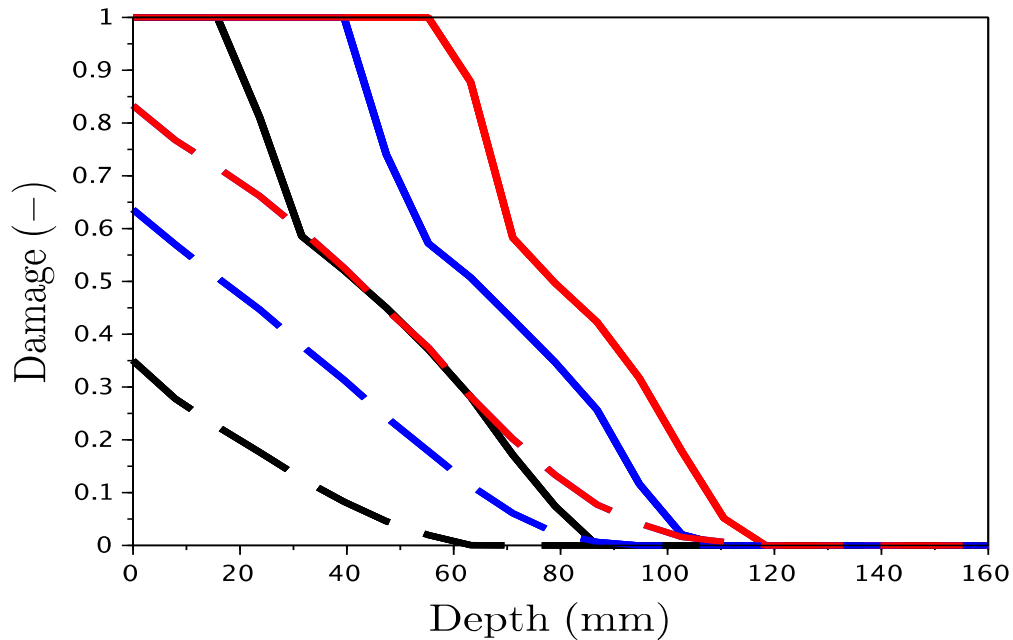


**Figure 14-7 Top View Showing the Crack Opening Width CBS Wedge LDPM at Varied Operation Duration**

To interpret the crack openings to the residual strength of concrete in the irradiated zone, it is necessary to resort to a separate model of a representative volume of concrete subject to a comparable cracking pattern. As mentioned previously, cracks form and grow because of biaxial loading created by confining boundary conditions. Hence, a plain concrete cube under biaxial compression was modeled. Cracking develops in parallel to the unloaded surface. Damage is defined as the ratio between the residual strength to the pristine strength of the uncracked cube and is associated with the created crack volume averaged over 5 mm slices. Establishing this correspondence between the crack volume and damage makes it possible to analyze the irradiation-induced crack significance in the CBS. Arbitrarily, beyond a crack volume of 15%, damage is considered maximized ( $d = 1$ ). Thus, the radial profiles of the crack volume at varied operation times are processed to obtain the damage radial profiles. These profiles exhibit a sharp drop that makes it possible to determine the damage depth. Within the damaged depth, the damage profiles are much sharper (solid lines in Figure 14-8) than the profiles obtained from the finite element simulation using Grizzly (dashed lines in Figure 14-8). Whereas the maximum damage value at the surface of the CBS gradually increases with the operation time, its value is always maximum in the interpretation of the LDPM simulations. In the LDPM simulation, the RIVE value near the surface of the concrete creates a *delamination* of cement paste located between the liner and the first *layer* of aggregates and spalling of the aggregates located in the immediate nearby region. In the finite element model, the heterogeneities created by aggregates of varied size are not represented. Thus, the induced microcracking is not represented either. It must also be recognized that representing concrete as a homogenized continuum material, assuming a representative material dimension of  $> \sim 10$  cm, is questionable, whereas the internal loading governed by the radiation-induced expansion exhibits a strong gradient. Finally, the isotropic damage model assumed in the finite element is inherently not conceived to accurately model such anisotropic loading conditions.

Nevertheless, the estimates of the damage depths (i.e., the depth defined by  $d > 0$ ) obtained from both modeling strategies are comparable. Those calculated from the LDPM simulations are 8.5, 10.5, and 11.5 cm, respectively at 40, 60, and 80 years of operation. The corresponding values calculated from the finite element model are 6.5, 9, and 12 cm, respectively.

The results are for this study and not generic, the methodology can be used for estimating damage depth.



**Figure 14-8 Comparison of the Damage Profile in the CBS Obtained Using LDPM (Solid Lines) and Finite Element Model (Dashed Lines) at 40, 60 and 80 Years of Operation (in Black, Blue and Red, Respectively)**

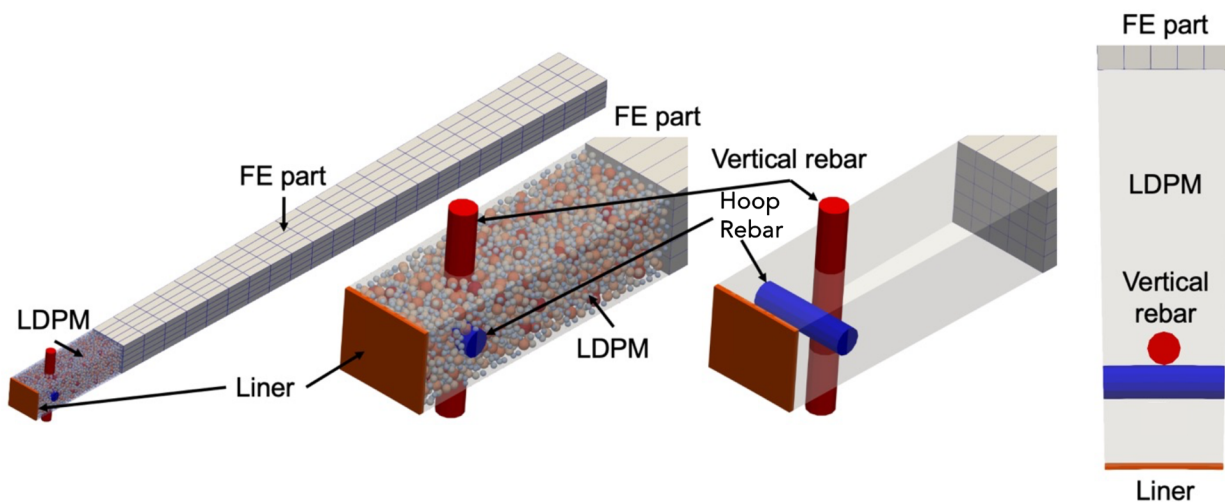
#### Limitations

1. The representation of the liner as a bonded plate in both models is simplified and does not account for the presence of varied connectors. Hence, the modeled irradiation-induced expansion of the concrete pushing the liner toward the reactor cavity is not constrained by the anchoring effect of the liner connectors. Depending on the length, spacing, and geometry of the anchor, the local stress field and RIVE-induced cracking will be affected locally. Detailed models of the anchoring system would be needed to address this question.
2. The simulation results can be extrapolated to the case of an unlined CBS. In such a case, simulated irradiation-induced expansion and damage would produce spalling of the concrete cover. Nevertheless, the following must be acknowledged:
  - a. The models assume a very high quartz content (92%) in the aggregate—aggregate GA(F)—which leads to RIVE values close to the maximum possible value.
  - b. The aggregate RIVE is calculated from the interpretation of literature data obtained at fast neutron flux much higher than in PWR operation. The data collected from the LVR-15 irradiation experiment presented in this report show an important decrease of the RIVE rate when the fast neutron flux decrease by an order of magnitude. At 80 years of operation, the irradiation transport simulations

conducted with VERA-Shift lead to a fluence of approximately  $2 \times 10^{19} \text{ n.cm}^{-2}$  ( $E > 10 \text{ keV}$ ) at the surface of the concrete shield. At that fluence and at a temperature of  $65^\circ\text{C}$ , quartz RIVE is estimated at approximately 0.8% using the empirical expressions derived from the IMAC database. It was shown in this report that those RIVE estimates match the dimensional changes observed from the JEEP-II irradiation experiments published by Maruyama et al. (2017). Considering that the post-irradiation dimensional changes measured from the LVR-15 experiment on aggregate GA(F) are at least  $\sim 4$  times lower than the changes obtained from the JEEP-II irradiation experiments, it is possible to estimate the equivalent fluence to reach a RIVE of  $0.8\% / 4 = 0.2\%$ . Such an expansion is reached at  $\sim 6.5 \times 10^{18} \text{ n.cm}^{-2}$  ( $E > 10 \text{ keV}$ ), which corresponds to an operation time of  $\sim 80 / 3 \sim 27$  years in the structural simulations.

#### 14.4.2 In-Service Irradiation Effects on the Bond Strength of Steel Reinforcement

The objective of the simulation presented in this section is to provide an assessment of the effects of in-service irradiation-induced damage in the CBS wall on the residual bond strength of the embedded reinforcements.



**Figure 14-9 Details of the CBS Wedge Model Used to Simulate the Effects of In-Service Irradiation on the Bond Strength of the Embedded Reinforcement**

As previously explained, modeling the entire CBS using LDPM would be computationally prohibitive. However, it is possible to model a representative volume, a wedge of the CBS, assuming axisymmetric boundary conditions in the plane. In the vertical direction, simulating the boundary conditions of a slice in height is also challenging in the absence of the structural details. Nevertheless, assuming fixed-fixed top and bottom boundary conditions forces all expansion in the radial direction, which represents the conservative case scenario.

The simulated wedge geometry is presented in Figure 14-9, which shows different views of the components and embedded reinforcement. The horizontal and vertical rebars are #8 (25.4 mm in diameter), as detailed previously. The horizontal rebar is restrained using the same axisymmetric boundary conditions for both the LDPM and FE meshes.

The proposed simulation explores a virtual scenario of a pullout test performed on the embedded vertical reinforcement bar after up to 80 years of operation. The objective of this simulation is to evaluate how irradiation-induced cracking in the CBS affects the residual bond strength of the reinforcement.

To conduct the pullout test, the vertical rebar extends beyond the top and bottom of the sector. During the irradiation period, the concrete section remains fixed-fixed, preventing movement at the reinforcing bar ends. Consequently, in the simulation, displacement history is applied solely to the top node of the rebar after the irradiation period concludes.

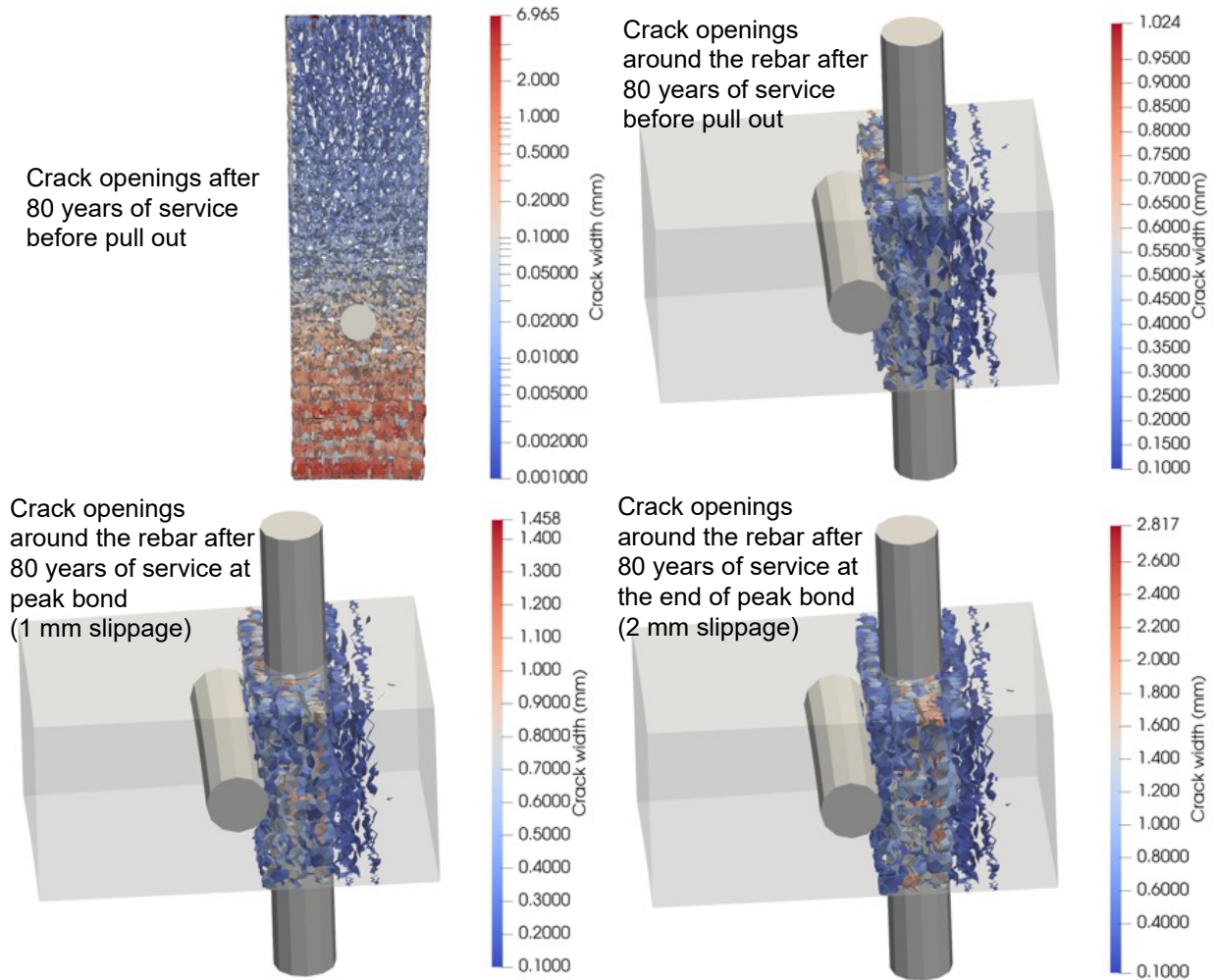
Two simulation scenarios are under consideration here resembling those used for pullout tests on cylindrical specimens. The first scenario assumes bond law parameters from Table 14-1 without introducing any RIVE-induced damage in the bond model, thus focusing only on the effects of RIVE on the bulk concrete using LDPM. Once again, no reduction in bond strength was observed when modeling the wedge with undamaged bond law parameters, as anticipated from previous pullout test simulations. This suggests that the bulk concrete surrounding the rebar experiences radial movement exclusively.

Upon examining crack openings and their orientation as depicted in Figure 14-10, several observations emerge. Initially, prior to the pullout process and after 80 years of service, the largest crack opening measures approximately 7 mm near the liner (Figure 14-10, top left). However, upon closer inspection around the rebars, it becomes evident that most crack openings within the rebar zone are 0.4 mm or smaller, with only a few reaching 1 mm, arranged in radial rings (in Figure 14-10, top right).

Furthermore, at peak bond strength, corresponding to around 1 mm of slippage, the maximum crack width observed was 1.5 mm, but the majority of cracks remain under 1.0 mm (Figure 14-9, bottom left). Towards the end of the peak bond strength plateau, at approximately 2.0 mm of slippage, most crack widths measure within 1.0 mm, with very few extending to 2.8 mm. This predicted behavior is realistic, attributed to the axisymmetric restraint on the sides and fixed positions at the top and bottom, preventing complete disintegration of the bulk concrete at this irradiation level.

However, the presence of cracks up to 1.5 mm around the rebar is expected to impact the bond strength, a factor that can only be accurately captured by adjusting the bond law parameters accordingly.

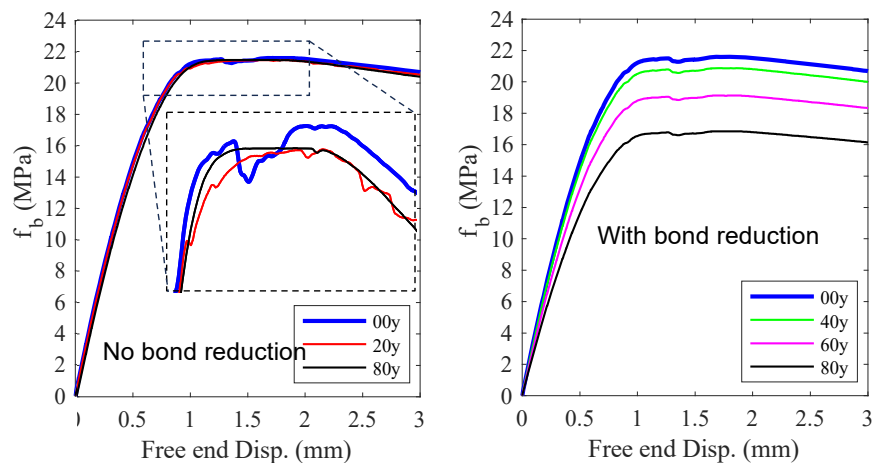




**Figure 14-10 Cracking in the CBS at 80 Years of Service: (Top Left and Right) Before Rebar Pullout, (Bottom Left) at 1.0 mm Slippage, and (Bottom Right) at 2.0 mm Slippage**

Therefore, assuming that the bond law parameters are affected proportionally to the square root of the residual compressive strength, the pullout strength of the irradiated reinforcement bar in service can be estimated. In the simulation approach, predicted reductions in compressive strength of the concrete located near the rebar are incorporated. Because the concrete cover is 3 in., the estimated reduction factors in Figure 14-7 at 3 and 4 in. are averaged and listed in the second column of Table 14-2 for 40, 60, and 80 years. These reduction factors allow for computation of the compressive strength ratio ( $f_{cr}$ ) and the corresponding bond strength ratio ( $f_{br}$ ), presented in the last two columns of Table 14-2. Using these reduction factors, the pullout behavior of the vertical rebar in the wedge is predicted as illustrated in Figure 14-11.





**Figure 14-11 Prediction of Pullout Behavior of a #8 Rebar in the CBS at Different Operation Times: (Left) Neglecting the Influence of the Loss of Concrete Strength on Bond Law Parameters; (Right) Considering that Influence**

**Table 14-1 Bond-Slip Model Parameters for #8 Rebar in Pristine Concrete Con-A**

Parameter	Value
<b>B1 (MPa)</b>	21.6
<b>B3 (MPa)</b>	8.64
<b>S1 (mm)</b>	0.92
<b>S2 (mm)</b>	1.72
<b>S3 (mm)</b>	14.0
<b><math>K_r</math> (-)</b>	1.50

**Table 14-2 Effect of Irradiation on Compressive and Bond Strength Ratios**

Age	Damage %	$f_{cr}$	$f_{br}=f_{cr}^{0.5}$
<b>40 years</b>	6.5	0.935	0.967
<b>60 years</b>	21.4	0.785	0.886
<b>80 years</b>	39.1	0.609	0.780

## 15 CONCLUSIONS

This research study pursued two objectives: first, a scoping study including the design, execution, and analysis of the first-of-a-kind irradiation experiment of reinforced concrete specimens aimed at obtaining data on the irradiated bond strength of steel in concrete; and second, the analysis of in-service irradiation effects on the performance of concrete biological shields in pressurized water reactors.

### 15.1 Irradiation Scoping Study

#### 15.1.1 Irradiation Scoping Study Summary

A novel irradiation experiment was conducted in collaboration with the Centrum výzkumu Řež (CV REZ) in the Czech Republic. This initiative came after the shutdown of the IFE's test reactor JEEP II in Kjeller, Norway, leading to the selection of the LVR-15 test reactor at the CV REZ as a suitable alternative for JEEP II of IFE in April 2019. The original plan was for the IFE facilities to replicate conditions from well-documented experiments on plain concrete specimens for the Japan Concrete Aging Management Program (published in the Journal of Advanced Concrete Technology by Maruyama et al., 2017), but the change in reactor provided valuable insights into the effects of fast neutron flux on concrete aggregates.

Concrete materials—including aggregate, sand, and cement sourced from Professor Maruyama at the University of Nagoya—matched those used in the Japan Concrete Aging Management Program (JCAMP). Two concrete formulations were tested using two types of coarse aggregate: 92% quartz meta-chert and felsic sandstone.

The University of Tennessee, Knoxville, oversaw the fabrication protocol, unique mold design, and execution of varied specimens.

Three testing conditions were considered to assess separate effects of temperature and irradiation:

- *Irradiated condition*: irradiation at an average fast neutron fluence of  $\sim 1.12 \times 10^{19} \text{ n.cm}^{-2}$  ( $E > 0.1 \text{ MeV}$ ), an average gamma dose of  $\sim 1 \text{ GGy}$ , and a monitored temperature ranging between  $37^\circ\text{C}$  and  $52^\circ\text{C}$
- *Heat cured condition*: heat curing at the irradiation temperature without irradiation
- *Cold condition*: cured at room temperature and no irradiation

The irradiation experiment lasted approximately 800 days (accounting for outages). Each of the three specimens set for the three testing conditions included plain concrete specimens and reinforced concrete specimens, thus maximizing the number of specimens in the irradiation capsule. Irradiation conditions in the test reactor imposed limitations on the dimensions of the specimens (diameter: 40 mm), so a companion study was conducted at the University of Tennessee, Knoxville, to analyze the effects of reinforcement, aggregate, and concrete specimen sizes using unirradiated specimens.

Varied characterization and testing techniques assessed the physical and mechanical properties of aggregate, concrete, and reinforced concrete pre- and post-irradiation and heat

curing. Techniques included visual and optical microscopy, x-ray computed tomography, mass and dimensional measurements, ultrasound wave velocity, splitting tests, compression tests, and bond testing. Mechanical testing setups were adapted and modified to accommodate non-standard specimen dimensions and operational constraints in the hot cells. Importantly, a successful jacketing method ensured that all pullout tests reached the planned bond failure mode, facilitating interpretation of steel-concrete bond properties. Notably, despite limited specimen numbers per category (size, curing method, concrete formulation, etc.), bond test results exhibited remarkable consistency.

### 15.1.2 Irradiation Scoping Study Results

The main results of the scoping studies are presented below

1. **Evidence of fast neutron effects on damage production in rock-forming aggregates.** The dominant effect of fast neutron irradiation is radiation-induced volumetric expansion (RIVE) of minerals and concrete. A comparison of aggregate expansion in the LVR-15 reactor (position XK1), aggregates of the same chemical composition irradiated in the JEEP-II reactor (from the JCAMP study), and estimates from empirical models and MOSAIC simulations suggests that fast neutron flux significantly influences the radiation-induced damage to rock-forming minerals. Post-irradiation examination of specimens from the LVR-15 reactor revealed dimensional changes at least four times lower than expected values for comparable fast neutron fluence and temperature conditions. The difference between the LVR-15 and the JEEP-II experiments are the fast neutron flux ( $\sim 3.6 \times 10^{11} \text{ n.cm}^{-2} \text{ s}^{-1}$ ,  $E > 0.1 \text{ MeV}$  in LVR-15 against  $\sim 3.6 \times 10^{12} \text{ n.cm}^{-2} \text{ s}^{-1}$  in JEEP-II) the gamma dose rate ( $< 94 \text{ kGy.h}^{-1}$  in LVR-15 against  $\sim 300 \text{ kGy.h}^{-1}$  in JEEP-II), and the duration of the experiments ( $\sim 400$  days in the LVR-15 against 25–45 days in the JEEP-II for comparable fluence), leading to variation of the gamma dose ( $\sim 1 \text{ GGy}$  in LVR-15 against  $\sim 200$  to  $300 \text{ MGy}$  in JEEP-II).

The mechanism responsible for the difference in RIVE amplitudes associated with fast neutron flux requires further study. It is currently hypothesized that defects recovery during irradiation may play a role. Additional characterization work, including x-ray diffraction (XRD) analysis not conducted in this study, is essential to investigate and validate this hypothesis. Considering that the in-service fast neutron flux in a pressurized water reactor (PWR) is estimated to be on the order of  $1\text{--}2 \times 10^{10} \text{ n.cm}^{-2} \text{ s}^{-1}$  ( $E > 0.1 \text{ MeV}$ ), the significance of defects recovery may be even more pronounced during in-service irradiation. Characterizing concrete irradiated in-service (e.g., samples harvested from the concrete biological shield (CBS) wall of PWRs currently undergoing decommissioning) is valuable when addressing these questions. Comparisons were made between the post-irradiation dimensional changes and mechanical properties of concrete specimens irradiated in the LVR-15/XK1 position and data obtained by the JCAMP team from specimens irradiated in the JEEP-II reactor at comparable fast neutron fluences and temperatures. Consistently, the LVR-15 experiment showed lower radiation-induced expansion of aggregates, resulting in reduced expansion of concrete and a lower reduction in Young's modulus.

2. **Bond strength of steel embedded concrete.** Because of size limitations primarily caused by irradiation-induced heating, the pullout specimens used in this study were 40 mm in diameter and 60 mm in height, with a maximum aggregate size of less than 13 mm and an embedded steel #2 bar diameter of approximately 6 mm. These dimensions are not representative of those typically found in real-world concrete structures such as

the CBS walls. To comprehensively understand and estimate the size effect on the bond strength of steel bars embedded in concrete, a specific campaign was conducted using varied concrete dimensions (diameters: 40 mm, 80 mm, and 160 mm), bar diameters (#2, #4, and #8, corresponding to 6.3 mm, 12.7 mm, and 25.4 mm), and maximum aggregate sizes (9.5 mm, 12.7 mm, 19.0 mm, and 25.4 mm), all cured at room temperature. Each set of dimensions included 24 tests in total, and the bond strength was characterized by measuring the pullout force against bar slippage, consistently resulting in a slipping failure mode. Upon normalization of the data to account for the bar and concrete dimensions, as well as the geometry factor associated with the height and spacing of bar ribs and the square root of concrete compressive strength, it was observed that no additional scaling factor is needed to derive the bond strength for aggregate sizes when the bar diameter exceeds 12.7 mm (#4). However, for the #2 bar, an additional scaling factor of approximately 0.75–0.85 was required to accurately determine the bond strength.

In the 18 bond tests conducted with #2 bars embedded in Con-A and Con-B concrete subjected to various conditions (irradiation, heat curing, and room temperature curing), results showed remarkable consistency except for the premature failure observed in the B11R specimen. Notably, the bond strength of Con-B specimens appeared unaffected by the testing conditions, including irradiation at a fast neutron fluence of approximately  $1.1 \times 10^{19} \text{ n.cm}^{-2}$  ( $E > 0.1 \text{ MeV}$ ), a gamma dose of about 1 GGy, and an irradiation temperature of approximately  $45^\circ\text{C} \pm 5^\circ\text{C}$ , as well as heat curing at the irradiation temperature or room temperature curing. In contrast, Con-A specimens subjected to heat curing exhibited a bond strength approximately 15% higher than that of specimens cured at room temperature. However, specimens irradiated under the same conditions showed a slight decrease of approximately 8% in bond strength compared to room temperature–cured specimens.

Attempts to normalize the data using the square root of the apparent compressive strength did not yield conclusive results due to challenges associated with the size of the 'donut' specimens (40 mm in height), triaxial stress effects, and specimen alignment in the hot cells. Instead, normalization using the splitting strength (which is typically assumed to be linearly proportional to the square root of the unconfined compression strength according to ACI318-19) provided better, albeit imperfect, consistency across the varied bond tests. Normalized bond strengths were very similar when comparing data from irradiated and room temperature cured specimens. Therefore, it can be concluded that under the tested irradiation conditions, which induced an aggregate radiation-induced linear expansion of less than approximately 0.2%, the reduction in bond strength of steel reinforcement embedded in irradiated concrete can be attributed to the reduced strength properties of the irradiated concrete in the immediate vicinity of the reinforcement bar.

## **15.2     Modeling and Structural Significance of Irradiation on the Integrity of the Biological Shield Wall**

Different modeling and simulation tools were employed to interpret the results of the scoping study experiments and to assess the long-term in-service irradiation effects on the integrity of the CBS wall.

### 15.2.1 Simulation of Scoping Study Tests

1. **MOSAIC Simulation:** MOSAIC, a fast Fourier transform-based code, was utilized to evaluate the RIVE of aggregate specimens irradiated in the LVR15/XK1 position. The simulation results confirmed observed flux effects by comparing the post-irradiation changes of aggregates irradiated in the LVR15 reactor with those from the JEEP-II reactor.
2. **Lattice-Discrete Particle Model (LDPM):** LDPM was employed to calculate mass loss, dimensional changes, and the irradiation-induced alterations in tensile and compressive strengths of plain concrete specimens irradiated in the LVR15/XK1 position. The simulation outcomes aligned well with post-irradiation data, demonstrating LDPM's capability to model mechanical effects of irradiation on concrete. Additionally, LDPM showed that irradiation-induced drying shrinkage compensated for reduced RIVE of aggregates, thereby explaining the relatively low magnitude and variability in post-irradiation dimensional changes.
3. **LDPM for Bond Strength Modeling:** LDPM was further utilized to model bond strength tests, focusing on determining the properties of the bond interface between reinforcing bars and surrounding concrete. This interface includes the mortar layer between bar ribs and extends slightly beyond the rib tips, which is crucial for understanding shear fracture during bar slippage. Analysis from these tests concluded that bond strength is directly influenced by the square-root of the residual compressive strength of the concrete. Hence, the bond strength is indirectly influenced by the radiation-induced expansion of the surrounding aggregates. The validity of this result is limited to the data obtained within the test conditions, i.e., at a fluence around  $10^{19}$  n/cm<sup>2</sup>. It is hypothesized that this result remains valid at higher RIVE-induced damage provided the aggregate is not severely damaged. Further research is needed to confirm this hypothesis.

### 15.2.2 Structural Integrity of the CBS Wall

A literature review was conducted on structural simulations of in-service irradiated concrete:

- **Radiation Effects:** Fast neutron flux attenuation leads to non-uniform radiation-induced expansion within the concrete structure. Near the mid fuel core elevation, expansion peaks near the reactor wall surface and decreases radially outward. This gradient results in significant biaxial compression stresses in the orthoradial (hoop) and vertical directions, contributing to concrete damage both from intrinsic irradiation effects (material damage) and mechanical stresses.
- **Quantification of Damage Depth:** Two methods were tested to quantify the time-evolution of irradiation-induced damage depth:
  - Nonlinear finite element analysis (FEA) applied to a simplified reinforced concrete model of the CBS.
  - LDPM applied to a representative volume of the CBS at the mid fuel core elevation.

Comparison between FEA and LDPM results revealed the following:

- Nonlinear evolution of damage depth occurred over operational duration, with a decreasing propagation rate over time
- FEA tended to underestimate the damage depth by up to about 20 mm compared to LDPM, which better accounted for the absence of scale separation between aggregate size and the strong gradient of radiation-induced expansion. This 20 mm value corresponds to the case of an aggregate that is very rich in quartz.

Assuming that the RIVE rate and amplitude are derived from test reactor data (under accelerated conditions), estimates indicate that the damage depth extends beyond the region subject to a fast neutron fluence higher than  $10^{19}$  n/cm<sup>2</sup> ( $E > 0.1$  MeV). Therefore, the structural evaluation should be based on the damage depth and include the assessment of any embedded steel elements within the damage zone, including reinforcement, liner attachments, and equipment base plate anchorages. These simulations and analyses provide critical insights into the complex effects of long-term irradiation on the structural integrity of concrete, particularly in scenarios relevant to nuclear reactor biological shield walls.



## 16 REFERENCES

- Abdellatef, M., Boumakis, I., Wan-Wendner, R. and Alnaggar, M. (2019). Lattice Discrete Particle Modeling of concrete coupled creep and shrinkage behavior: A comprehensive calibration and validation study, *Construction and Building Materials*, 211: 629-645.
- ACI Committee 318. Building Code Requirements for Structural Concrete : (ACI 318-19) ; and Commentary (ACI 318R-95). Farmington Hills, MI :American Concrete Institute, 2019.
- ACI Committee 349. Evaluation of Existing Nuclear Safety Related Concrete Structures (349 349.3R-02). Farmington Hills, MI :American Concrete Institute, 2020.
- Andreev, V. I. and Kapliy, D. A. (2014). Stress-State of a Thick-Walled Cylindrical Shell under the Combined Action of Radiation and Temperature Field, *Advanced Materials Research*, 1006–1007:177–180.
- Alnaggar, M., di Luzio, G. and Cusatis, G. (2017). Modeling Time-Dependent Behavior of Concrete Affected by Alkali Silica Reaction in Variable Environmental Conditions. *Materials*. 10(5):471.
- Alnaggar, M. and Bhanot, N. (2018). A Machine Learning Approach for the Identification of the Lattice Discrete Particle Model Parameters, *Engineering Fracture Mechanics* , 197: 160–175.
- Avramova, M. N. (2009). CTF: A Thermal Hydraulic Sub-Channel Code for LWR Transient Analyses, User's Manual. *Pennsylvania State University Department of Nuclear Engineering*.
- Baggio, P., Majorana, C. E. and Schrefler, B. A. (1995). Thermo-Hygro-Mechanical Analysis of Concrete, *International Journal for Numerical Methods in Fluids*, 20:573–595.
- Baral, A., Tajuelo Rodriguez, E., Hunnicutt, W. A., Cakmak, E., Hongbin, S., Ilavsky, J., Le Pape, Y., Rosseel, T. M. and Garg, N. (2022). Ultra-High Gamma Irradiation of Calcium Silicate Hydrates: Impact on Mechanical Properties, Nanostructure, and Atomic Environments, *Cement and Concrete Research*, 158:106855.
- Bažant, Z. P. and Becq-Giraudon, E. (2002). Statistical Prediction of Fracture Parameters of Concrete and Implications for Choice of Testing Standard, *Cement Concrete and Research*, 32(4):529–556.
- Bažant, Z. P. and Jirásek, M. (2018). Creep and Hygrothermal Effects in Concrete Structures, 225, *Solid Mechanics and Its Applications*, Springer.
- Biwer, B., Ma, D., Xi, Y. and Jing, Y. (2021). Review of Radiation-Induced Concrete Degradation and Potential Implications for Structures Exposed to High Long-Term Radiation Levels in Nuclear Power Plants, NUREG/CR-7280, ANL/EVS-20/8, *U.S. Nuclear Regulatory Commission*,
- Bruck, P. M., Esselman, T. C., Elaidi, B. M., Wall, J. J. and Wong, E. L. (2019). Structural Assessment of Radiation Damage in Light Water Power Reactor Concrete Biological Shield walls, *Nuclear Engineering and Design*, 350:9–20.



Bykov, V. N., Denisov, A. V., Dubrovskii, V. B., Korenevskii, V. V., Krivokoneva, G. K. and Muzalevskii, L. P. (1981). Effect of Irradiation Temperature on the Radiation Expansion of Quartz, *Atomnaya Energiya*, 51(3):593–595.

Cheniour, A., Li, Y., Sanahuja, J., Le Pape, Y., Tajuelo Rodriguez, E., Anovitz, L. M., Polavaram, K. C., Grag, N. and Rosseel, T. M. (2022). FFT-Based Model for Irradiated Aggregate Microstructures in Concrete, *Materials and Structures*, 55(214).

Cheniour, A., Davidson, E., Le Pape, Y., Pandya, T., Collins, B., Spencer, B., Godfrey, A. and Asgari, M. (2023). A Structural Model of the long-term degradation of the Concrete Biological Shield, *Nuclear Engineering and Design*, 405:112217.

Collins, B. et al. (2016). *MPACT VERA Input User's Manual* Version 2.2.0, No. CASL-U-2016-1109-000.

Cusatis, G. and Cedolin, L. (2007). Two-Scale Study of Concrete Fracturing Behavior, *Engineering Fracture Mechanics*, 74(1–2):3–17.

Cusatis, G., Pelessone, D. and Mencarelli, A. (2011a). Lattice Discrete Particle Model (LDPM) for Concrete Failure Behavior of Concrete. I: Theory, *Cement and Concrete Composites*, 33(9):881–890.

Cusatis, G., Mencarelli, A., Pelessone, D. and Baylot, J. (2011b). Lattice Discrete Particle Model (LDPM) for Failure Behavior of Concrete. II: Calibration and Validation, *Cement and Concrete Composites*, 33( 9):891–905.

Dabrowski, M., Glinicki, M. A., Kuziak, J., Jóźwiak-Niedźwiedzka, D. and Dziedzic, K. (2022). Effects of 2 MGy Gamma Irradiation on the Steel Corrosion in Cement-Based Composites, *Construction and Building Materials*, 342:127967.

Denisov, A. V., Dubrovskii, V. B. and Solovyov, V. N. (2012). Radiation Resistance of Mineral and Polymer Construction Materials, ZAO MEI Publishing House.

Di Luzio, G. and G. Cusatis (2003). A New Constitutive Model for Concrete-Steel Bond Behavior. In N. Bićanić, R. de Borst, H. Mang, G. Meschke, & A. A. Balkema (Eds.), *Proceedings of the EURO-C 2003 Conference*.

Di Luzio, G. and Cusatis, G. (2009). Hygro-Thermo-Chemical Modeling of High Performance Concrete. I: Theory, *Cement and Concrete Composites*, 31(5):301–308.

Di Luzio, G. and Cusatis, G. (2009). Hygro-Thermo-Chemical Modeling of High-Performance Concrete. II: Numerical Implementation, Calibration, and Validation, *Cement and Concrete Composites*, 31(5):309–324.

Di Luzio, G. and Gianluca Cusatis, G. (2013). Solidification–microprestress–microplane (SMM) theory for concrete at early age: Theory, validation and application, *International Journal of Solids and Structures*, 50(6): 957-975

Dubrovskii, V. B., Ibragimov, Sh. Sh., Ladygyn, A. Ya. and Pergamenshchik, B. K. (1966). The Effect of Neutron Irradiation on Certain Properties of Refractory Concretes, *Atomnaya Energiya*, 21(4):108–112

Dubrovskii, V. B., Ibragimov, Sh. Sh., Kulakovskii, M. Ya., Ladygin, A. Ya. and Pergamenshchik, B. K. (1967). Radiation Damage in Ordinary Concrete, *Atomnaya Énergiya*, 23(4):310–316.

Elleuch, L. F., Dubois, F. and Rappeneau, J. (1972). Effects of Neutron Radiation on Special Concretes and Their Components, *Special Publication of The American Concrete Institute*, 43:1071–1108

Esselman, T. and Bruck, P. (2018). Expected Condition of Concrete Exposed to Radiation at Age 80 Years of Reactor Operation, ORNL/TM-2018/769, Oak Ridge National Laboratory.

Field, K. G., Remec, I. and Le Pape, Y. (2015). Radiation Effects on Concrete for Nuclear Power Plants – Part I: Quantification of Radiation Exposure and Radiation Effects, *Nuclear Engineering and Design*, 282:126–143.

Fujiwara, K., Ito, M., Sasanuma, M., Tanaka, H., Hirotsu, K., Onizawa, K., Suzuki, M. and Amezawa, H. (2009). Experimental Study of the Effect of Radiation Exposure to Concrete. *Proceedings of the 20th International Conference on Structural Mechanics in Reactor Technology*, Vol. SMiRT 20 - Division I, No. Paper 1891 : Espoo, Finland.

Gardner, N. J. (1990). Effect of Temperature on the Early-Age Properties of Type I, Type II, and Type III/Fly ash Concretes with Temperature, *ACI Materials Journal*, 87(1):68–78.

Gérard, B., Pijaudier-Cabot, G. and Laborderie, C. (1998). Coupled Diffusion-Damage Modelling and the Implications on Failure Due to Strain Localization, *International Journal of Solids and Structures*, 35(31–32):4107–4120.

Geuzaine, C. and Remacle, J.-F. (2009). Gmsh: A 3-D Finite Element Mesh Generator with built-in Pre- and Post-Processing Facilities, *International Journal for Numerical Methods in Engineering*, 79(11):1309–1331.

Giorla, A., Le Pape, Y. and Huang, H. (2016). Meso-Scale Modeling of Irradiation in Pressurized Water Reactor Concrete Biological Shield, 2016-05, Saouma, V., Bolander, J. and Landis, E. (Eds.), *Proceedings of FraMCoS-9* : Berkeley, CA.

Giorla, A.B. (2016b). Simulation of Concrete Members Affected by Alkali-Silica Reaction with Grizzly, ORNL/ TM-2016/523, Oak Ridge National Laboratory.

Giorla, A., Le Pape, Y. and Dunant, C. (2017). Computing Creep-Damage Interactions in Irradiated Concrete, *Journal of Nanomechanics and Micromechanics* , Vol. 04017001.

Graves, H., Le Pape, Y., Naus, D., Rashid, J., Saouma, V., Sheikh, A. and Wall, J. (2014). Expanded Material Degradation Assessment (EMDA), Volume 4: Aging of Concrete, No. NUREG/CR-7153, ORNL/TM-2011/545, U.S. Nuclear Regulatory Commission.

Gray, B. S. (1971). The Effects of Reactor Radiation on Cement and Concrete, *Proceedings of an Information Exchange Meeting on 'Results of Concrete Irradiation Programmes'*, Vol. EUR 4751 f-e : Brussels, Belgium.

Hamon, F. (2013). Modèle D'endommagement de MAZARS, *Code\_Aster, Manuel de Référence, Fascicule R7* , Vol. 1, p. 1–15

Hilsdorf, H. K., Kropp, J. and Koch, H. J. (1978). The Effects of Nuclear Radiation on the Mechanical Properties of Concrete, *Special Publication of The American Concrete Institute*, 55:223–254

Hookham, C. J. (1991). Structural Aging Assessment Methodology for Concrete Structures in Nuclear Power Plants, ORNL/NRC/LTR-90/17, *Oak Ridge National Laboratory*.

IFE information (2019). Permanent Closure of JEEP II Research Reactor at Kjeller, *Public Information Notice*, April 25, 2019, <https://ife.no/en/permanent-closure-of-the-jeep-ii-research-reactor-at-kjeller/>

JSCE 2007. Standard Specifications for Concrete Structures (2007). *Materials and Construction*, Japan Society of Civil Engineers, JSCE, No.7.

Kambayashi, D., Sasano H., Sawada, S., Suzuki, K. and Maruyama, I. (2020). Numerical Analysis of a Concrete Biological Shielding Wall under Neutron Irradiation by 3D RBSM, *Journal of Advanced Concrete Technology*, 18:617–632

Kaplan, M. F. (1971). Concrete for Pressure Vessels, Shielding and Containment of Nuclear Reactors: A Report on the American Concrete Institute Seminar, Concrete for Nuclear Reactors; held at the Bundesanstalt für Materialprüfung (BAM), Berlin, 5-9 October, 1970, *Nuclear Engineering and Design*, 16:369–374.

Kaplan, M. F. (1989). Concrete Radiation Shielding: Nuclear Physics, Concrete Properties, Design and Construction. *Longman Scientific and Technical*, 457 p.

Khmurovska, Y., Štemberk, P., Fekete, T. and Eurajoki, T. (2019). Numerical Analysis of VVER-440/213 Concrete Biological Shield Undernormal Operation, *Nuclear Engineering and Design*, 350:58–66.

Khmurovska, Y. and Štemberk, P. (2021). RBSM-Based Model for Prediction of Radiation-Induced Volumetric Expansion of Concrete Aggregates, *Construction and Building Materials*, 294(2):123553.

Kochunas, B., Collins, B., Stimpson, S., Salko, R., Jabaay, D., Graham, A., Liu, Y., Kim, K.-S., Wieselquist, W., Godfrey, A., Clarno, K., Palmtag, S., Downar, T. and Gehin, J. (2016). VERA Core Simulator Methodology for PWR Cycle Depletion. *Nuclear Science and Engineering*, 186:217–231.

Kommendant, G.J., Polivka, M. and Pirtz, D. (1976). Study of Concrete Properties for Prestressed Concrete Reactor Vessels, Final Report – Part II, Creep and Strength Characteristics of Concrete at Elevated Temperatures. *Tech Rep. UCSESM 76-3, University of California*, Berkeley, prepared for the General Atomic Company.

Kontani, O., Sawada, S., Maruyama, I., Takizawa, M. and Sato, O. (2013). Evaluation of Irradiation Effects on Concrete Structure – Gamma Ray Irradiation Tests on Cement Paste, *Proceedings of the ASME 2013 Power Conference POWER2013*, No. 98099 : Boston, MA, USA.

Krishnan, N.M.A., Le Pape, Y., Sant, G. and Bauchy, M. (2018). Effect of Irradiation on Silicate Aggregates' Density and Stiffness, *Journal of Nuclear Materials*, 512:126–136.

- Krishnan, N. M. A., Ravinder, R., Kumar, R., Le Pape, Y., Sant, G, and Bauchy, M. (2019). Density-Stiffness Scaling in Minerals upon Disordering: Irradiation vs. Vitrification, *Acta Materialia*, (166):611–617.
- Kwon, J. and Motta, A. T. (2000). Gamma Displacement Cross Sections in Various Materials, *Annals of Nuclear Energy*, 27(18):1627–1642.
- Le Caër, S., Dezerald, L., Boukari, K., Lainé, M., Taupin, S., Kavanagh, R., Johnston, C., Foy, E., Charpentier, T., Krakowiak, K., Pellenq, R., Ulm, F.-J., Tribello, G., Kohanoff, J. and Saúl, A. (2017). Production of H<sub>2</sub> by Water Radiolysis in Cement Paste under Electron Irradiation: A Joint Experimental and Theoretical Study, *Cement and Concrete Research*, 100:110–118.
- Le Pape, Y. (2015). Structural Effects of Radiation-Induced Volumetric Expansion on Unreinforced Concrete Biological Shields, *Nuclear Engineering and Design*, 295:534–548.
- Le Pape, Y., Field, K. G. and Remec, I. (2015b). Radiation Effects in Concrete for Nuclear Power Plants – Part II: Perspective from Micromechanical Modeling, *Nuclear Engineering and Design*, 282:144–157.
- Le Pape, Y. (2016). IMAC Database v.0.1. – Minerals, ORNL/TM-2016/753.
- Le Pape, Y., Alsaïd, M. H. F. and Giorla, A. B. (2018). Rock-Forming Minerals Radiation-Induced Volumetric Expansion – Revisiting the Literature Data, *Journal of Advanced Concrete Technology*, 16:191-209.
- Le Pape, Y. (2020). Radiation Effects in Concrete for Nuclear Systems, 2nd Edition. *Comprehensive Nuclear Materials*, Vol. 4, Elsevier.
- Le Pape, Y., Sanahuja, J. and Alsaïd, M. H. F. (2020b). Irradiation-Induced Damage in Concrete-Forming Aggregates -- Revisiting Literature Data through Micromechanics, *Materials and Structures*, 53(62):1–35.
- Lettow, S. (2006). *Ein Verbundelement für nichtlineare Finite Elemente Analysen - Anwendung auf Übergreifungsstöße (Bond Element for nonlinear Finite Element Analysis - Application to Lap Splices)*. Ph.D. thesis, Kassel University, Kassel.
- Li, Y., Le Pape, Y., Tajuelo Rodriguez, E., Torrence, C. E., Arregui Mena, D., Rosseel, T. M. and Sircar, M. (2020). Microstructural Characterization and Assessment of Mechanical Properties of Concrete Based on Combined Elemental Analysis Techniques and Fast-Fourier Transform-Based Simulations, *Construction and Building Materials*, 257(10):119500.
- Luikov, A. V. (1975). Systems of Differential Equations of Heat and Mass Transfer in Capillary-Porous Bodies (Review), *International Journal of Heat and Mass Transfer*, 18:1–14.
- Majorana, C. E., Salomoni, V. A. and Schrefler, B. A. (1998). Hygrothermal and Mechanical Model of Concrete at High Temperature, *Materials and Structures*, 31:378–386.
- Matijević, M., Pevec, Dubravko and Trontl, Krešimir (2015). Boration Modeling of the PWR Biological Shield Using SCALE 6.1 Hybrid Shielding Methodology, *Annals of Nuclear Energy*, 85:979–994.

- Maruyama, I., Nishioka, Y., Igarashi, G. and Matsui, K. (2014a). Microstructural and Bulk Property Changes in Hardened Cement Paste during the First Drying Process, *Cement and Concrete Research*, 58:20–34.
- Maruyama, I. and Sasano, H. (2014b). Strain and Crack Distribution in Concrete during Drying, *Materials and Structures*, 47(3):517–532.
- Maruyama, I., Sasano, H., Nishioka, Y. and Igarashi, G. (2014c). Strength and Young's modulus Change in Concrete Due to Long-Term Drying and Heating up to 90°C, *Cement and Concrete Research*, 66:48–63.
- Maruyama, I., Kontani, O., Takizawa, M., Sawada, S., Ishikawa, S., Yasukouchi, J., Sato, O., Etoh, J. and Igari, T. (2017). Development of the Soundness Assessment Procedure for Concrete Members Affected by Neutron and Gamma-Irradiation, *Journal of Advanced Concrete Technology*, 15:440–523.
- Mayer, G. and Gigon, J. (1956). Effets des Neutrons Rapides sur Quelques Constantes Physiques du Quartz Cristallin et de la Silice Vitreuse, *Le Journal de Physique et le Radium*, 18:109–114.
- Mayer, G. and Lecomte, M. (1960). Effet des Neutrons Rapides sur le Quartz Cristallin et la Silice Vitreuse, *Le Journal de Physique et le Radium*, 21(12):846–852.
- Mazars, J. and Pijaudier-Cabot, G. (1989). Continuum Damage Theory --Application to Concrete, *Journal of Engineering Mechanics – ASCE*, 115:345–365.
- McDowall, D. C. (1971). The Effects of Gamma Radiation on the Creep Properties of Concrete, *Proceedings of an Information Exchange Meeting on 'Results of Concrete Irradiation Programmes'*, Vol. EUR 4751 f-e : Brussels, Belgium, p. 55–69.
- Mirhosseini, S., Polak, M. A. and Pandey, M. (2014). Nuclear Radiation Effect on the Behavior of Reinforced Concrete Elements, *Nuclear Engineering and Design*, 269:57–65.
- Murty, K. L. (1984). Is Neutron Radiation Always Detrimental to Metal (Steels)? *Letters to Nature*, 308:51–52.
- Naus, D. J. (2005). The Effect of Elevated Temperature on Concrete Materials and Structures – A Literature Review, No. ORNL/TM-2005/553, *Oak Ridge National Laboratory*, Oak Ridge, TN.
- Pelessone, D. (2009). MARS: Modeling and Analysis of the Response of Structures—User's Manual. Beach, CA: ES3
- Pijaudier-Cabot, G. and Mazars, J. (2001). Damage Models for Concrete. Lemaitre, Jean (Ed.), *Handbook of Materials Behavior Models*, Failures of Materials, Elsevier, Vol. 2, p. 500–512
- Pignatelli, I., Kumar, A., Alizadeh, R., Le Pape, Y., Bauchy, M. and Sant, G. (2016). A Dissolution-Precipitation Mechanism Explains the origin of Concrete Creep in Moist Environments, *J. Chem. Phys.*, 145:054701.

Pomaro, B., Salomoni, V. A., Gramegna, F., Prete, G. and Majorana, C. E. (2011). Radiation Damage Evaluation on Concrete within a Facility for Selective Production of Exotic Species (SPES Project), Italy, *Journal of Hazardous Materials*, 194:169–177.

Pomaro, B., Xotta, G., Salomoni, V.A. and Majorana, C.E. (2022). A Thermo-Hydro-Mechanical Numerical Model for plain Irradiated Concrete in Nuclear Shielding. *Materials and Structures*, 55(14).

Remec, I., Field, K. G., Naus, D. J., Rosseel, T. M. and Busby, J. T. (2013). Concrete Aging and Degradation in NPPs: LWRs Program R&D Progress Report, *ANS Winter Meeting and Nuclear Technology Expo*, Washington, D.C.

Remec, I. (2015). Status Report on Defining a Unified Parameter for Characterization of Radiation Intended for Evaluation of Radiation-Induced Degradation of Concrete, No. ORNL/LTR-2015/542, *Oak Ridge National Laboratory*.

Remec, I., Rosseel, T. M., Field, K. G. and Le Pape, Y. (2018). Radiation-Induced Degradation of Concrete in NPPs, Sparks, M. H., DePriest, K. R. and Vehar, D. W. (Eds.). *Reactor Dosimetry: 16th International Symposium*, Vol. ASTM STP1608: 201–211.

Risner, J., Alpan, A. and Yang, J. (2020). Radiation Evaluation Methodology for Concrete Structures, No. NUREG/CR-7281 ORNL/SPR-2020/1572, *U.S. Nuclear Regulatory Commission*.

Rymeš, J., Maruyama, I., Shimamoto, R., Tachibana, A., Tanaka, Y., Sawada, S., Ichikawa, Y. and Kontani, O. (2019). Long-term Material Properties of a Thick Concrete Wall Exposed to Ordinary Environmental Conditions in a Nuclear Reactor Building: The Contribution of Cement Hydrates and Feldspar Interaction, *Journal of Advanced Concrete Technology*, 17(5):195-215.

Salomoni, V. A., Majorana, C. E., Pomaro, B., Xotta, G. and Gramegna, F. (2014). Macroscale and Mesoscale Analysis of Concrete as a Multiphase Material for Biological Shields against Nuclear Radiation, *International Journal for Numerical and Analytical Methods in Geomechanics*, 38:418–535.

Schrefler, B. A., Simoni, L. and Majorana, C. E. (1989). A General Model for the Mechanics of Saturated-Unsaturated Porous Materials, *Materials and Structures*, 22:323–334.

Shen, L., Li, W., Zhou, X., Feng, J., di Luzio, G., Ren, Q., & Cusatis, G. (2020). Multiphysics Lattice Discrete Particle Model for the Simulation of Concrete Thermal Spalling, *Cement and Concrete Composites*, 106, 103457.

Spencer, B. W., Hoffman, W. M., Biswas, S., Jiang, W., Giorla, A. and Backman, M. A. (2021) Grizzly and BlackBear: Structural Component Aging Simulation Codes, *Nuclear Technology*, 207(7): 981–1003.

Tajuelo Rodriguez, E., Richardson, I. G., Black, L., Boehm-Courjault, E., Nonat, A. and Skibsted, J. (2015). Composition, Silicate Anion Structure and Morphology of Calcium-Silicate Hydrates (C-S-H) Synthesised by Silica-Lime Reaction and by Controlled Hydration of Tricalcium Silicate (C<sub>3</sub>S), *Advances in Applied Ceramics*, 114(7):362–371.

Torrence, C. E., Giorla, A. B., Li, Y., Tajuelo Rodriguez, E., Mena, J. D. Arregui, Rosseel, T. M. and Le Pape, Y. (2021). MOSAIC: An Effective FFT-based Numerical Method to Assess Aging Properties of Concrete, *Journal of Advanced Concrete Technology*, 19(2):149–167.

Torrenti, J.M. and Le Roy, R. (2018). Analysis of Some Basic Creep Tests on Concrete and Their Implications for Modeling. *Structural Concrete*, 19 (2), 483–488.

Vecchio, F. and Collins, M. P. (1982). The Response of Reinforced Concrete to In-Plane Shear and Normal Stresses, No. 82-03, *University of Toronto*.

Vecchio, F. J. and Collins, M. P. (1986). The Modified Compression-Field Theory for Reinforced Concrete Elements Subjected to Shear, *ACI Journal*, 83:219–231.

Verrall, S. and Fitzpatrick, J. (1985). Design Concepts to Minimize the Activation of the Biological Shield of Light-Water Reactors, No. EUR 8804 Commission of the European Communities, *Commission of the European Communities*,

Wall, J. J. (2016). Structural Disposition of Neutron Radiation Exposure in BWR Vessel Support Pedestals, No. 3002008128, *Electric Power Research Institute*.

Yokokura, K., Wada, H., Kontani, O. and Maruyama, I. (2017). Concrete Strength Evaluation of Massive Concrete Structures Based on the Data Obtained from Decommissioning Nuclear Power Plant, *Transactions, SMiRT-24*.

Zhang, J., Pomaro, B., Mazzucco, G., Freinrich Dongmo, B., Majorana, C. and Salomoni, V. (2024). A 3D Coupled Thermo-Mechanical and Neutron Diffusion Numerical Model for Irradiated Concrete, *International Journal of Mechanical Sciences*, 264:108806.

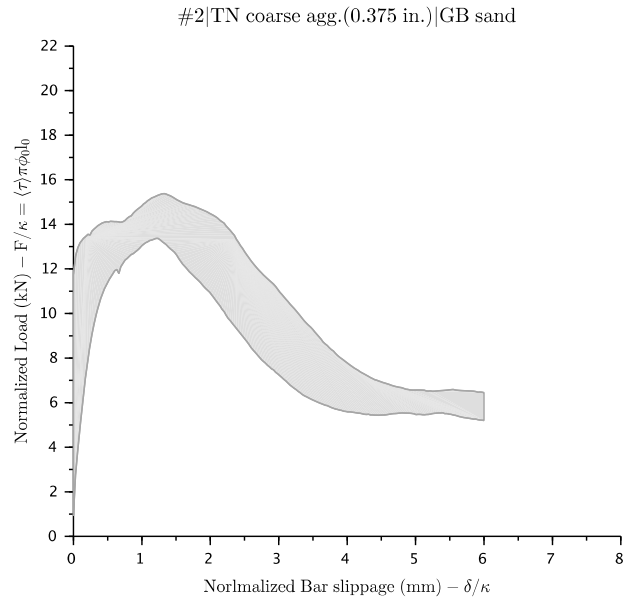
Zubov, V. G. and Ivanov, A. T. (1966). Expansion of Quartz Caused by Irradiation with Fast Neutrons, *Soviet Physics Crystallography*, 11(3):372–374.

## **APPENDIX A   BOND TEST RESULTS – SCALE EFFECTS CAMPAIGN**

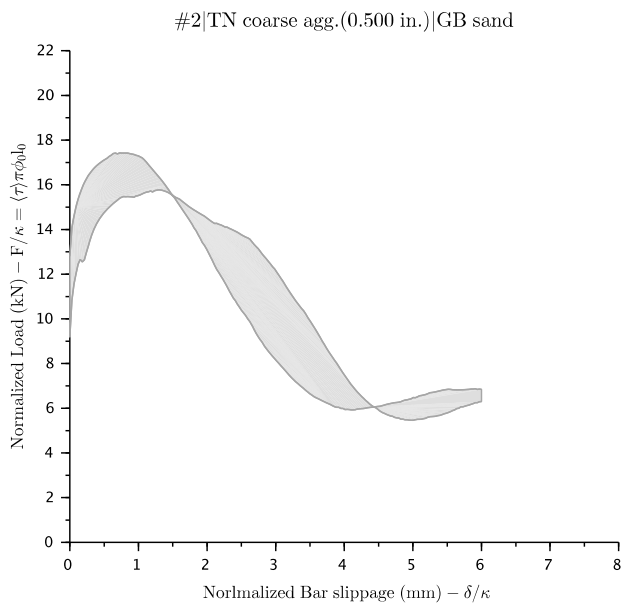
### **A.1   Bond Test Results – Scale Effects Studies**

#### **A.1.1   Dimensional Factors**

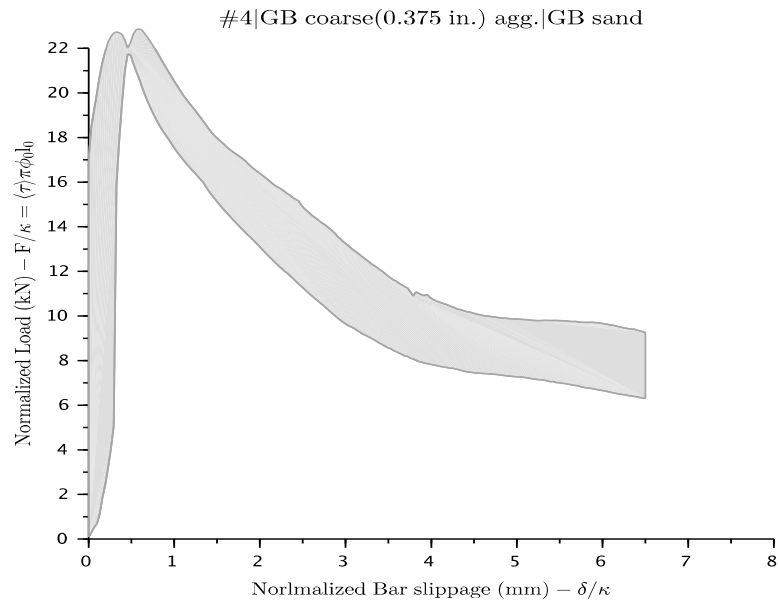




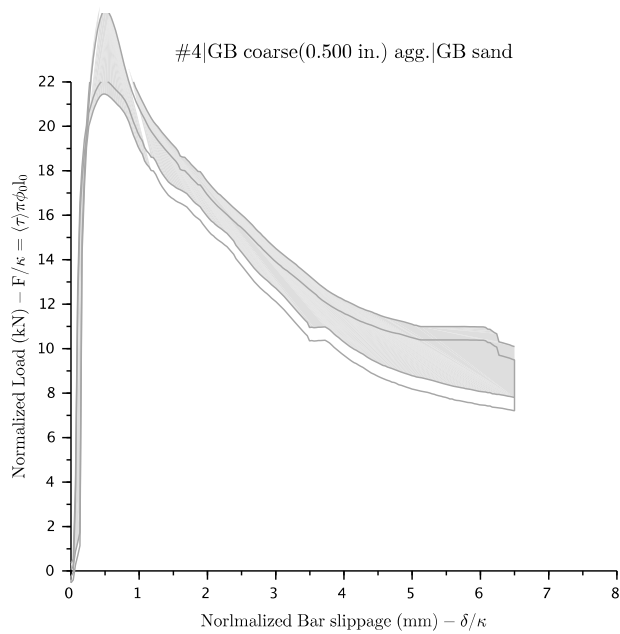
**Figure A-1** Normalized Pullout Force  $F/(\kappa^2)$  vs. Normalized Slippage. #2  
| TN Coarse Aggregate (0.375 in.) | GB Sand



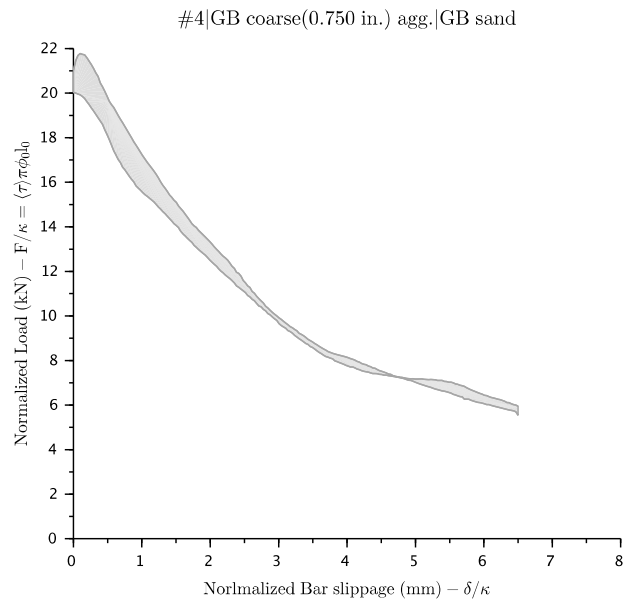
**Figure A-2** Normalized Pullout Force  $F/(\kappa^2)$  vs. Normalized Slippage. #2  
| TN Coarse Aggregate (0.500 in.) | GB Sand



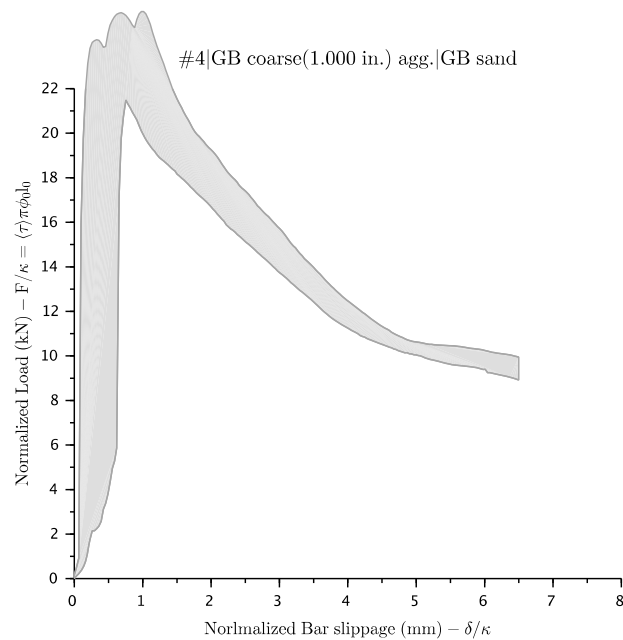
**Figure A-3** Normalized Pullout Force  $F/(\kappa^2)$  vs. Normalized Slippage. #4  
| GB Coarse Aggregate (0.375 in.) | GB Sand



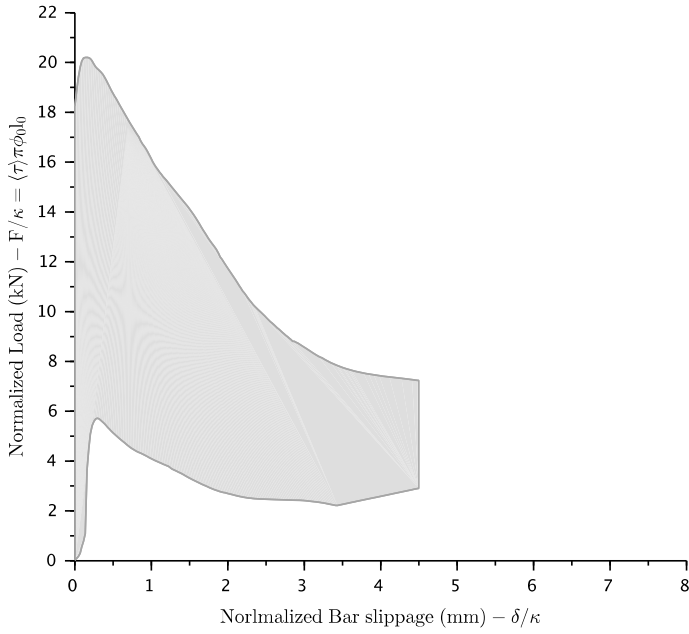
**Figure A-4** Normalized Pullout Force  $F/(\kappa^2)$  vs. Normalized Slippage. #4  
| GB Coarse Aggregate (0.500 in.) | GB Sand



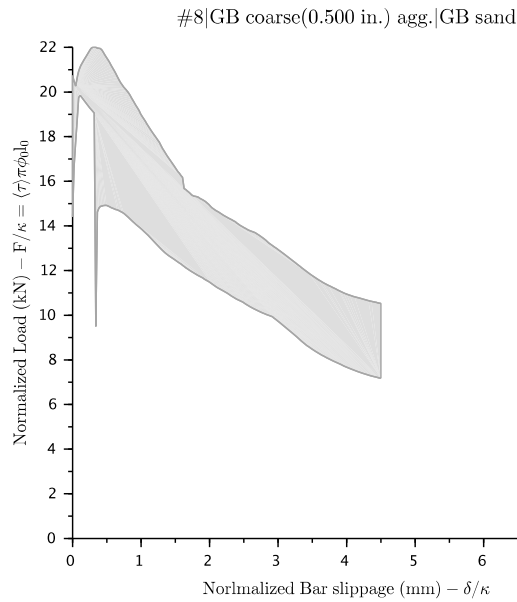
**Figure A-5** Normalized Pullout Force  $F/(\kappa^2)$  vs. Normalized Slippage. #4  
| GB Coarse Aggregate (0.750 in.) | GB Sand



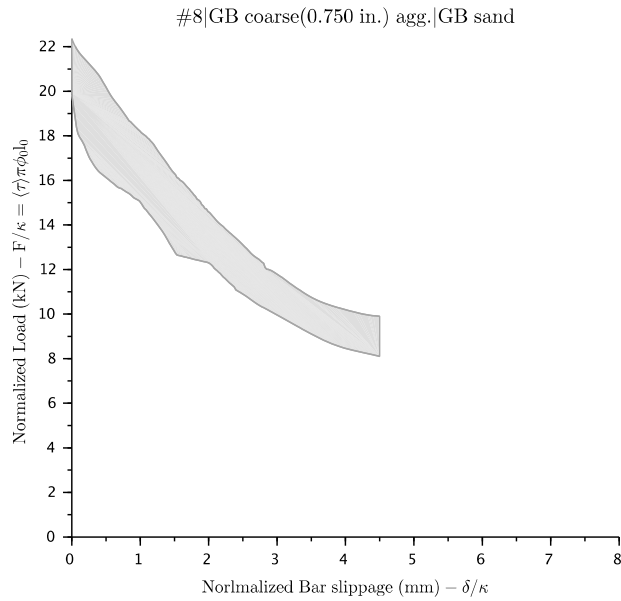
**Figure A-6** Normalized Pullout Force  $F/(\kappa^2)$  vs. Normalized Slippage. #4  
| GB Coarse Aggregate (1.000 in.) | GB Sand



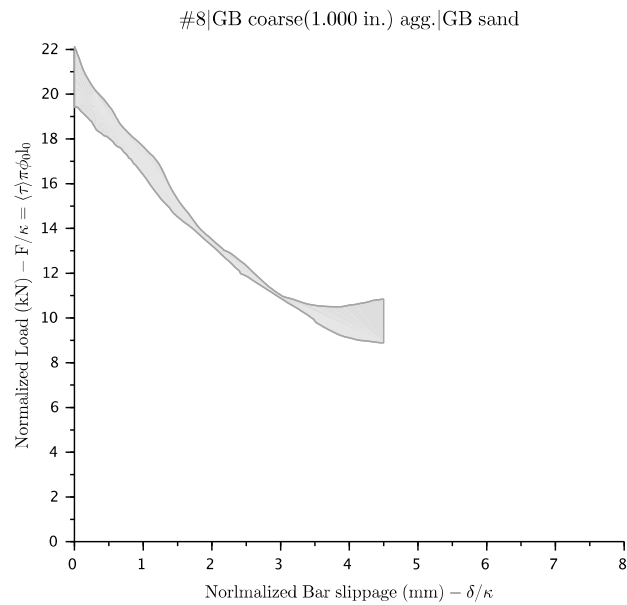
**Figure A-7** Normalized Pullout Force  $F/(\kappa^2)$  vs. Normalized Slippage. #4  
| GB Coarse Aggregate (0.375 in.) | GB Sand



**Figure A-8** Normalized Pullout Force  $F/(\kappa^2)$  vs. Normalized Slippage. #4  
| GB Coarse Aggregate (0.500 in.) | GB Sand

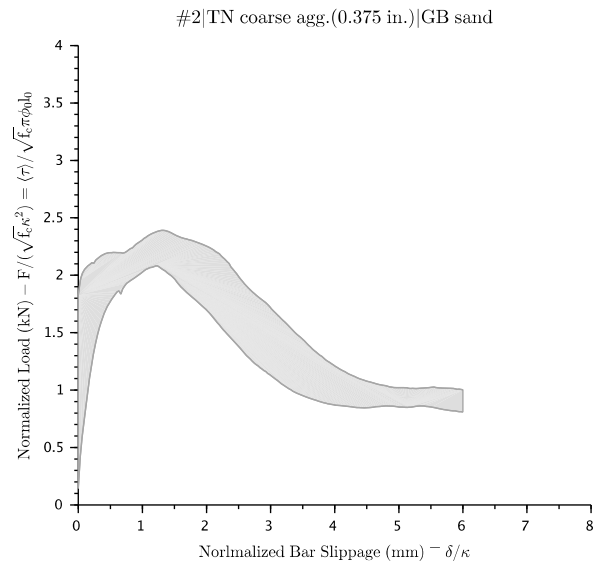


**Figure A-9** Normalized Pullout Force  $F/(\kappa^2)$  vs. Normalized Slippage. #4  
| GB Coarse Aggregate (0.750 in.) | GB Sand

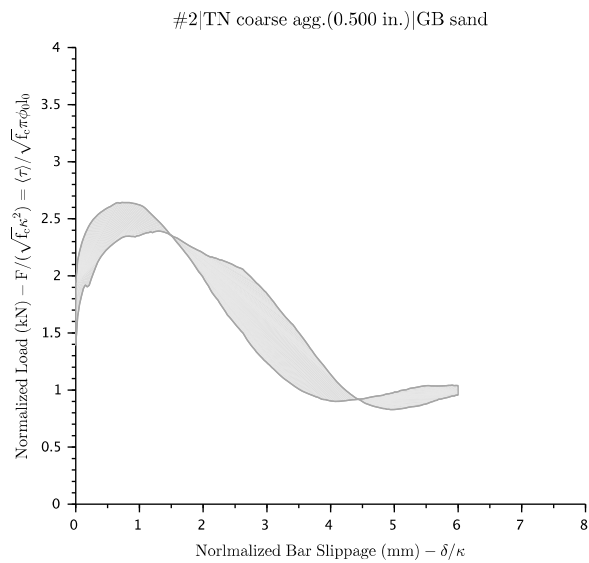


**Figure A-10** Normalized Pullout Force  $F/(\kappa^2)$  vs. Normalized Slippage. #4  
| GB CoarseAggregate (1.000 in.) | GB Sand

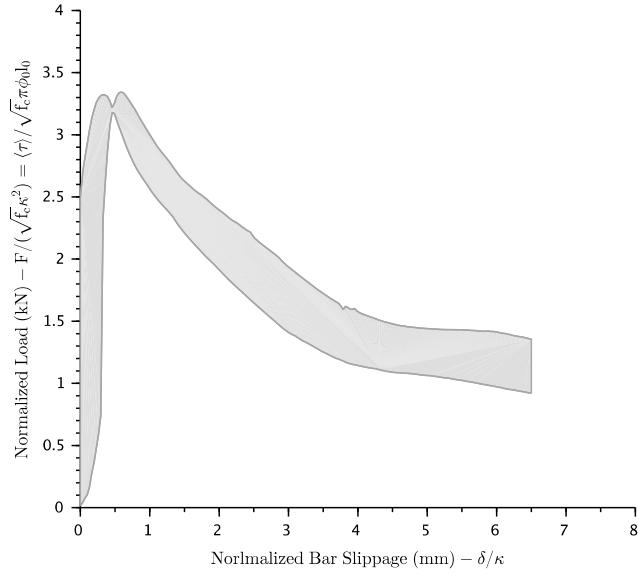
## A.1.2 Strength Factor



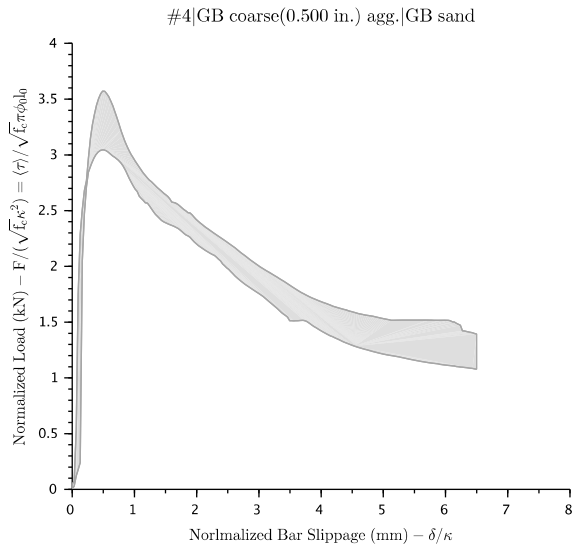
**Figure A-11** Normalized Pullout Force  $F/(\kappa^2 \sqrt{f_c})$  vs. Normalized Slippage. #2  
| TN Coarse Aggregate (0.375 in.) | GB Sand



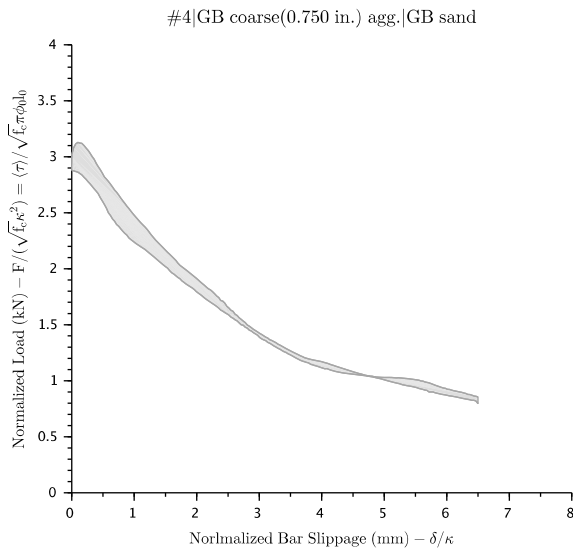
**Figure A-12** Normalized Pullout Force  $F/(\kappa^2 \sqrt{f_c})$  vs. Normalized Slippage. #2  
| TN Coarse Aggregate (0.500 in.) | GB Sand



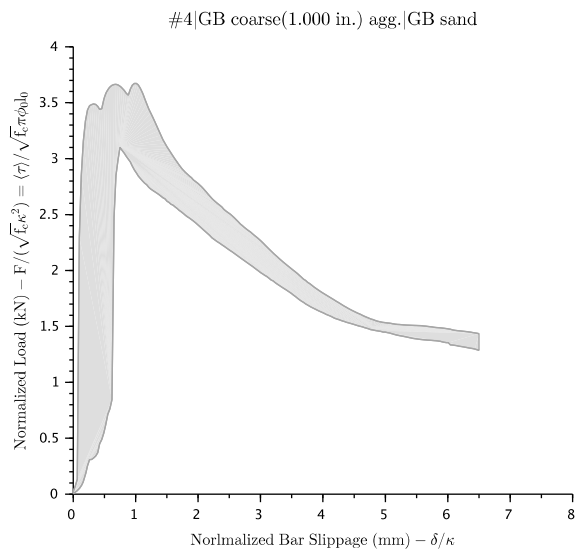
**Figure A-13** Normalized Pullout Force  $F / (\kappa^2 \sqrt{f_c})$  vs. Normalized Slippage. #4 | GB Coarse Aggregate (0.375 in.) | GB Sand



**Figure A-14** Normalized Pullout Force  $F / (\kappa^2 \sqrt{f_c})$  vs. Normalized Slippage. #4 | GB Coarse Aggregate (0.500 in.) | GB Sand

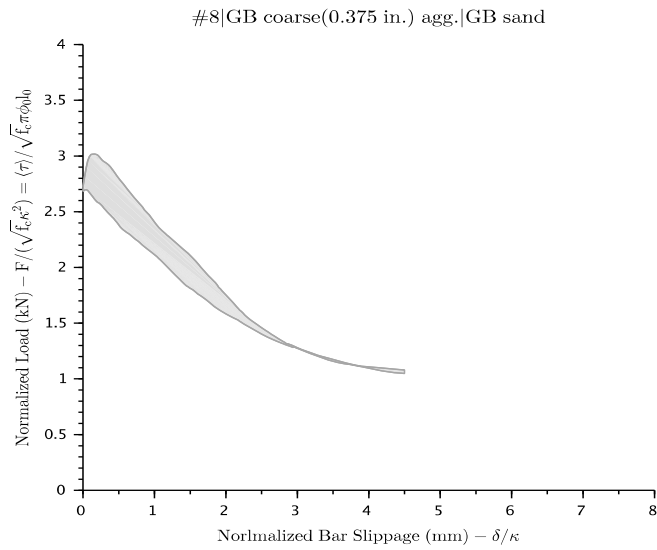


**Figure A-15** Normalized Pullout Force  $F/(\kappa^2 \sqrt{f_c})$  vs. Normalized Slippage. #4  
| GB Coarse Aggregate (0.750 in.) | GB Sand

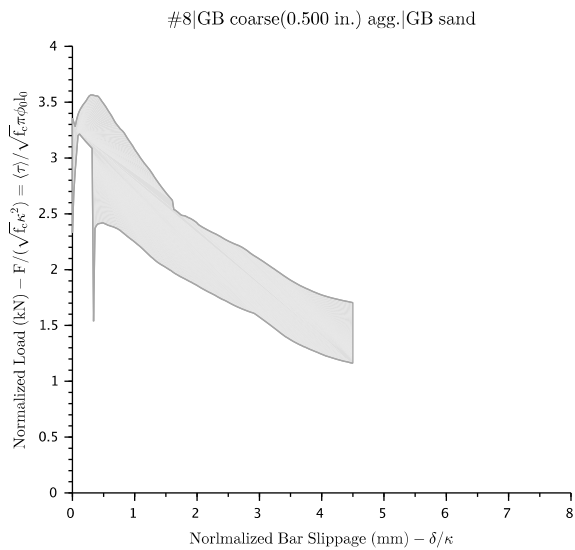


**Figure A-16** Normalized Pullout Force  $F/(\kappa^2 \sqrt{f_c})$  vs. Normalized Slippage. #4  
| GB Coarse Aggregate (1.000 in.) | GB Sand

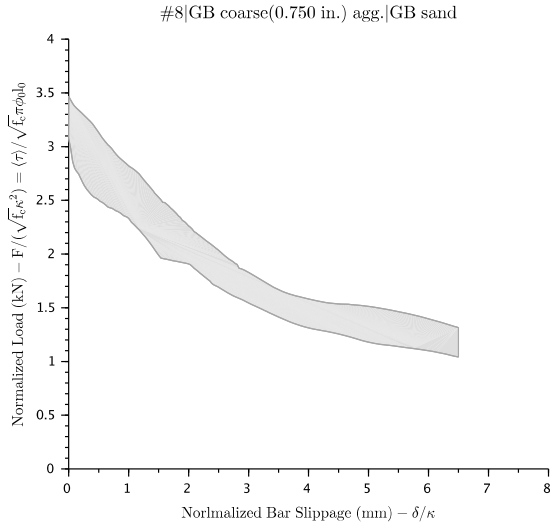




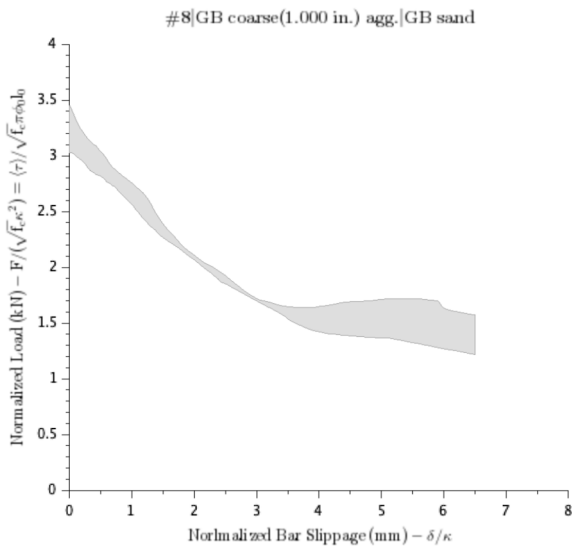
**Figure A-17** Normalized Pullout Force  $F/(\kappa^2 \sqrt{f_c})$  vs. Normalized Slippage. #8  
| GB Coarse Aggregate (0.375 in.) | GB Sand



**Figure A-18** Normalized Pullout Force  $F/(\kappa^2 \sqrt{f_c})$  vs. Normalized Slippage. #8  
| GB Coarse Aggregate (0.500 in.) | GB Sand

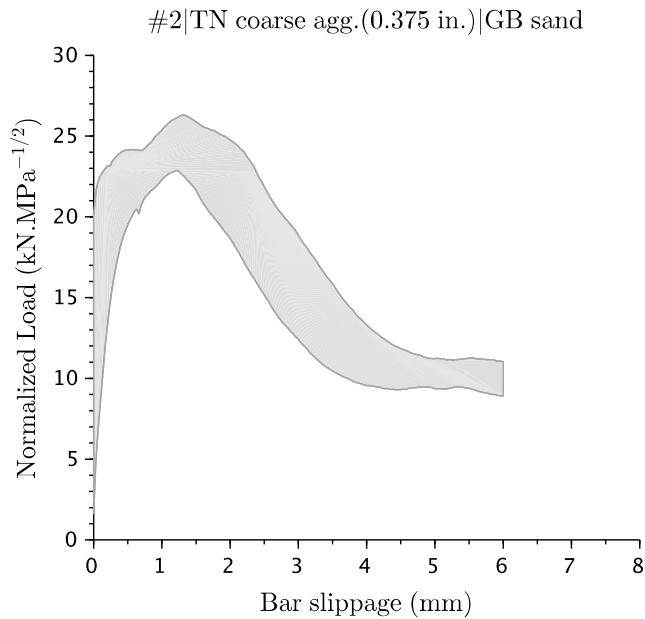


**Figure A-19** Normalized Pullout Force  $F/(\kappa^2 \sqrt{f_c})$  vs. Normalized Slippage. #8  
| GB Coarse Aggregate (0.750 in.) | GB Sand

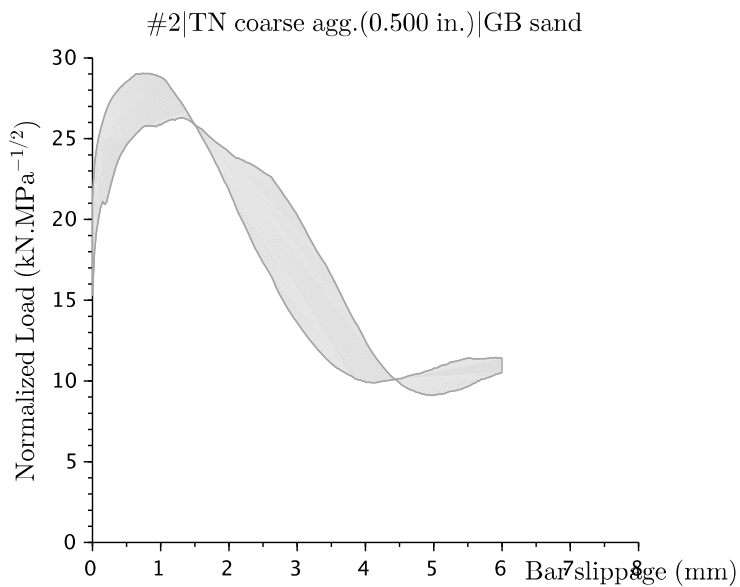


**Figure A-20** Normalized Pullout Force  $F/(\kappa^2 \sqrt{f_c})$  vs. Normalized Slippage. #8  
| GB Coarse Aggregate (1.000 in.) | GB Sand

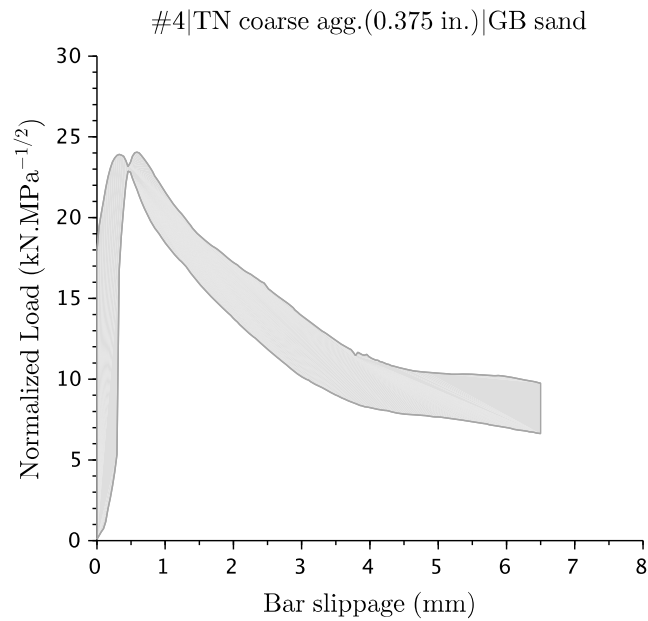
### A.1.3 Combined Strength and Rib Factors



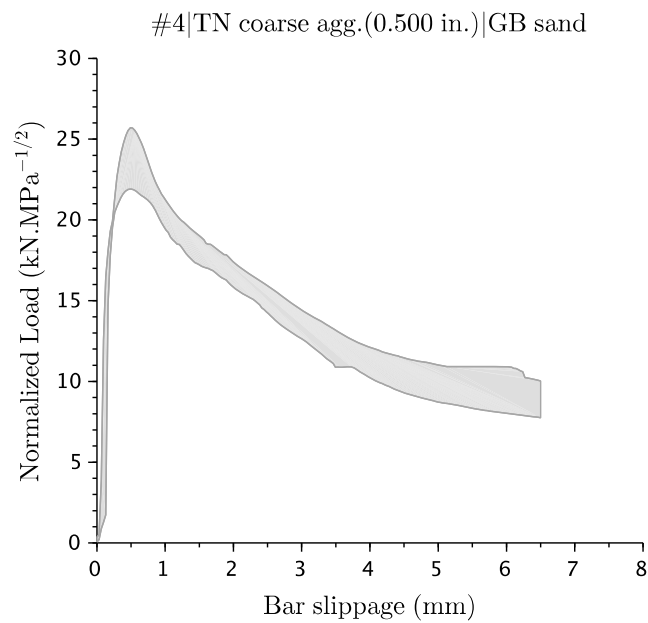
**Figure A-21** Normalized Pullout Force  $F/(\kappa^2 \sqrt{f_c} f_r^{0.8})$  vs. Normalized Slippage. #2 | GB Coarse Aggregate (0.375 in.) | GB Sand



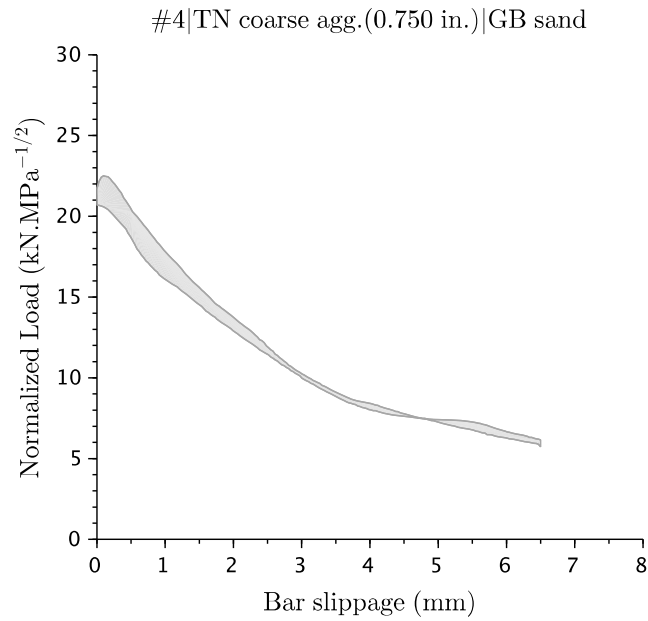
**Figure A-22** Normalized Pullout Force  $F/(\kappa^2 \sqrt{f_c} f_r^{0.8})$  vs. Normalized Slippage. #2 | GB Coarse Aggregate (0.500 in.) | GB Sand



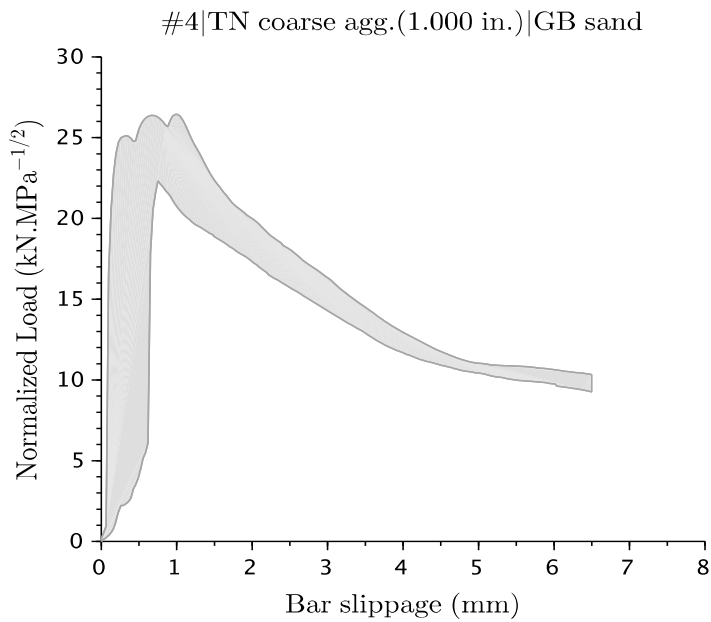
**Figure A-23** Normalized Pullout Force  $F/(\kappa^2 \sqrt{f_c} f_r^{0.8})$  vs. Normalized Slippage. #4 | GB Coarse Aggregate (0.375 in.) | GB Sand.



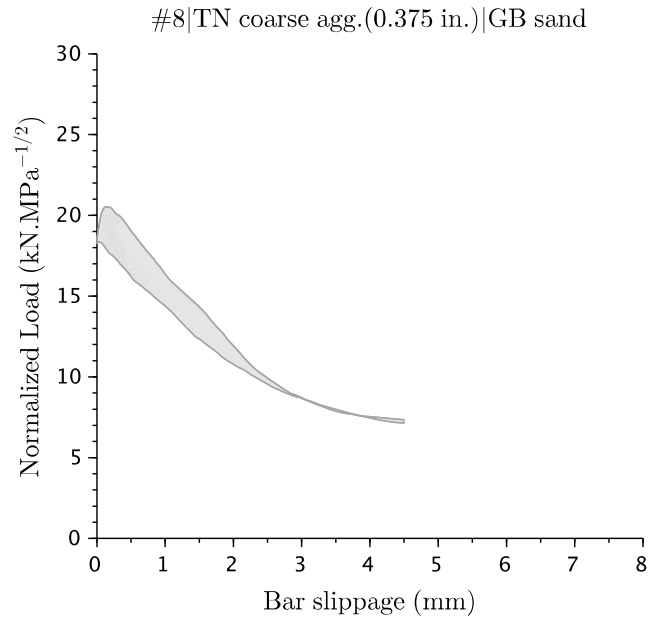
**Figure A-24** Normalized Pullout Force  $F/(\kappa^2 \sqrt{f_c} f_r^{0.8})$  vs. Normalized Slippage. #4 | GB Coarse Aggregate (0.500 in.) | GB Sand



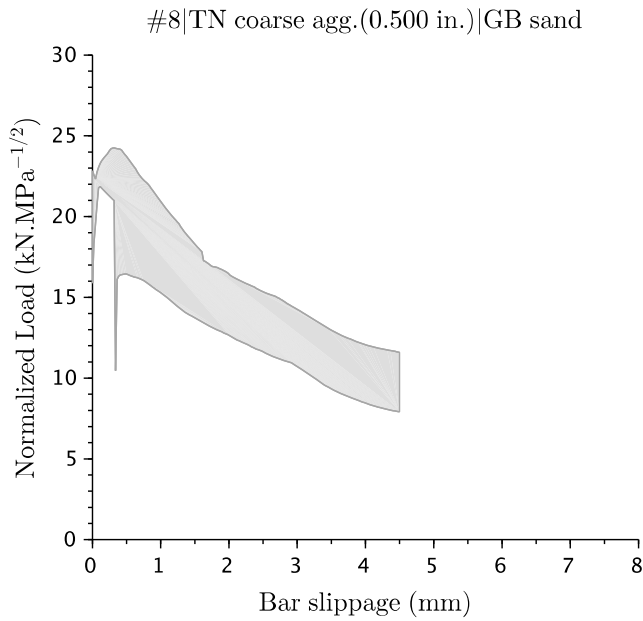
**Figure A-25** Normalized Pullout Force  $F/(\kappa^2 \sqrt{f_c} f_r^{0.8})$  vs. Normalized Slippage. #4 | GB Coarse Aggregate (0.750 in.) | GB Sand



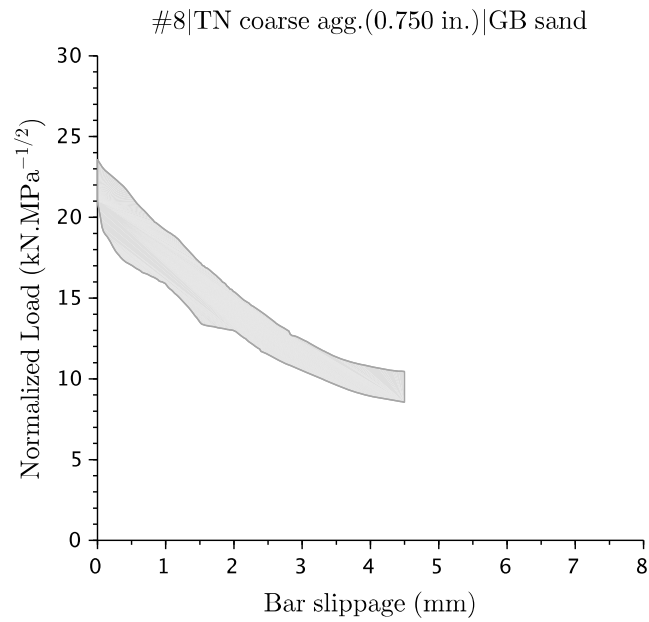
**Figure A-26** Normalized Pullout Force  $F/(\kappa^2 \sqrt{f_c} f_r^{0.8})$  vs. Normalized Slippage. #4 | GB Coarse Aggregate (1.000 in.) | GB Sand



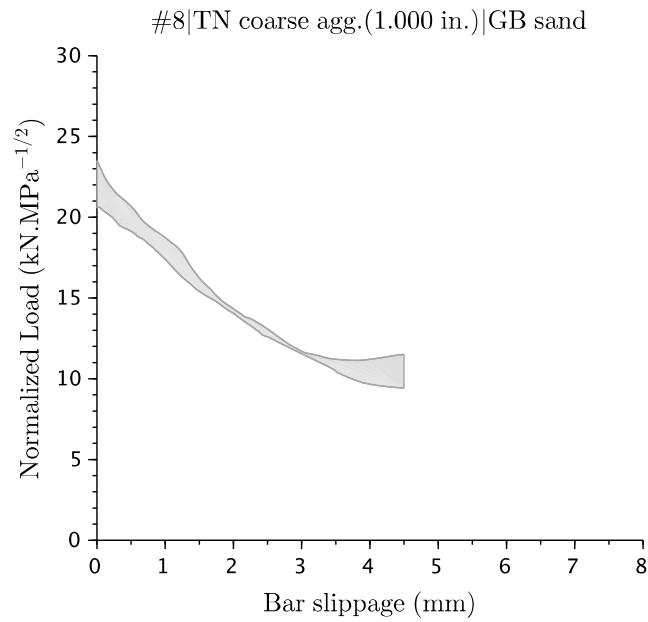
**Figure A-27** Normalized Pullout Force  $F/(\kappa^2 \sqrt{f_c} f_r^{0.8})$  vs. Normalized Slippage. #8  
| GB Coarse Aggregate (0.375 in.) | GB Sand



**Figure A-28** Normalized Pullout Force  $F/(\kappa^2 \sqrt{f_c} f_r^{0.8})$  vs. Normalized Slippage. #8  
| GB Coarse aggregate (0.500 in.) | GB Sand



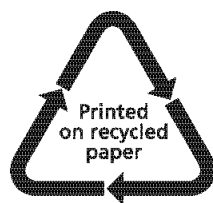
**Figure A-29** Normalized Pullout Force  $F/(\kappa^2 \sqrt{f_c} f_r^{0.8})$  vs. Normalized Slippage. #8  
| GB Coarse Aggregate (0.750 in.) | GB Sand



**Figure A-30** Normalized Pullout Force  $F/(\kappa^2 \sqrt{f_c} f_r^{0.8})$  vs. Normalized Slippage. #8  
I Coarse Aggregate (1.000 in.) | GB Sand

<b>NRC FORM 335</b> (12-2010) NRCMD 3.7		<b>U.S. NUCLEAR REGULATORY COMMISSION</b>		<b>1. REPORT NUMBER</b> (Assigned by NRC, Add Vol., Supp., Rev., and Addendum Numbers, if any.)  <b>NUREG/CR-7312</b>	
<b>BIBLIOGRAPHIC DATA SHEET</b> <i>(See instructions on the reverse)</i>					
<b>2. TITLE AND SUBTITLE</b>  <b>Irradiation Effects on Reinforced Concrete Structures – Experimental and Analytical Study on Irradiated Concrete–Steel Bonding, Modeling and Simulation of Structural Response</b>				<b>3. DATE REPORT PUBLISHED</b>	
				MONTH <b>July</b>	YEAR <b>2025</b>
<b>5. AUTHOR(S)</b>  Yann Le Pape, Mohammed Alnaggar, Elena Tajuelo Rodriguez and Adam Brooks				<b>4. FIN OR GRANT NUMBER</b>	
				<b>6. TYPE OF REPORT</b>  Technical	
<b>8. PERFORMING ORGANIZATION - NAME AND ADDRESS</b> (If NRC, provide Division, Office or Region, U. S. Nuclear Regulatory Commission, and mailing address; if contractor, provide name and mailing address.) Oak Ridge National Laboratory One Bethel Valley Road Oak Ridge TN 37831				<b>7. PERIOD COVERED (Inclusive Dates)</b>	
				<b>9. SPONSORING ORGANIZATION - NAME AND ADDRESS</b> (If NRC, type "Same as above", if contractor, provide NRC Division, Office or Region, U. S. Nuclear Regulatory Commission, and mailing address.) Office of Regulatory Research U.S. Nuclear Regulatory Commission Washington, D.C. 20555-0001	
<b>10. SUPPLEMENTARY NOTES</b> Madhumita Sircar					
<b>11. ABSTRACT (200 words or less)</b>  This report details the research findings of the US Nuclear Regulatory Commission's project IAA #31310018S0021, which investigates the effects of irradiation on bond strength in concrete structures, focusing on reinforced concrete in nuclear power plants. The project involved a unique irradiation experiment conducted by Oak Ridge National Laboratory and Centrum Vizkumu Rež, using concrete samples with aggregates from the Japan Concrete Aging Management Program. Specimens were irradiated for about 800 days in the LVR-15 reactor, receiving a significant neutron flux of $\sim 10^{19}$ n/cm <sup>2</sup> (E > 0.1 MeV) and gamma dose of $\sim 1$ GGy. The study also included a parallel experiment to separate the effects of temperature from irradiation. Pre- and post-irradiation testing included microscopy, x-ray tomography, ultrasound, compression, and bond tests. Results showed that irradiation, particularly fast neutron flux, significantly impacted concrete aggregates' expansion. The bond strength between steel reinforcement and irradiated concrete was found to depend on the residual compressive strength of the concrete, with a scaling factor necessary to accurately predict bond strength. In addition, the study used advanced numerical models, including lattice discrete particle model and finite element analysis, to propose guidelines for assessing irradiation effects on concrete biological shields, especially regarding damage depth.					
<b>12. KEY WORDS/DESCRIPTORS</b> (List words or phrases that will assist researchers in locating the report.)  Concrete, irradiation, neutron, gamma, steel-concrete bond, irradiation damage, irradiation experiment				<b>13. AVAILABILITY STATEMENT</b> unlimited	
				<b>14. SECURITY CLASSIFICATION</b> <i>(This Page)</i> unclassified	
				<i>(This Report)</i> unclassified	
				<b>15. NUMBER OF PAGES</b>	
				<b>16. PRICE</b>	





Federal Recycling Program



UNITED STATES  
NUCLEAR REGULATORY COMMISSION  
WASHINGTON, DC 20555-0001  
OFFICIAL BUSINESS



**NUREG/CR-7312**

**Irradiation Effects on Reinforced Concrete Structures – Experimental and Analytical  
Study on Irradiated Concrete–Steel Bonding, Modeling and Simulation of Structural  
Response**

**July 2025**